Simulating the Developing Heart: Mechanistic Modeling of Left Ventricular Growth in Borderline Left Heart Hypoplasia

By

Ashley A. Hiebing

A dissertation submitted in partial fulfillment of

the requirements for the degree of

Doctor of Philosophy

(Biomedical Engineering)

at the

UNIVERSITY OF WISCONSIN–MADISON

2026

Date of final oral examination: 12/02/2025

The dissertation is approved by the following members of the Final Oral Committee:

Colleen Witzenburg, Assistant Professor, Biomedical Engineering

Kristyn Masters, Professor, Biomedical Engineering

Alejandro Roldán Alzate, Associate Professor, Mechanical Engineering

Darryl Thelen, Professor, Mechanical Engineering

J. Carter Ralphe, Professor, Pediatrics

This work is dedicated to every young woman struggling to find her way.

Keep fighting. It’s worth it.

Abstract

Congenital heart disease (CHD) remains the most prevalent major birth defect, affecting millions of children globally each year. Though advances in surgical and medical care have substantially improved survival, long-term morbidity persists, often due to maladaptive cardiac and vascular remodeling. Whether from congenital lesions or their surgical correction, abnormal ventricular loading leads to complex growth and remodeling processes that initially compensate for increased stress but ultimately lead to dysfunction and heart failure. Predicting these growth patterns, particularly in children whose hearts are concurrently undergoing somatic development, remains a significant clinical challenge.

This dissertation develops a unified computational framework linking hemodynamics and ventricular growth across health and disease, with specific applications to coarctation of the aorta (CoA) and borderline left heart (BLH) hypoplasia. A reduced-order lumped parameter circulation model was first used to study the hemodynamic and structural consequences of CoA and its surgical repair in a rabbit model. By employing inverse modeling to fit simulation outputs to experimental data, we identified persistent reductions in ascending aortic compliance even after CoA correction, suggesting enduring vascular remodeling.

To establish a healthy baseline for pathologic growth studies, the circulation model was extended and coupled to a strain-based growth model to simulate normal somatic

ventricular growth during infancy. Using weight-based allometric scaling and maturation functions to generate input parameters, the model simulated normal cardiac growth from birth to three years of age. Model validation against published clinical data confirmed that outputs for pressures, chamber volumes, and wall thicknesses fell within expected physiological ranges.

Building upon these validated results, the framework was applied to simulate staged left ventricular recruitment (SLVR), a novel surgical strategy for infants with BLH. Through simultaneous simulations across a range of patient phenotypes, we explored the factors governing successful versus unsuccessful SLVR outcomes, where success was defined by the current clinical standard of a post-SLVR indexed left ventricular end-diastolic volume > 40 ml/m^2. Machine learning analysis of model results identified initial left ventricular end-diastolic volume Z-score, presence of endocardial fibroelastosis, and degree of aortic valve regurgitation as key determinants of SLVR success or failure. Successful cases demonstrated balanced hypertrophic growth (increased wall thickness and cavity volume), whereas failed cases exhibited minimal adaptive hypertrophy beyond somatic growth expectations.

Overall, this work integrates somatic development and pathologic adaptation into a cohesive computational growth framework. The models advance our understanding of how persistent mechanical abnormalities drive both adaptive and maladaptive remodeling, providing tools for optimizing surgical decision-making in complex congenital heart disease.

Acknowledgements

I never wanted to be an engineer. As a kid, when adults asked me what I wanted to be when I grew up, I would say, “An artist.” As a teenager, my answer vacillated between “A writer, maybe?” and a despondent shrug, depending on the day. The only classes I enjoyed were art and English—math classes were spent reading novels or catching up on sleep. In my mind, there were two types of people: math people and non-math people, and I was a proud member of the latter.

I never wanted a PhD, either. Again, that was something I had decided was reserved for others, a higher echelon that I was never meant to reach. Certainly not something a two-time college dropout should even be allowed to want, much less earn.

Third time’s the charm, I suppose.

A lot of people helped me become what I never thought I could be. First off, I want to thank my advisor and certified Math Person, Dr. Colleen Witzenburg. Throughout my time at UW, you’ve needed to be a mentor, a manager, a teacher, a peer, a therapist, and a friend. You have thoroughly excelled at every role. I am a better scientist because of you, but more importantly, I am a better *person* because of you. I’ll forever be grateful for whatever twist of fate made us both show up way too early to the UW event at BMES 2018. Thank you for taking a chance on me.

Colleen’s values are reflected in the people she chooses for her lab; I’m honored to have had the opportunity to work alongside so many kind, intelligent people. To my fellow veteran grad students—Daniel, Callyn, Cate, and Matt—thank you for your understanding,

advice, and delightful senses of humor. To Azmal, Peyton, and Diya: you're going to do great. Please make better lab notebooks than I did.

I would also like to thank my committee members: Dr. Kristyn Masters, Dr. Alejandro Roldán Alzate, Dr. Darryl Thelen, and Dr. Carter Ralphe for their guidance and insightful suggestions, especially when my thesis project needed to take a considerable detour. In addition, the Department of Biomedical Engineering as a whole is full of lovely people with whom I've had the pleasure of meeting during my time here. In particular, thank you to David Esteves, Janna Pollock, Mondira Saha-Muldowney, Dr. Pam Kreeger, Dr. Paul Campagnola, Sam Jost, Shanna Hargrove, and Vishmaa Ramsaroop-Briggs for great conversations and all your efforts to keep the department running through pandemics, floods, and Monday mornings.

Graduate school can be hard, but other things in life are much, much harder. I owe a huge debt of gratitude to Dr. Bailey, Dr. Zafar, and everyone at UW's Carbone Cancer Center for making those "other things" a little easier to bear.

No matter where I end up, I'll always be an East Side girl. Shoutout to a few local places I'm really going to miss: Ford's Gym, Jenifer Street Market, Rotunda Café, Wilalby's, The Majestic Theatre, Chocolate Shoppe, Glass Nickel Pizza, Olbrich Gardens, Batch Bakehouse, Banzo, and all the tiny unnamed spots around our beautiful lakes where I've done a lot of sitting and thinking over the years.

Though I have historically been a bit self-conscious about revealing myself as a K-pop fangirl, I would be remiss not to acknowledge how much joy it's brought to my life. Two

groups in particular, Girls' Generation and Dreamcatcher, have provided much-needed sources of escapism throughout this process. If anyone wants to hear another dissertation, feel free to ask me about either of them.

To my friends, both near and far: Billy, Alex, Corinne, Allison, Maude, and all my Discord buddies who helped keep me (mostly) sane during COVID, cancer treatment, thesis writing, and everything else. Y'all are amazing.

Finally, to my wife, Lili. Honestly, I've spent days trying to write this paragraph; I think I've written and erased it a hundred times hoping to come up with something that isn't just a load of maudlin cliches. The best I can do is limit it to only one: the most important lesson I've learned during graduate school is that our time on this earth is painfully finite. Thank you for choosing to spend it with me.

Table of Contents

LIST OF FIGURES

Page

Chapter 1

Chapter 2

Chapter 3

Chapter 4

Chapter 5

LIST OF TABLES

Chapter 3

Chapter 5

Chapter 1: Introduction

Abbreviations

BLH: borderline left heart

CHD: congenital heart disease

CoA: coarctation of the aorta

LV: left ventricle

RV: right ventricle

SLVR: staged left ventricular recruitment

SV: single ventricle

Background and Clinical Motivation

Congenital heart disease (CHD) affects between 560,000 to 7 million children born per year, making it the most common form of major birth defects [1, 2]. Advances in care have significantly reduced mortality rates, with the largest reduction occurring in infants and children with severe forms of CHD [2, 3], where surgical intervention is required in the first year of life. The number of adults living with severe CHDs now rivals the number of children [4], and it is expected that 85% of children born today with severe CHDs can expect to live into adulthood [5]. However, with that reduction comes increased rates of complications persisting well past adolescence, including systemic or pulmonary hypertension, aneurysm, and arrhythmias [3].

All CHDs lead to abnormal loading of the ventricles [6]. For example, coarctation of the aorta leads to pressure overload of the left ventricle (LV) due to increased afterload [7],

while the LV of a patient with a large ventricular septal defect can experience volume overload from pulmonary over-circulation arising from left-to-right shunting [8]. The ventricles adapt to the abnormal loading conditions at both the macroscopic and microscopic levels in a simultaneous process of growth and remodeling (colloquially, these are often combined into a singular "remodeling"). During growth, cardiomyocytes respond to increased stress and strain by hypertrophying, expanding the ventricular cavity volume in response to volume overload (eccentric hypertrophy) and/or increasing the ventricular wall thickness in response to pressure overload (concentric hypertrophy) [9]. During remodeling, the cellular composition and extracellular matrix of the ventricle changes, often characterized by myocyte hypertrophy or apoptosis, fibroblast infiltration, and interstitial fibrosis [10]. Though in the short term growth and remodeling can initially attenuate the increased stress from abnormal loading patterns, in the long term it is ultimately a maladaptive process—the abnormal ventricles produce abnormal hemodynamics, which lead to adverse remodeling in the intrathoracic great vessels, which leads to abnormal loading of the ventricles. This vicious cycle continues until the ventricles can no longer compensate, with heart failure soon to follow [11].

Even with treatment, most abnormal loading conditions are not completely eliminated, particularly when remodeling has already occurred [12–14]. Occasionally, abnormal loading is inherently part of the treatment itself. Patients with hypoplastic left heart syndrome, for example, will unavoidably experience both types of overloading to various degrees throughout the course of surgical palliation, which reroutes blood flow in each of

the three staged surgeries [15]. These multiplicative changes to ventricular loading in both pathology and treatment make predicting outcomes—especially in growing children—incredibly challenging.

Computational models are useful tools for addressing this challenge. By translating the cardiovascular system into discrete interconnected elements, the in-silico environment allows researchers to overcome limitations of traditional studies: patient populations are potentially infinite, computational models are risk free, and the effects of interventions can be analyzed in isolation. Cardiovascular models have been designed with a wide range of fidelity, from three-dimensional models replicating patient-specific anatomy from MR or CT imaging to zero-dimensional models of the average adult human circulation [16]. All have their own benefits and drawbacks. Higher-order models are ideal for analyzing local effects such as myocardial stress and strain distributions [17], velocity profiles [18], and energy losses [19], and are often preferred when modeling individual patients [16]. However, they pay for their precision with high computational expense, making simulation of long-term, iterative processes like growth and remodeling impractical for clinical translation [20]. In contrast, reduced-order models sacrifice local spatial fidelity for speed, allowing for the efficient simulation of global hemodynamics. Faster computation times give reduced-order models an advantage in tasks that require numerous consecutive simulations, such as growth modeling, patient-specific parameterization, and sensitivity and uncertainty analyses [21, 22]. Of those tasks, growth modeling has proved the most challenging, with the highest potential benefits in making longitudinal predictions. For soft tissues, two

methods are commonly employed in computational models: the simpler volumetric growth theory, which treats the tissue as a uniform material [23], and the more complex constrained mixture theory, which considers multiple constituents, each with their own rates of cell turnover and evolving material properties [24]. For a more thorough explanation of soft tissue growth models, we refer interested readers to reviews by Humphrey [25] and Yoshida and Holmes [26].

Vascular Remodeling and Load: Lessons from Coarctation of the Aorta

Coarctation of the aorta (CoA) is a congenital cardiovascular lesion that typically presents as a localized narrowing of the proximal descending aorta just distal to the left subclavian artery. The constriction forces the LV to work harder to pump blood to the systemic circulation, often leading to concentric LV hypertrophy as well as hypertension [27–30]. The vessels surrounding the coarctation remodel in response to the abnormal flow pattern: proximal to the coarctation, vessel walls present with fibrosis, intimal thickening, and elastin degradation, all of which increase stiffness [31, 32]. Immediately downstream of the coarctation, a high velocity jet impacts the aortic wall, increasing wall shear stress and causing endothelial dysfunction [12].

Much of this adverse remodeling—and the symptoms that come with it—appears to persist even after coarctation repair [29, 30, 33]. However, the incidence and time course of the remodeling are highly variable, and no single clinical metric fully describes the interplay between cardiovascular remodeling and function. To that end, we developed a zero-dimensional lumped parameter model of the heart and circulation capable of simulating

aortic coarctation, then used it to estimate differences in ascending aortic compliance and peripheral resistance from imaging and catheterization data collected using a rabbit model of CoA and correction [34]. We used an inverse modeling approach, fitting our unknown input parameters by minimizing the difference between model hemodynamic outputs and experimental measurements. By examining the final values of those parameters between each group, we could gain insight into similarities and differences between the control, CoA, and treated groups. In particular, we found that we could not match the hemodynamics of the CoA or the treated group without reducing ascending aortic compliance from its control value, suggesting these groups experienced aortic remodeling that persisted after coarctation repair. In addition, both groups required an increase in the parameter dictating LV thickness, though the magnitude of increase was less in the corrected group, and the increase in measured thickness between the corrected and control groups was not significant. This suggests the potential for a partial reversal of hypertrophy after treatment, aligning with results in humans with CoA [35]. However, the model only considered a single moment in time—determining the time course of growth requires a more sophisticated approach.

Somatic Growth: Baseline for Understanding Pathologic Growth

Unless driven by exercise or pregnancy, ventricular growth in adults is invariably a pathologic process. In children, however, this is not the case. All children and adolescents, healthy or not, experience normal somatic growth of all their tissues, including the cardiovascular system. To effectively simulate pathologic ventricular growth in children, it

is essential to account for somatic growth. This area is underexplored in growth modeling—to our knowledge, pediatric growth modeling has been limited to skin and bone in humans [36, 37] and aortas in developing mice [38].

To model ventricular growth in children, we modified the aforementioned circulation model to represent a healthy infant's cardiovascular system and connected it to a two-dimensional model of the ventricles, which use a volumetric growth method to grow and atrophy in the circumferential and radial directions with changes in ventricular strain (Figures 1-2). Using weight-based allometric scaling [39] and maturation functions [40], we generated a matrix of input parameters from birth to three years of age. We validated the model throughout this age range by comparing outputs to clinical measurements of pressures, ventricular and atrial volumes, and ventricular thicknesses. All model outputs for this ventricular growth model fell within two standard deviations of multiple studies of healthy infants.

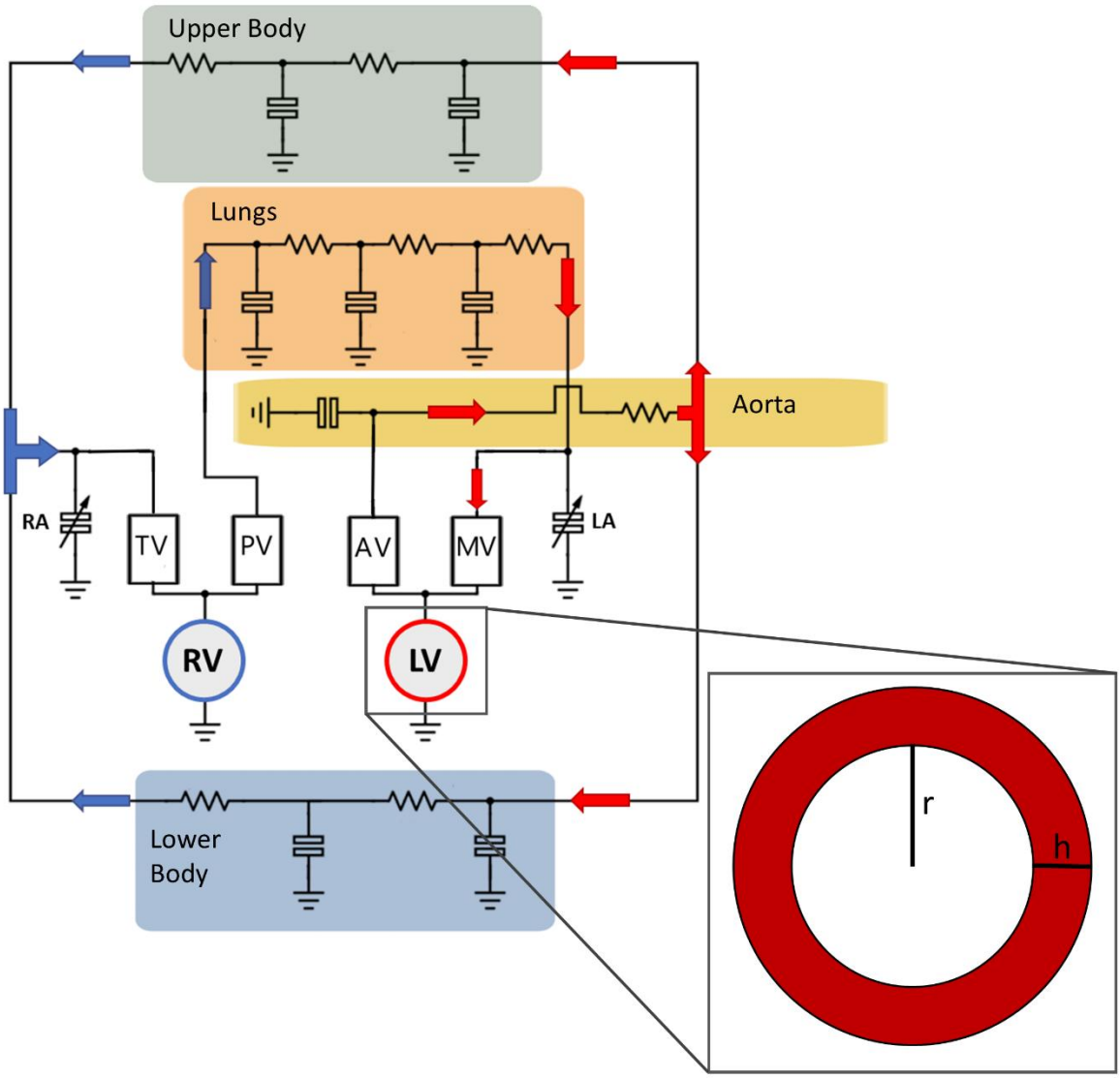

Figure 1: Schematic of the normal infant circulation model, coupled with the ventricular growth model. Inset: simplified left ventricular geometry. AV: aortic valve; h: ventricular thickness; LA: left atrium; LV: left ventricle; MV: mitral valve; PV: pulmonary valve; r: ventricular radius; RA: right atrium; RV: right ventricle; TV: tricuspid valve

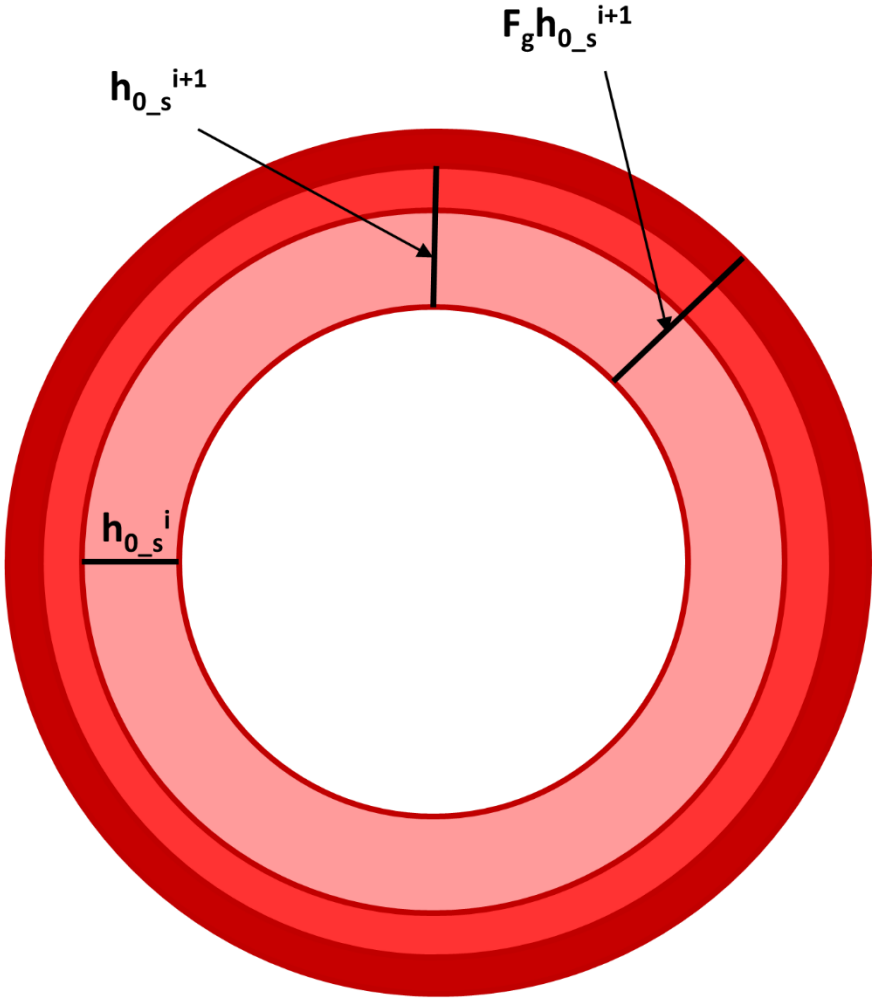

Figure 2: Illustration of concentric ventricular growth in the model. At day i, the ventricle has a somatic unloaded thickness, h_{0_s}. At day i+1, the ventricle has a new somatic unloaded thickness, and some additional thickness due to pathology, determined by multiplying the somatic thickness by growth tensor F_g. Eccentric growth follows the same pattern, using unloaded cavity radius r0.

To test the model's ability to superimpose pathologic growth onto somatic growth, we simulated CoA by gradually increasing the resistance associated with the ascending aorta to represent progressive restriction as the tissue around the coarctation grows with age. This led to expected increases in LV thickness, end-diastolic volume, and systemic blood pressure—in addition to the normal development-driven trajectories of these metrics.

Exploring Pathologic and Adaptive Growth in Borderline Left Heart

The central clinical challenge addressed by this thesis concerns the LV growth of patients with borderline left heart (BLH) undergoing staged left ventricular recruitment (SLVR). BLH is a subset of left heart hypoplasia, wherein the LV and associated structures such as the mitral valve and aorta fail to develop properly in utero [41]. BLH is associated with a broad spectrum of defects, including complex aortic stenosis with or without coarctation, Shone's complex, unbalanced atrioventricular septal defects, double outlet right ventricle, hypoplastic left heart syndrome with mitral and aortic stenosis, and interrupted aortic arch with ventricular septal defect, among others [41, 42]. The large variability in phenotypes complicates treatment decisions. If the LV is near-normal size with only minor inflow or outflow tract defects, clinicians can opt to perform a biventricular repair soon after birth. If the LV is considered too small to salvage, the patient is initiated on a single ventricle (SV) palliation pathway, ultimately converting the RV or combined RV-LV into a single systemic ventricle. Both options are not without significant risk. Critically, when biventricular repair is performed and fails, there is rapid development of pulmonary hypertension and recurring obstructive lesions leading to difficulty listing for transplant and increased mortality [43–

45]. As the more traditional treatment option [43], the risks of SV palliation (consisting of three staged surgeries within the first few years of life) are now well-known, including shunt thrombosis, RV dysfunction, and Fontan (third stage) failure [46–48].

For patients with BLH—the gray area between the two extremes of left heart hypoplasia—the bi- versus univentricular decision is more challenging still. Though scoring systems have attempted to predict survival for patients undergoing early biventricular repair, they are heavily flawed. The most common systems are based on patients with critical aortic stenosis [49–51] rather than the more complex BLH, and more modern systems developed for BLH [52, 53] are based on retrospective analyses of single-center populations that included only 12 and 8 biventricular patients, respectively.

Within the past 15 years, SLVR has emerged as a strategy to postpone the critical treatment pathway decision for patients with BLH [54]. Patients are initially started on the SV pathway, typically completing two of the three staged palliative surgeries by 4-6 months of age. During the second surgical stage, rather than leaving the interatrial communication widely patent, it is made restrictive, forcing blood to flow into the hypoplastic LV while the RV continues to supply the majority of systemic flow. This state is maintained until the typical Fontan age (~ 2 to 3 years of age), when clinicians can assess the LV for adequate growth and commit to either an SV or biventricular pathway [55].

As it is a relatively new technique, several questions about the effectiveness of SLVR have yet to be answered, chief of which is the LV growth process itself. SLVR success is

determined using indexed LV end-diastolic volume (LVEDV), which only considers cavity dimensions, not overall LV mass or thickness. An increase in LV cavity volume without a concurrent increase in wall mass (dilatation, see Figure 3) can be indicative of decompensation, such as that seen in patients with dilated cardiomyopathy [56].

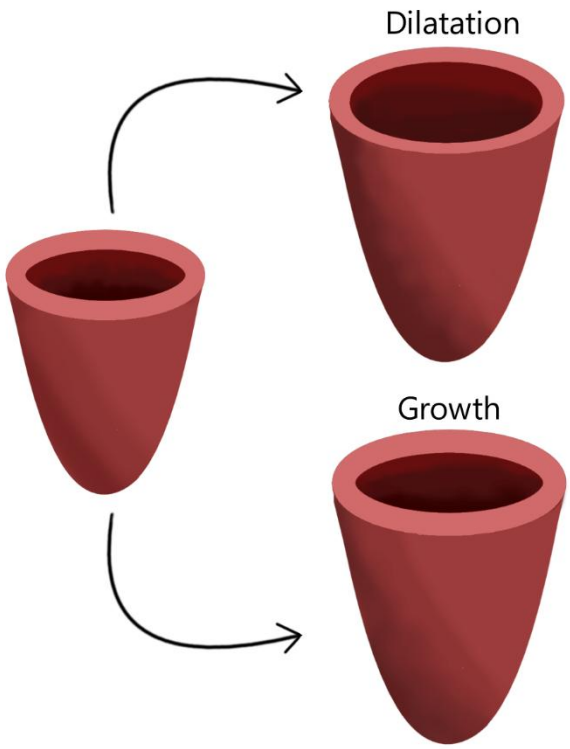

Figure 3: Patterns of ventricular hypertrophy. An increase in cavity volume without a concurrent increase in thickening presents as pathologic dilatation (top right).

Thus, our objective was to apply and extend our circulation and growth model framework to simulate SLVR to determine LV hypertrophy trajectories and patterns. By generating a simulated group of BLH patients with a variety of phenotypes, we determined which initial factors influence SLVR success and failure, providing insight into risk and resilience metrics. A predictive model trained on model results determined that initial LVEDV Z-score, the presence of endocardial fibroelastosis, and aortic valve regurgitation were the most important factors governing SLVR success and failure. We also explored whether observed LV growth in patients with a "successful" SLVR reflects healthy hypertrophy or maladaptive dilatation. According to model results, thickening generally matched dilatation in successful SLVR, suggesting LVEDV is an acceptable surrogate measurement for overall LV hypertrophy. In patients with unsuccessful SLVR, the LV did not demonstrate much growth beyond the expected somatic amount, i.e., they did not experience additional adaptive growth from SLVR.

Rationale and Hypotheses

This sequence of models builds a unified framework linking vascular mechanics, cardiac load, and ventricular growth in health and disease. With the CoA circulatory model (Chapter 3), we investigated how changes in pressure and flow drive vascular and ventricular remodeling. With the somatic infant growth model (Chapter 4), we established normal ventricular adaptation to developmental load. Finally, with the SLVR model (Chapter 5), we combined our approaches to explore maladaptive remodeling.

Our hypotheses were threefold:

1. Persistent mechanical abnormalities (e.g., elevated afterload or abnormal compliance) underlie maladaptive growth patterns.
2. SLVR patients do not experience proportional thickening of the LV wall during SLVR; their apparent increase in volume primarily reflects dilatation.
3. By integrating somatic and pathologic growth processes, we can predict which patients may achieve true functional hypertrophy sufficient for successful biventricular repair.

Chapter Overview

In Chapter 2, I review the literature on reduced-order cardiovascular modeling of SV pathologies. Chapter 3 describes the rabbit CoA circulation model and results. Chapter 4 covers the somatic infant growth model and validation. Chapter 5 presents the SLVR model, results, and analyses. Chapter 6 synthesizes insights, discusses clinical implications and limitations, and outlines future directions for our model and the computational modeling field as a whole.

REFERENCES

1. Hoffman JIE, Kaplan S (2002) The incidence of congenital heart disease. Journal of the American College of Cardiology 39:1890–1900. https://doi.org/10.1016/S0735-1097(02)01886-7

2. Khairy P, Ionescu-Ittu R, Mackie AS, et al (2010) Changing Mortality in Congenital Heart Disease. Journal of the American College of Cardiology 56:1149–1157. https://doi.org/10.1016/j.jacc.2010.03.085

3. Brida M, Gatzoulis MA (2019) Adult congenital heart disease: Past, present and future. Acta Paediatrica 108:1757–1764. https://doi.org/10.1111/apa.14921

4. Marelli AJ, Mackie AS, Ionescu-Ittu R, et al (2007) Congenital Heart Disease in the General Population: Changing Prevalence and Age Distribution. Circulation 115:163–172. https://doi.org/10.1161/CIRCULATIONAHA.106.627224

5. Gurvitz M, Dunn JE, Bhatt A, et al (2020) Characteristics of Adults With Congenital Heart Defects in the United States. Journal of the American College of Cardiology 76:175–182. https://doi.org/10.1016/j.jacc.2020.05.025

6. Graham TP (1991) Ventricular performance in congenital heart disease. Circulation 84:2259–2274. https://doi.org/10.1161/01.CIR.84.6.2259

7. Egbe AC, Reddy YNV, Obokata M, Borlaug BA (2020) Doppler-Derived Arterial Load Indices Better Reflect Left Ventricular Afterload Than Systolic Blood Pressure in Coarctation of Aorta. Circ: Cardiovascular Imaging 13:e009672. https://doi.org/10.1161/CIRCIMAGING.119.009672

8. Safa R, Dean A, Sanil Y, et al (2023) Effect of Preoperative Volume Overload on Left Ventricular Function Recovery After Ventricular Septal Defect Repair. The American Journal of Cardiology 203:253–258. https://doi.org/10.1016/j.amjcard.2023.06.118

9. De Simone G (2004) Concentric or Eccentric Hypertrophy: How Clinically Relevant Is the Difference? Hypertension 43:714–715. https://doi.org/10.1161/01.HYP.0000121363.08252.a7

10. Konstam MA, Kramer DG, Patel AR, et al (2011) Left Ventricular Remodeling in Heart Failure. JACC: Cardiovascular Imaging 4:98–108. https://doi.org/10.1016/j.jcmg.2010.10.008

11. Goldstein S, Ali AS, Sabbah H (1998) Ventricular Remodeling: Mechanisms and Prevention. Cardiology Clinics 16:623–632. https://doi.org/10.1016/S0733-8651(05)70039-4

12. Menon A, Eddinger TJ, Wang H, et al (2012) Altered hemodynamics, endothelial function, and protein expression occur with aortic coarctation and persist after repair. American Journal of Physiology-Heart and Circulatory Physiology 303:H1304–H1318. https://doi.org/10.1152/ajpheart.00420.2012

13. Goo HW, Park S-H (2020) Pattern Analysis of Left Ventricular Remodeling Using Cardiac Computed Tomography in Children with Congenital Heart Disease: Preliminary Results. Korean J Radiol 21:717. https://doi.org/10.3348/kjr.2019.0689

14. Grotenhuis HB, Cifra B, Mertens LL, et al (2019) Left ventricular remodelling in long-term survivors after the arterial switch operation for transposition of the great arteries. European Heart Journal - Cardiovascular Imaging 20:101–107. https://doi.org/10.1093/ehjci/jey072

15. Alphonso N, Angelini A, Barron DJ, et al (2020) Guidelines for the management of neonates and infants with hypoplastic left heart syndrome: The European Association for Cardio-Thoracic Surgery (EACTS) and the Association for European Paediatric and Congenital Cardiology (AEPC) Hypoplastic Left Heart Syndrome Guidelines Task Force. European Journal of Cardio-Thoracic Surgery 58:416–499. https://doi.org/10.1093/ejcts/ezaa188

16. Niederer SA, Lumens J, Trayanova NA (2019) Computational models in cardiology. Nat Rev Cardiol 16:100–111. https://doi.org/10.1038/s41569-018-0104-y

17. Meoli A, Cutrì E, Krishnamurthy A, et al (2015) A multiscale model for the study of cardiac biomechanics in single-ventricle surgeries: a clinical case. Interface Focus 5:20140079. https://doi.org/10.1098/rsfs.2014.0079

18. Qian Y, Liu JL, Itatani K, et al (2010) Computational Hemodynamic Analysis in Congenital Heart Disease: Simulation of the Norwood Procedure. Ann Biomed Eng 38:2302–2313. https://doi.org/10.1007/s10439-010-9978-5

19. Pekkan K, Frakes D, De Zelicourt D, et al (2005) Coupling Pediatric Ventricle Assist Devices to the Fontan Circulation: Simulations with a Lumped-Parameter Model. ASAIO Journal 51:618–628. https://doi.org/10.1097/01.mat.0000176169.73987.0d

20. Holmes JW, Lumens J (2018) Clinical Applications of Patient-Specific Models: The Case for a Simple Approach. J of Cardiovasc Trans Res 11:71–79. https://doi.org/10.1007/s12265-018-9787-z

21. Garber L, Khodaei S, Keshavarz-Motamed Z (2022) The Critical Role of Lumped Parameter Models in Patient-Specific Cardiovascular Simulations. Archives of Computational Methods in Engineering 29:2977–3000

22. Moulton MJ, Hong BD, Secomb TW (2017) Simulation of Left Ventricular Dynamics Using a Low-Order Mathematical Model. Cardiovasc Eng Tech 8:480–494. https://doi.org/10.1007/s13239-017-0327-9

23. Rodriguez EK, Hoger A, McCulloch AD (1994) Stress-dependent finite growth in soft elastic tissues. Journal of Biomechanics 27:455–467. https://doi.org/10.1016/0021-9290(94)90021-3

24. Humphrey JD, Rajagopal KR (2002) A constrained mixture model for growth and remodeling of soft tissues. Math Models Methods Appl Sci 12:407–430. https://doi.org/10.1142/S0218202502001714

25. Humphrey JD (2021) Constrained Mixture Models of Soft Tissue Growth and Remodeling – Twenty Years After. J Elast 145:49–75. https://doi.org/10.1007/s10659-020-09809-1

26. Yoshida K, Holmes JW (2021) Computational models of cardiac hypertrophy. Progress in Biophysics and Molecular Biology 159:75–85. https://doi.org/10.1016/j.pbiomolbio.2020.07.001

27. Ağbaş A, Gökalp S, Canpolat N, et al (2020) Is the burden of late hypertension and cardiovascular target organ damage in children and adolescents with coarctation of the aorta after early successful repair different to healthy controls? Cardiol Young 30:1305–1312. https://doi.org/10.1017/S104795112000205X

28. Rinnström D, Dellborg M, Thilén U, et al (2016) Left ventricular hypertrophy in adults with previous repair of coarctation of the aorta; association with systolic blood pressure in the high normal range. International Journal of Cardiology 218:59–64. https://doi.org/10.1016/j.ijcard.2016.05.033

29. Eerola A, Jokinen E, Boldt T, et al (2007) Left ventricular hypertrophy persists after successful treatment for coarctation of the aorta. Scandinavian Cardiovascular Journal 41:370–377. https://doi.org/10.1080/14017430701397839

30. Egbe AC, Miranda WR, Warnes CA, et al (2021) Persistent Hypertension and Left Ventricular Hypertrophy After Repair of Native Coarctation of Aorta in Adults. Hypertension 78:672–680. https://doi.org/10.1161/HYPERTENSIONAHA.121.17515

31. Dunnill MS (1959) Histology of the aorta in coarctation. J Pathol 78:203–207. https://doi.org/10.1002/path.1700780122

32. Sehested J, Baandrup U, Mikkelsen E (1982) Different reactivity and structure of the prestenotic and poststenotic aorta in human coarctation. Implications for baroreceptor function. Circulation 65:1060–1065. https://doi.org/10.1161/01.CIR.65.6.1060

33. Sendzikaite S, Sudikiene R, Tarutis V, et al (2020) Prevalence of arterial hypertension, hemodynamic phenotypes, and left ventricular hypertrophy in children after coarctation repair: a multicenter cross-sectional study. Pediatr Nephrol 35:2147–2155. https://doi.org/10.1007/s00467-020-04645-w

34. Hiebing AA, Culver MA, LaDisa JF, Witzenburg CM (2025) Computational model of coarctation of the aorta in rabbits suggests persistent ascending aortic remodeling post-correction. Biomech Model Mechanobiol 24:683–700. https://doi.org/10.1007/s10237-025-01933-y

35. Egbe AC, Miranda WR, Connolly HM (2021) Predictors of left ventricular reverse remodelling after coarctation of aorta intervention. European Heart Journal - Cardiovascular Imaging 22:1168–1173. https://doi.org/10.1093/ehjci/jeaa199

36. Zöllner AM, Buganza Tepole A, Gosain AK, Kuhl E (2012) Growing skin: tissue expansion in pediatric forehead reconstruction. Biomech Model Mechanobiol 11:855–867. https://doi.org/10.1007/s10237-011-0357-4

37. Libby J, Marghoub A, Johnson D, et al (2017) Modelling human skull growth: a validated computational model. J R Soc Interface 14:20170202. https://doi.org/10.1098/rsif.2017.0202

38. Wagenseil JE (2011) A constrained mixture model for developing mouse aorta. Biomech Model Mechanobiol 10:671–687. https://doi.org/10.1007/s10237-010-0265-z

39. West GB, Brown JH, Enquist BJ (1997) A General Model for the Origin of Allometric Scaling Laws in Biology. Science 276:122–126. https://doi.org/10.1126/science.276.5309.122

40. Anderson BJ, Holford NHG (2009) Mechanistic Basis of Using Body Size and Maturation to Predict Clearance in Humans. Drug Metabolism and Pharmacokinetics 24:25–36. https://doi.org/10.2133/dmpk.24.25

41. Albrahimi E, Korun O (2024) Contemporary management of borderline left ventricle. European Journal of Cardio-Thoracic Surgery 66:ezae247. https://doi.org/10.1093/ejcts/ezae247

42. Corno A (2005) Borderline left ventricle. European Journal of Cardio-Thoracic Surgery 27:67–73. https://doi.org/10.1016/j.ejcts.2004.10.034

43. Hickey EJ, Caldarone CA, Blackstone EH, et al (2007) Critical left ventricular outflow tract obstruction: The disproportionate impact of biventricular repair in borderline cases. The Journal of Thoracic and Cardiovascular Surgery 134:1429-1437.e7. https://doi.org/10.1016/j.jtcvs.2007.07.052

44. Cavigelli-Brunner A, Bauersfeld U, Prêtre R, et al (2012) Outcome of Biventricular Repair in Infants With Multiple Left Heart Obstructive Lesions. Pediatr Cardiol 33:506–512. https://doi.org/10.1007/s00246-011-0142-2

45. Freund JE, den Dekker M, Blank C, et al (2015) Midterm Follow-Up After Biventricular Repair of the Hypoplastic Left Heart Complex. Ann Thorac Surg 99:2150–6. http://dx.doi.org/10.1016/j.athoracsur.2015.02.030

46. Alsaied T, Bokma JP, Engel ME, et al (2017) Factors associated with long-term mortality after Fontan procedures: a systematic review. Heart 103:104–110. https://doi.org/10.1136/heartjnl-2016-310108

47. Ghanayem NS, Allen KR, Tabbutt S, et al (2012) Interstage mortality after the Norwood procedure: Results of the multicenter Single Ventricle Reconstruction trial. The Journal of Thoracic and Cardiovascular Surgery 144:896–906. https://doi.org/10.1016/j.jtcvs.2012.05.020

48. Kaplinski M, Ittenbach RF, Hunt ML, et al (2020) Decreasing Interstage Mortality After the Norwood Procedure: A 30-Year Experience. JAHA 9:e016889. https://doi.org/10.1161/JAHA.120.016889

49. Colan SD, McElhinney DB, Crawford EC, et al (2006) Validation and Re-Evaluation of a Discriminant Model Predicting Anatomic Suitability for Biventricular Repair in Neonates With Aortic Stenosis. Journal of the American College of Cardiology 47:1858–1865. https://doi.org/10.1016/j.jacc.2006.02.020

50. Rhodes LA, Colan SD, Perry SB, et al (1991) Predictors of survival in neonates with critical aortic stenosis. Circulation 84:2325–2335. https://doi.org/10.1161/01.CIR.84.6.2325

51. Lofland GK, McCrindle BW, Williams WG, et al (2001) Critical aortic stenosis in the neonate: A multi-institutional study of management, outcomes, and risk factors. The Journal of Thoracic and Cardiovascular Surgery 121:10–27. https://doi.org/10.1067/mtc.2001.111207

52. Mart CR, Eckhauser AW (2014) Development of an Echocardiographic Scoring System to Predict Biventricular Repair in Neonatal Hypoplastic Left Heart Complex. Pediatr Cardiol 35:1456–1466. https://doi.org/10.1007/s00246-014-1009-0

53. Plymale JM, Frommelt PC, Nugent M, et al (2017) The Infant with Aortic Arch Hypoplasia and Small Left Heart Structures: Echocardiographic Indices of Mitral and Aortic Hypoplasia Predicting Successful Biventricular Repair. Pediatr Cardiol 38:1296–1304. https://doi.org/10.1007/s00246-017-1661-2

54. Emani SM, McElhinney DB, Tworetzky W, et al (2012) Staged Left Ventricular Recruitment After Single-Ventricle Palliation in Patients With Borderline Left Heart

Hypoplasia. Journal of the American College of Cardiology 60:1966–1974. https://doi.org/10.1016/j.jacc.2012.07.041

55. Dafflisio G, Emani SM (2025) Don't Give up on the Left Ventricle! Surgical Strategies for Recruitment of the Borderline Left Heart. Seminars in Thoracic and Cardiovascular Surgery: Pediatric Cardiac Surgery Annual 28:13–20. https://doi.org/10.1053/j.pcsu.2025.02.009

56. Spirito P, Maron BJ, Bonow RO, Epstein SE (1987) Occurrence and significance of progressive left ventricular wall thinning and relative cavity dilatation in hypertrophic cardiomyopathy. The American Journal of Cardiology 60:123–129. https://doi.org/10.1016/0002-9149(87)90998-2

Chapter 2: In Silico Hemodynamics of the Single Ventricle: Lumped Parameter Approaches

Abstract

Single ventricle (SV) pathologies encompass a group of severe congenital heart defects that result in a heart with a single functional ventricle supporting both systemic and pulmonary circulations. Management is palliative in nature, typically proceeding through three surgical stages (S1P-S3P). Each stage profoundly alters cardiovascular anatomy and physiology, modifying ventricular loading conditions, vascular resistances, and flow throughout the circulatory system. Computational models have emerged as useful tools for elucidating the complex hemodynamics of SV physiology, testing surgical variations, and guiding clinical decision-making. Among these, lumped parameter models (LPMs) provide a computationally efficient framework for simulating global hemodynamics by leveraging electrical circuit analogies. This review focuses on the development of SV LPMs by first tracing the history of cardiovascular LPMs, including governing equations and key assumptions. We then address their application to SV physiology, distinguishing between uncoupled (zero-dimensional) and multiscale models that couple the LPM to higher-order (typically 3D finite-element) representations. For each palliative stage—S1P, S2P, and S3P—we summarize major modeling efforts, highlight insights gained, and discuss limitations. Finally, we explore emerging directions in SV LPM research, including fetal

interventions, non-surgical modeling opportunities, and the need for cross-disciplinary collaboration.

Abbreviations

ABG: assisted bidirectional Glenn

AV: atrioventricular

BCPA: bidirectional cavopulmonary anastomosis

CFD: computational fluid dynamics

CHD: congenital heart disease

CO: cardiac output

DO2: oxygen delivery (to tissues)

EDPVR: end-diastolic pressure-volume relationship

ESPVR: end-systolic pressure-volume relationship

FAV: fetal aortic valvuloplasty

HLHS: hypoplastic left heart syndrome

IVC: inferior vena cava

LPM: lumped parameter model

LV: left ventricle

mBTT: modified Blalock-Thomas-Taussig (shunt)

PVR: pulmonary vascular resistance

Qp:Qs: pulmonary-to-systemic flow split

RBTT: reverse Blalock-Thomas-Taussig (shunt)

RV: right ventricle

RVPA: right ventricle-to-pulmonary artery (shunt)

S1P: Stage 1 Palliation

S2P: Stage 2 Palliation

S3P: Stage 3 Palliation

SV: single ventricle

SVC: superior vena cava

TCPC: total cavopulmonary connection

VAD: ventricular assist device

1. Introduction

“Single ventricle” (SV) is a general term used to describe a range of congenital cardiac abnormalities resulting in a heart with a single functional ventricle. Conditions include hypoplastic left/right heart syndrome, tricuspid atresia, double-inlet left ventricle, and unbalanced atrioventricular septal defects [1]. Though SV pathologies are rare, comprising only 7.7% of all congenital heart disease (CHD) diagnoses, they are responsible for nearly a quarter of all neonatal CHD deaths [2]. Additionally, current SV treatment strategies are not curative, and survivors face lifelong, debilitating declines in overall health, burdened by persistent dysfunction not only in the cardiovascular system, but also across the gastrointestinal, pulmonary, and renal systems [3, 4]. In the aggregate, these comorbidities lead to increased hospitalizations and healthcare resource utilization [5]. On an individual level, they can lead to a decline in self-assessed quality of life and mental health [6].

Infants with SV defects typically require immediate treatment within the first week of life to ensure their functional ventricle can supply both systemic and pulmonary circulations [7]. However, this anatomic configuration places the single ventricle under significant

overloading, with some estimating a three-fold increase in stroke volume [8]. As this state is unsustainable in the long term, the current standard of care involves staged palliative surgeries. The initial surgery stabilizes the patient while their pulmonary vasculature develops and pulmonary resistance decreases. Follow-up procedures reconfigure the functional ventricle to provide only systemic flow, reducing the overloading. Ultimately, a total cavopulmonary connection is placed to bypass the heart entirely, connecting both venae cavae to the pulmonary artery to provide passive flow to the lungs. The specifics of each surgery vary depending on the SV pathology, their subtypes, and the patient's individual physiology. This review largely focuses on SV patients with left-sided lesions requiring three staged palliative surgeries, denoted as S1P, S2P, and S3P.

Each of these surgeries, particularly when combined with the anatomical heterogeneity inherent to the SV population, brings its own challenges in hemodynamic management [9]. In patients with a single right ventricle (RV), S1P, commonly termed the Norwood procedure, joins the main pulmonary trunk to the hypoplastic aorta to form a neo-aorta to provide systemic flow. Pulmonary flow is supplied by a systemic-to-pulmonary shunt, which together result in both pressure and volume overloading of the RV. This overload is relieved by S2P, when a bidirectional cavopulmonary anastomosis or hemi-Fontan operation supplies pulmonary flow via the superior vena cava (SVC). Despite being considered a more stable physiology than the Norwood, S2P and the S2P-S3P interstage period is not without complications, such as cavopulmonary shunt failure, pulmonary artery stenosis, and RV decompensation [10–12]. Finally, the long-term complications of

the third-stage Fontan procedure are well known, including liver fibrosis, protein-losing enteropathy, and plastic bronchitis [9, 13–15]. The high rate of morbidity and mortality, the relatively small patient population, and the large amount of individual variability make studying SV hemodynamics both onerous and vitally necessary.

Computational models provide researchers and clinicians with powerful tools to estimate physiological aspects of cardiovascular disease and their treatments—including temporal and spatial variations in flow, pressure, heart and vessel wall deformation, and circulatory feedback—as well as the hemodynamic effects of comorbidities. The in-silico environment allows researchers to overcome limitations of traditional studies: patient populations are potentially infinite, computational models are risk free, and the effects of interventions can be analyzed in isolation. Models can either be generalized, in which the anatomical and physiological patient data used to inform the model are aggregated, or patient-specific, in which the model is calibrated to a specific individual. A generalized model represents a "typical" patient, providing insight into how an intervention might affect the group as a whole. While these models can capture important trends, care needs to be taken to address population variability and overinterpretation. Patient-specific models, on the other hand, are inherently limited in their applicability to a population, even within the same pathology. But they can inform clinical decision-making for that individual patient, such as risk prediction and virtual treatment planning [16, 17]. Computational models are particularly useful for CHDs [18–20], where the patient population is limited,

phenotypically heterogeneous, and often physically fragile, making traditional randomized controlled trials a challenge.

Despite these benefits, computational modelers have historically faced their share of quandaries, particularly in assigning boundary conditions. For example, many early computational fluid dynamics (CFD) models of the cardiovascular system simulated arterial flow using idealized, symmetrical geometries with rigid walls [21, 22]. Velocity profiles were prescribed at the inlet(s) to achieve desired flow rates, with a zero-pressure condition at the outlet(s). Though these early CFD simulations could produce three-dimensional velocity fields and quantify local wall shear stress, they could not produce accurate pressure fields [16], and their use was limited to artery segments experiencing fully-developed laminar flow—a far cry from the type of flow found in complex CHDs [23–25].

As computational power grew exponentially in the late 1990s and early 2000s, researchers quickly pivoted to constructing patient-specific anatomical models from CT or MR imaging, but the problem of boundary conditions remained. While phase-contrast MRI allowed for the implementation of more realistic flow profiles at the inlet, achieving realistic outflow conditions was more challenging, with inaccuracies caused by assumptions (e.g., constant pressure at each outlet) propagating upstream, affecting flow, velocity, and pressure field calculations [26, 27]. Furthermore, regardless of their level of anatomic sophistication, these models were isolated from the rest of the circulation—local phenomena could not

affect global hemodynamics, and vice-versa. Modeling the whole human cardiovascular system in a three-dimensional CFD solver, however, was and remains intractable.

The answer to this problem required—perhaps counterintuitively for cutting-edge modelers—a simpler approach. Decades earlier, researchers had recreated the entire circulation as a zero-dimensional model of networked "lumped" compartments, leveraging hydraulic and electrical circuit analogies to describe flow rate and pressure in each compartment [28, 29]. What these lumped parameter models (LPM) lacked in geometric fidelity, they made up for in their ability to simulate global hemodynamics. Joining an LPM to a higher-order model allowed for automatic conservation of volume throughout the system, more realistic preloads and afterloads for the 3D component, and a fast, robust approach to determining initial conditions and fitting parameters [30, 31].

In this article, we will review LPMs in the context of SV pathologies. We begin with an overview of the history and governing equations of LPMs, followed by a separation of SV models into two categories: "uncoupled" standalone LPMs and "coupled" multiscale models. Each category is further divided into models simulating S1P, S2P, or S3P. Finally, we offer perspectives on where SV LPMs are headed in the near term, highlight current knowledge gaps, and propose recommendations for addressing these challenges.

2. Lumped Parameter Models

Using electrical circuit concepts, LPMs reduce the cardiovascular system into discrete compartments (Figure 1). In an LPM, blood flow is analogous to current, compartmental

pressure difference is analogous to voltage, and resistors, capacitors, and inductors simulate vascular resistance, vascular compliance, and blood inertia, respectively. LPMs are governed by the same zero-dimensional differential equations as circuits, enabling the computation of time-varying pressures, flows, and volumes. LPMs converge to steady-state solutions in seconds on an average desktop computer [32, 33], a significant advantage over their CFD counterparts, which can require hours or days of runtime on high performance computing clusters for a single cardiac cycle [34–41]. This advantage is most evident for analyses requiring many repeated simulations, such as global sensitivity analyses and uncertainty quantifications of input parameters.

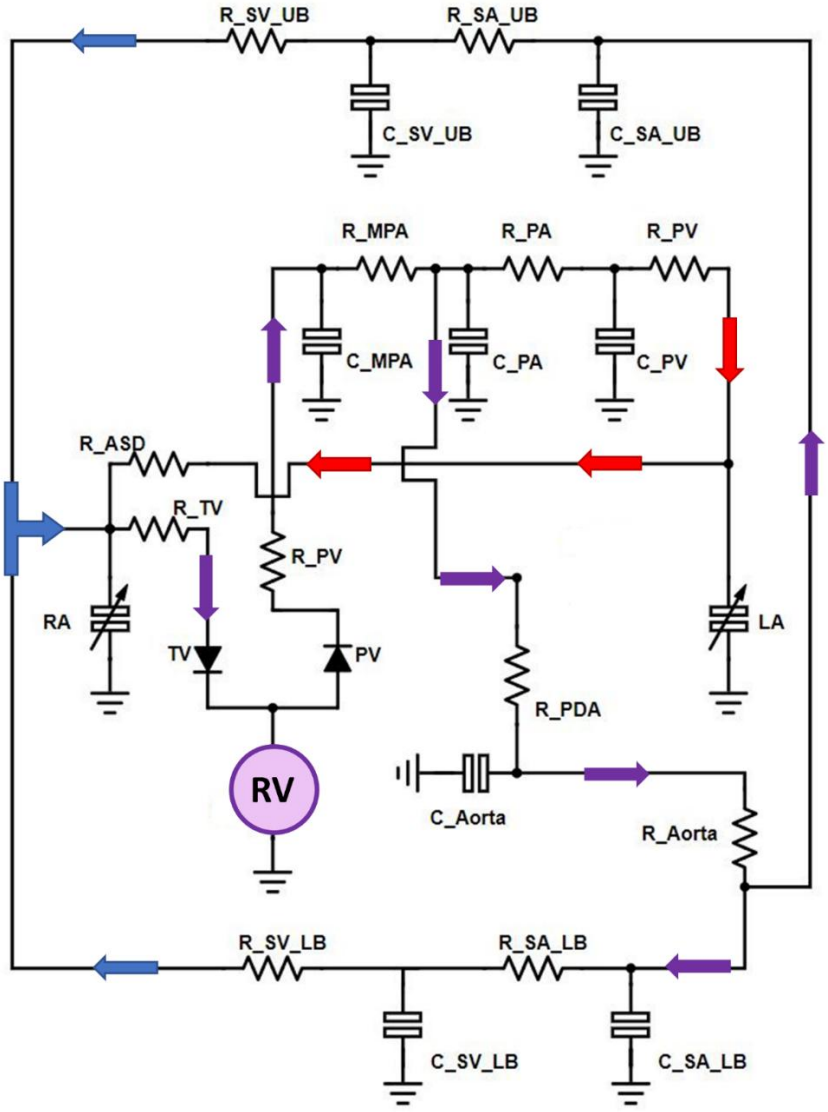

Figure 1: A circuit schematic of a lumped parameter model, representing hypoplastic left heart syndrome prior to treatment. The cardiovascular system is divided into compartments, where heart chambers are simulated using time-varying-elastances, valves are represented as ideal diodes, and vessels are simulated using combinations of resistors and capacitors. Arrows describe the direction of blood flow, with their colors representing relative levels of oxygenation (red: fully oxygenated; blue: deoxygenated; purple: partially oxygenated)

Broadly speaking, cardiovascular LPMs are composed of two types of components: vessels and heart chambers. Vessel hemodynamics were first mathematically described in 1899 by German physiologist Otto Frank, most well-known for the Frank-Starling law relating cardiac volume to contraction [42]. Termed a "two-element Windkessel," this simple model utilizes a resistor and capacitor to simulate systemic arterial hemodynamics. Flow, *Q*, against the total peripheral vessel resistance, *R*, obeys a relationship analogous to Ohm's Law:

$$Q = \frac{(P_{up} - P_{down})}{R}, \tag{1}$$

where $P_{up} - P_{down}$ indicates the pressure difference across the total peripheral resistance. The capacitor, *C*, representing the elastic component of the large arteries that enables flow storage (i.e., vessel compliance), is defined as the slope of the overall systemic arterial pressure-flow relationship:

$$C = \frac{dQ}{dP} \tag{2}$$

If linear elasticity is assumed, *C* simplifies to a constant. Though the two-element Windkessel can describe the pressure and flow of mid-sized systemic arteries, it fails to capture wave transmission effects in large elastic arteries. This weakness is highlighted most definitively by Fourier analysis, where the two-element Windkessel's performance falls far below measured values of both amplitude and phase in the aorta, particularly at

higher frequencies [43, 44]. To remedy this, a second resistor, termed the ‘characteristic impedance,’ is placed proximally to the capacitor and peripheral resistance to account for local inertia in the very proximal section of large elastic arteries [45]. This “three-element Windkessel” outperforms its two-element counterpart in the time and frequency domains [44–46]. However, it underestimates the true value of characteristic impedance and overestimates total arterial compliance [47]. This led to the inclusion of an inductor, L, to represent the inertia of the whole arterial system, either replacing the characteristic impedance or placed in parallel with it. The consideration of mass acceleration along with viscous resistance requires a first order differential equation to relate the pressure difference and flow, such that

$$P_{up} - P_{down} = RQ + L\frac{dQ}{dt} \tag{3}$$

In practice, combinations of two-, three-, and four-element Windkessels are also used to represent different vessel types when the arterial system is not lumped into a single compartment. For example, flow dynamics in arterioles and capillaries can be simplified to a single resistor, because the vessel walls are relatively rigid (eliminating the capacitor), flow is steady (eliminating the characteristic impedance), and energy loss is dominated by friction (eliminating the inductor) [33, 48]. This reduces the amount of parameters that must be measured or fit to experimental data, simplifying model calibration, ensuring parameter identifiability, and reducing uncertainty in the predicted hemodynamics.

A primary benefit of LPMs is the ease with which they can simulate the heart as a source of pulsatile pressure and flow, a much more difficult process in three dimensions. Each chamber is simulated individually, with or without interaction via the atrial septum, ventricular septum, or pericardium. The decision of which chambers to model depends on the application: models focused on the systemic circulation need only simulate the left ventricle (LV) [49–51] or the LV and left atrium [52–54], whereas models exploring oxygen transport [55, 56], pulmonary hypertension [57, 58], or septal defects [59–61] will by necessity require inclusion of the right heart.

A common way of simulating cardiac contraction employs a time-varying elastance function,

$$E(t) = \frac{P(t)}{V(t) - V_0}, \tag{4}$$

where E(t) is the instantaneous elastance of the chamber, and P(t) and V(t) are the instantaneous chamber pressure and volume. V_0, variably termed the "unloaded," "zero-pressure," "unstressed," "slack," or "fixed correction" volume, is the point at which the end-systolic pressure-volume relationship crosses the volume axis, independent of contractile state (see Figure 2) [62].

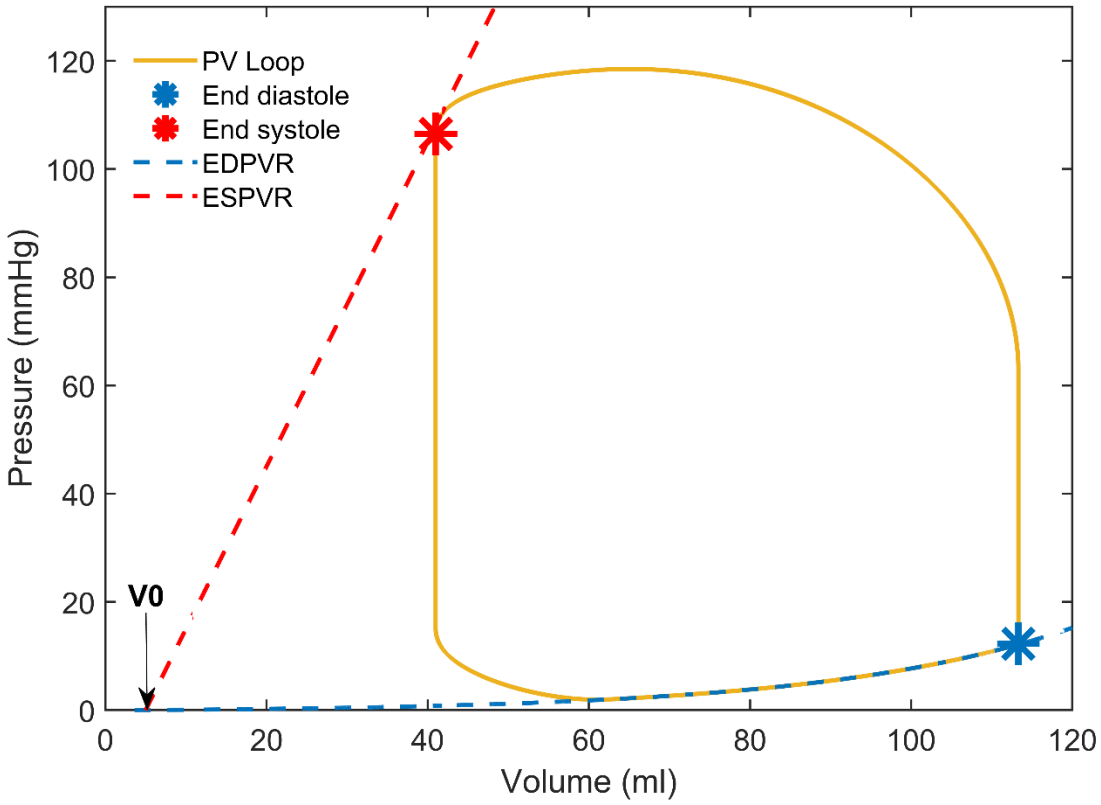

Figure 2: Pressure volume loop (orange solid line), with end-diastolic pressure-volume relationship (blue dashed line), end-systolic pressure-volume relationship (red dashed line). End diastole marked with blue star, end systole marked with red star, unloaded volume (V_0) marked with black arrow.

By rearranging Eqn. 4, chamber pressure can be computed throughout the cardiac cycle using a predetermined function for E(t), such as a sine curve [63], a combined sine-exponential curve [64], or a double-Hill function [65] (Figure 3a-c). Alternatively, if time-matched measures of ventricular volume and pressure are available, the elastance function can be determined explicitly [62, 66] (Figure 3d). E(t) may also be normalized with respect to time and amplitude, such that it acts as an activation function that describes only the timing of systole and diastole. In this case, the end-systolic pressure-volume relationship (ESPVR) typically takes the form of:

$$P_{es} = E_{es} * (V_{es} - V_0), \tag{5}$$

where Pes is the end-systolic pressure, Ees is the end-systolic elastance of the pumping chamber, and Ves is the end-systolic volume. However, experimentalists have argued a nonlinear relationship may be more appropriate in situations with hypo- or hyper-contractility [67]. The end-diastolic pressure-volume relationship (EDPVR) can be linear, but numerous experimental investigations support the use of an exponential function [66, 68–74]:

$$P_{ed} = A * [\exp\big(B * (V_{ed} - V_0)\big) - 1] \tag{6}$$

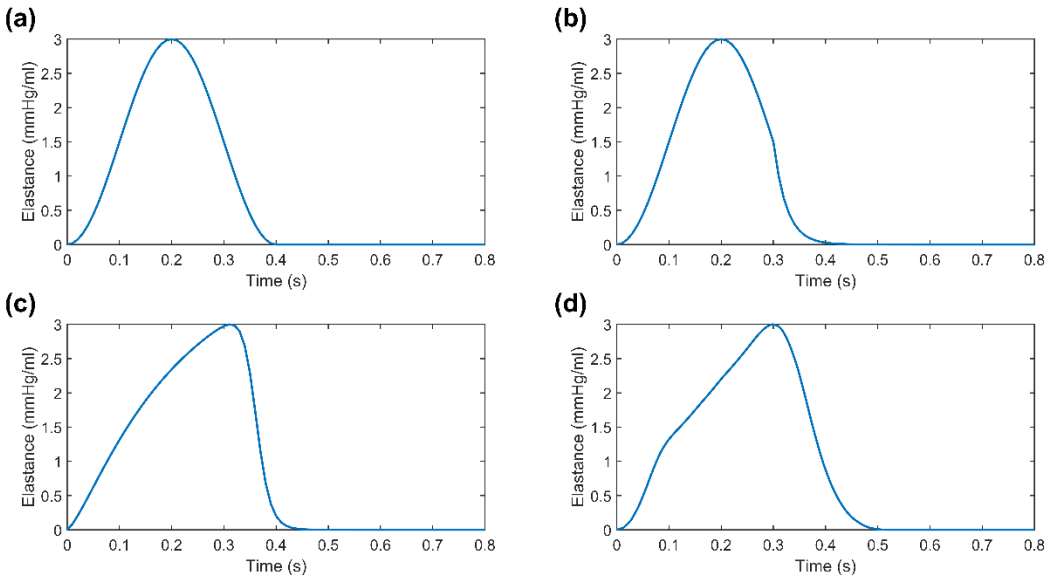

Figure 3: Examples of time-varying elastance curves. a) Sinusoid [63]; b) Sinusoid with exponential decay [64]; d) double-Hill function [75]; d) derived from experimental measurements of time-matched ventricular pressures and volumes [66]

Though its ease of implementation makes it a popular choice for modeling the heart chambers, the classic time-varying elastance model as proposed by Suga et al. [62] is not without flaws. Notably, it assumes a linear relationship between instantaneous pressure and volume, though later work showed this relationship to be parabolic in shape, including at end systole [67, 76]. This calls load independence—the time-varying elastance model's greatest strength—into question, as a varying ESPVR slope inherently implies that contractility must vary with end-systolic volume [77]. To address this, Suga et al. [78] and Ishide et al. [79] experimentally quantified the effects of preload (i.e., end-diastolic volume), afterload (peripheral resistance), ejection onset timing, and ejection velocity on ESVPR linearity in the healthy heart using isovolumetric contraction as a baseline. Increasing preload caused a 5 to 20% reduction in end-systolic pressure as ejection fraction increased from 55 to 75%, but neither ejection onset timing, ejection velocity, nor afterload significantly altered end-systolic pressure. Alternatives to the time-varying elastance model include Hill's three parametric model [80–82], electro-mechanical or chemo-mechanical models that couple microscopic functions to macroscopic behavior [83–85], and the stress-based "single fiber" model [86–89]. Despite its potential drawbacks, however, the time-varying elastance model's assumptions tend to be deemed sufficient for simulating chamber dynamics, and it continues to see widespread use in LPMs [77].

The four valves within the heart are arguably as complex as the chambers they reside within. The valves (mitral, tricuspid, aortic, and pulmonary) are responsible for maintaining

unidirectional flow in and out of the ventricles. Thus, the simplest approach to model the valves in an LPM is to treat them as ideal diodes: when the pressure in the downstream compartment (e.g., the LV for the mitral valve) is lower than that of the upstream compartment (e.g., the left atrium), the valve is open. When the pressure is higher, the valve is closed. The diode is commonly combined with a linear or nonlinear resistance to simulate some degree of frictional loss due to blood flowing through the valve. In reality, valve dynamics are far more intricate. All valves have leaflets that must act in concert with the fibrous annuli surrounding them to open and close dozens of times per minute in humans. In terms of solid mechanics, the valves are layered and anisotropic [90–92], experience large multimodal deformations in vivo, and, in the case of the atrioventricular (AV) valve (mitral and tricuspid) leaflets, are asymmetric and unequally sized [93]. Motion within the AV valves is further complicated by the presence of chordae tendineae and papillary muscles, which prevent the leaflets from prolapsing into the atria during systole. In terms of fluid-structure interaction, the flow of blood (a non-Newtonian fluid) through the valves is incredibly disordered and experiences rapid acceleration and deceleration [94, 95]. Of course, the zero-dimensional nature of LPMs precludes most of these features from being fully delineated in silico, but more sophisticated LPM-compatible alternatives to the diode model have been proposed, such as those utilizing time-dependent drag coefficients [81], opening angles [82, 96], terms accounting for acceleration-induced losses [97, 98], and time-varying inductance [75, 99]. Unlike the diode model, each of these alternatives considers the valve orifice area throughout the cardiac cycle, enabling

simulations of clinically relevant valve pathologies such as stenosis (incomplete opening) and regurgitation (incomplete closure).

3. Lumped Parameter Models in the Context of Single Ventricle Pathologies

Modeling SV pathologies with LPMs is a relatively new entry in the history of computational modeling. In 1996, Dubini and colleagues coupled an LPM of the pulmonary circulation to a 3D finite element model of the total cavopulmonary connection (TCPC) used in the Fontan procedure [100]. The LPM comprised few elements when compared to more modern counterparts—a constant pressure reservoir for the right atrium and two parallel resistors for the lungs—but it allowed for the reproduction of pulmonary afterload. A similar coupled setup was used by de Leval and colleagues that same year, this time to investigate pulmonary artery stenosis in conjunction with a TCPC [101].

Both studies used LPMs as a support to the primary 3D model, providing a modifiable and computationally efficient boundary condition to one inlet of their finite element model, thus avoiding a completely open-looped system. While this method, termed multiscale modeling, continues to be commonly used when simulating SV pathologies, separate "uncoupled" lumped parameter models have been developed for all three surgical stages of SV treatment. This section will explore these two modeling types, further delineated by surgical stage.

3.1. Uncoupled Lumped Parameter Models

Uncoupled LPMs have been developed in tandem with multiscale models for studying mechanisms of SV and its treatments. Both uncoupled LPMs and multiscale models can offer insights into global hemodynamics. However, the lack of a 3D component is a double-edged sword: uncoupled LPMs are orders of magnitude faster than their multiscale counterparts, but they sacrifice the ability to determine local fluid dynamics.

3.1.1. Stage 1 Palliation (S1P)

The Norwood procedure, also called S1P, is typically performed in the first week of life and has three main goals [7]:

1) Provide systemic blood flow from the functional ventricle to the reconstructed aorta,
2) Reinstitute controlled pulmonary flow, and
3) Establish an interatrial communication to allow venous return to bypass the hypoplastic ventricle [9, 102].

The classic Norwood procedure achieves the second objective using a modified Blalock-Thomas-Taussig (mBTT) shunt, which provides pulmonary blood flow by connecting the innominate or subclavian artery to the pulmonary arteries. Migliavacca et al. [103] developed an early uncoupled LPM of the Norwood anatomy with an mBTT shunt using clinical catheterization data of SV patients for model inputs and validation. They explored the effects of shunt size, pulmonary and systemic vascular resistance, and heart rate on

hemodynamics and oxygen delivery. Their model showed that while the standard 3.5 mm diameter mBTT shunt provided optimal oxygen delivery at rest, it failed to provide optimal oxygen delivery during simulated exercise conditions, as pulmonary flow could not increase. Historically, the choice of appropriate shunt size for the Norwood was a challenging decision [104, 105], and one that was not feasible to rigorously test in patients, making it ideal for an in silico investigation. This model has become significantly influential in the field, forming the basis of numerous other S1P LPMs, uncoupled and multiscale, for over two decades [106–112]. Other uncoupled LPMs simulating mBTT shunts have examined the effects of tricuspid regurgitation [99] and the addition of ventricular assist devices [106, 113]. Notably, Pant et al. [99] adopted a patient-specific approach, addressing the difficult task of parameter estimation by utilizing data assimilation techniques via an unscented Kalman filter.

For patients with a hypoplastic LV, pulmonary blood flow can also be provided by a right ventricle-to-pulmonary artery (RVPA) shunt during S1P [114]. This method eliminates the “coronary steal” effect of diastolic runoff inherent to the mBTT shunt [7, 115], but it introduces its own diastolic complication in the form of regurgitation into the right ventricle [115, 116]. Shimizu et al. [117] investigated this effect by modeling valved and non-valved RVPA shunts. They determined that both valved and non-valved RVPA shunts have improved mechanical efficiency (the ratio of stroke work to systolic pressure-volume area) over the mBTT shunt due to a reduction in RV end-diastolic volume, even with regurgitation from the non-valved shunt.

A third option for S1P is the hybrid procedure, wherein the ductus arteriosus is stented and bands are placed around the right and left pulmonary arteries to limit pulmonary flow [7]. This method avoids cardiopulmonary bypass, making it a more attractive option for high-risk neonates [118, 119]. Uncoupled LPMs have explored pulmonary arterial band tightness and ductus arteriosus stent size as variables [120–122]. One model by Shimizu et al. [123] compared the hemodynamics and ventricular energetics of the hybrid procedure to the Norwood with an RVPA shunt, finding that the hybrid procedure resulted in increased pulse pressure and decreased mechanical efficiency. Young et al. [122] took the additional step of comparing their uncoupled LPM of the hybrid procedure to an equivalent multiscale model, demonstrating close equivalence (<10% difference) in most hemodynamic and ventricular energetic outputs between the two models.

3.1.2. Stage 2 Palliation (S2P)

The Glenn procedure, also called S2P, is commonly performed when the patient is between three to six months of age. The procedure can either be elective, when the pulmonary arteries are deemed sufficiently mature, or nonelective, in cases of progressive hypoxemia, shunt occlusion, atrioventricular valvular insufficiency, or ventricular dysfunction [124]. During S2P, the mBTT or RVPA shunt is taken down and the SVC is anastomosed to the right pulmonary artery. This surgical technique, known as the bidirectional cavopulmonary anastomosis (BCPA) was first modeled with an LPM by Pennati et al. in 1997 [125]. Though results from their previous 3D CFD simulations were used to inform some aspects of the LPM, it was not a true multiscale model with coupled 0D-3D components. This model and

its later expansion [126] investigated competing flows between the BCPA and the main pulmonary artery, which is occasionally left in its native configuration if allowed by patient anatomy. This creates a paradoxical situation: the additional pulmonary flow is beneficial for oxygen delivery, which is chronically impaired in Glenn patients [127]. However, it also risks increasing the pressure in the SVC to intolerable levels. The pulmonary-to-systemic flow split (Qp:Qs) is dependent on pulmonary vascular resistance (PVR) and the amount of RV outflow tract obstruction, making it difficult to predict how beneficial this configuration will be for an individual patient. By simulating varying amounts of PVR and outflow obstruction, Pennati et al. determined a range of both values that would lead to an "optimal" post-surgical outcome (defined as a Qp:Qs between 0.75 and 1.25 and SVC pressure less than 15 mmHg).

Other models have used "virtual surgeries" to explore the conversion from S1P to S2P and S2P to S3P. For example, Pant et al. [128] developed an uncoupled LPM that simulates AV regurgitation due to either incomplete leaflet closure or prolapse. They modeled the hemodynamic effects of regurgitation before and after S2P, finding that while the volume unloading of the RV in S2P reduces regurgitation, the effect is offset and ultimately worsened by an increase in ventricular pressure. AV regurgitation is common in this population [129], and Pant et al.'s model suggests that correction of moderate to severe regurgitation prior to or during S2P will improve outcomes. Liang et al. [130] expanded on this concept by identifying changes in hemodynamic outputs (e.g., central venous pressure and oxygenated flow) under normal conditions as well as with AV regurgitation, diastolic

dysfunction, systolic dysfunction, and variations in PVR and lower body arterial resistance. They considered both the BCPA, used in S2P, and the TCPA, used in S3P. In contrast to the pronounced effects of AV regurgitation during S2P demonstrated by Pant et al., Liang and colleagues found AV regurgitation to have less of an impact on S2P hemodynamics compared to increased PVR and the presence of diastolic dysfunction. Notably, both models are based on SV patients with a functional LV and therefore mitral valve regurgitation rather than tricuspid. Whether the results could be applicable to both AV valves is an important consideration, especially given the very different loading conditions faced by each valve in a normal biventricular circulation [131].

Conover et al. [132] took on the significant challenge of simulating virtual surgery for all three stages. Available patient-specific data (body surface area, heart rate, pressures, pulmonary and systemic vascular resistances, shunt type, presence of collaterals or coarctation, etc.) were used to tune the heart and circulation model after allometric scaling determined “base” values for the circulation parameters. To validate post-surgical simulations, Qp:Qs, systemic arterial saturation, mean pulmonary artery pressure, and systemic venous saturation (none of which were used to tune the model) from twenty catheterization reports spanning each stage were compared to model outputs. Of these, only the difference between arterial and venous saturations (SaO2 – SvO2) was statistically significantly different between measurements and model outputs in the S1P and S2P simulations. However, these differences were considered too small to be clinically significant.

Finally, Vallecilla et al. explored situations beyond the surgery itself, modeling the effects of high altitude exposure [133] and exercise [134] on S2P physiology. High altitude was simulated by increasing PVR and heart rate, and exercise was simulated with the same changes along with a reduction in systemic vascular resistance. Both simulated conditions highlighted the deficiencies of S2P physiology: even under ideal conditions, patients experience poor oxygen saturations and decreased cardiac function. Furthermore, as both models demonstrate, any factor that increases the stress on the S2P system only serves to exacerbate these deleterious effects.

3.1.3. Stage 3 Palliation (S3P)

The final stage of SV palliation, the Fontan surgery, has garnered the most attention from the modeling community. This is likely because patients are ideally expected to live with a Fontan circulation for decades, in contrast to the shorter durations of the Norwood and Glenn. However, reduced cardiac output and chronic systemic venous congestion are inherent to Fontan physiology, and if transplant referral is not timely, patients enter a vicious cycle known as “Fontan failure” that ends with multiorgan dysfunction and death [135].

Given this prospect, Fontan failure is of particular interest to clinicians and researchers. Non-pulsatile flow to the pulmonary circulation and chronically elevated central venous pressure can lead to a host of issues for SV patients, presenting as multiple and potentially interrelated phenotypes: Fontan failure with reduced ejection fraction, preserved ejection fraction, abnormal lymphatics, or even relatively “normal” cardiac function despite

noncardiac organ dysfunction [136]. Though failure occurs in a quarter of all Fontan patients by age twenty, only 2.5-3.6% of such patients will undergo transplantation [137, 138]. As treatment advances and more children with single ventricles—particularly those with right heart dominance—survive into adulthood, understanding appropriate management and treatment of Fontan failure becomes all the more critical [139].

Uncoupled LPMs of Fontan physiology have aided this effort. In 2001, Cavalcanti et al. [140] used catheterization pressures from twelve Fontan patients, half of whom had symptoms of Fontan failure, as inputs to their model, holding back measured pressures in the venae cavae and pulmonary arteries to serve as validation. They found close agreement between those measurements and model outputs for both groups, suggesting that inefficiency of the cavopulmonary connection and a concurrent increase in atrial pressure can lead to the pressure alterations in the venous and pulmonary circulations observed in patients with Fontan failure. The model did not, however, fully replicate the reduced cardiac output (CO) reported in Fontan failure patients, implicating additional mechanisms beyond pressure disturbances, such as ventricular dysfunction or compensatory cardiac inhibition.

In the years following, several researchers have attempted to elucidate these mechanisms. By leveraging the discrete yet interconnected nature of LPMs, Liang et al. [141] compared Fontan and biventricular circulations, deducing that while PVR, ventricular diastolic function, and systemic vascular compliance all play major roles in regulating CO, no

parameter has a linear relationship with CO, nor is any single relationship free from the influence of other cardiac parameters. This complexity was further emphasized in their later patient-specific expansion, where, for example, the parameter controlling PVR needed to vary from 23-411% of its base value to adequately match measured hemodynamics from four patients [142]. Though Watrous and Chin [143] found a similar impact of PVR and end-diastolic elastance on CO as Liang et al. in their Fontan model, a significant reduction in end-systolic elastance was also required to match target hemodynamic outputs. In a sensitivity analysis of their normal and failing Fontan models, Doyle et al. [144] also found that ventricular systolic elastance played a large role in CO. Unlike the other two models, however, their model was less sensitive to PVR compared to its systemic counterpart, possibly due to a lack of separation of upper and lower body circulations. Ultimately, the lack of consensus among these models of Fontan failure mirrors the observed range of clinical phenotypes and implicates systolic *and* diastolic cardiac dysfunction as well as pulmonary and systemic vascular maladaptation in the reduction of CO.

This reduction in CO is most pronounced during exercise. For patients who are asymptomatic or exhibit a normal CO during rest, it may be a sign of early Fontan failure [145, 146]. To that end, modelers have simulated exercise conditions to directly study its effects in the Fontan circulation [143, 147–149]. Rather than prescribing a simple increase in heart rate and decrease in vascular resistance to simulate exercise, Magosso et al. [147] developed a robust model that includes arterial and cardiopulmonary baroreflex control, variations in intrathoracic pressure to represent the effects of respiration, and a parallel

oscillating conductance in the skeletal muscle compartment to simulate vasodilation. Compared to normal subjects with a biventricular circulation, they found that though Fontan patients have a higher heart rate during exercise, heart rate elevation alone was insufficient to compensate for their inability to increase or maintain stroke volume. Magosso et al. posited that this inability is caused by an increased resistance to venous return in the Fontan conduit. The resulting insufficient CO stimulates the baroreflex system, which increases systemic vascular resistance in an attempt to maintain adequate blood pressure, leading to a diminished aerobic capacity. Like Cavalcanti et al.'s model of Fontan failure, despite matching experimental data well for heart rate and pressures, the model overestimated CO, possibly due to a lack of changes to ventricular parameters. Kung et al. [149] addressed this shortcoming by determining relationships between input parameters—both vascular and cardiac—and metabolic rate, fitting them to experimental and literature data. By doing so they could quantitatively investigate the effects of various levels of exercise on individual Fontan patients, including metrics such as PVR, which can only be measured invasively and is difficult to acquire during exercise.

For patients in end-stage Fontan failure, ventricular assist devices (VAD) can serve as effective tools for bridging to heart transplant by easing elevated systemic venous and ventricular filling pressures [150]. However, the complex cardiovascular anatomy of SV patients and the poor health of those chosen for VAD support have limited its use, resulting in a paucity of clinical data [150–153]. To fill this knowledge gap, LPMs connecting a VAD component to Fontan anatomy have explored continuous- versus pulsatile-flow pumps

[40, 154], patient-specific indications for VAD use in Fontan failure [155], left (TCPC) versus right-sided (left pulmonary artery) microaxial pumps [156], the effects of VAD support in a swine model of Fontan circulation [157], partial versus total cavopulmonary assistance [158], and comparisons between right, left, and biventricular VADs in Fontan failure [120]. Overall, while most models show the use of a VAD in select patients with Fontan failure could increase CO and reduce venous pressures, the effect on PVR—a major component of Fontan failure risk [159]—is unclear.

3.2. Multiscale Models

By adding a three-dimensional component to the zero-dimensional LPM, multiscale models are ideal for analyzing local effects such as myocardial stress and strain distributions [160], velocity profiles [161], and energy losses [162]. The 3D component—a vascular section, a shunt, or the heart itself—can either be a generalized geometry (e.g., a tube or prolate spheroid) or, more commonly in recent times, a patient-specific reconstruction from MR or CT imaging.

3.2.1. S1P

The various shunt types in the first palliative surgical stage make multiscale models useful for investigating surgical choices. For example, creating patient-specific models contrasting an mBTT shunt (brachiocephalic or right subclavian artery to right pulmonary artery or left subclavian artery to left pulmonary artery) with a central shunt (ascending aorta to main pulmonary artery) is an intuitive process given a 3D representation of the anatomy. In a purely 0D LPM, a meaningful analysis would require separate compartments

for each artery, likely complicating the already arduous task of parameter optimization. In addition, the three-dimensional aspect of multiscale models is ideal for testing various shunt geometries beyond the simple diameter changes investigated by uncoupled LPMs, such as tapering or curvature, making them valuable tools for surgical planning.

As with uncoupled LPMs, Migliavacca and colleagues were early pioneers in S1P multiscale models: in 2004, they used their previous LPM [103] as the 0D component of two multiscale models to compare the performance of mBTT and central shunts on coronary and pulmonary blood flow [163]. A central shunt, though less common than the mBTT shunt, has two theoretical advantages due to its more proximal location to the heart. First, it was hypothesized that it would provide more balanced flow to the lungs than the mBTT shunt, and second, that it would be superior in avoiding the “coronary steal” effect, where blood is diverted through the shunt instead of to the coronary arteries during diastole. With the aid of computational models, these theories could be more rigorously examined than they could be in vivo. Like most multiscale models of its era, the 3D component in the model developed by Migliavacca et al. used an idealized shunt geometry where blood vessel diameters in the 3D component were taken from angiocardiograms. They also assumed rigid walls, leading to an atypically extended period of flow reversal in the aortic arch. Surprisingly, they found that neither lung flow balance nor coronary steal were improved by the central shunt—though not significant, the central shunt actually resulted in slightly less flow to the coronary arteries on average when compared to the mBTT shunt (2.9% versus 3.5%). Furthermore, in more downstream vessels in the systemic

and pulmonary circulations, the relatively low resistance of the central shunt led to greater amplitude of flow and pressure oscillations. While this result favors the mBTT shunt, its more distal position relative to the central shunt caused an undesirable phase delay between systemic and pulmonary flows and pressure waveforms. In a subsequent study using the same model, this group reported similar findings when investigating variations in shunt size [107]. As in their previous study, the central shunt produced slightly worse coronary perfusion than the mBTT shunt, a trend that was consistent at all shunt lengths and diameters. Coronary steal could be reduced in the central shunt if the diameter was reduced, but this, of course, came at a cost to pulmonary flow. Finally, this group took a patient-specific approach to this question over a decade later, modeling one patient with a central shunt and another comparably-sized patient with an mBTT shunt [35]. Two additional models of hypothetical subjects were also created by coupling each patient's tuned LPM with another patient's MRI-derived 3D anatomy. Using the same 3D geometry (either central or mBTT shunt) while varying the LPM led to significantly different time-averaged flows and pressures, particularly in the upper body arteries (a two-fold increase in right subclavian arterial flow for the mBTT shunt anatomy and a reduction by half for the central shunt anatomy). In contrast, using identical LPMs while varying the 3D anatomy led to more comparable hemodynamics (<= 23% absolute difference), highlighting the necessity of accurately fitting LPM parameters in patient-specific multiscale models.

Other researchers have leveraged the fine spatial detail of multiscale models to investigate variations in shunt shape and placement. Though changes in shunt diameter can be

approximated as functions of pressure and flow in a 0D model (see Migliavacca et al. 2001 [103], Young et al. 2013 [121], Shimizu et al. 2016 [123]), the effects are better captured in a 3D model, where diameter changes can be directly prescribed, either throughout the entire length of the shunt or as a localized narrowing or dilatation. It is also possible to model different shunt insertion locations and angles in relation to surrounding vessels, an important consideration due to the degree of anatomical variance in this patient population. Such an approach was taken by Esmaily Moghadam et al. [111] using the aforementioned multiscale model by Migliavacca et al. [163] as a base. After conducting a survey of clinical experts, they considered three mBTT shunt design parameters to maximize oxygen delivery (DO2) to the systemic and coronary circulations: diameter, location on both the brachiocephalic and pulmonary arteries, and angle of attachment. Of the three, shunt diameter had the largest impact on DO2: a larger diameter improved coronary DO2, while a smaller diameter proved more beneficial for systemic DO2. Shunt anastomosis location played a reduced yet substantial role. Attachment more distal to the aorta was favorable for coronary DO2 and a proximal attachment was favorable for systemic DO2. A midrange shunt diameter and placement with a slightly offset attachment angle provided the best compromise between coronary and systemic DO2. Arthurs et al. [164] took a patient-specific approach to mBTT shunt design, modeling the anatomy and hemodynamics of a 4-month-old child with hypoplastic left heart syndrome (HLHS) using pre-S2P catheterization, MRI, and angiography measurements and images. In this case, matching the data necessitated simulating some amount of shunt occlusion. Confirming the presence or severity of shunt occlusion in the patient was not possible with the

available MRI resolution, suggesting the possibility of using computational modeling as a means of enhancing the utility of existing patient data. The occlusion was modeled as a 22% reduction in diameter across the length of the shunt, a perhaps controversial choice given mBTT shunt occlusion is more common at the pulmonary artery junction rather than a uniform distribution throughout the shunt [165–167]. This diameter reduction was then carried over into a subsequent analysis of a hypothetical flared shunt design for the same patient. Flaring the distal end produced slight increases in pulmonary artery flow and mean pressure (6% and 4%, respectively), which may be helpful for underdeveloped pulmonary arteries. While the existence, location, and severity of the patient's shunt occlusion was not confirmed in this study, it is plausible this information could be obtained in future clinical studies when shunts are removed at S2P with no additional imaging or risk to the patient.

As with uncoupled LPMs, multiscale models have also been used to investigate the hybrid S1P procedure, often modifying the 3D component to simulate obstruction of the ductal stent, a common complication of the hybrid procedure [168, 169]. Two such examples—generalized and patient-specific—were developed by Ceballos and colleagues [170, 171]. The first modeled four variations of hybrid procedure anatomy: with and without 90% preductal arch stenosis and with and without a reverse Blalock-Thomas-Taussig (RBTT) shunt. An RBTT shunt varies from the mBTT shunt in that the innominate or right subclavian artery is connected to the main pulmonary artery and the flow direction is generally pulmonary-to-systemic rather than systemic-to-pulmonary. The RBTT shunt can be placed

either reactively or prophylactically as a backup source of perfusion if the aortic arch becomes obstructed. As expected, when Ceballos et al. simulated aortic arch stenosis they found reduced flow to the coronary and carotid arteries, leading to zones of stagnation, reversal, and recirculation—all of which increase thrombosis risk. Though the model indicated these deleterious effects to coronary and carotid flow could be eliminated by the addition of an RBTT shunt, the shunt itself had inherent zones of recirculation and stagnation, ultimately suggesting the danger of thrombosis is incompletely ameliorated. This model was extended in 2019 by simulating hemodynamics in a patient-derived anatomy. After generating the 3D component, a 90% preductal arch stenosis was then manually imposed, and RBTT shunts of various diameters (3.0, 3.5, and 4.0 mm) were analyzed for both the nominal and stenosed anatomies. Though the reductions in flow and pressure in the coronary and carotid arteries due to the stenosis were less pronounced than in the generalized geometry of the previous study (10-15% versus 30%), the addition of an RBTT shunt of any diameter returned pressures and flows to near-nominal values. Comparing these results to those from Esmaily Moghadam et al., [111] who simulated a traditional mBTT shunt, increasing RBTT diameter improved systemic DO2 in the nominal hybrid configuration. However, this benefit was offset by low flow velocity and disorganized flow within the shunt, again increasing the risk of thrombosis. Both groups went on to develop other models of the hybrid procedure exploring particle embolization and shunt placement in cases of arch obstruction. DeCampli and colleagues [172] compared hybrid S1P with mBTT and RVPA shunts, and Migliavacca and colleagues [110, 173] investigated varying sizes of pulmonary bands and ductal stents.

One of the primary advantages of computational modeling is feasibility testing. Novel, even controversial modifications to conventional treatments can be developed and implemented in a risk-free environment, with only the most promising among them then making their way into animal models and eventually human patients. An example is the S1P bidirectional cavopulmonary anastomosis, also known as the assisted bidirectional Glenn (ABG). By removing the need for the RV to supply both systemic and pulmonary circulations in parallel, Glenn physiology is an inherently more stable state than that of the Norwood. However, high PVR in the neonatal period precludes skipping the Norwood in favor of the Glenn, as low pulmonary flow and elevated central venous pressure would be inevitable. The ABG aims to remedy this issue with the addition of an end-to-side shunt between the brachiocephalic artery and the SVC. This approach leverages the ejector pump effect, where a high pressure flowstream (from the systemic artery) mixes with a lower pressure flowstream (from the SVC). The inlet of the high pressure flowstream is tapered, increasing velocity and, in theory, producing a higher pressure in the pulmonary arteries without substantially increasing the pressure in the SVC. Several groups have attempted to test this theory in silico. Verma et al. designed a six-parameter constrained shape optimization problem for the shunt using a generalized anatomy at varying levels of PVR (2.3, 4.3, and 7.1 WUm^2) [174]. Of the six geometric parameters considered, only the outlet area had a significant effect on hemodynamics, and only simulations with the lowest PVR resulted in an increase in pulmonary flow (which was modest at 13%) without a simultaneous increase in SVC pressure. Shang et al. [175] later brought the model into the patient-specific realm, simulating three pre-S2P patient anatomies and comparing the

performance of an ABG with the patients' existing S1P physiology (an mBTT shunt for Patients A and B and a central shunt for Patient C) and a hypothetical BCPA. PVR was set to either the patient's baseline level (3, 3, and 6 WUm^2), or doubled. As in the previous study, while there were modest improvements in pulmonary arterial flow rate and pressure (ranging from 15 to 20%) with the ABG over the traditional BCPA, any ejector pump effect was not strong enough to prevent unwanted increases in SVC pressure, even at baseline (low) PVR. This may be ameliorated by altering the shunt outlet to be slit-shaped, as shown by Jia et al. [176], with the caveat that such a shape would be more prone to occlusion. However, it is probable that the lower Reynolds number, reduced injection pressure, and shorter mixing distance within the shunt compared to those of an industrial ejector pump will prevent the ABG from ever seeing fruition in the clinic. Still, these types of in silico investigations are vital for safely and effectively determining the direction of modern treatment—including which routes will lead to dead ends.

3.2.2. S2P

For S2P, the primary surgical options for single ventricle patients are the BCPA or hemi-Fontan. Though both achieve the goal of unloading the RV by supplying pulmonary flow via a superior cavopulmonary anastomosis, they differ in their approach. The BCPA simply connects the SVC to the right pulmonary artery, while the hemi-Fontan additionally maintains the continuity of the SVC and the right atrium, preventing flow into the atrium with a homograft patch. The hemi-Fontan justifies its higher degree of complexity by

facilitating later S3P conversion to the total cavopulmonary connection, specifically the intracardiac tunnel variety.

As in S1P, multiscale S2P models often explore more nuanced differences in surgical configurations than their uncoupled counterparts. Comparisons between the two S2P techniques slightly favor the BCPA, which results in shorter cardiopulmonary bypass times and fewer post-operative complications, though overall transplant-free survival appears to be equal [177]. Modelers have sought to determine if there are further differences in the underlying fluid dynamics. Corsini et al. [178], for example, replicated the anatomy and hemodynamics of a patient prior to hemi-Fontan surgery, then performed "virtual surgery," excising the S1P shunt from the 3D component and creating either a BCPA or hemi-Fontan while imposing the geometric constraints of the surrounding organs and vessels. Post-operative model validation, though sparse, included brachial cuff pressure and SVC pressure, with hemi-Fontan model outputs in good agreement with both measurements. Model outputs indicated differences between the two surgical methods were minimal, with the only exception being a higher power loss at the surgical junction for the hemi-Fontan. However, the losses were small in comparison to inlet and cardiac powers, indicating that surgical geometry had little impact on the behavior of the overall circulation at rest. Similar differences were found in a more extensive study by Kung et al. [179]. They modeled six patients, performing virtual BCPA and hemi-Fontan procedures for each. With the inclusion of more patients, the difference in power loss between the two methods disappeared: in one patient, the hemi-Fontan model produced a higher power loss than the BCPA. In three

other patients, the opposite occurred. For the remaining two patients, power losses were minimal for both methods. When considering all six patients, there were no significant differences between the hemi-Fontan and BCPA models for CO, SVC pressure, left:right pulmonary flow distribution, or systemic DO2, and the power losses of either geometry were relatively small when compared to the rest of the circulation. Notably, a limitation of both these studies—as with the vast majority of S1P and S2P models—is that patients were only simulated at rest. As indicated by Corsini et al. [178], hemodynamics can vary widely with changes in circulatory parameters due to physiological states, e.g., sedation or agitation. Indeed, an earlier study by Kung and colleagues [180] modeling two patients with virtual hemi-Fontans generated a surgical junction power loss greater than systemic losses when simulating the vasodilation and increased heart rate associated with exercise states (equivalent to crying for the age range under consideration). Therefore, the debate about whether one surgical option is superior to the other remains unsettled.

Left pulmonary artery stenosis is a common complication for post-S1P patients, particularly those with mBTT shunts [181, 182]. While it is unclear what degree of stenosis necessitates additional treatment, such as ballooning or stenting, the non-pulsatile flow introduced by S2P makes any obstruction in the pulmonary arteries concerning. Using MR images of a patient with 50% left pulmonary artery stenosis as the basis of their 3D component, Ma et al. [183] investigated the hemodynamic impact of four degrees of stenosis in BCPA physiology: 0%, 25%, 50%, and 75%. Of the four, only 75% stenosis produced significant changes in lung perfusion, power loss, wall shear stress, and

oscillatory shear index. These findings were largely corroborated by Schiavazzi et al. [184] using a patient-specific approach coupled with clinical judgment. They simulated stenoses of 35-80% qualitatively graded by physicians as minimal, mild, moderate, or severe, and evaluated model results according to the clinically significant metrics of right:left pulmonary artery flow split <30% and/or a mean pressure drop of >3.0 mmHg as treatment thresholds. However, applying the thresholds to individual patients led to a clinically significant stenosis range of 48% to 79%, emphasizing the importance of inter-patient variability and suggesting caution when attempting to define thresholds from generalized models.

Other multiscale S2P models have simulated more unusual clinical scenarios, such as veno-venous collateral occlusion [185] and hybrid comprehensive Stage 2, a variation of S2P for a subset of patients who receive the hybrid S1P procedure [25, 186]. Lastly, unlike the other models described in this review, one particularly unique S2P model made its patient-derived 3D component the single ventricle itself, rather than some portion of the vasculature. Cutrì et al. [187] sought to investigate fiber orientation in the RV of a patient with HLHS. As the actual orientation of cardiac fibers in SV patients is unknown and especially difficult to assume for a systemic RV, Cutrì and colleagues simulated two simplified cases: a physiologically typical RV fiber orientation (ranging from -60° at the epicardium to +90° at the endocardium with respect to the circumferential direction) and a physiologically typical LV fiber orientation (from -60° at the epicardium to +60° at the endocardium). After tuning a purely 0D LPM to produce outputs matching measured

patient hemodynamics, the SV component of the LPM was replaced with the finite element SV. The passive behavior of the myocardium in the finite element SV was modeled using Holzapfel and Ogden's hyperelastic constitutive equation [188] to account for anisotropy in fiber and cross-fiber directions. The active behavior was modeled using the Lumens TriSeg approach [89] to account for sarcomere length and mechanical activation. Virtual BCPA surgery was performed by modifying the LPM, and the two fiber orientation cases were compared. While both cases produced similar hemodynamics, making it impossible to determine which orientation was closer to the patient's actual fiber distribution, they produced different local mechanics. When the cardiac fibers of the SV were set to the typical LV orientation, strain patterns were homogeneous (though higher in magnitude) and stresses were lower than when the typical RV orientation was imposed, implying that a shift toward a more LV-like fiber orientation could be beneficial for a systemic RV.

3.2.3. S3P

Multiscale models of S3P capture a considerable breadth of surgical innovations and physiological states, arguably leading to the greatest impact on clinical practice among all stages and model types described herein.

The earliest of these models aimed to characterize flow patterns in different configurations of the TCPC. Using a relatively simple LPM consisting only of pulmonary afterload, in 1996 Dubini et al. [100] and de Leval et al. [101] simulated various degrees of SVC-to-inferior vena cava (IVC) offset, IVC-to-pulmonary artery angle, and IVC anastomosis diameter in their 3D component, with the goal of reducing energy loss within the TCPC and optimizing

flow distribution between the lungs. However, they discovered that these goals were at odds with one another: while an offset of 0.5-0.7 cm was ideal for flow distribution, it came at the expense of energy efficiency. This power loss was remedied by enlarging the IVC anastomosis diameter, though the authors acknowledged this would require patch enlargement of both caval connections, complicating surgery. Nearly two decades later, a study of 131 Fontan patients indicated that an offset is commonly used in practice [189], though pulmonary artery diameter proved much more significant in determining lung flow distribution, an aspect the early models neglected to explore.

As in uncoupled LPM Fontan models, the importance of exercise testing in assessing cardiovascular health has made it a popular target for modelers. Sundareswaran et al. [190] modeled 16 different patient anatomies, using energy loss across the TCPC to determine 16 individual TCPC resistances. Mean SVR and PVR values from 40 Fontan patient catheter studies were used to calibrate the LPM, with compliance and impedance values coming from literature. Pressures (systemic arterial systolic and diastolic, and systemic venous) and CO were left out for model validation. To compare performance during exercise, a non-specific biventricular LPM was designed using equivalent vascular parameters, with the exception of venous compliance, which was 4.6x greater than in the SV LPM. Exercise was simulated by increasing CO by varying amounts depending on the age of the patient. For the SV and biventricular models, this was accomplished by increasing heart rate and decreasing SVR and PVR by 50% and 40%, respectively. The biventricular model additionally had its contractile parameters modified, an adaptation to

replicate the significant impairment observed in Fontan patients [191]. The biventricular model, even with the same PVR and SVR values as the SV models, nearly doubled CO during exercise. This was not the case with the SV simulations: in particular, TCPC resistance was a powerful detriment to CO during exercise and highly variable among individual patients, even with the same PVR. The resistance of the "worst" TCPC was 10x higher than the "best" TCPC, suggesting substantial room for improvement in TCPC design. Marsden et al. [192] implemented a more sophisticated method for simulating exercise, including respiratory effects, resistance adjustments of morphometry-based arterial trees, and increased IVC flow rates, based on clinical exercise data in Fontan patients. They found predicating Fontan success on TCPC energy efficiency alone to be inadequate, even when considering it in the context of rest and exercise states. Of the six patients modeled, the patient with the best energy efficiency had the highest SVC pressure during both rest and exercise, and the patient with the best IVC flow distribution had one of the lowest values of energy efficiency, leading the authors to advise modelers to think more broadly when attempting to optimize Fontan designs. Baretta et al. [193] also included a respiration model in their investigation of different TCPC configurations (T-shaped, offset, and Y-shaped) under rest and exercise states, generating more physiologically realistic venous waveforms. Perhaps surprisingly, given the promise the Y-shaped graft has for hepatic flow distribution and energy loss [194], the TCPC configuration had negligible impact on hemodynamics, and the Y-shaped graft offered only minor improvements in energy efficiency under exercise conditions (mean of 94.2%, compared to 91.7% for T-shaped and 92.5% for offset).

Multiscale S3P models have also had their share of feasibility studies for novel approaches to alleviate the effects of Fontan failure. Throckmorton et al. [195] modeled an axial flow blood pump placed into the IVC for both idealized and patient-specific anatomies at varying degrees of Fontan failure. The pump significantly decreased IVC pressure (from 20.49 mmHg to 12.57 mmHg for the worst-case Fontan scenario) while reducing particle residence time, though blood damage indices were higher than the control simulation due to the pump's impeller blades. Albal et al. [196] addressed the common use of a fenestration between the Fontan conduit and right atrium. Designed as a type of pressure-relief valve to prevent IVC hypertension, the fenestration nevertheless can cause reduced pulmonary flow due to excessive right-to-left shunting. Albal and colleagues built benchtop in vitro systems to test several novel valved fenestration designs and used the results to fit their in silico fenestration resistance. A plus-shaped valved model was compared to a typical circular fenestration with the same effective orifice area, producing more controlled flow and pressure drops across the fenestration as IVC pressure exceeded 5 mmHg. However, the typically sluggish flow in the Fontan circuit increases the risk of thromboembolism [197], and the authors warn the leaflets in the proposed plus-shaped fenestration may amplify that risk to an untenable degree. Lastly, Ni et al. [198] introduced the ejector pump effect of the S1P assisted bidirectional Glenn described previously (see Section 3.2.1) to the Fontan circulation via a bifurcated shunt from the aorta to the left and right pulmonary artery inflows. After optimizing geometric parameters under steady-state conditions to reduce IVC pressure, the final shunt model and surrounding vessels were coupled to a non-steady-state LPM. While the ejector pump design appeared to work

better here than in ABG models, decreasing IVC pressure by 2.9 mmHg and increasing systemic DO2 by 22%, it was under highly idealized conditions: a rigid, non-patient-specific geometry, a Qp:Qs capped at 1.5, and a 60% reduction in PVR based on data from adult Fontan patients with aortopulmonary collaterals. Several of these issues have been addressed in an updated version of the model, which emphasizes an injection jet shunt is most effective when operating in tandem with the fenestration [199].

Aiding surgical planning is an aspirational goal for many modelers seeking to translate their work from the theoretical to the practical. Though a direct impact on surgical decision making is still rare, a patient-specific model by Ahmed et al. [200] demonstrates the potential of the field. A two-year-old patient was experiencing complications believed to be caused by dilatation of the patient's lateral tunnel Fontan. The patient's clinical team was considering a surgical revision, where a custom-made endograft deployed within the Fontan pathway would stabilize and redirect flow. The modeling team created a coupled 3D-0D model fitted to the patient's anatomy and hemodynamics. When surgery was simulated, the results showed that rather than decreasing the pressure in the IVC and reducing hepatic venous reflux, the proposed graft—due to its reduced diameter and stiffness—would actually increase IVC pressure and hepatic reflux. These outcomes were deemed unfavorable for the patient, and based on the model results and feasibility issues, the clinical team decided to pursue other options.

4. Future Directions

Looking ahead, there is substantial opportunity to expand and improve lumped parameter models of SV pathologies. With few exceptions, such as the Fontan failure and exercise models presented in Sections 3.1.3 and 3.2.3, both uncoupled and multiscale models have focused primarily on surgical intervention, with some consideration for comorbidities such as valve regurgitation [99, 201], pulmonary stenosis [183, 202], and collateral vessel formation [185, 201]. While essential, surgical palliation is only the beginning of treatment for SV patients. Advances in surgical intervention and interstage monitoring have significantly reduced SV mortality [203, 204], ushering in a new era of care focused on reducing the impact of comorbidities and improving quality of life. Many common comorbidities have yet to be considered, including bicuspid aortic valve, ventricular septal defects, anomalous pulmonary venous return, arrhythmias, pulmonary edema, and endocardial fibroelastosis [7, 205]. As we enter this new phase in SV patient care, models exploring situations like cardiopulmonary resuscitation (Stromberg et al. 2022 [206]) and high altitude exposure (Vallecilla et al. 2014 [133]) will become increasingly important. Relatedly, to our knowledge no existing models address the wide range of medications commonly used to treat SV patients, such as inotropes, sedatives, analgesics, vasodilators, antiarrhythmics, and diuretics [7, 207]. Indeed, multiscale models integrating cell signaling and chemo-bio-mechanical processes could explore new avenues of SV disease progression and treatment [208]. Further, as more Fontan patients survive into adulthood, one major life experience, pregnancy, has received increased attention in the SV research community [209]. Understandably, the risk of complications for a pregnant SV

patient is much higher than in their healthy biventricular peers. However, the effects of pregnancy on the Fontan circulation are still poorly understood and difficult to research given the paucity of data, making computational models potentially useful in understanding and mitigating risk.

Though this review has focused on models simulating SV conditions post-birth, these pathologies develop in utero, leading to an interest in potential fetal interventions [210]. Recently, two multiscale models have been developed to investigate one such intervention: fetal aortic valvuloplasty (FAV). FAV aims to prevent progression to HLHS by balloon inflating the fetus's stenotic aortic valve. With the outflow tract less obstructed, blood flows more easily into and out of the LV, encouraging left heart growth and increasing the likelihood of biventricular circulation at birth [211, 212]. To better characterize the drastic change in cardiovascular biomechanics experienced by fetuses undergoing this procedure, Wong et al. [213] created a multiscale model of pre-intervention fetal circulation, combining 4D ultrasound-derived finite element models of the heart with an LPM of the fetal circulation developed by Pennati et al. [214]. They calibrated the model to five healthy fetuses and five fetuses with evolving HLHS with gestation ages of 22 to 38 weeks, finding drastically different flow patterns between the two groups. In the HLHS group, mitral valve stenosis caused a fast and narrow diastolic inflow jet, which led to elevated vorticity and wall shear stress at the left ventricular apex. In contrast, the healthy group had a wide and slow inflow jet, and elevations in vorticity and wall shear stress occurred at the mid-ventricle region. Valve malformations were also responsible for

elevated intraventricular pressure gradients and energy losses in both systole and diastole. Lastly and perhaps most importantly, the HLHS LV had reduced blood turnover (i.e., the amount of blood pumped to the aorta versus residual LV blood); this suggests a hypoxic environment for the endocardium, which the authors posited could be linked to fetal development of endocardial fibroelastosis. A follow-up study using the same methodology explored FAV itself, modeling 6 healthy and 9 HLHS fetuses at various gestational ages [215]. Their goal was to determine if pre-FAV biomechanical model parameters could robustly predict univentricular and biventricular outcomes. One model parameter, peak systole myofiber stress, was significantly higher in the biventricular FAV group than either the univentricular FAV or healthy groups. As stresses are not measurable clinically, a correlation analysis between this parameter and common echo measurements was used to develop an empirical equation for estimating peak stress. The stress estimated via this equation was statistically superior to other model biomechanical parameters (normalized peak LV pressure, normalized work done, normalized myocardial contractility) and individual echo measurements (e.g., end-diastolic volume) in predicting univentricular versus biventricular results in a separate retrospective cohort (AUC = 0.91, n = 37). The authors hypothesized that the ability to withstand higher stresses indicates healthier myocardium, and therefore these hypoplastic LVs are better able to support a biventricular circulation. The peak stress equation developed in this study could become an important diagnostic tool for clinicians to predict which patients will benefit from FAV and achieve a biventricular outcome, while avoiding FAV in individuals for whom the procedure offers no clear advantage.

Science is a collaborative effort, and computational modeling is no exception. To develop useful hypotheses and the tools to test them, modelers must collaborate closely with surgeons, cardiologists, interventionalists, statisticians, and data scientists. Such partnerships are essential for collecting the robust data needed to calibrate and validate computer models. For example, the immediate post-S1P period is particularly challenging to simulate due to a deficit of age-appropriate measurements. Most models rely on pre-S2P echocardiogram and catheter data such as that collected by Migliavacca et al. [103] in 2001, even though measurements taken at 4-6 months of age may not be applicable to newborns. This is particularly notable in the case of PVR, which changes dramatically after birth [216, 217] and is often a highly sensitive parameter in the LPMs that include it [113, 141, 214, 218, 219]. Primeaux et al. [41] attempted to overcome this limitation. They first created a generalized pre-S2P multiscale model by altering a patient-specific geometry (generated using MRI) with morphological data (e.g., aortic diameter) from healthy and HLHS patients at the pre-S2P timepoint. Hemodynamic measurements (e.g., systolic arterial pressure) from multiple pre-S2P studies were used to fit the LPM parameters. They then scaled the 3D component down using morphological data from the post-S1P timepoint, refitting the LPM parameters to available post-S1P literature data to create a population-level representative post-S1P model. Though the post-S1P and pre-S2P model outputs differed in predictable ways, such as flow increasing with age, the post-S1P model demonstrated notably higher pulmonary arterial pressures, likely due to increased PVR. However, the utility of this result was stymied by the very issue the research team hoped to address: the absence of pulmonary pressure data at the post-S1P timepoint for validation.

This example also highlights a persistent conundrum in modeling SV pathologies: is it realistic to create a "generalized" model for conditions with such a wide range of anatomic phenotypes and hemodynamic variability? Primeaux et al. tuned their input parameter set using weighted mean values of hemodynamic and morphological measurements, combining data from multiple studies, but large ranges of reported data and discrepancies between studies make it challenging to interpret these types of results—no patient is 'average' in all respects. On the other hand, a patient-specific model is of limited utility if it cannot be quickly adapted to simulate multiple different patient data sets. In light of this, model components must be thoughtfully designed, parameter choices must be grounded in statistical methods, and data for both parameter tuning and validation must be plentiful for computational models to move beyond theoretical use cases.

Further, to encourage reproducibility, improve model performance, and prevent the "black box effect," model code and its associated documentation should be made open source—freely available and publicly accessible—whenever possible. Despite a growing awareness of the benefits of open source data and code across scientific disciplines [220–223], this practice is still uncommon in the cardiovascular modeling field, with SimVascular [224] and CRIMSON [225] being the only prominent open source models at this time.

5. Conclusion

Lumped parameter cardiovascular models, whether standalone or coupled to higher order models, provide an endlessly modular testing ground for exploring hemodynamics, treatments, and comorbidities associated with single ventricle pathologies. The low-cost,

low-risk nature of LPMs makes them ideal for a patient population that is limited in number, highly heterogeneous, and often physically fragile. As more children with single ventricles survive into adulthood, the need for individualized treatment plans will only increase. The computational efficiency and customizability of LPMs make them an attractive option for bedside analysis, with the potential to impact clinical decision-making.

Author's Contributions

AH: Performed the literature analysis and investigation, wrote the original manuscript draft, and created the figures; CW: Conceptualized the review, contributed to writing and editing the manuscript, and provided final approval of the manuscript.

Acknowledgements

Support for this research was provided by the University of Wisconsin-Madison, Office of the Vice Chancellor for Research with funding from the Wisconsin Alumni Research Foundation.

Funding

This work was supported by the Additional Ventures Expansion Award (Grant ID: 1434600)

Availability of Data and material

Not applicable.

Code Availability

Not applicable.

Conflict of interest

No authors report a conflict of interest and there are no relationships with industry for this work.

References

1. Rao PS (2021) Single Ventricle—A Comprehensive Review. Children 8:441. https://doi.org/10.3390/children8060441

2. O'Leary PW (2002) Prevalence, clinical presentation and natural history of patients with single ventricle. Prog Pediatr Cardiol 16:31–38. https://doi.org/10.1016/S1058-9813(02)00042-5

3. Collins RT, Fram RY, Tang X, et al (2013) Impact of anatomical subtype and medical comorbidities on hospitalizations in adults with single ventricle congenital heart disease. Int J Cardiol 168:4596–4601. https://doi.org/10.1016/j.ijcard.2013.07.164

4. Tabtabai S, DeFaria Yeh D, Stefanescu A, et al (2015) National Trends in Hospitalizations for Patients With Single-Ventricle Anatomy. Am J Cardiol 116:773–778. https://doi.org/10.1016/j.amjcard.2015.05.053

5. Karamlou T, Diggs BS, Welke K, et al (2012) Impact of Single-Ventricle Physiology on Death After Heart Transplantation in Adults With Congenital Heart Disease. Ann Thorac Surg 94:1281–1288. https://doi.org/10.1016/j.athoracsur.2012.05.075

6. Marshall KH, D'Udekem Y, Sholler GF, et al (2020) Health-Related Quality of Life in Children, Adolescents, and Adults With a Fontan Circulation: A Meta-Analysis. J Am Heart Assoc 9:e014172. https://doi.org/10.1161/JAHA.119.014172

7. Alphonso N, Angelini A, Barron DJ, et al (2020) Guidelines for the management of neonates and infants with hypoplastic left heart syndrome: The European Association for Cardio-Thoracic Surgery (EACTS) and the Association for European Paediatric and Congenital Cardiology (AEPC) Hypoplastic Left Heart Syndrome Guidelines Task Force. Eur J Cardiothorac Surg 58:416–499. https://doi.org/10.1093/ejcts/ezaa188

8. Arnold RR, Loukanov T, Gorenflo M (2014) Hypoplastic Left Heart Syndrome â€“ Unresolved Issues. Front Pediatr 2:. https://doi.org/10.3389/fped.2014.00125

9. Ohye RG, Schranz D, D'Udekem Y (2016) Current Therapy for Hypoplastic Left Heart Syndrome and Related Single Ventricle Lesions. Circulation 134:1265–1279. https://doi.org/10.1161/CIRCULATIONAHA.116.022816

10. Alsoufi B, Deshpande S, McCracken C, et al (2015) Results of heart transplantation following failed staged palliation of hypoplastic left heart syndrome and related single ventricle anomalies. Eur J Cardiothorac Surg 48:792–799. https://doi.org/10.1093/ejcts/ezu547

11. Greenberg JW, Pribble CM, Singareddy A, et al (2021) The Failed Bidirectional Glenn Shunt: Risk Factors for Poor Outcomes and the Role of Early Reoperation. World J

Pediatr Congenit Heart Surg 12:760–764. https://doi.org/10.1177/21501351211044129

12. Friedman KG, Salvin JW, Wypij D, et al (2011) Risk factors for failed staged palliation after bidirectional Glenn in infants, who have undergone stage one palliation☆. Eur J Cardiothorac Surg S1010794011001230. https://doi.org/10.1016/j.ejcts.2011.01.056

13. Trusty PM, Slesnick TC, Wei ZA, et al (2018) Fontan Surgical Planning: Previous Accomplishments, Current Challenges, and Future Directions. J Cardiovasc Transl Res 11:133–144. https://doi.org/10.1007/s12265-018-9786-0

14. Wald RM, Mertens LL (2022) Hypoplastic Left Heart Syndrome Across the Lifespan: Clinical Considerations for Care of the Fetus, Child, and Adult. Can J Cardiol 38:930–945. https://doi.org/10.1016/j.cjca.2022.04.028

15. Yabrodi M, Mastropietro CW (2017) Hypoplastic left heart syndrome: from comfort care to long-term survival. Pediatr Res 81:142–149. https://doi.org/10.1038/pr.2016.194

16. Taylor CA, Figueroa CA (2009) Patient-Specific Modeling of Cardiovascular Mechanics. Annu Rev Biomed Eng 11:109–134. https://doi.org/10.1146/annurev.bioeng.10.061807.160521

17. Peirlinck M, Costabal FS, Yao J, et al (2021) Precision medicine in human heart modeling: Perspectives, challenges, and opportunities. Biomech Model Mechanobiol 20:803–831. https://doi.org/10.1007/s10237-021-01421-z

18. Garber L, Khodaei S, Keshavarz-Motamed Z (2022) The Critical Role of Lumped Parameter Models in Patient-Specific Cardiovascular Simulations. Arch Comput Methods Eng 29:2977–3000

19. Shimizu S, Une D, Kawada T, et al (2018) Lumped parameter model for hemodynamic simulation of congenital heart diseases. J Physiol Sci 68:103–111. https://doi.org/10.1007/s12576-017-0585-1

20. Biglino G, Capelli C, Bruse J, et al (2017) Computational modelling for congenital heart disease: how far are we from clinical translation? Heart 103:98–103. https://doi.org/10.1136/heartjnl-2016-310423

21. Perktold K, Resch M, Peter RO (1991) Three-dimensional numerical analysis of pulsatile flow and wall shear stress in the carotid artery bifurcation. J Biomech 24:409–420. https://doi.org/10.1016/0021-9290(91)90029-M

22. Taylor CA, Hughes TJR, Zarins CK (1998) Finite Element Modeling of Three-Dimensional Pulsatile Flow in the Abdominal Aorta: Relevance to Atherosclerosis. Ann Biomed Eng 26:975–987. https://doi.org/10.1114/1.140

23. Hsia T-Y, Migliavacca F, Pittaccio S, et al (2004) Computational fluid dynamic study of flow optimization in realistic models of the total cavopulmonary connections. J Surg Res 116:305–313. https://doi.org/10.1016/j.jss.2003.08.004

24. Migliavacca F, Dubini G (2005) Computational modeling of vascular anastomoses. Biomech Model Mechanobiol 3:235–250. https://doi.org/10.1007/s10237-005-0070-2

25. Hameed M, Prather R, Divo E, et al (2021) Computational fluid dynamics investigation of the novel hybrid comprehensive stage II operation. JTCVS Open 7:308–323. https://doi.org/10.1016/j.xjon.2021.04.009

26. Vignon-Clementel IE, Alberto Figueroa C, Jansen KE, Taylor CA (2006) Outflow boundary conditions for three-dimensional finite element modeling of blood flow and pressure in arteries. Comput Methods Appl Mech Eng 195:3776–3796. https://doi.org/10.1016/j.cma.2005.04.014

27. Kim HJ, Vignon-Clementel IE, Figueroa CA, et al (2009) On Coupling a Lumped Parameter Heart Model and a Three-Dimensional Finite Element Aorta Model. Ann Biomed Eng 37:2153–2169. https://doi.org/10.1007/s10439-009-9760-8

28. Snyder MF, Rideout VC (1969) Computer Simulation Studies of the Venous Circulation. IEEE Trans Biomed Eng BME-16:325–334. https://doi.org/10.1109/TBME.1969.4502663

29. Westerhof N, Bosman F, De Vries CJ, Noordergraaf A (1969) Analog studies of the human systemic arterial tree. J Biomech 2:121–143. https://doi.org/10.1016/0021-9290(69)90024-4

30. Quarteroni A, Veneziani A (2003) Analysis of a geometrical multiscale model based on the coupling of ODEs and PDEs for blood flow simulations. Multiscale Model Simul 1:173–195. http://dx.doi.org/10.1137/S1540345902408482

31. Vignon-Clementel IE, Figueroa CA, Jansen KE, Taylor CA (2010) Outflow boundary conditions for 3D simulations of non-periodic blood flow and pressure fields in deformable arteries. Comput Methods Biomech Biomed Engin 13:625–640. https://doi.org/10.1080/10255840903413565

32. Ježek F, Kulhánek T, Kalecký K, Kofránek J (2017) Lumped models of the cardiovascular system of various complexity. Biocybern Biomed Eng 37:666–678. https://doi.org/10.1016/j.bbe.2017.08.001

33. Braakman R, Sipkema P, Westerhof N (1989) A dynamic nonlinear lumped parameter model for skeletal muscle circulation. Ann Biomed Eng 17:593–616. https://doi.org/10.1007/BF02367465

34. Chiastra C, Wu W, Dickerhoff B, et al (2016) Computational replication of the patient-specific stenting procedure for coronary artery bifurcations: From OCT and CT imaging

to structural and hemodynamics analyses. J Biomech 49:2102–2111. https://doi.org/10.1016/j.jbiomech.2015.11.024

35. Corsini C, Migliavacca F, Hsia T-Y, Pennati G (2018) The influence of systemic-to-pulmonary arterial shunts and peripheral vasculatures in univentricular circulations: Focus on coronary perfusion and aortic arch hemodynamics through computational multi-domain modeling. J Biomech 79:97–104. https://doi.org/10.1016/j.jbiomech.2018.07.042

36. Andersson M, Lantz J, Ebbers T, Karlsson M (2015) Quantitative Assessment of Turbulence and Flow Eccentricity in an Aortic Coarctation: Impact of Virtual Interventions. Cardiovasc Eng Technol 6:281–293. https://doi.org/10.1007/s13239-015-0218-x

37. Del Bianco F, Colli Franzone P, Scacchi S, Fassina L (2018) Electromechanical effects of concentric hypertrophy on the left ventricle: A simulation study. Comput Biol Med 99:236–256. https://doi.org/10.1016/j.compbiomed.2018.06.004

38. Dong H, Liu M, Qin T, et al (2022) A novel computational growth framework for biological tissues: Application to growth of aortic root aneurysm repaired by the V-shape surgery. J Mech Behav Biomed Mater 127:105081. https://doi.org/10.1016/j.jmbbm.2022.105081

39. Figueroa CA, Humphrey JD (2014) Pressure Wave Propagation in Full-body Arterial Models: A Gateway to Exploring Aging and Hypertension. Procedia IUTAM 10:382–395. https://doi.org/10.1016/j.piutam.2014.01.033

40. Pekkan K, Frakes D, De Zelicourt D, et al (2005) Coupling Pediatric Ventricle Assist Devices to the Fontan Circulation: Simulations with a Lumped-Parameter Model. ASAIO J 51:618–628. https://doi.org/10.1097/01.mat.0000176169.73987.0d

41. Primeaux J, Salavitabar A, Lu JC, et al (2021) Characterization of Post-Operative Hemodynamics Following the Norwood Procedure Using Population Data and Multi-Scale Modeling. Front Physiol 12:603040. https://doi.org/10.3389/fphys.2021.603040

42. Sagawa K (1990) Translation of Otto frank's paper "Die Grundform des arteriellen Pulses" zeitschrift für biologie 37: 483–526 (1899). J Mol Cell Cardiol 22:253–254. https://doi.org/10.1016/0022-2828(90)91459-K

43. Westerhof N, Lankhaar J-W, Westerhof BE (2009) The arterial Windkessel. Med Biol Eng Comput 47:131–141. https://doi.org/10.1007/s11517-008-0359-2

44. Stergiopulos N, Meister JJ, Westerhof N (1995) Evaluation of methods for estimation of total arterial compliance. Am J Physiol-Heart Circ Physiol 268:H1540–H1548. https://doi.org/10.1152/ajpheart.1995.268.4.H1540

45. Westerhof N, Elzinga G, Sipkema P (1971) An artificial arterial system for pumping hearts. J Appl Physiol 31:776–781. https://doi.org/10.1152/jappl.1971.31.5.776

46. Toorop GP, Westerhof N, Elzinga G (1987) Beat-to-beat estimation of peripheral resistance and arterial compliance during pressure transients. Am J Physiol-Heart Circ Physiol 252:H1275–H1283. https://doi.org/10.1152/ajpheart.1987.252.6.H1275

47. Stergiopulos N, Westerhof BE, Westerhof N (1999) Total arterial inertance as the fourth element of the windkessel model. Am J Physiol-Heart Circ Physiol 276:H81–H88. https://doi.org/10.1152/ajpheart.1999.276.1.H81

48. Beyar R, Hausknecht MJ, Halperin HR, et al (1987) Interaction between cardiac chambers and thoracic pressure in intact circulation. Am J Physiol-Heart Circ Physiol 253:H1240–H1252. https://doi.org/10.1152/ajpheart.1987.253.5.H1240

49. Ben-Assa E, Brown J, Keshavarz-Motamed Z, et al (2019) Ventricular stroke work and vascular impedance refine the characterization of patients with aortic stenosis. Sci Transl Med 11:eaaw0181. https://doi.org/10.1126/scitranslmed.aaw0181

50. Keshavarz-Motamed Z, Garcia J, Gaillard E, et al (2014) Non-Invasive Determination of Left Ventricular Workload in Patients with Aortic Stenosis Using Magnetic Resonance Imaging and Doppler Echocardiography. PLoS ONE 9:e86793. https://doi.org/10.1371/journal.pone.0086793

51. Keshavarz-Motamed Z, Garcia J, Pibarot P, et al (2011) Modeling the impact of concomitant aortic stenosis and coarctation of the aorta on left ventricular workload. J Biomech 44:2817–2825. https://doi.org/10.1016/j.jbiomech.2011.08.001

52. Casas B, Lantz J, Viola F, et al (2017) Bridging the gap between measurements and modelling: a cardiovascular functional avatar. Sci Rep 7:6214. https://doi.org/10.1038/s41598-017-06339-0

53. Itu L, Sharma P, Georgescu B, et al (2014) Model based non-invasive estimation of PV loop from echocardiography. In: 2014 36th Annual International Conference of the IEEE Engineering in Medicine and Biology Society. IEEE, Chicago, IL, pp 6774–6777

54. Zhu S, Luo L, Yang B, et al (2017) Improving hemodynamics of cardiovascular system under a novel intraventricular assist device support via modeling and simulations. Comput Assist Surg 22:221–231. https://doi.org/10.1080/24699322.2017.1389400

55. Broomé M, Maksuti E, Bjällmark A, et al (2013) Closed-loop real-time simulation model of hemodynamics and oxygen transport in the cardiovascular system. Biomed Eng OnLine 12:69. https://doi.org/10.1186/1475-925X-12-69

56. Thiel J-N, Costa AM, Wiegmann B, et al (2025) Quantifying the influence of combined lung and kidney support using a cardiovascular model and sensitivity analysis-

informed parameter identification. Comput Biol Med 186:109668. https://doi.org/10.1016/j.compbiomed.2025.109668

57. Tang H, Dai Z, Wang M, et al (2020) Lumped-Parameter Circuit Platform for Simulating Typical Cases of Pulmonary Hypertensions from Point of Hemodynamics. J Cardiovasc Transl Res 13:826–852. https://doi.org/10.1007/s12265-020-09953-y

58. Colunga AL, Colebank MJ, REU Program, Olufsen MS (2023) Parameter inference in a computational model of haemodynamics in pulmonary hypertension. J R Soc Interface 20:20220735. https://doi.org/10.1098/rsif.2022.0735

59. Keramati H, Van Houts L, Chen CK, et al (2021) Multiscale modeling of a modified BLALOCK-TAUSSIG surgery in a PATIENT-SPECIFIC tetralogy of Fallot. Int J Numer Methods Biomed Eng 37:e3436. https://doi.org/10.1002/cnm.3436

60. Esmaily-Moghadam M, Murtuza B, Hsia T-Y, Marsden A (2015) Simulations Reveal Adverse Hemodynamics in Patients With Multiple Systemic to Pulmonary Shunts. J Biomech Eng 137:031001. https://doi.org/10.1115/1.4029429

61. Korurek M, Yildiz M, Yüksel A, Şahin A (2012) Simulation of Eisenmenger syndrome with ventricular septal defect using equivalent electronic system. Cardiol Young 22:301–306. https://doi.org/10.1017/S1047951111001478

62. Suga H, Sagawa K, Shoukas AA (1973) Load Independence of the Instantaneous Pressure-Volume Ratio of the Canine Left Ventricle and Effects of Epinephrine and Heart Rate on the Ratio. Circ Res 32:314–322. https://doi.org/10.1161/01.RES.32.3.314

63. Santamore WP, Burkhoff D (1991) Hemodynamic consequences of ventricular interaction as assessed by model analysis. Am J Physiol-Heart Circ Physiol 260:H146–H157. https://doi.org/10.1152/ajpheart.1991.260.1.H146

64. Burkhoff D, Tyberg JV (1993) Why does pulmonary venous pressure rise after onset of LV dysfunction: a theoretical analysis. Am J Physiol-Heart Circ Physiol 265:H1819–H1828. https://doi.org/10.1152/ajpheart.1993.265.5.H1819

65. Stergiopulos N, Meister JJ, Westerhof N (1996) Determinants of stroke volume and systolic and diastolic aortic pressure. Am J Physiol-Heart Circ Physiol 270:H2050–H2059. https://doi.org/10.1152/ajpheart.1996.270.6.H2050

66. Caggiano LR, Holmes JW, Witzenburg CM (2022) Individual variability in animal-specific hemodynamic compensation following myocardial infarction. J Mol Cell Cardiol 163:156–166. https://doi.org/10.1016/j.yjmcc.2021.10.008

67. Burkhoff D, Sugiura S, Yue DT, Sagawa K (1987) Contractility-dependent curvilinearity of end-systolic pressure-volume relations. Am J Physiol-Heart Circ Physiol 252:H1218–H1227. https://doi.org/10.1152/ajpheart.1987.252.6.H1218

68. Diamond G, Forrester JS, Hargis J, et al (1971) Dlastolic Pressure-Volume Relationship in the Canine Left Ventricle. Circ Res 29:267–275. https://doi.org/10.1161/01.RES.29.3.267

69. Glantz SA, Kernoff RS (1975) Muscle stiffness determined from canine left ventricular pressure-volume curves. Circ Res 37:787–794. https://doi.org/10.1161/01.RES.37.6.787

70. Janz RF, Grimm AF (1973) Deformation of the Diastolic Left Ventricle. Biophys J 13:689–704. https://doi.org/10.1016/S0006-3495(73)86015-1

71. Spotnitz HM, Sonnenblick EH, Spiro D (1966) Relation of Ultrastructure to Function in the Intact Heart: Sarcomere Structure Relative to Pressure Volume Curves of Intact Left Ventricles of Dog and Cat. Circ Res 18:49–66. https://doi.org/10.1161/01.RES.18.1.49

72. Taylor R, Covell J, Sonnenblick E, Ross J (1967) Dependence of ventricular distensibility on filling of the opposite ventricle. Am J Physiol-Leg Content 213:711–718. https://doi.org/10.1152/ajplegacy.1967.213.3.711

73. Laks MM, Garner D, Swan HJC (1967) Volumes and Compliances Measured Simultaneously in the Right and Left Ventricles of the Dog. Circ Res 20:565–569. https://doi.org/10.1161/01.RES.20.5.565

74. Forrester JS, Diamond G, Parmley WW, Swan HJC (1972) Early Increase in Left Ventricular Compliance after Myocardial Infarction. J Clin Invest 51:598–603. https://doi.org/10.1172/JCI106849

75. Mynard JP, Davidson MR, Penny DJ, Smolich JJ (2012) A simple, versatile valve model for use in lumped parameter and one-dimensional cardiovascular models. Int J Numer Methods Biomed Eng 28:626–641. https://doi.org/10.1002/cnm.1466

76. Kass DA, Beyar R, Lankford E, et al (1989) Influence of contractile state on curvilinearity of in situ end-systolic pressure-volume relations. Circulation 79:167–178. https://doi.org/10.1161/01.CIR.79.1.167

77. Lankhaar J-W, Rövekamp FA, Steendijk P, et al (2009) Modeling the Instantaneous Pressure–Volume Relation of the Left Ventricle: A Comparison of Six Models. Ann Biomed Eng 37:1710–1726. https://doi.org/10.1007/s10439-009-9742-x

78. Suga H, Kitabatake A, Sagawa K (1979) End-systolic pressure determines stroke volume from fixed end-diastolic volume in the isolated canine left ventricle under a

constant contractile state. Circ Res 44:238–249. https://doi.org/10.1161/01.RES.44.2.238

79. Ishide N, Shimizu Y, Maruyama Y, et al (1980) Effects of changes in the aortic input impedance on systolic pressure-ejected volume relationships in the isolated supported canine left ventricle. Cardiovasc Res 14:229–243. https://doi.org/10.1093/cvr/14.4.229

80. Grood ES, Mates RE, Falsetti H (1974) A Model of Cardiac Muscle Dynamics. Circ Res 35:184–196. https://doi.org/10.1161/01.RES.35.2.184

81. Žáček M, Krause E (1996) Numerical simulation of the blood flow in the human cardiovascular system. J Biomech 29:13–20. https://doi.org/10.1016/0021-9290(95)00027-5

82. Werner J, Bohringer D, Hexamer M (2002) Simulation and prediction of cardiotherapeutical phenomena from a pulsatile model coupled to the Guyton circulatory model. IEEE Trans Biomed Eng 49:430–439. https://doi.org/10.1109/10.995681

83. Díaz-Zuccarini V, LeFèvre J (2007) An energetically coherent lumped parameter model of the left ventricle specially developed for educational purposes. Comput Biol Med 37:774–784. https://doi.org/10.1016/j.compbiomed.2006.07.002

84. Le Rolle V, Carrault G, Richard P-Y, et al (2009) A Tissue-Level Electromechanical Model of the Left Ventricle: Application to the Analysis of Intraventricular Pressure. Acta Biotheor 57:457–478. https://doi.org/10.1007/s10441-009-9092-y

85. Bhattacharya-Ghosh B, Schievano S, Díaz-Zuccarini V (2012) A multi-physics and multi-scale lumped parameter model of cardiac contraction of the left ventricle: A conceptual model from the protein to the organ scale. Comput Biol Med 42:982–992. https://doi.org/10.1016/j.compbiomed.2012.07.010

86. Arts T, Bovendeerd PH, Prinzen FW, Reneman RS (1991) Relation between left ventricular cavity pressure and volume and systolic fiber stress and strain in the wall. Biophys J 59:93–102. https://doi.org/10.1016/S0006-3495(91)82201-9

87. Arts T, Delhaas T, Bovendeerd P, et al (2005) Adaptation to mechanical load determines shape and properties of heart and circulation: the CircAdapt model. Am J Physiol-Heart Circ Physiol 288:H1943–H1954. https://doi.org/10.1152/ajpheart.00444.2004

88. Bovendeerd PHM, Borsje P, Arts T, Van De Vosse FN (2006) Dependence of Intramyocardial Pressure and Coronary Flow on Ventricular Loading and Contractility: A Model Study. Ann Biomed Eng 34:1833–1845. https://doi.org/10.1007/s10439-006-9189-2

89. Lumens J, Delhaas T, Kirn B, Arts T (2009) Three-Wall Segment (TriSeg) Model Describing Mechanics and Hemodynamics of Ventricular Interaction. Ann Biomed Eng 37:2234–2255. https://doi.org/10.1007/s10439-009-9774-2

90. Jett S, Laurence D, Kunkel R, et al (2018) An investigation of the anisotropic mechanical properties and anatomical structure of porcine atrioventricular heart valves. J Mech Behav Biomed Mater 87:155–171. https://doi.org/10.1016/j.jmbbm.2018.07.024

91. Billiar KL, Sacks MS (2000) Biaxial Mechanical Properties of the Natural and Glutaraldehyde Treated Aortic Valve Cusp—Part I: Experimental Results. J Biomech Eng 122:23–30. https://doi.org/10.1115/1.429624

92. Eckert CE, Zubiate B, Vergnat M, et al (2009) In Vivo Dynamic Deformation of the Mitral Valve Annulus. Ann Biomed Eng 37:1757–1771. https://doi.org/10.1007/s10439-009-9749-3

93. Sacks MS, David Merryman W, Schmidt DE (2009) On the biomechanics of heart valve function. J Biomech 42:1804–1824. https://doi.org/10.1016/j.jbiomech.2009.05.015

94. Borazjani I, Ge L, Sotiropoulos F (2008) Curvilinear immersed boundary method for simulating fluid structure interaction with complex 3D rigid bodies. J Comput Phys 227:7587–7620. https://doi.org/10.1016/j.jcp.2008.04.028

95. Töger J, Kanski M, Carlsson M, et al (2012) Vortex Ring Formation in the Left Ventricle of the Heart: Analysis by 4D Flow MRI and Lagrangian Coherent Structures. Ann Biomed Eng 40:2652–2662. https://doi.org/10.1007/s10439-012-0615-3

96. Korakianitis T, Shi Y (2006) Numerical simulation of cardiovascular dynamics with healthy and diseased heart valves. J Biomech 39:1964–1982. https://doi.org/10.1016/j.jbiomech.2005.06.016

97. Szabó G, Soans D, Graf A, et al (2004) A new computer model of mitral valve hemodynamics during ventricular filling☆. Eur J Cardiothorac Surg 26:239–247. https://doi.org/10.1016/j.ejcts.2004.03.018

98. Garcia D, Pibarot P, Durand L-G (2005) Analytical modeling of the instantaneous pressure gradient across the aortic valve. J Biomech 38:1303–1311. https://doi.org/10.1016/j.jbiomech.2004.06.018

99. Pant S, Corsini C, Baker C, et al (2016) Data assimilation and modelling of patient-specific single-ventricle physiology with and without valve regurgitation. J Biomech 49:2162–2173. https://doi.org/10.1016/j.jbiomech.2015.11.030

100. Dubini G, De Leval MR, Pietrabissa R, et al (1996) A numerical fluid mechanical study of repaired congenital heart defects. Application to the total cavopulmonary connection. J Biomech 29:111–121. https://doi.org/10.1016/0021-9290(95)00021-6

101. De Leval MR, Dubini G, Migliavacca C§ F, et al (1996) Use of computational fluid dynamics in the design of surgical procedures: Application to the study of competitive flows in cavopulmonary connections. J Thorac Cardiovasc Surg 111:502–513. https://doi.org/10.1016/S0022-5223(96)70302-1

102. Norwood WI, Kirklin JK, Sanders SP (1980) Hypoplastic left heart syndrome: Experience with palliative surgery. Am J Cardiol 45:87–91. https://doi.org/10.1016/0002-9149(80)90224-6

103. Migliavacca F, Pennati G, Dubini G, et al (2001) Modeling of the Norwood circulation: effects of shunt size, vascular resistances, and heart rate. Am J Physiol-Heart Circ Physiol 280:H2076–H2086. https://doi.org/10.1152/ajpheart.2001.280.5.H2076

104. Photiadis J, Hübler M, Sinzobahamvya N, et al (2005) Does size matter? Larger Blalock–Taussig shunt in the modified Norwood operation correlates with better hemodynamics☆. Eur J Cardiothorac Surg 28:56–60. https://doi.org/10.1016/j.ejcts.2005.03.033

105. Ishino K, Stümper O, De Giovanni JJV, et al (1999) The modified norwood procedure for hypoplastic left heart syndrome: Early to intermediate results of 120 patients with particular reference to aortic arch repair. J Thorac Cardiovasc Surg 117:920–930. https://doi.org/10.1016/S0022-5223(99)70373-9

106. Yuan V, De Gaetano F, Osouli K, et al (2023) Investigating the hemodynamics of Berlin Heart EXCOR support in Norwood patients across diverse clinical scenarios with computational modeling. Artif Organs 47:1133–1150. https://doi.org/10.1111/aor.14544

107. Laganà K, Balossino R, Migliavacca F, et al (2005) Multiscale modeling of the cardiovascular system: application to the study of pulmonary and coronary perfusions in the univentricular circulation. J Biomech 38:1129–1141. https://doi.org/10.1016/j.jbiomech.2004.05.027

108. Bove EL, Migliavacca F, De Leval MR, et al (2008) Use of mathematic modeling to compare and predict hemodynamic effects of the modified Blalock–Taussig and right ventricle–pulmonary artery shunts for hypoplastic left heart syndrome. J Thorac Cardiovasc Surg 136:312-320.e2. https://doi.org/10.1016/j.jtcvs.2007.04.078

109. Hsia T-Y, Migliavacca F, Pennati G, et al (2009) Management of a Stenotic Right Ventricle-Pulmonary Artery Shunt Early After the Norwood Procedure. Ann Thorac Surg 88:830–838. https://doi.org/10.1016/j.athoracsur.2009.05.051

110. Corsini C, Cosentino D, Pennati G, et al (2011) Multiscale models of the hybrid palliation for hypoplastic left heart syndrome. J Biomech 44:767–770. https://doi.org/10.1016/j.jbiomech.2010.11.001

111. Esmaily Moghadam M, Migliavacca F, Vignon-Clementel IE, et al (2012) Optimization of Shunt Placement for the Norwood Surgery Using Multi-Domain Modeling. J Biomech Eng 134:051002. https://doi.org/10.1115/1.4006814

112. Baker CE, Corsini C, Cosentino D, et al (2013) Effects of pulmonary artery banding and retrograde aortic arch obstruction on the hybrid palliation of hypoplastic left heart syndrome. J Thorac Cardiovasc Surg 146:1341–1348. https://doi.org/10.1016/j.jtcvs.2013.01.038

113. Peer SM, Yildirim C, Desai M, et al (2022) Mechanical support of pulmonary blood flow as a strategy to support the Norwood circulation-lumped parameter model study. Eur J Cardiothorac Surg 62:ezac262. https://doi.org/10.1093/ejcts/ezac262

114. Sano S, Ishino K, Kawada M, et al (2003) Right ventricle–pulmonary artery shunt in first-stage palliation of hypoplastic left heart syndrome. J Thorac Cardiovasc Surg 126:504–509. https://doi.org/10.1016/S0022-5223(02)73575-7

115. Ohye RG, Sleeper LA, Mahony L, et al (2010) Comparison of Shunt Types in the Norwood Procedure for Single-Ventricle Lesions. N Engl J Med 362:1980–1992. https://doi.org/10.1056/NEJMoa0912461

116. Wong J, Lamata P, Rathod RH, et al (2017) Right ventricular morphology and function following stage I palliation with a modified Blalock–Taussig shunt versus a right ventricle-to-pulmonary artery conduit. Eur J Cardiothorac Surg 51:50–57. https://doi.org/10.1093/ejcts/ezw227

117. Shimizu S, Une D, Shishido T, et al (2011) Norwood procedure with non-valved right ventricle to pulmonary artery shunt improves ventricular energetics despite the presence of diastolic regurgitation: a theoretical analysis. J Physiol Sci 61:457–465. https://doi.org/10.1007/s12576-011-0166-7

118. Karamlou T, Overman D, Hill KD, et al (2015) Stage 1 hybrid palliation for hypoplastic left heart syndrome—assessment of contemporary patterns of use: An analysis of The Society of Thoracic Surgeons Congenital Heart Surgery Database. J Thorac Cardiovasc Surg 149:195-202.e1. https://doi.org/10.1016/j.jtcvs.2014.08.020

119. Honjo O, Caldarone CA (2010) Hybrid Palliation for Neonates With Hypoplastic Left Heart Syndrome: Current Strategies and Outcomes. Korean Circ J 40:103. https://doi.org/10.4070/kcj.2010.40.3.103

120. Di Molfetta A, Amodeo A, Fresiello L, et al (2015) Simulation of Ventricular, Cavo-Pulmonary, and Biventricular Ventricular Assist Devices in Failing F ontan. Artif Organs 39:550–558. https://doi.org/10.1111/aor.12434

121. Young A, Gourlay T, McKee S, Danton MHD (2013) Computational modelling to optimize the hybrid configuration for hypoplastic left heart syndrome†. Eur J Cardiothorac Surg 44:664–672. https://doi.org/10.1093/ejcts/ezt096

122. Young A, Gourlay T, McKee S, Danton MHD (2014) Computational modelling of the hybrid procedure in hypoplastic left heart syndrome: A comparison of zero-dimensional and three-dimensional approach. Med Eng Phys 36:1549–1553. https://doi.org/10.1016/j.medengphy.2014.08.015

123. Shimizu S, Kawada T, Une D, et al (2016) Hybrid stage I palliation for hypoplastic left heart syndrome has no advantage on ventricular energetics: a theoretical analysis. Heart Vessels 31:105–113. https://doi.org/10.1007/s00380-014-0604-6

124. Meza JM, Hickey EJ, Blackstone EH, et al (2017) The Optimal Timing of Stage 2 Palliation for Hypoplastic Left Heart Syndrome: An Analysis of the Pediatric Heart Network Single Ventricle Reconstruction Trial Public Data Set. Circulation 136:1737–1748. https://doi.org/10.1161/CIRCULATIONAHA.117.028481

125. Pennati G, Migliavacca F, Dubini G, et al (1997) A mathematical model of circulation in the presence of the bidirectional cavopulmonary anastomosis in children with a univentricular heart. Med Eng Phys 19:223–234. https://doi.org/10.1016/S1350-4533(96)00071-9

126. Pennati G, Migliavacca F, Dubini G, et al (2000) Use of Mathematical Model to Predict Hemodynamics in Cavopulmonary Anastomosis with Persistent Forward Flow. J Surg Res 89:43–52. https://doi.org/10.1006/jsre.1999.5799

127. Bertolizio G, DiNardo JA, Laussen PC, et al (2015) Evaluation of Cerebral Oxygenation and Perfusion With Conversion From an Arterial-to-Systemic Shunt Circulation to the Bidirectional Glenn Circulation in Patients With Univentricular Cardiac Abnormalities. J Cardiothorac Vasc Anesth 29:95–100. https://doi.org/10.1053/j.jvca.2014.06.001

128. Pant S, Corsini C, Baker C, et al (2018) A Lumped Parameter Model to Study Atrioventricular Valve Regurgitation in Stage 1 and Changes Across Stage 2 Surgery in Single Ventricle Patients. IEEE Trans Biomed Eng 65:2450–2458. https://doi.org/10.1109/TBME.2018.2797999

129. Tseng SY, Siddiqui S, Di Maria MV, et al (2020) Atrioventricular Valve Regurgitation in Single Ventricle Heart Disease: A Common Problem Associated With Progressive Deterioration and Mortality. J Am Heart Assoc 9:e015737. https://doi.org/10.1161/JAHA.119.015737

130. Liang F, Senzaki H, Yin Z, et al (2013) Transient Hemodynamic Changes upon Changing a BCPA into a TCPC in Staged Fontan Operation: A Computational Model Study. Sci World J 2013:486815. https://doi.org/10.1155/2013/486815

131. Pozzoli A, Zuber M, Reisman M, et al (2018) Comparative Anatomy of Mitral and Tricuspid Valve: What Can the Interventionlist Learn From the Surgeon. Front Cardiovasc Med 5:80. https://doi.org/10.3389/fcvm.2018.00080

132. Conover T, Hlavacek AM, Migliavacca F, et al (2018) An interactive simulation tool for patient-specific clinical decision support in single-ventricle physiology. J Thorac Cardiovasc Surg 155:712–721. https://doi.org/10.1016/j.jtcvs.2017.09.046

133. Vallecilla C, Khiabani RH, Sandoval N, et al (2014) Effect of high altitude exposure on the hemodynamics of the bidirectional Glenn physiology: Modeling incremented pulmonary vascular resistance and heart rate. J Biomech 47:1846–1852. https://doi.org/10.1016/j.jbiomech.2014.03.021

134. Vallecilla C, Khiabani RH, Trusty P, et al (2015) Exercise capacity in the Bidirectional Glenn physiology: Coupling cardiac index, ventricular function and oxygen extraction ratio. J Biomech 48:1997–2004. https://doi.org/10.1016/j.jbiomech.2015.03.034

135. Konstantinov IE, Schulz A, Buratto E (2022) Heart transplantation after Fontan operation. JTCVS Tech 13:182–191. https://doi.org/10.1016/j.xjtc.2022.01.020

136. Book WM, Gerardin J, Saraf A, et al (2016) Clinical Phenotypes of Fontan Failure: Implications for Management: Fontan Phenotypes. Congenit Heart Dis 11:296–308. https://doi.org/10.1111/chd.12368

137. Shi WY, Yong MS, McGiffin DC, et al (2016) Heart transplantation in Fontan patients across Australia and New Zealand. Heart 102:1120–1126. https://doi.org/10.1136/heartjnl-2015-308848

138. Pundi KN, Johnson JN, Dearani JA, et al (2015) 40-Year Follow-Up After the Fontan Operation. J Am Coll Cardiol 66:1700–1710. https://doi.org/10.1016/j.jacc.2015.07.065

139. Rychik J, Atz AM, Celermajer DS, et al (2019) Evaluation and Management of the Child and Adult With Fontan Circulation: A Scientific Statement From the American Heart Association. Circulation 140:. https://doi.org/10.1161/CIR.0000000000000696

140. Cavalcanti S, Gnudi G, Masetti P, et al (2001) Analysis by mathematical model of haemodynamic data in the failing Fontan circulation. Physiol Meas 22:209–222. https://doi.org/10.1088/0967-3334/22/1/324

141. Liang F, Senzaki H, Kurishima C, et al (2014) Hemodynamic performance of the Fontan circulation compared with a normal biventricular circulation: a computational model

study. Am J Physiol-Heart Circ Physiol 307:H1056–H1072. https://doi.org/10.1152/ajpheart.00245.2014

142. Liang F, Sughimoto K, Matsuo K, et al (2014) Patient-specific assessment of cardiovascular function by combination of clinical data and computational model with applications to patients undergoing Fontan operation. Int J Numer Methods Biomed Eng 30:1000–1018. https://doi.org/10.1002/cnm.2641

143. Watrous RL, Chin AJ (2017) Model-Based Comparison of the Normal and Fontan Circulatory Systems—Part III: Major Differences in Performance With Respiration and Exercise. World J Pediatr Congenit Heart Surg 8:148–160. https://doi.org/10.1177/2150135116679831

144. Doyle MG, Chugunova M, Roche SL, Keener JP (2021) Lumped parameter models for two-ventricle and healthy and failing extracardiac Fontan circulations. Math Med Biol J IMA 38:442–466. https://doi.org/10.1093/imammb/dqab012

145. Shachar GB, Fuhrman BP, Wang Y, et al (1982) Rest and exercise hemodynamics after the Fontan procedure. Circulation 65:1043–1048. https://doi.org/10.1161/01.CIR.65.6.1043

146. La Gerche A, Gewillig M (2010) What Limits Cardiac Performance during Exercise in Normal Subjects and in Healthy Fontan Patients? Int J Pediatr 2010:1–8. https://doi.org/10.1155/2010/791291

147. Magosso E, Cavalcanti S, Ursino M (2002) Theoretical analysis of rest and exercise hemodynamics in patients with total cavopulmonary connection. Am J Physiol-Heart Circ Physiol 282:H1018–H1034. https://doi.org/10.1152/ajpheart.00231.2001

148. Koeken Y, Arts T, Delhaas T (2012) Simulation of the Fontan circulation during rest and exercise. In: 2012 Annual International Conference of the IEEE Engineering in Medicine and Biology Society. IEEE, San Diego, CA, pp 6673–6676

149. Kung E, Pennati G, Migliavacca F, et al (2014) A Simulation Protocol for Exercise Physiology in Fontan Patients Using a Closed Loop Lumped-Parameter Model. J Biomech Eng 136:081007. https://doi.org/10.1115/1.4027271

150. Cedars A, Kutty S, Danford D, et al (2021) Systemic ventricular assist device support in Fontan patients: A report by ACTION. J Heart Lung Transplant 40:368–376. https://doi.org/10.1016/j.healun.2021.01.011

151. VanderPluym CJ, Rebeyka IM, Ross DB, Buchholz H (2011) The use of ventricular assist devices in pediatric patients with univentricular hearts. J Thorac Cardiovasc Surg 141:588–590. https://doi.org/10.1016/j.jtcvs.2010.06.038

152. Mackling T, Shah T, Dimas V, et al (2012) Management of Single-Ventricle Patients With Berlin Heart EXCOR Ventricular Assist Device: Single-Center Experience. Artif Organs 36:555–559. https://doi.org/10.1111/j.1525-1594.2011.01403.x

153. Chen S, Rosenthal DN, Murray J, et al (2020) Bridge to Transplant with Ventricular Assist Device Support in Pediatric Patients with Single Ventricle Heart Disease. ASAIO J 66:205–211. https://doi.org/10.1097/MAT.0000000000000983

154. Di Molfetta A, Ferrari G, Iacobelli R, et al (2017) Concurrent use of continuous and pulsatile flow Ventricular Assist Device on a fontan patient: A simulation study: CONTINUOUS VS. PULSATILE VAD IN FONTAN. Artif Organs 41:32–39. https://doi.org/10.1111/aor.12859

155. Durham LA, Dearani JA, Burkhart HM, et al (2011) Application of Computer Modeling in Systemic VAD Support of Failing Fontan Physiology. World J Pediatr Congenit Heart Surg 2:243–248. https://doi.org/10.1177/2150135110397386

156. Haggerty CM, Fynn-Thompson F, McElhinney DB, et al (2012) Experimental and numeric investigation of Impella pumps as cavopulmonary assistance for a failing Fontan. J Thorac Cardiovasc Surg 144:563–569. https://doi.org/10.1016/j.jtcvs.2011.12.063

157. Di Molfetta A, Amodeo A, Fresiello L, et al (2016) The use of a numerical model to simulate the cavo-pulmonary assistance in Fontan circulation: a preliminary verification. J Artif Organs 19:105–113. https://doi.org/10.1007/s10047-015-0874-5

158. Shimizu S, Kawada T, Une D, et al (2016) Partial cavopulmonary assist from the inferior vena cava to the pulmonary artery improves hemodynamics in failing Fontan circulation: a theoretical analysis. J Physiol Sci 66:249–255. https://doi.org/10.1007/s12576-015-0422-3

159. Egbe AC, Connolly HM, Miranda WR, et al (2017) Hemodynamics of Fontan Failure: The Role of Pulmonary Vascular Disease. Circ Heart Fail 10:e004515. https://doi.org/10.1161/CIRCHEARTFAILURE.117.004515

160. Meoli A, Cutrì E, Krishnamurthy A, et al (2015) A multiscale model for the study of cardiac biomechanics in single-ventricle surgeries: a clinical case. Interface Focus 5:20140079. https://doi.org/10.1098/rsfs.2014.0079

161. Qian Y, Liu JL, Itatani K, et al (2010) Computational Hemodynamic Analysis in Congenital Heart Disease: Simulation of the Norwood Procedure. Ann Biomed Eng 38:2302–2313. https://doi.org/10.1007/s10439-010-9978-5

162. Pekkan K, Kitajima HD, De Zelicourt D, et al (2005) Total Cavopulmonary Connection Flow With Functional Left Pulmonary Artery Stenosis: Angioplasty and Fenestration In

Vitro. Circulation 112:3264–3271.
https://doi.org/10.1161/CIRCULATIONAHA.104.530931

163. Migliavacca F, Laganà K, Pennati G, et al (2004) global mathematical modelling of the norwood circulation: a multiscale approach for the study of the pulmonary and coronary arterial perfusions. Cardiol Young 14:71–76.
https://doi.org/10.1017/S1047951104006614

164. Arthurs CJ, Agarwal P, John AV, et al (2017) Reproducing Patient-Specific Hemodynamics in the Blalock–Taussig Circulation Using a Flexible Multi-Domain Simulation Framework: Applications for Optimal Shunt Design. Front Pediatr 5:78.
https://doi.org/10.3389/fped.2017.00078

165. Gladman G, McCrindle BW, Williams WG, et al (1997) The modified blalock-taussig shunt: Clinical impact and morbidity in fallot's tetralogy in the current era. J Thorac Cardiovasc Surg 114:25–30. https://doi.org/10.1016/S0022-5223(97)70113-2

166. Jubair KAA, Fagih MRA, Jarallah ASA, et al (1998) Results of 546 Blalock-Taussig shunts performed in 478 patients. Cardiol Young 8:486–490.
https://doi.org/10.1017/S1047951100007150

167. Moszura T, Zubrzycka M, Michalak KW, et al (2010) Acute and late obstruction of a modified Blalock–Taussig shunt: a two-center experience in different catheter-based methods of treatment. Interact Cardiovasc Thorac Surg 10:727–731.
https://doi.org/10.1510/icvts.2009.219741

168. Egan MJ, Hill SL, Boettner BL, et al (2011) Predictors of Retrograde Aortic Arch Obstruction After Hybrid Palliation of Hypoplastic Left Heart Syndrome. Pediatr Cardiol 32:67–75. https://doi.org/10.1007/s00246-010-9820-8

169. Stoica SC, Philips AB, Egan M, et al (2009) The Retrograde Aortic Arch in the Hybrid Approach to Hypoplastic Left Heart Syndrome. Ann Thorac Surg 88:1939–1947.
https://doi.org/10.1016/j.athoracsur.2009.06.115

170. Ceballos A, Argueta-Morales IR, Divo E, et al (2012) Computational Analysis of Hybrid Norwood Circulation With Distal Aortic Arch Obstruction and Reverse Blalock-Taussig Shunt. Ann Thorac Surg 94:1540–1550.
https://doi.org/10.1016/j.athoracsur.2012.06.043

171. Ceballos A, Prather R, Divo E, et al (2019) Patient-Specific Multi-Scale Model Analysis of Hemodynamics Following the Hybrid Norwood Procedure for Hypoplastic Left Heart Syndrome: Effects of Reverse Blalock–Taussig Shunt Diameter. Cardiovasc Eng Technol 10:136–154. https://doi.org/10.1007/s13239-018-00396-w

172. Prather R, Seligson J, Ni M, et al (2018) Patient-specific multiscale computational fluid dynamics assessment of embolization rates in the hybrid Norwood: effects of size and

placement of the reverse Blalock–Taussig shunt. Can J Physiol Pharmacol 96:690–700. https://doi.org/10.1139/cjpp-2018-0002

173. Hsia T-Y, Cosentino D, Corsini C, et al (2011) Use of Mathematical Modeling to Compare and Predict Hemodynamic Effects Between Hybrid and Surgical Norwood Palliations for Hypoplastic Left Heart Syndrome. Circulation 124:. https://doi.org/10.1161/CIRCULATIONAHA.110.010769

174. Verma A, Esmaily M, Shang J, et al (2018) Optimization of the Assisted Bidirectional Glenn Procedure for First Stage Single Ventricle Repair. World J Pediatr Congenit Heart Surg 9:157–170. https://doi.org/10.1177/2150135117745026

175. Shang JK, Esmaily M, Verma A, et al (2019) Patient-Specific Multiscale Modeling of the Assisted Bidirectional Glenn. Ann Thorac Surg 107:1232–1239. https://doi.org/10.1016/j.athoracsur.2018.10.024

176. Jia D, Peroni M, Khalapyan T, Esmaily M (2021) An Efficient Assisted Bidirectional Glenn Design With Lowered Superior Vena Cava Pressure for Stage-One Single Ventricle Patients. J Biomech Eng 143:071008. https://doi.org/10.1115/1.4050170

177. Edelson JB, Ravishankar C, Griffis H, et al (2020) A Comparison of Bidirectional Glenn vs. Hemi-Fontan Procedure: An Analysis of the Single Ventricle Reconstruction Trial Public Use Dataset. Pediatr Cardiol 41:1166–1172. https://doi.org/10.1007/s00246-020-02371-6

178. Corsini C, Baker C, Kung E, et al (2014) An integrated approach to patient-specific predictive modeling for single ventricle heart palliation. Comput Methods Biomech Biomed Engin 17:1572–1589. https://doi.org/10.1080/10255842.2012.758254

179. Kung E, Corsini C, Marsden A, et al (2020) Multiscale Modeling of Superior Cavopulmonary Circulation: Hemi-Fontan and Bidirectional Glenn Are Equivalent. Semin Thorac Cardiovasc Surg 32:883–892. https://doi.org/10.1053/j.semtcvs.2019.09.007

180. Kung E, Baretta A, Baker C, et al (2013) Predictive modeling of the virtual Hemi-Fontan operation for second stage single ventricle palliation: Two patient-specific cases. J Biomech 46:423–429. https://doi.org/10.1016/j.jbiomech.2012.10.023

181. Januszewska K, Kolcz J, Mroczek T, et al (2005) Right ventricle-to-pulmonary artery shunt and modified Blalock–Taussig shunt in preparation to hemi-Fontan procedure in children with hypoplastic left heart syndrome. Eur J Cardiothorac Surg 27:956–961. https://doi.org/10.1016/j.ejcts.2005.03.003

182. Caspi J, Pettitt TW, Mulder T, Stopa A (2008) Development of the Pulmonary Arteries After the Norwood Procedure: Comparison Between Blalock-Taussig Shunt and Right

Ventricular–Pulmonary Artery Conduit. Ann Thorac Surg 86:1299–1304. https://doi.org/10.1016/j.athoracsur.2008.06.016

183. Ma L, Liu Y, Zhao X, et al (2014) Hemodynamic Influence of Different Pulmonary Stenosis Degree in Glenn Procedure: A Numerical Study. Adv Mech Eng 6:472370. https://doi.org/10.1155/2014/472370

184. Schiavazzi DE, Kung EO, Marsden AL, et al (2015) Hemodynamic effects of left pulmonary artery stenosis after superior cavopulmonary connection: A patient-specific multiscale modeling study. J Thorac Cardiovasc Surg 149:689-696.e3. https://doi.org/10.1016/j.jtcvs.2014.12.040

185. The Modeling of Congenital Hearts Alliance (MOCHA) Investigators, Corsini C, Baker C, et al (2015) Integration of Clinical Data Collected at Different Times for Virtual Surgery in Single Ventricle Patients: A Case Study. Ann Biomed Eng 43:1310–1320. https://doi.org/10.1007/s10439-014-1113-6

186. Das A, Hameed M, Prather R, et al (2023) In-Silico and In-Vitro Analysis of the Novel Hybrid Comprehensive Stage II Operation for Single Ventricle Circulation. Bioengineering 10:135. https://doi.org/10.3390/bioengineering10020135

187. Cutrì E, Meoli A, Dubini G, et al (2017) Patient-specific biomechanical model of hypoplastic left heart to predict post-operative cardio-circulatory behaviour. Med Eng Phys 47:85–92. https://doi.org/10.1016/j.medengphy.2017.06.024

188. Holzapfel GA, Ogden RW (2009) Constitutive modelling of passive myocardium: a structurally based framework for material characterization. Philos Trans R Soc Math Phys Eng Sci 367:3445–3475. https://doi.org/10.1098/rsta.2009.0091

189. Tang E, Restrepo M, Haggerty CM, et al (2014) Geometric Characterization of Patient-Specific Total Cavopulmonary Connections and its Relationship to Hemodynamics. JACC Cardiovasc Imaging 7:215–224. https://doi.org/10.1016/j.jcmg.2013.12.010

190. Sundareswaran KS, Pekkan K, Dasi LP, et al (2008) The total cavopulmonary connection resistance: a significant impact on single ventricle hemodynamics at rest and exercise. Am J Physiol-Heart Circ Physiol 295:H2427–H2435. https://doi.org/10.1152/ajpheart.00628.2008

191. Senzaki H, Masutani S, Ishido H, et al (2006) Cardiac Rest and Reserve Function in Patients With Fontan Circulation. J Am Coll Cardiol 47:2528–2535. https://doi.org/10.1016/j.jacc.2006.03.022

192. Marsden AL, Reddy VM, Shadden SC, et al (2010) A New Multiparameter Approach to Computational Simulation for Fontan Assessment and Redesign. Congenit Heart Dis 5:104–117. https://doi.org/10.1111/j.1747-0803.2010.00383.x

193. Baretta A, Corsini C, Marsden AL, et al (2012) Respiratory effects on hemodynamics in patient-specific CFD models of the Fontan circulation under exercise conditions. Eur J Mech - BFluids 35:61–69. https://doi.org/10.1016/j.euromechflu.2012.01.012

194. Trusty PM, Wei Z, Sales M, et al (2020) Y-graft modification to the Fontan procedure: Increasingly balanced flow over time. J Thorac Cardiovasc Surg 159:652–661. https://doi.org/10.1016/j.jtcvs.2019.06.063

195. Throckmorton AL, Carr JP, Tahir SA, et al (2011) Mechanical Cavopulmonary Assistance of a Patient-Specific Fontan Physiology: Numerical Simulations, Lumped Parameter Modeling, and Suction Experiments: PATIENT-SPECIFIC MODELING OF CAVOPULMONARY ASSIST. Artif Organs 35:1036–1047. https://doi.org/10.1111/j.1525-1594.2011.01339.x

196. Albal PG, Menon PG, Kowalski W, et al (2013) Novel Fenestration Designs for Controlled Venous Flow Shunting in Failing F ontans With Systemic Venous Hypertension. Artif Organs 37:66–75. https://doi.org/10.1111/aor.12011

197. Daley M, Buratto E, King G, et al (2022) Impact of Fontan Fenestration on Long-Term Outcomes: A Propensity Score–Matched Analysis. J Am Heart Assoc 11:e026087. https://doi.org/10.1161/JAHA.122.026087

198. Ni MW, Prather RO, Rodriguez G, et al (2018) Computational Investigation of a Self-Powered Fontan Circulation. Cardiovasc Eng Technol 9:202–216. https://doi.org/10.1007/s13239-018-0342-5

199. Prather R, Das A, Farias M, et al (2022) Parametric investigation of an injection-jet self-powered Fontan circulation. Sci Rep 12:2161. https://doi.org/10.1038/s41598-022-05985-3

200. Ahmed Y, Tossas-Betancourt C, Van Bakel PAJ, et al (2021) Interventional Planning for Endovascular Revision of a Lateral Tunnel Fontan: A Patient-Specific Computational Analysis. Front Physiol 12:718254. https://doi.org/10.3389/fphys.2021.718254

201. Chin AJ, Watrous RL (2015) Model-Based Comparison of the Normal and Fontan Circulatory Systems—Part II: Major Differences in Performance Characteristics. World J Pediatr Congenit Heart Surg 6:360–373. https://doi.org/10.1177/2150135115581386

202. Guadagni G, Bove EL, Migliavacca F, Dubini G (2001) Effects of pulmonary afterload on the hemodynamics after the hemi-Fontan procedure. Med Eng Phys 23:293–298. https://doi.org/10.1016/S1350-4533(01)00035-2

203. Michielon G, DiSalvo G, Fraisse A, et al (2020) In-hospital interstage improves interstage survival after the Norwood stage 1 operation. Eur J Cardiothorac Surg 57:1113–1121. https://doi.org/10.1093/ejcts/ezaa074

204. Kaplinski M, Ittenbach RF, Hunt ML, et al (2020) Decreasing Interstage Mortality After the Norwood Procedure: A 30-Year Experience. J Am Heart Assoc 9:e016889. https://doi.org/10.1161/JAHA.120.016889

205. Backes ER, Afonso NS, Guffey D, et al (2023) Cumulative comorbid conditions influence mortality risk after staged palliation for hypoplastic left heart syndrome and variants. J Thorac Cardiovasc Surg 165:287-298.e4. https://doi.org/10.1016/j.jtcvs.2022.01.056

206. Stromberg D, Carvalho K, Marsden A, et al (2022) Standard CPR versus interposed abdominal compression CPR in shunted single ventricle patients: comparison using a lumped parameter mathematical model. Cardiol Young 32:1122–1128. https://doi.org/10.1017/S1047951121003917

207. Thompson EJ, Foote HP, King CE, et al (2021) A systematic review of the evidence supporting post-operative medication use in congenital heart disease. Cardiol Young 31:707–733. https://doi.org/10.1017/S1047951121001463

208. Paukner D, Humphrey JD, Cyron CJ (2024) Multiscale homogenized constrained mixture model of the bio-chemo-mechanics of soft tissue growth and remodeling. Biomech Model Mechanobiol 23:2115–2136. https://doi.org/10.1007/s10237-024-01884-w

209. Montanaro C, Boyle S, Wander G, et al (2024) Pregnancy in patients with the Fontan operation. Eur J Prev Cardiol 31:1336–1344. https://doi.org/10.1093/eurjpc/zwae157

210. Schidlow DN, Freud L, Friedman K, Tworetzky W (2017) Fetal interventions for structural heart disease. Echocardiography 34:1834–1841. https://doi.org/10.1111/echo.13667

211. Freud LR, McElhinney DB, Marshall AC, et al (2014) Fetal Aortic Valvuloplasty for Evolving Hypoplastic Left Heart Syndrome: Postnatal Outcomes of the First 100 Patients. Circulation 130:638–645. https://doi.org/10.1161/CIRCULATIONAHA.114.009032

212. Friedman KG, Freud L, Escobar-Diaz M, et al (2015) Left Ventricular Remodeling and Function in Children with Biventricular Circulation After Fetal Aortic Valvuloplasty. Pediatr Cardiol 36:1502–1509. https://doi.org/10.1007/s00246-015-1193-6

213. Wong HS, Wiputra H, Tulzer A, et al (2022) Fluid Mechanics of Fetal Left Ventricle During Aortic Stenosis with Evolving Hypoplastic Left Heart Syndrome. Ann Biomed Eng 50:1158–1172. https://doi.org/10.1007/s10439-022-02990-5

214. Pennati G, Bellotti M, Fumero R (1997) Mathematical modelling of the human foetal cardiovascular system based on Doppler ultrasound data. Med Eng Phys 19:327–335. https://doi.org/10.1016/S1350-4533(97)84634-6

215. Green L, Chan WX, Prakash I, et al (2024) Pre-intervention myocardial stress is a good predictor of aortic valvuloplasty outcome for fetal critical aortic stenosis and evolving HLHS. J Physiol 602:663–681. https://doi.org/10.1113/JP285475

216. Lakshminrusimha S (2012) The Pulmonary Circulation in Neonatal Respiratory Failure. Clin Perinatol 39:655–683. https://doi.org/10.1016/j.clp.2012.06.006

217. Lyrene RK, Philips JB (1984) Control of Pulmonary Vascular Resistance in the Fetus and Newborn. Clin Perinatol 11:551–564. https://doi.org/10.1016/S0095-5108(18)30901-1

218. Zhang X, Haneishi H, Liu H (2019) Multiscale modeling of the cardiovascular system for infants, children, and adolescents: Age-related alterations in cardiovascular parameters and hemodynamics. Comput Biol Med 108:200–212. https://doi.org/10.1016/j.compbiomed.2019.03.021

219. Watrous RL, Chin AJ (2014) Model-Based Comparison of the Normal and Fontan Circulatory Systems: Part I: Development of a General Purpose, Interactive Cardiovascular Model. World J Pediatr Congenit Heart Surg 5:372–384. https://doi.org/10.1177/2150135114529450

220. Stodden V, Seiler J, Ma Z (2018) An empirical analysis of journal policy effectiveness for computational reproducibility. Proc Natl Acad Sci 115:2584–2589. https://doi.org/10.1073/pnas.1708290115

221. Culina A, Van Den Berg I, Evans S, Sánchez-Tójar A (2020) Low availability of code in ecology: A call for urgent action. PLOS Biol 18:e3000763. https://doi.org/10.1371/journal.pbio.3000763

222. Gezelter JD (2015) Open Source and Open Data Should Be Standard Practices. J Phys Chem Lett 6:1168–1169. https://doi.org/10.1021/acs.jpclett.5b00285

223. Langenkamp M, Yue DN (2022) How Open Source Machine Learning Software Shapes AI. In: Proceedings of the 2022 AAAI/ACM Conference on AI, Ethics, and Society. ACM, Oxford United Kingdom, pp 385–395

224. Updegrove A, Wilson NM, Merkow J, et al (2017) SimVascular: An Open Source Pipeline for Cardiovascular Simulation. Ann Biomed Eng 45:525–541. https://doi.org/10.1007/s10439-016-1762-8

225. Arthurs CJ, Khlebnikov R, Melville A, et al (2021) CRIMSON: An open-source software framework for cardiovascular integrated modelling and simulation. PLOS Comput Biol 17:e1008881. https://doi.org/10.1371/journal.pcbi.1008881

Chapter 3: Computational Model of Coarctation of the Aorta in Rabbits Suggests Persistent Ascending Aortic Remodeling Post-Correction

Abstract

Coarctation of the aorta (CoA) is a common congenital cardiovascular lesion that presents as a localized narrowing of the proximal descending aorta. While improvements in surgical and catheter-based techniques have increased short-term survival, there is a high long-term risk of hypertension and a reduced average lifespan despite correction. Computational models can be used to estimate aortic remodeling and peripheral vascular compensation, potentially serving as key tools in developing a mechanistic understanding of the interplay between pre-treatment dynamics, post-treatment recovery, and long-term hypertension risk. In this study, we developed a lumped parameter model of the heart and circulation to simulate CoA. After fitting model parameters using imaging and catheterization data from healthy rabbits, we then used the model to estimate differences in ascending aortic compliance and peripheral resistance between the healthy group and rabbits with both untreated and corrected CoA using their imaging and catheterization data. CoA was defined by the current putative clinical treatment threshold (a pressure gradient > 20 mmHg). Model inputs were fitted such that outputs matched reported stroke volume, ejection fraction, systolic and diastolic aortic pressure, peak aortic flow, mean and peak blood pressure gradients, and upper-to-lower body flow split, with all results falling within one standard deviation of the data for all groups. In the untreated CoA and corrected simulations, a decrease in ascending aortic compliance was necessary to match reported hemodynamics.

This suggests exposure to a pressure gradient > 20 mmHg results in vascular remodeling that persists after repair, a process strongly correlated with hypertension.

1. INTRODUCTION

Coarctation of the aorta (CoA) is a congenital cardiovascular lesion that typically presents as a localized narrowing of the proximal descending aorta just distal to the left subclavian artery. Each year, approximately 1 in every 1,800 infants born in the United States is diagnosed with CoA, making it one of the most common congenital heart defects [1]. While surgical or catheter-based interventions can restore flow and reduce the blood pressure gradient across the coarctation site to normal levels, successful repair of CoA does not ensure long-term cardiovascular health. Even after CoA correction, structural and functional changes in the heart and vasculature occur frequently, leading to long-term complications such as re-coarctation, aortic aneurysms, and hypertension [2–5]. In particular, despite early and effective surgical repair, the incidence of hypertension in treated CoA patients in the years following their intervention has been reported to range from 30-50% [3, 6–11]. Survival studies document a 20% increased mortality compared to age matched controls presumed secondary to the consequences of accelerated hypertension that is often resistant to standard medical therapy [6, 8, 9].

Maladaptive remodeling, a complex response to abnormal loading conditions that negatively affects a tissue's structure and function, has been implicated in much of the morbidity presenting after treatment for CoA [12–14]. In the setting of CoA, remodeling can occur in the left ventricle (in the form of hypertrophy and fibrosis), the proximal aorta

(increased intima-media thickness and stiffness), and the more distal vasculature in the upper body (impaired vasoreactivity), however the incidence and time course of this remodeling are highly variable. Prior to correction, patients with severe or long-standing CoA typically exhibit high systemic pressure and above-normal left ventricular (LV) mass. However, following successful CoA repair, the relationship between hypertension and LV hypertrophy is less clear. Though some studies report an association between late-onset hypertension and LV hypertrophy [15–17], others indicate LV hypertrophy is equally likely in normotensive and hypertensive CoA patients post-correction [10, 18, 19]. After repair, antecedent LV hypertrophy begins to regress. In many patients, however, LV hypertrophy resumes following this regression. This pattern has been reported in both the presence and absence of hypertension in adult and pediatric patients [5, 19].

In the proximal aorta, histologic analysis of tissue from untreated coarctation patients indicates increased stiffness, presenting as fibrosis, intimal thickening, and collagen degradation [20, 21]. This remodeling and its resultant decrease in proximal aortic compliance is strongly correlated with hypertension [22–24]. Unfortunately, it is challenging to assess aortic remodeling noninvasively. The two most common non-invasive metrics of aortic stiffness are pulse wave velocity and aortic distensibility. Using cardiac MRI, pulse wave velocity can be determined for a section of the aorta as the ratio of aortic length to the time delay in flow [25]. A larger pulse wave velocity indicates a faster response and greater aortic stiffness, but results are inherently impacted by the temporal resolution of phase-contrast MRI. Aortic distensibility is the ratio of the change in aortic

diameter to the change in pressure during the cardiac cycle, normalized to the minimum dimension. Therefore, aortic distensibility provides a local measure of aortic stiffness, but it requires pressure measurements. These pressures cannot be captured from the aorta noninvasively and are thus approximated from brachial cuff pressures, which can lead to an overestimation of central aortic pressure [26]. Control and normotensive corrected CoA patients have similar pulse wave velocities and distensibility in the ascending aorta, but hypertensive CoA patients exhibit significantly higher pulse wave velocity and lower distensibility [25].

Peripheral vascular compensation may also be impaired in coarctation patients, though it is challenging to assess since it inherently quantifies a change in vessel dimensions in response to a change in hemodynamic loading. One method of assessment, flow-mediated dilation, uses echocardiographic imaging of the brachial artery prior to and immediately following a stimulus, such as the inflation and deflation of a sphygmomanometer cuff placed distally on the arm or the administration of a vasodilatory agent such as nitroglycerin. In patients with CoA, flow-mediated dilation indicates a reduction in the vasodilatory response. Jesus et al. [27] reported patients with native or recurrent CoA exhibited a significant multi-fold decrease in percent change in radial arterial diameter following both occlusion and nitrate administration in comparison with healthy controls. Following CoA correction, however, there are mixed results. Using the occlusion method, Meyer et al. [28] reported a significantly lower change in the radial arterial diameter from baseline in patients with surgically corrected coarctation in

comparison with control subjects, indicating a reduction in vasodilatory capacity. Similar results were found using glyceryl trinitrate as the dilatory agent [29]. In contrast, both de Divitiis et al. [30] and Cuypers et al. [31] reported no difference in the percent change in radial arterial diameter following occlusion or nitroglycerin between patients with surgically corrected coarctation and age-matched controls. Results from Heger et al. [8] suggest that age at surgical repair is influential in long-term vasodilatory impairment. They report that a reduction in the percent change in radial arterial diameter following occlusion and administration of nitroglycerin was only significant in patients for whom coarctation repair was performed after 9 years of age. However, the International Brachial Artery Reactivity Task Force advises caution in interpreting the results of flow mediated dilation testing, since baseline diameter varies with patient size and baseline pressure, and there is evidence that smaller arteries are generally more reactive [32].

In short, no single clinical metric can evaluate the interplay between cardiovascular remodeling and function. However, computational modeling has emerged as a valuable investigative tool to study these interactions. In the context of CoA to date, modelers have used computational fluid dynamics techniques from non-invasive imaging to estimate pressure and the blood pressure gradient, wall shear stress and oscillatory shear index, and turbulent kinetic energy [33–38]. Furthermore, these approaches have been used to investigate the effects of surgical approach, stent design, and valve morphology [35, 39–42]. Modern fluid-structure interaction approaches can even account for aortic wall motion and elasticity, thereby permitting estimation of strain, wall tension, and wall stress,

all of which have been shown to serve as stimuli for remodeling [33, 43–46]. While these sophisticated finite element methods are able to capture geometric detail of the aortic arch, there has been a resurgence of interest in lumped parameter approaches [47, 48], which “lump” portions of the circulatory system into discrete compartments. Each compartment is represented as a combination of resistors, capacitors, and inductors, using electrical circuits as an analogy for blood vessels and associated physiology. Such models enable coupling of the aorta to the heart and circulation, provide realistic boundary conditions, and are much less computationally expensive. Lumped parameter models have been successfully used in isolation to model aortic coarctation, demonstrating increased simulation speed, reduced parameter requirements, and the ability to inherently estimate aortic compliance [49, 50]. Computer models could be key tools to develop a mechanistic understanding of the interplay between pre-correction and post-correction hemodynamics with long-term remodeling and the potential risk for hypertension. Thus, the objective of this investigation was to 1) develop a lumped parameter model of the heart and circulation capable of simulating aortic coarctation, and 2) utilize the model to estimate differences in ascending aortic compliance and peripheral resistance from imaging and catheterization data collected using a rabbit model of CoA and correction. Analysis of the model fitting scheme and parameter uncertainty, as well as comparison to histologic observations were then conducted to validate the model. These results indicated a novel, testable hypothesis concerning persistent maladaptive remodeling in the distal arteries of the upper body.

2. METHODS

A predictive computational model of cardiac hypertrophy and hemodynamics in canines [51] was modified to replicate the previously published cardiac hypertrophy and hemodynamic measurements from three groups of rabbits [14, 52]: a control group, an untreated coarctation group, and a corrected coarctation group. In the experimental study by Wendell et al., after approval by the Institutional Care and Use Committees of Marquette University and the Medical College of Wisconsin, a permanent (silk) or dissolvable (Vicryl) suture was tied around the descending thoracic aorta of the CoA and corrected groups of rabbits, respectively, at 10 weeks of age against a 16 gauge (1.6 mm) stainless steel wire in order to induce aortic coarctation. The surgery was considered successful if it produced a 20-mmHg blood pressure gradient, defined as the difference in pressure above and below the coarctation [53], the current putative clinical treatment threshold. Within one week of CoA induction, rabbits began to develop a pronounced vascular stenosis, accompanied by elevated blood pressure above the coarctation, and over time, substantial left ventricular hypertrophy. Rabbits in the corrected group, which underwent the creation of CoA with a degradable suture (Vicryl), also developed an initial stenosis, similar to the CoA group. In the corrected group, however, the suture dissolved after approximately 5 weeks, restoring blood pressure to normal levels for ~17 weeks before the end of the experimental duration. Control rabbits did not undergo surgery. MRI and intravascular blood pressure measurements were performed at 32 weeks for all three groups.

2.1. Control Group

The original canine computational model [51, 54] consisted of a six-compartment lumped parameter circulatory model linked to a strain-based ventricular growth function. Compartments were represented by 2-element (one resistance and one capacitance) or 3-element (a proximal resistance, a distal resistance, and a capacitance) Windkessels. For the current study, only the circulatory portion of the model was used, and additional compartments were added to explicitly represent the ascending aorta and the upper and lower systemic vasculature.

A serialized approach was used to modify the original six-compartment lumped parameter circulatory model from canines to an eight-compartment model for rabbits (see Figure 1). First, the ventricles were simulated using time-varying elastances, where ventricular end-systolic and end-diastolic pressure-volume relationships were defined by

$$P_{ES} = Ees * (V_{ES} - V_0) \quad (1)$$

$$P_{ED} = B * \exp[A * (V_{ED} - V_0)] - B \quad (2)$$

respectively, where Ees was end-systolic elastance, V_0 was the unloaded volume, and A and B were coefficients describing the exponential shape of the end-diastolic pressure-volume relationship [54–56]. The normalized time-varying elastance was computed from time-matched pressure-volume measurements in rats [57]. Unloaded volume V_0 was calculated as follows:

$$V_0 = \frac{V_{ED}}{2.54^3} \quad (3)$$

where V_{ED}, the end-diastolic volume, was determined by dividing reported stroke volume by reported ejection fraction for the control rabbits [52]. The value 2.54 was allometrically scaled from our previous studies in dogs [51, 58]. In these studies, the end-diastolic circumferential stretch relative to the unloaded state was estimated from end-diastolic pressure and segment length data recorded during inferior vena cava occlusions [59]. Then, Ees was computed by rearranging Equation 1 and inputting the measured end-systolic volume and proximal systolic blood pressure [52], which was assumed equivalent to end-systolic LV pressure. B remained at the canine value since it has a scaling factor of zero. From this, A was calculated by rearranging Equation 2:

$$A = \frac{1}{V_{ED} - V_0}\left(\ln\left(\frac{P_{ED}}{B} + 1\right)\right. \quad (4)$$

where P_{ED}, the end-diastolic pressure, was set to 7 mmHg [60]. Right ventricular parameters were kept at the same values as the left, with the exceptions of end-systolic elastance and B, which were set at 43% of the LV value [55].

Next, vascular parameters for the six-compartment circulatory model (Supplemental Figure 1) were allometrically scaled from the original canine values assuming a rabbit weight of 3.47 kg [52] and a canine weight of 23.4 kg [51, 61]. Supplemental Section 3 provides more detail on the allometric scaling process. Measured heart rate was inputted

directly into the model. Parameters associated with the three-element Windkessel simulating the systemic arterial vasculature were previously found to be highly dependent on the location of arterial blood flow and pressure measurements [51]. Therefore, the three parameters associated with the systemic arteries (*Rcs, Csa*, and *Rsa* in Supplemental Figure 1) were refit along with stressed blood volume (*SBV* in Supplemental Figure 1) to minimize the weighted mean-squared error between model outputs and stroke volume, ejection fraction, systolic and diastolic ascending aortic pressures, and peak ascending aortic flow reported by Wendell et al. using the built-in MATLAB function *fminsearch*. Each mean squared difference was weighted by the squared measurement standard deviation and parameters were all initialized at their scaled values.

Then, a compartment was added to the model to separate the ascending aorta from the systemic arteries (Supplemental Figure 2). In general, vessel beds are represented by capacitors in parallel with resistors. Therefore, the capacitances and resistances associated with the ascending aorta and distal systemic arterial compartments (*Caa* and *Raa* and *Csa* and *Rsa*, respectively, in Supplemental Figure 2) as well as *SBV* were refit using the previously fitted values from the six-compartment model as initial conditions to minimize the weighted mean-squared error between model outputs and the aforementioned hemodynamic measurements reported by Wendell et al., as well as reported mean and peak blood pressure gradients between the ascending and descending aorta. Initial values for the seven-compartment *Caa* and *Csa* were double the value of the six-compartment *Csa*, while initial values for *Raa* and *Rsa* were half the value of the six-

compartment *Rsa*. The systemic characteristic resistance (*Rcs* in Supplemental Figure 2) in the seven-compartment model was set to its fitted value from the six-compartment model.

Lastly, the systemic arterial compartment was split into two compartments to separate the upper and lower body. Two additional resistors were added: one to represent the resistance of the descending aorta, and another for the head and neck vessels (*Rda* and *Rhn*, respectively, in Figure 2 and Supplemental Figure 3), which in rabbits comprises the innominate and left subclavian arteries arising from the aortic arch. The ascending aorta (*Raa*) and descending aorta (*Rda*) resistances were made equivalent and determined based on reported control rabbit ascending aortic diameter [14]. A parallel split of the systemic arterial capacitance and resistance produces identical blood flow and pressure for the entire circulatory model when the resistance is multiplied by the same factor compliance is divided by (i.e., $Cub = Clb = 1/x*Csa$ and $Rub = Rlb = x*Rsa$). Therefore, *Rhn*, *Raa*, and *x* were fitted to minimize the weighted mean-squared error between model outputs and the aforementioned hemodynamic measurements reported by Wendell et al., as well as reported mean and peak aortic blood pressure gradients and the upper to lower body flow split (unpublished data from Menon et al. 2012a). *Rhn* and *Raa* were initialized to the previously fitted value of *Raa* and the proportionality constant, *x*, was initialized to 0.5. *SBV* and *Caa* were set to the final values from the seven-compartment model. The final input parameters for the eight-compartment model of the healthy control group of rabbits are listed in Table 1.

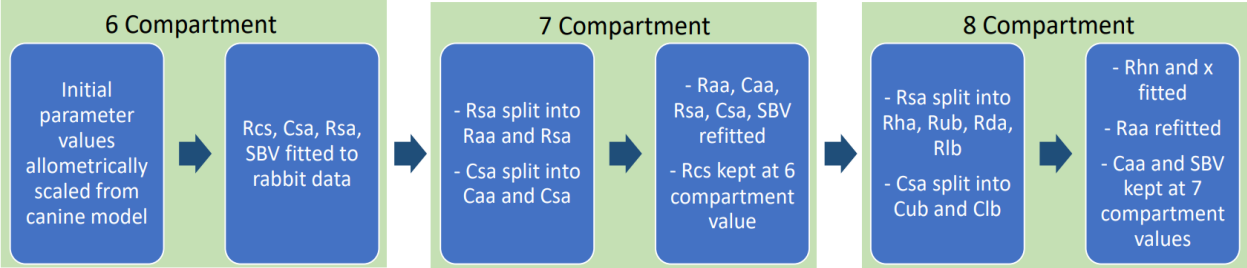

Figure 1: Schematic of the model fitting process for the control group. In the six-compartment model the systemic arteries were simulated by a three-element Windkessel consisting of a characteristic resistance (Rcs), a capacitance (Csa), and an arterial resistance (Rsa). The stressed blood volume (SBV) indicated the circulatory blood volume that contributed to stress. In the seven-compartment model the ascending aorta was simulated by a three-element Windkessel consisting of a characteristic resistance (Rcs), a capacitance (Caa), and an arterial resistance (Raa), and the systemic arteries were represented by a capacitor (Rsa) in parallel with a resistor (Csa). In the eight-compartment model the resistance of the head and neck vessels (Rhn) and descending aorta (Rda) were represented separately and the ratio between the resistances and capacitances simulating the upper and lower body systemic arteries was determined by a proportionality constant (x)

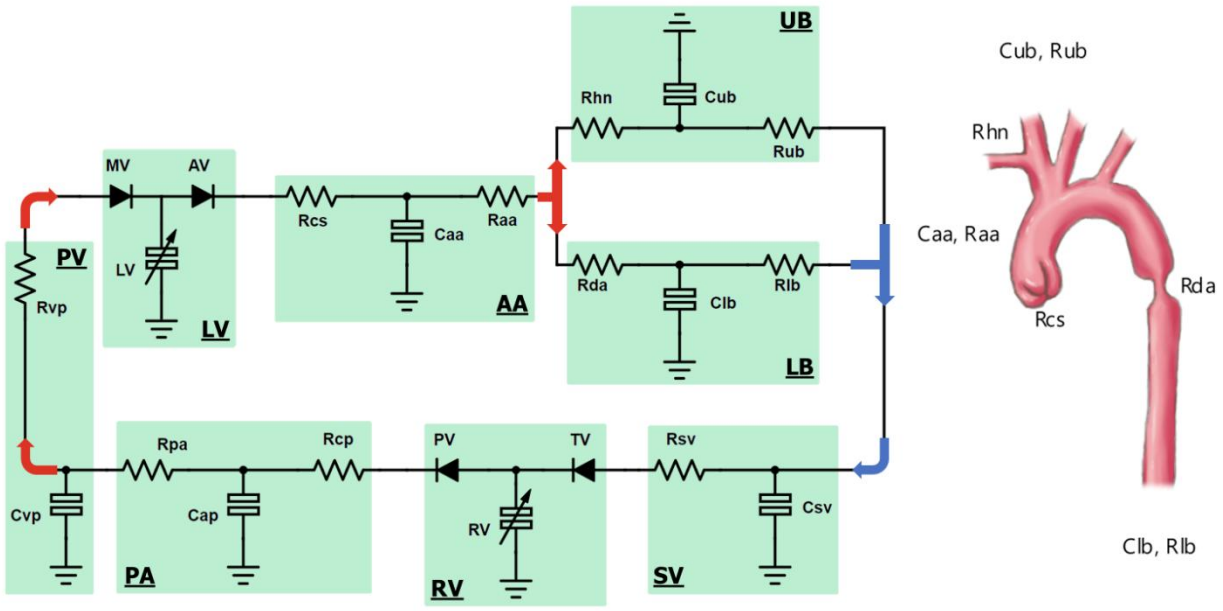

Figure 2: Left: Schematic of the circuit model used to simulate the pressure-volume relationship of the cardiovascular system in the setting of untreated and treated CoA, with the eight compartments designated by teal boxes (PV, pulmonary veins; LV, left ventricle; AA, ascending aorta; UB, upper body arteries; LB, lower body arteries; SV, systemic veins; RV, right ventricle; PA, pulmonary arteries). The left and right ventricles (LV and RV) were simulated using time-varying elastances. Ascending aorta behavior was simulated by a three-element Windkessel consisting of a characteristic resistance (Rcs), a capacitance (Caa), and an arterial resistance (Raa). The pulmonary arterial behavior was also simulated by a three-element Windkessel (Rcp, Cpa, Rpa). Other vessels were represented by capacitors in parallel with resistors for the upper body arteries (Cub and Rub), lower body arteries (Clb and Rlb), systemic veins (Csv and Rsv), and pulmonary veins (Cpv and Rpv). The head and neck vessels (Rhn) and descending aorta (Rda) were represented separately by resistances. Pressure sensitive diodes (TV, PV, MV, and AV) represented the tricuspid, pulmonary, mitral, and aortic valves, respectively. Arrows indicate the direction of blood flow and blood oxygenation levels. Right: Representative illustration of coarctation in a rabbit aorta, labeled with equivalent model compartments

Table 1: Parameter Values for Eight-Compartment Control Rabbit Model		
Heart Parameters		
Parameter	***LV***	***RV***
End-systolic Elastance (Ees), mmHg/mL	65.2[+]	27.9[+]
Unloaded Volume (V0), mL	0.188[+]	0.188[+]
Coefficient for EDPVR (B), mmHg	0.35*	0.15*
Coefficient for EDPVR (A), 1/mL	1.05[+]	1.05[+]
Unloaded thickness (h_0), cm	0.580[+]	-
Circulation Parameters		
Heart Rate (HR), beats/min	156[+]	
Stressed Blood Volume (SBV), mL	39.5[v]	
	Pulmonary	***Systemic***
Characteristic Resistance (Rcp/Rcs), mmHg·s/mL	0.251*	0.709[x]
Ascending Aortic Resistance (Raa), mmHg·s/mL	-	0.594[•]
Descending Aortic Resistance (Rda), mmHg·s/mL	-	0.594[•]
Head and Neck Arterial Resistance (Rhn), mmHg·s/mL	-	3.48[•]
Arterial Resistance (Rpa : Rub/Rlb), mmHg·s/mL	1.26*	36.7[•]
		16.0[•]
Venous Resistance (Rpv/Rsv), mmHg·s/mL	0.063*	0.063*
Ascending Aortic Capacitance (Caa), mL/mmHg	-	0.100[v]
Arterial Capacitance (Cpa : Cub/Clb), mL/mmHg	0.297*	0.0862[•]
		0.197[•]
Venous Capacitance (Cvp/Csv), mL/mmHg	0.445*	2.52*

*allometrically scaled from canine parameters *[51]*, assuming a canine weight of 23.4 kg and a rabbit weight of 3.47 kg.

[+] input directly or computed directly from reported data *[52]*

[x] fitted using six-compartment model (Supplemental Figure 1)

[v] fitted using seven-compartment model (Supplemental Figure 2)

[•] fitted using eight-compartment model (Supplemental Figure 3)

EDPVR, end-diastolic pressure-volume relationship

The circulatory and ventricular parameters were used to calculate pressures and volumes in each compartment as well as the flows between them using the differential equation-based lumped-parameter circulatory model solved with a fixed-step, fourth-order Runge-Kutta integrator. The model was run until it reached steady state, defined as compartmental volumes at the beginning and end of the cardiac cycle being within 0.05 mL of each other. Total aortic flow was determined by integrating the flow from the LV to the ascending aorta over the cardiac cycle. Hemodynamic outputs (stroke volume, ejection fraction, systolic and diastolic ascending aortic pressures, peak ascending aortic flow, mean and peak aortic blood pressure gradients, and upper to lower body flow split) were saved and compared to measurements, with success defined as model outputs falling within one standard deviation of the data.

To determine the ventricular parameters for the untreated coarctation and corrected groups, values for control LV dimensions and material properties were required. Assuming a spherical ventricle, the unloaded inner radius, r_0, was

$$r_0 = \left(V_0 \frac{3}{4\pi}\right)^{1/3}, \tag{5}$$

and unloaded thickness, h_0, was

$$h_0 = \left(V_{wall} \frac{3}{4\pi} + {r_0}^3\right)^{1/3} - r_0 \tag{6}$$

where *Vwall*, the ventricular wall volume, was assumed invariant to pressurization and set such that the model end-diastolic thickness matched the control group mean anteroseptal wall thickness reported by Wendell et al. at the reported end-diastolic volume. Hoop stress relates the control unloaded ventricular dimensions (r_0 and h_0) and pressure-volume relationship parameters (A, B, V_0, and Ees) to the intrinsic ventricular material property parameters (a, b, and e) via the following relationships [51]:

$$a = AV_0 \tag{7}$$

$$b = \frac{B}{2}\frac{r_0}{h_0} \tag{8}$$

$$e = \frac{2\pi}{3} Ees \frac{{r_0}^4}{h_0} \tag{9}$$

2.2. Coarctation Group

Aortic coarctation was simulated in four steps. First, CoA is characterized by a stenosis in the descending aorta (DA), therefore the descending aortic resistance (*Rda*) was increased. Menon et al. (2012a) indicated a diameter decrease of 72% at the coarctation site, therefore a proportional increase in *Rda* was prescribed, assuming resistance was inversely proportional to cross-sectional area [62]. Second, following prolonged CoA, ventricular hypertrophy was observed, therefore an increase in unloaded ventricular thickness was prescribed such that end-diastolic thickness matched the mean value reported by Wendell et al. Third, CoA resulted in remodeling of the proximal ascending aorta, involving a slight but significant

increase in diameter [14]. Therefore, as with *Rda*, a proportional decrease in ascending aortic resistance (*Raa*) was prescribed. The previously fitted value of ascending aortic compliance (*Caa*) was also refitted for the coarctation group. Lastly, the peripheral vasculature can constrict or dilate in response to coarctation and chronic remodeling. Therefore, the upper and lower body arterial resistances (*Rub* and *Rlb*, respectively) were also fitted. Parameter changes are listed in Table 2.

Table 2: Parameter adjustments for each group			
Parameter	**Control**	**CoA**	**Corrected**
Rda	0.594	7.63 [+]	0.594 [+]
h_0	0.580	0.841 [+]	0.748 [+]
Raa	0.594	0.418 [+]	0.509 [+]
Caa	0.100	0.056 [•]	0.039 [•]
Rub	36.7	43.8 [•]	30.8 [•]
Rlb	16.0	20.7 [•]	15.7 [•]

[+] prescribed based on reported differences in measured dimensions

[•] fitted based on reported differences in measured hemodynamics

Hypertrophy was assumed to be concentric, therefore the coarctation unloaded inner radius, c_r0, and unloaded volume, c_V0, were kept at control values. Pathology was assumed to only alter ventricular thickness, therefore ventricular material properties (a, b, and e) were also kept at control values. Thus, of the remaining coarctation ventricular parameters,

$$c\_A = \frac{3a}{4\pi}\frac{1}{{c\_r_0}^3} \tag{20}$$

$$c\_B = 2b\frac{c\_h_0}{c\_r_0} \tag{31}$$

$$c\_Ees = \frac{3e}{2\pi}\frac{c\_h_0}{{c\_r_0}^4}, \tag{42}$$

changes in unloaded thickness, c_h0, linearly affected only passive stiffness parameter c_B and elastance parameter c_Ees. As in the control group, c_h0 was set to match the reported mean end-diastolic anteroseptal wall thickness and results were compared with the reported hemodynamics of the coarctation group. *Caa*, *Rub*, and *Rlb* were optimized by minimizing the weighted mean-squared error in stroke volume, ejection fraction, systolic and diastolic ascending aortic pressures and flow, mean and peak aortic blood pressure gradients, and upper to lower body flow split.

2.3. Corrected Group

Corrected CoA was simulated much like the coarctation group. However, to model the correction of aortic coarctation, *Rda* was reset to its control value. Though less pronounced than in the CoA group, ventricular hypertrophy was observed in the corrected rabbits, therefore an increase in unloaded ventricular thickness was prescribed such that end-diastolic thickness matched the mean value reported by Wendell et al. There was also a slight increase in ascending aortic diameter observed in the corrected group, leading to the prescription of a proportional decrease in *Raa*. The ascending aortic compliance (*Caa*) and upper and lower body arterial resistances (*Rub* and *Rlb*, respectively) were again refitted for the corrected group.

3. RESULTS

3.1. Parameter Fitting

Out of 27 total input parameters, 10 were fitted to produce hemodynamic outputs matching reported measurements in the control group. Of the remaining 17 parameters, 9 were allometrically scaled from their respective canine values [51, 61] and 8 were determined or computed directly from data [52]. Unloaded LV cavity volume, $V0$, was calculated from the reported control group stroke volume and ejection fraction (Equation 3). Heart rate was inputted directly and $h0$ was set to 5.80 mm to produce the end-diastolic anteroseptal thickness of 2.44 mm reported by Wendell et al. Model outputs for the control simulation matched reported measured stroke volume, ejection fraction, systolic and diastolic ascending aortic pressures, peak ascending aortic flow, mean and peak blood

pressure gradients [52], and upper to lower body flow split (unpublished data from [14] within 0.15 standard deviations (Table 3).

As discussed previously in Section 2.2 and illustrated in Table 2, several parameters needed to be adjusted from their fitted control values to match measured hemodynamics in the untreated CoA rabbits. Changes in *Rda*, *Raa*, and *c_h0* were prescribed based on reported differences in the diameter of the coarctation site (a reduction of 72%), the diameter of the ascending aorta (an increase of 19%), and the mean end-diastolic anteroseptal wall thickness (4.42 mm), respectively. Fitted values of *Rub* and *Rlb* increased 17.6% and 25.6% from their control group values, respectively, while the fitted value of *Caa* decreased by 56.4%. Resulting model hemodynamics matched reported hemodynamics in the untreated CoA group within 0.75 standard deviations.

In the corrected group, the diameter of the coarctation was largely restored after the aortic suture dissolved. Therefore, *Rda* was reset to its control value. Changes in *Raa* and *c_h0* were prescribed based on reported differences in the diameter of the ascending aorta (an increase of 8%), and the mean end-diastolic anteroseptal wall thickness (3.70 mm), respectively. Note that although there were trends toward larger measurements in reported ascending aortic thickness and LV end-diastolic thickness when compared to controls, these differences were not statistically significant. Fitted values of *Caa* and *Rub* decreased 59.0% and 15.3% from their control values, respectively. Resulting model hemodynamics matched reported hemodynamics in the corrected group within one standard deviation.

3.2. Group Comparison

The untreated CoA simulation produced a characteristic large increase in ventricular pressure. In the corrected simulation, LV pressure was largely restored to control values, as expected, despite increased ESPVR (Figure 3).

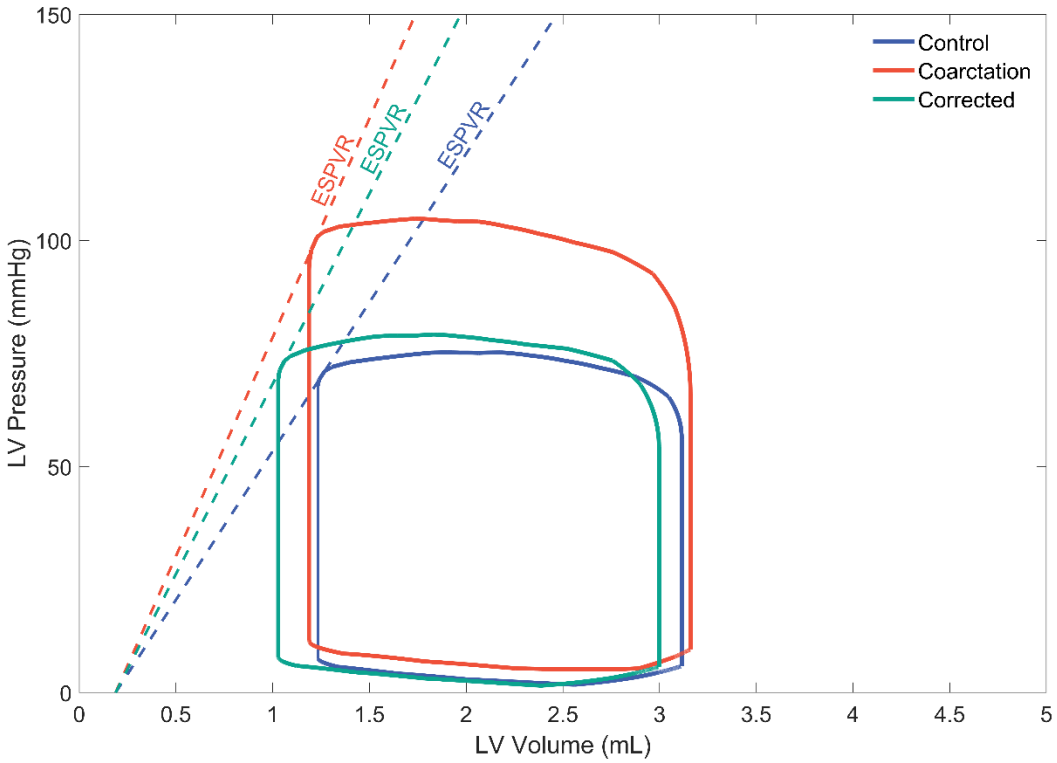

Figure 3: Simulated pressure-volume loops for the control (blue), coarctation (red), and corrected (green) groups. Dashed lines represent linearized end systolic pressure volume relationships (ESPVR)

Ascending aortic systolic and diastolic blood pressures matched reported measurements well, falling within half a standard deviation for all groups (Figure 4). The blood pressure gradients across the coarctation region (or, for the control group, from the ascending to descending aorta) also agreed well with reported measurements, falling within three-fourths of a standard deviation for all groups. Maximum aortic flow was within 0.26 of a standard deviation for all three groups (Figure 5). The ratio of upper body to lower body flow was within 1/25 of a standard deviation for all groups. Stroke volume was within one standard deviation, and ejection fraction was within three-fourths of a standard deviation. Complete model results for all groups are listed in Table 3.

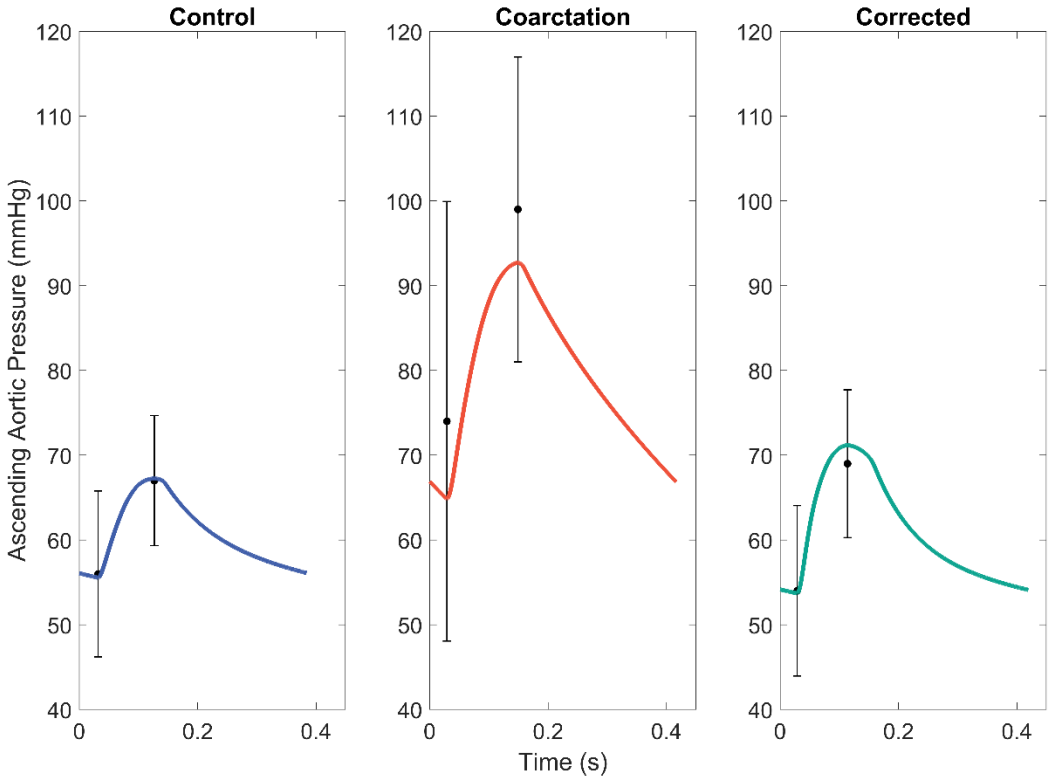

Figure 4: Model ascending aortic systolic and diastolic pressures over one cardiac cycle for the control (blue), coarctation (red), and corrected (green) groups, compared to measured data (black) [52]. Error bars indicate one standard deviation

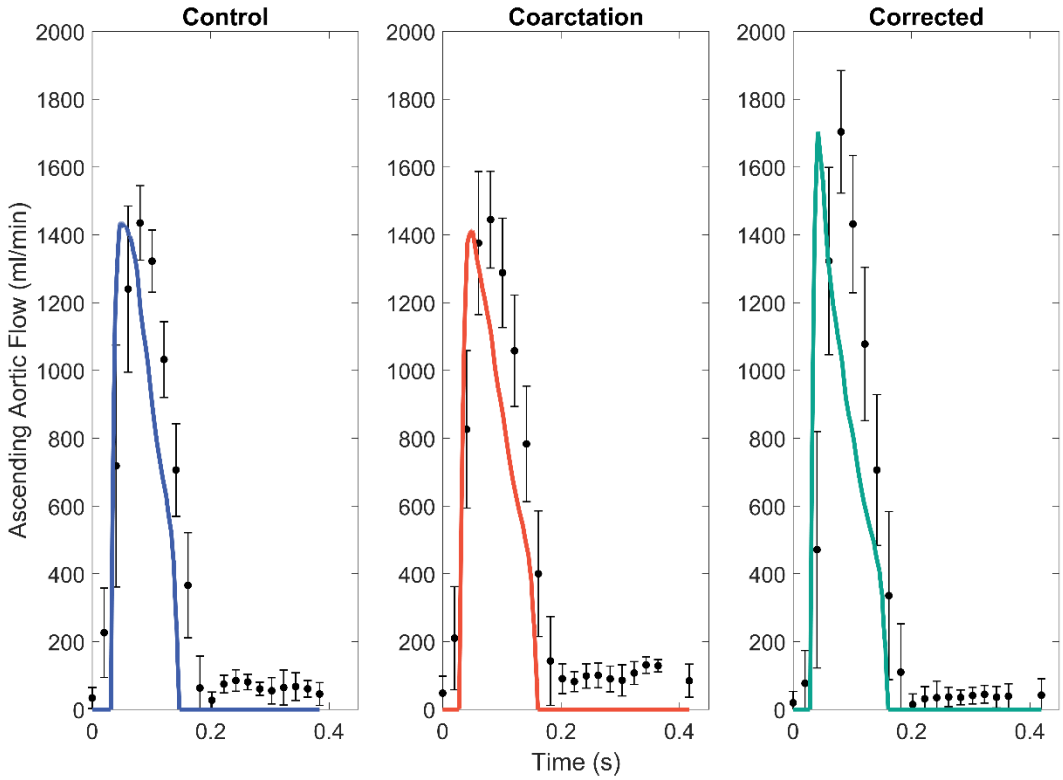

Figure 5: Model ascending aortic flow over one cardiac cycle for the control (blue), coarctation (red), and corrected (green) groups, compared to measured data (black) [52]. Error bars indicate one standard deviation

Table 3: Model results compared to reported experimental measurements (Wendell et al)

Index	Control	Model	Z-score	CoA	Model	Z-score	Corrected	Model	Z-score
BPG, mean (mmHg)	3.27 ± 4.32	3.76	0.11	20.1 ± 4.75	20.2	0.01	2.61 ± 3.46	4.01	0.42
BPG, peak (mmHg)	10.8 ± 7.34	9.90	-0.12	31.0 ± 8.64	32.8	0.21	17.0 ± 4.32	13.8	-0.68
SV (mL)	1.87 ± 0.53	1.95	0.15	1.99 ± 0.56	1.85	-0.24	1.93 ± 0.26	2.16	0.94
EF %	60.6 ± 4.82	60.8	0.04	66.4 ± 6.24	61.7	-0.75	65.0 ± 7.88	68.1	0.43
Upper/lower flow split	0.30 ± 0.04	0.30	0	0.37 ± 0.04	0.37	0.04	0.33 ± 0.04	0.33	-0.01
Maximum AA flow (mL/min)	1435 ± 110	1424	-0.10	1445 ± 143	1466	0.15	1704 ± 68.3	1656	-0.56
AA SBP (mmHg)	67 ± 7.67	67.2	0.02	99 ± 18.0	90.0	-0.50	69 ± 8.73	71.4	0.26
AA DBP (mmHg)	56 ± 9.79	57.0	0.10	74 ± 25.9	70.9	-0.12	54 ± 10.05	55.6	0.11

4. DISCUSSION

Previous studies of CoA have shown an increase in the stiffness of the ascending aorta before and after corrective surgery when compared to controls, suggesting some extent of proximal aortic remodeling is irreversible [12, 14, 63]. In particular, histologic evidence of similar increases in ascending aortic thickness without increases in functional elastin or smooth muscle have been reported for both the CoA and corrected groups in the presently simulated rabbit model [14, 64]. These findings validate the results produced by our computer model from fitting the non-terminal data [52]: in both the untreated CoA and corrected simulations, a decrease in ascending aortic compliance was necessary to match reported hemodynamics, suggesting the rabbits with CoA underwent vascular remodeling that persisted after repair. Indeed, this was the case experimentally, as nearly all of the cardiac function data from Wendell et al. were from the same animals as the arterial data featured in Menon et al. 2012a, b.

4.1. Peripheral Resistance and Proximal Aortic Remodeling

In the study by Wendell et al., the corrected group experienced restored diameter of the coarctation region after dissolving of the Vicryl suture used to create the coarctation, resulting in a reduced blood pressure gradient when compared to the untreated CoA group. Despite this reduction, the corrected group experienced a significantly larger peak aortic flow than the control or CoA groups. However, total flow and ascending aortic pressures did not differ from control, indicating flow acceleration in the corrected group and suggesting irreversible aortic stiffening proximal to the coarctation. Vascular compensation primarily occurs in small arteries and arterioles, which exhibit a pronounced myogenic response to pressure changes—when pressure increases, smooth muscle cells relax, resulting in vasodilation

and increased lumen flow; when pressure decreases, they contract, resulting in vasoconstriction and decreased lumen flow. In this experimental study, the flow to the upper body increased by 31.2% and 13.5% for the CoA and corrected groups, respectively, and the flow to the lower body decreased by 4.2% and 1.2% for the CoA and corrected groups, respectively (Wendell et al. 2017, Mendell et al. 2012a), suggesting vascular compensation plays a prominent role in the hemodynamic differences between groups. We explored the effects of peripheral resistance changes and ascending aortic remodeling by modeling three parameter cases for the CoA and corrected simulations (Figures 6 and 7, respectively).

CoA group:

- **Case 1:** For the first case, only *Rda*, *Raa*, and unloaded thickness *c_h0* were adjusted based on coarctation group measurement data (see Section 2.2). All other parameters were left at control values. Though these parameters were sufficient to match diastolic ascending aortic pressure, stroke volume, and ejection fraction within one standard deviation of the data, they were not sufficient to match systolic ascending aortic pressure, peak ascending aortic flow, mean blood pressure gradient, or peak blood pressure gradient.

- **Case 2:** In the second case, upper and lower body arterial resistances *Rub* and *Rlb* were allowed to change. *Rda*, *Raa*, and *c_h0* were set to their Case 1 values, and all other parameters were left at control values. This sufficed to reduce the peak

ascending aortic flow to appropriate levels and increase the mean and peak blood pressure gradients, but was not enough to match systolic ascending aortic pressure.

- **Case 3:** The third case is equivalent to Case 2 with the exception of ascending aortic compliance, *Caa*, which was allowed to change. Only by including this parameter in the fitting scheme could the ascending aortic systolic pressure data be matched within a standard deviation.

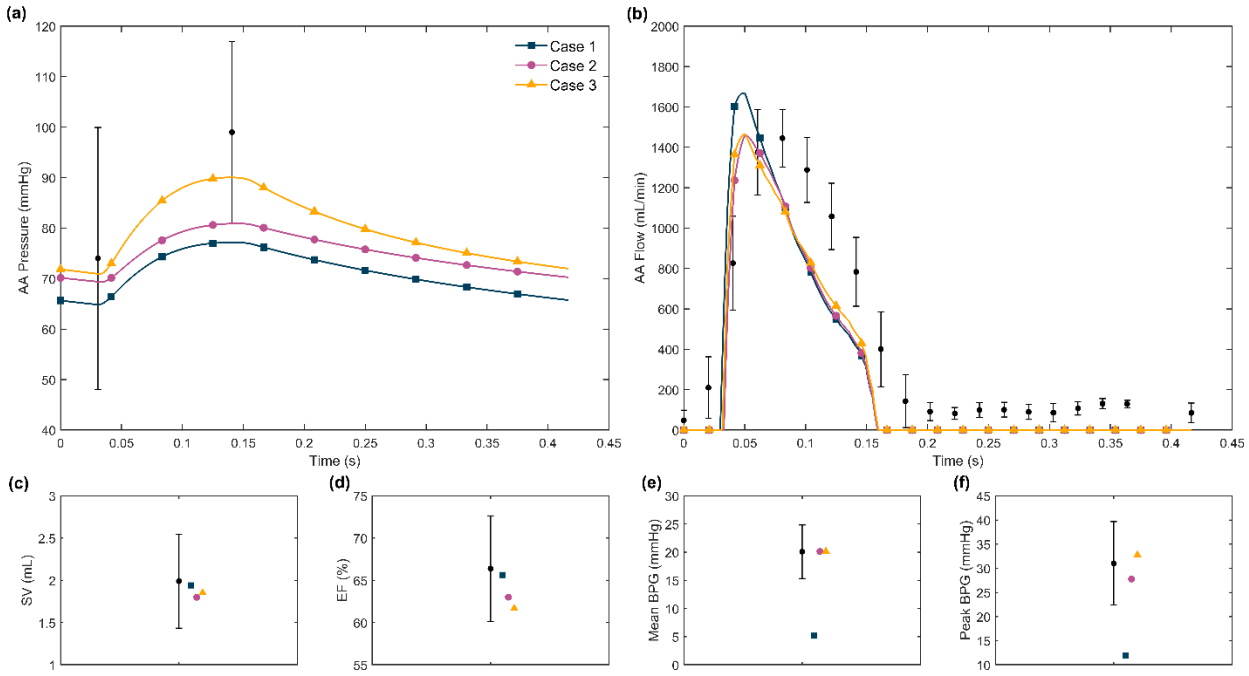

Figure 6: Parameter cases for the untreated coarctation simulation, with model outputs compared to reported measurements for (A) ascending aortic pressure, (B) ascending aortic flow, (C) stroke volume, (D) ejection fraction, (E) mean blood pressure gradient, and (F) peak blood pressure gradient [52]. In Case 1 (blue squares), only ascending aortic resistance (Raa), descending aortic resistance (Rda), and unloaded thickness c_h0 were adjusted based on CoA group measurement data. All other parameters were left at control values. For Case 2 (purple dots), upper and lower body arterial resistances (Rub and Rlb) were allowed to change. Rda, Raa, and c_h0 were set to their Case 1 values, and all other parameters were left at control values. In Case 3 (yellow triangles), parameters were equivalent to Case 2, with the exception of ascending aortic compliance, Caa, which was allowed to change. Error bars indicate one standard deviation

Corrected group:

- **Case 1:** To represent a complete reversal of the coarctation, the first case for the corrected group used the same parameters as the control group, with the exception of *Raa* and *c_h0*, which were adjusted based on corrected group measurement data. Though these parameters produced ascending aortic pressures, peak ascending aortic flow, stroke volume, ejection fraction, and a mean blood pressure gradient that matched the data within a standard deviation, the peak blood pressure gradient fell short.

- **Case 2:** As in the CoA Case 2, *Rub* and *Rlb* were allowed to change. This had minimal effect on outputs, including the peak blood pressure gradient.

- **Case 3:** With the addition of *Caa* to the fitting scheme in Case 2, peak blood pressure gradient could be matched.

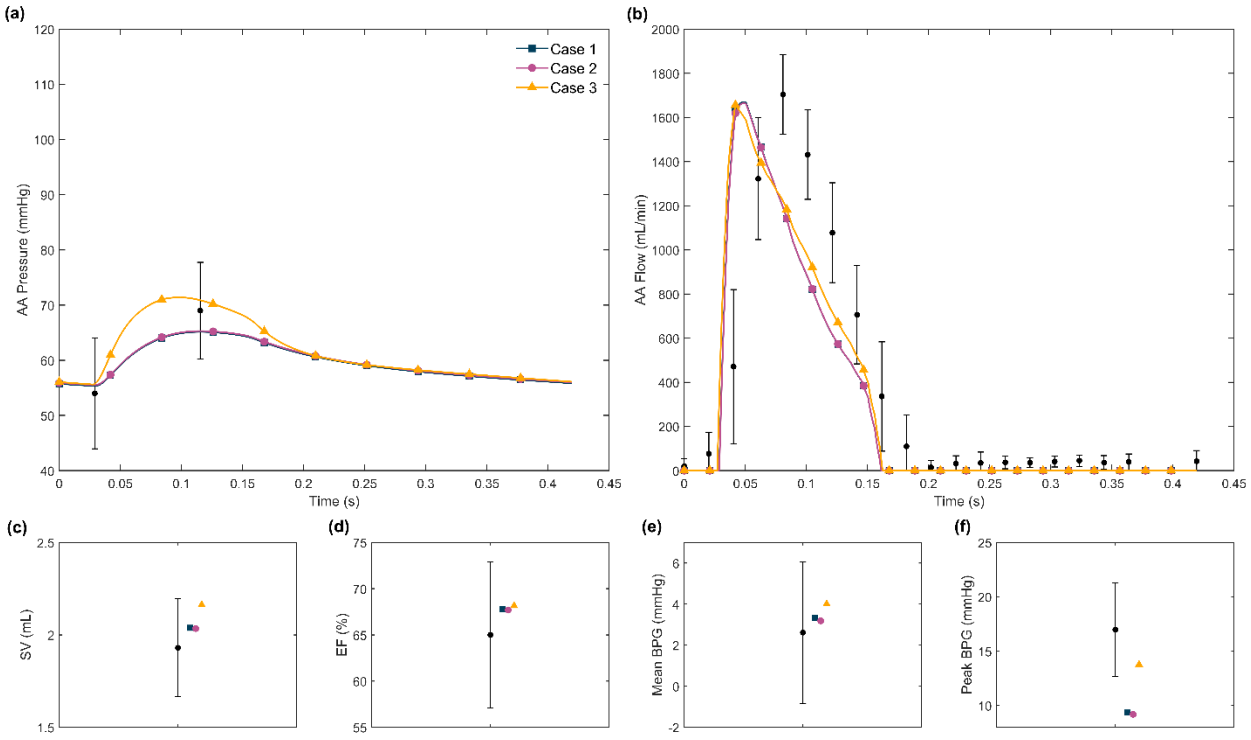

Figure 7: Parameter cases for the corrected simulation, with model outputs compared to reported measurements for (A) ascending aortic pressure, (B) ascending aortic flow, (C) stroke volume, (D) ejection fraction, (E) mean blood pressure gradient, and (F) peak blood pressure gradient [52]. In Case 1 (blue squares), all parameters were kept at control values with the exception of Raa and c_h0, which were adjusted based on corrected group measurement data. For Case 2 (purple dots), upper and lower body arterial resistances (Rub and Rlb) were allowed to change, with all other parameters left at their Case 1 values. In Case 3 (yellow triangles), parameters were equivalent to Case 2, with the exception of ascending aortic compliance, Caa, which was allowed to change. Error bars indicate one standard deviation

To further evaluate our modeling results, we used a frequentist analysis [65, 66] to estimate the uncertainty in the parameters fitted in the coarctation and corrected simulations: *Caa*, *Rub*, and *Rlb*. This approach considers the local sensitivity of each best-fit parameter to experimental data and the sum-squared error produced by best-fit model evaluations, enabling computation of parameter confidence intervals. Figure 8 shows the 95% confidence intervals for the control model as well as the best-fit untreated CoA and corrected models. *Caa* confidence intervals for both the untreated CoA and corrected models were well below the control model, confirming that a reduction in ascending aortic compliance was necessary to capture the differences in the experimental data between the control, untreated CoA, and corrected rabbits. Furthermore, the confidence intervals for *Caa* in the untreated CoA and corrected models overlapped, consistent with observations that remodeling occurred in these groups. Menon et al. (2012a) observed statistically similar increases in ascending aortic thickness with reduced smooth muscle function and elastin fragmentation in both the untreated CoA and corrected rabbits, validating our model results.

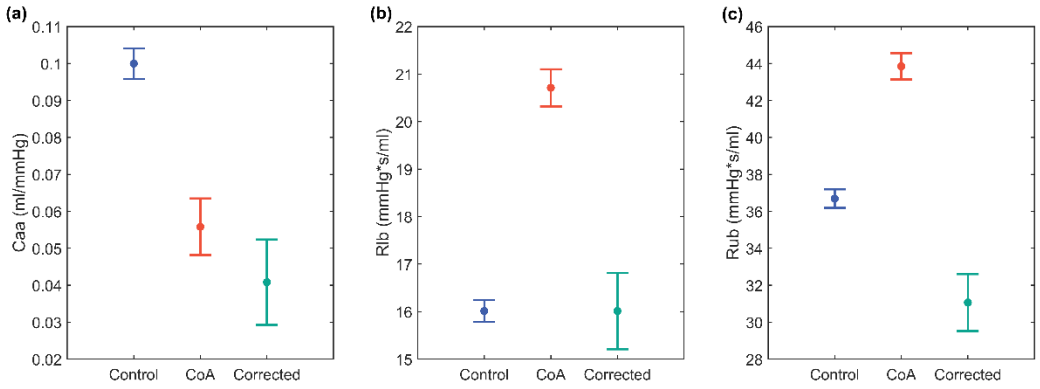

Figure 8: Parameter uncertainty quantification for control, untreated CoA, and corrected models. (A) the ascending aortic capacitance (Caa), (B) the resistance of lower body arteries (Rlb), and (C) the resistance of upper body arteries (Rub). Error bars indicate 95% confidence intervals determined for each parameter from a frequentist uncertainty analysis

Similar remodeling in the carotid arteries has also been observed in CoA with hypertension [14, 67, 68]. Therefore, we investigated including the head and neck arterial resistance (*Rhn*) and the upper body arterial compliance (*Cub*) in the CoA and corrected group parameter optimizations. For the head and neck arteries, we assumed they experience the same proportional increase in diameter as the proximal ascending aorta and thus decreased *Rhn* from the control value by the same percentage as *Raa* from its control value. To capture the remodeling observed in the larger head and neck arteries, we assumed that *Cub* would be less than the control value but that—since this capacitor represents the response of the entire upper body—this reduction would not be more than that of *Caa*. The final fitted values of *Caa, Rub*, and *Rlb* differed slightly (< 9% and < 3% for the CoA and corrected simulations, respectively) from their previously fitted values. *Cub* was 61% of its control value for the CoA simulation and 99% of its control value for the corrected simulation (Supplemental Table 1). The addition *Rhn* and *Cub* to the optimization scheme did not improve model results for either the CoA or corrected simulations (Supplemental Table 2).

Menon et al. (2012a) reported blood pressure measurements in the carotid and femoral arteries of control, CoA, and corrected rabbits. These measurements were not used to fit our computer models, enabling further evaluation of vascular compensation. In the CoA group the carotid pressure increased by 35.9%. If we assume that this increase was consistent across the entire upper body, *Rub* would have increased by an amount similar to our model fit (16.3% vs. 19.4%, Table 2). The change in pressure outpaced the change in flow, potentially suggesting

overstretching during dilation as a stimulus for long-term smooth muscle cell dysfunction and remodeling, including the shift to higher levels of non-muscle myosin and lower levels of smooth muscle myosin (Menon et al. 2012a). In the corrected group, there was a decrease in the carotid pressure of 4.7%. Again, if this decrease was consistent throughout the upper body, then combined with the increase in flow this would have resulted in a large decrease in *Rub*, consistent with our model result (-9.9% vs. -16.1%, Table 2). This drop in resistance potentially indicates incomplete vasoconstriction in the upper body arteries with correction and supports the thesis that remodeling reduces the long-term compensatory ability of the upper body distal vasculature. A reduction in the ability of the upper body vasculature to dilate and contract due to a reduction in smooth muscle function or extracellular matrix deposition could be a potential mechanism for long-term hypertension risk despite CoA correction. Based on these results, experiments focused on measures of distal arterial upper body pressure and vasoreactivity are of high future interest with corresponding immunohistochemical investigations. The femoral pressure increased by 9.8% in the CoA group, but though the resistance would increase if this pressure applied to the entire lower body (27.8%), consistent with our modeling result (29.4%, Table 2), the decrease in flow suggests vasoconstriction rather than vasodilation and muscle cell contraction rather than stretching. In the corrected group, the femoral pressure decreased by 4.9%, producing a slight increase in resistance (4.3%), in contrast to our modeling result which indicated a slight decrease (-1.9%). The confidence interval on *Rlb* from our uncertainty analysis (Figure 8b) indicate it does not differ significantly from control and spans both a slight positive and negative change. Therefore, this discrepancy is not meaningful.

We also performed additional simulations to determine if the hemodynamic differences in the corrected group could be explained by incomplete repair of the coarctation. Allowing descending aortic parameters (*Rda* and *Cda*) to change while keeping other parameters equivalent to control values failed to match mean and peak blood pressure gradients within a standard deviation of the measured data. As in the untreated coarctation group, simulating persistent remodeling in the ascending aorta was necessary to match reported hemodynamics.

4.2. Limitations

We assumed a simplified spherical geometry when representing the ventricles in our model. Though this assumption did not impact our ability to match reported hemodynamics or ventricular dimensions within a standard deviation, a more realistic geometry would produce a physically meaningful ventricular wall volume and may facilitate a closer model fit to experimental data. The simple nature of this model does make it extremely fast, however, requiring 1.4 seconds to run on a desktop computer with 16 GB RAM, a 64-bit operating system, and a 3.0 GHz Intel Core i7-9700 CPU, expediting both automated parameter fitting and uncertainty analysis.

We chose to model the coarctation as a proportional change in the descending aortic resistance based on measurements of coarctation site diameter (unpublished data from Menon et al. 2012a), assuming resistance was roughly inversely proportional to cross-sectional area [62]. Others have simulated CoA in a lumped parameter model using a semi-analytical formulation of the net pressure gradient across a stenosis, where the stenosis is

modeled by a resistor in parallel with an inductor and the net pressure gradient is a function of the instantaneous flow rate and the energy loss coefficient [49, 69]. In this approach, coarctation severity is simulated by reducing the effective orifice area, which directly alters both resistance and inductance together. We opted to not include an inductor in our model. Stergiopulos et al. [70] compared the ability of a 4-element Windkessel (with a parallel inductor) to a 3-element Windkessel to simulate ascending aortic hemodynamics in dogs. Both produced pressure waves that closely matched the data when the flow was input. Therefore, without detailed frequency data, we chose to limit the number of unidentifiable parameters. Additionally, calculating the energy loss coefficient would require measurements of aortic diameter distal to the coarctation, which were not available. Alternative methods of calculating the pressure gradient require measurements of blood velocity and coarctation length [71, 72], neither of which were measured in the rabbit experimental studies.

Collateral vessels can form to attenuate the hemodynamic consequences of the coarctation [73, 74]. While collateral vessels have not been directly observed in this animal model [14, 38, 64], proximal versus distal catheter blood pressure measurements were consistent with those in the setting of collateral vessels [75]. The caliber of intercostal arteries at harvest further suggests collateralization, despite not being able to resolve these arteries by MRI. Experimentally, Azarnoosh et al. [46] measured the total upper body flow in this rabbit model by subtracting flows from the arteries proximal to the coarctation (the right and left coronary and subclavian arteries) from the total systemic flow, which was

determined by integrating the area under the ascending aorta PC-MRI waveform. Thus, while collateralization was not explicitly considered in the computer model, the increase in upper body flow and reduction in blood pressure gradient that can result from collateralization were considered during model fitting.

Changes in arterial compliance are represented in our computer model by changing the value of arterial capacitors *Caa* and *Cub*. These capacitance changes cannot differentiate between compliance changes due to geometry (changes in wall thickness or radius) and stiffness (due to microstructural changes in elastin, collagen, and smooth muscle). Terminal histologic analysis of ascending aortic tissue indicates these effects are likely occurring simultaneously. Both untreated CoA and corrected rabbits exhibited increases in ascending aortic thickness and reductions in functional elastin and smooth muscle [14, 64]. Multiscale microstructural [58, 76] and continuum constitutive [77] computer models can capture the effects of tissue microstructure on overall mechanical behavior. While such models would be capable of delineating the effects of microstructural remodeling and vessel thickness, fitting model parameters would necessitate terminal structural and geometric data. Predictive computational models [78–82] which simulate alterations in tissue constituent mass due to pathologic loading could potentially address this concern, but their application to aortic coarctation is recent and limited [83]. In particular, the constrained mixture approach [84] has been applied to simulate temporal alterations in elastin, collagen, and smooth muscle content in large arteries. However, validation of

these predictions currently relies on detailed quantitative estimations of these proportions from histopathology, which can only be conducted terminally.

Lastly, we assumed constant myocardial material properties in all three groups. Animal studies of LV pressure overload caused by aortic banding have shown ventricular remodeling includes collagenous fibrosis [85]. Additionally, histologic analysis indicates patients with heart failure and a preserved ejection fraction alongside hypertension have higher myocardial collagen content than healthy controls or those without hypertension [86]. However, biopsy is not feasible in most patients. Late gadolinium enhanced cardiovascular MRI is a common noninvasive approach to quantify focal or replacement myocardial fibrosis, such as that seen in ischemic heart disease. T1 mapping is also emerging as a newer technique capable of detecting diffuse fibrosis, which is more common in hypertensive heart disease. While both techniques have been applied to CoA patients post-correction, fibrosis was not detected [67, 87]. As part of this study, we were able to conduct preliminary histologic analyses on left ventricular samples from one control and one untreated CoA rabbit that had been preserved from the previously published experimental study (Wendell et al. 2017). Short axis slices were stained with picrosirius red and imaged under polarized light to visualize collagen. We did not observe any obvious difference in collagen content, and automated quantification indicated that the collagen area fraction was essentially the same in the control and untreated CoA ventricular samples (2.6% and 2.5%, respectively). In the future, if we find experimental

evidence that myocardial material properties change with CoA or its correction, accounting for this in the computational model would be relatively straightforward.

4.3. Conclusion

There is increasing evidence that the degree of distal vascular, ascending aortic, and ventricular remodeling due to CoA is likely linked to the duration and severity of the coarctation (Menon et al. 2012a; Azarnoosh et al. 2023). There is also evidence that following successful aortic coarctation correction, reversal of this remodeling may be incomplete or impossible, leading to chronic hypertension. Computational models can play several roles in understanding the incidence, mechanisms, and presentation of pathologic remodeling in CoA. For instance, preclinical animal models, though invaluable for determining the underlying mechanisms driving adverse remodeling, are resource intensive. They also require careful planning to ensure that measurements are comprehensive and contribute to our understanding of cause and effect relationships. Therefore, in future simulations we will use our validated model to investigate the trade-off in CoA severity and duration (i.e., different correction timing) to evaluate their individual roles in the time course and reversibility of remodeling. These results will inform timing decisions in both data collection and termination for future preclinical studies. They will also enable us to prioritize data collection. For example, while previous terminal histology indicated potentially irreversible remodeling was occurring in the ascending aorta following coarctation correction, our computational model suggests that there may be additional

persistent dysfunction in the upper body arteries, leading us to prioritize vasoreactivity assessment and terminal immunohistochemistry in these vessels in the future.

From the clinical perspective, while animal models of CoA—aided by insights from computational models—can define timing and severity boundaries prior to studies on human patients, some methods of data collection used in animal models are undesirable or impossible for human studies. Our computational model identified the persistent reduction in ascending aortic compliance following CoA correction when only non-terminal data was considered. This indicates promise for development as a clinical tool to estimate a patient's level of maladaptive vascular remodeling and predict their long-term hypertension risk.

Sources of funding

Research reported was partially supported by Advancing a Healthier Wisconsin (Project #5520519), the American Heart Association (AHA) under award numbers 15GRNT25700042 and 20CDA35210754 (J.F. LaDisa and C.M. Witzenburg, respectively), the National Science Foundation (Graduate Research Fellowship to A.A. Hiebing), and the National Institutes of Health (NIH) National Heart, Lung, and Blood Institute under award numbers R01HL142955 (J.F. LaDisa) and R15HL096096 (J.F. LaDisa). The content is solely the responsibility of the authors and does not necessarily represent the official views of Advancing a Healthier Wisconsin, the AHA, the NSF, or the NIH.

REFERENCES

1. Mai CT, Isenburg JL, Canfield MA, et al (2019) National population-based estimates for major birth defects, 2010–2014. Birth Defects Research 111:1420–1435. https://doi.org/10.1002/bdr2.1589

2. Cohen M, Fuster V, Steele PM, et al (1989) Coarctation of the aorta. Long-term follow-up and prediction of outcome after surgical correction. Circulation 80:840–845. https://doi.org/10.1161/01.CIR.80.4.840

3. Kenny D, Polson JW, Martin RP, et al (2011) Hypertension and coarctation of the aorta: an inevitable consequence of developmental pathophysiology. Hypertens Res 34:543–547. https://doi.org/10.1038/hr.2011.22

4. Choudhary P, Canniffe C, Jackson DJ, et al (2015) Late outcomes in adults with coarctation of the aorta. Heart 101:1190–1195. https://doi.org/10.1136/heartjnl-2014-307035

5. Egbe AC, Miranda WR, Warnes CA, et al (2021) Persistent Hypertension and Left Ventricular Hypertrophy After Repair of Native Coarctation of Aorta in Adults. Hypertension 78:672–680. https://doi.org/10.1161/HYPERTENSIONAHA.121.17515

6. Clarkson PM, Nicholson MR, Barratt-Boyes BG, et al (1983) Results after repair of coarctation of the aorta beyond infancy: A 10 to 28 year follow-up with particular reference to late systemic hypertension. The American Journal of Cardiology 51:1481–1488. https://doi.org/10.1016/0002-9149(83)90661-6

7. O'Sullivan JJ (2002) Prevalence of hypertension in children after early repair of coarctation of the aorta: a cohort study using casual and 24 hour blood pressure measurement. Heart 88:163–166. https://doi.org/10.1136/heart.88.2.163

8. Heger M, Willfort A, Neunteufl T, et al (2005) Vascular dysfunction after coarctation repair is related to the age at surgery. International Journal of Cardiology 99:295–299. https://doi.org/10.1016/j.ijcard.2004.02.001

9. Brili S, Tousoulis D, Antoniades C, et al (2005) Evidence of vascular dysfunction in young patients with successfully repaired coarctation of aorta. Atherosclerosis 182:97–103. https://doi.org/10.1016/j.atherosclerosis.2005.01.030

10. Sendzikaite S, Sudikiene R, Tarutis V, et al (2020) Prevalence of arterial hypertension, hemodynamic phenotypes, and left ventricular hypertrophy in children after coarctation repair: a multicenter cross-sectional study. Pediatr Nephrol 35:2147–2155. https://doi.org/10.1007/s00467-020-04645-w

11. Sendzikaite S, Sudikiene R, Lubaua I, et al (2022) Multi-centre cross-sectional study on vascular remodelling in children following successful coarctation correction. J Hum Hypertens 36:819–825. https://doi.org/10.1038/s41371-021-00585-6

12. Xu J, Shiota T, Omoto R, et al (1997) Intravascular ultrasound assessment of regional aortic wall stiffness, distensibility, and compliance in patients with coarctation of the aorta. American Heart Journal 134:93–98. https://doi.org/10.1016/S0002-8703(97)70111-X

13. Ou P, Celermajer DS, Jolivet O, et al (2008) Increased central aortic stiffness and left ventricular mass in normotensive young subjects after successful coarctation repair. American Heart Journal 155:187–193. https://doi.org/10.1016/j.ahj.2007.09.008

14. Menon A, Eddinger TJ, Wang H, et al (2012) Altered hemodynamics, endothelial function, and protein expression occur with aortic coarctation and persist after repair. American Journal of Physiology-Heart and Circulatory Physiology 303:H1304–H1318. https://doi.org/10.1152/ajpheart.00420.2012

15. Bocelli A, Favilli S, Pollini I, et al (2013) Prevalence and Long-Term Predictors of Left Ventricular Hypertrophy, Late Hypertension, and Hypertensive Response to Exercise After Successful Aortic Coarctation Repair. Pediatr Cardiol 34:620–629. https://doi.org/10.1007/s00246-012-0508-0

16. Rinnström D, Dellborg M, Thilén U, et al (2016) Left ventricular hypertrophy in adults with previous repair of coarctation of the aorta; association with systolic blood pressure in the high normal range. International Journal of Cardiology 218:59–64. https://doi.org/10.1016/j.ijcard.2016.05.033

17. Ağbaş A, Gökalp S, Canpolat N, et al (2020) Is the burden of late hypertension and cardiovascular target organ damage in children and adolescents with coarctation of the aorta after early successful repair different to healthy controls? Cardiol Young 30:1305–1312. https://doi.org/10.1017/S104795112000205X

18. Krogmann ON, Rammos S, Jakob M, et al (1993) Left ventricular diastolic dysfunction late after coarctation repair in childhood: Influence of left ventricular hypertrophy. Journal of the American College of Cardiology 21:1454–1460. https://doi.org/10.1016/0735-1097(93)90323-S

19. Eerola A, Jokinen E, Boldt T, et al (2007) Left ventricular hypertrophy persists after successful treatment for coarctation of the aorta. Scandinavian Cardiovascular Journal 41:370–377. https://doi.org/10.1080/14017430701397839

20. Dunnill MS (1959) Histology of the aorta in coarctation. J Pathol 78:203–207. https://doi.org/10.1002/path.1700780122

21. Sehested J, Baandrup U, Mikkelsen E (1982) Different reactivity and structure of the prestenotic and poststenotic aorta in human coarctation. Implications for baroreceptor function. Circulation 65:1060–1065. https://doi.org/10.1161/01.CIR.65.6.1060

22. Dernellis J, Panaretou M (2005) Aortic Stiffness Is an Independent Predictor of Progression to Hypertension in Nonhypertensive Subjects. Hypertension 45:426–431. https://doi.org/10.1161/01.HYP.0000157818.58878.93

23. Mitchell GF, Guo C-Y, Benjamin EJ, et al (2007) Cross-Sectional Correlates of Increased Aortic Stiffness in the Community: The Framingham Heart Study. Circulation 115:2628–2636. https://doi.org/10.1161/CIRCULATIONAHA.106.667733

24. Kaess BM, Rong J, Larson MG, et al (2012) Aortic Stiffness, Blood Pressure Progression, and Incident Hypertension. JAMA 308:875. https://doi.org/10.1001/2012.jama.10503

25. Dijkema EJ, Slieker MG, Leiner T, Grotenhuis HB (2018) Arterioventricular interaction after coarctation repair. American Heart Journal 201:49–53. https://doi.org/10.1016/j.ahj.2018.04.004

26. Pauca AL, Wallenhaupt SL, Kon ND, Tucker WY (1992) Does Radial Artery Pressure Accurately Reflect Aortic Pressure? Chest 102:1193–1198. https://doi.org/10.1378/chest.102.4.1193

27. Jesus CA, Assef JE, Pedra SRFF, et al (2016) Serial assessment of arterial structure and function in patients with coarctation of the aorta undergoing stenting. Int J Cardiovasc Imaging 32:729–739. https://doi.org/10.1007/s10554-015-0827-3

28. Meyer AA, Joharchi MS, Kundt G, et al (2005) Predicting the risk of early atherosclerotic disease development in children after repair of aortic coarctation. European Heart Journal 26:617–622. https://doi.org/10.1093/eurheartj/ehi037

29. de Divitiis M, Pilla C, Kattenhorn M, et al (2003) Ambulatory blood pressure, left ventricular mass, and conduit artery function late after successful repair of coarctation of the aorta. Journal of the American College of Cardiology 41:2259–2265. https://doi.org/10.1016/S0735-1097(03)00480-7

30. De Divitiis M, Pilla C, Kattenhorn M (2002) Vascular dysfunction after repair of coarctation of the aorta: impact of early surgery. ACC Current Journal Review 11:85. https://doi.org/10.1016/S1062-1458(02)00582-2

31. Cuypers J, Leirgul E, Larsen TH, et al (2013) Assessment of Vascular Reactivity in the Peripheral and Coronary Arteries by Cine 3T-Magnetic Resonance Imaging in Young Normotensive Adults after Surgery for Coarctation of the Aorta. Pediatr Cardiol 34:661–669. https://doi.org/10.1007/s00246-012-0522-2

32. Corretti MC, Anderson TJ, Benjamin EJ, et al (2002) Guidelines for the ultrasound assessment of endothelial-dependent flow-mediated vasodilation of the brachial artery. Journal of the American College of Cardiology 39:257–265. https://doi.org/10.1016/S0735-1097(01)01746-6

33. LaDisa JF, Alberto Figueroa C, Vignon-Clementel IE, et al (2011) Computational Simulations for Aortic Coarctation: Representative Results From a Sampling of Patients. Journal of Biomechanical Engineering 133:091008. https://doi.org/10.1115/1.4004996

34. Arzani A, Dyverfeldt P, Ebbers T, Shadden SC (2012) In Vivo Validation of Numerical Prediction for Turbulence Intensity in an Aortic Coarctation. Ann Biomed Eng 40:860–870. https://doi.org/10.1007/s10439-011-0447-6

35. Wendell DC, Samyn MM, Cava JR, et al (2013) Including aortic valve morphology in computational fluid dynamics simulations: Initial findings and application to aortic coarctation. Medical Engineering & Physics 35:723–735. https://doi.org/10.1016/j.medengphy.2012.07.015

36. Lee JJ, D'Ancona G, Amaducci A, et al (2014) Role of Computational Modeling in Thoracic Aortic Pathology: A Review: COMPUTATIONAL AORTIC PATHOLOGIES. J Card Surg 29:653–662. https://doi.org/10.1111/jocs.12413

37. Zhu Y, Chen R, Juan Y-H, et al (2018) Clinical validation and assessment of aortic hemodynamics using computational fluid dynamics simulations from computed tomography angiography. BioMed Eng OnLine 17:53. https://doi.org/10.1186/s12938-018-0485-5

38. Ghorbannia A, Ellepola CD, Woods RK, et al (2022) Clinical, Experimental, and Computational Validation of a New Doppler-Based Index for Coarctation Severity Assessment. Journal of the American Society of Echocardiography 35:1311–1321. https://doi.org/10.1016/j.echo.2022.09.006

39. LaDisa, JF, Taylor CA, Feinstein JA (2010) Aortic coarctation: Recent developments in experimental and computational methods to assess treatments for this simple condition. Progress in Pediatric Cardiology 30:45–49. https://doi.org/10.1016/j.ppedcard.2010.09.006

40. Coogan JS, Chan FP, Taylor CA, Feinstein JA (2011) Computational fluid dynamic simulations of aortic coarctation comparing the effects of surgical- and stent-based treatments on aortic compliance and ventricular workload. Cathet Cardiovasc Intervent 77:680–691. https://doi.org/10.1002/ccd.22878

41. Jr. LaDisa JF, Dholakia RJ, Figueroa CA, et al (2011) Computational Simulations Demonstrate Altered Wall Shear Stress in Aortic Coarctation Patients Treated by

Resection with End-to-end Anastomosis: Altered Shear Stress after Coarctation Repair. Congenital Heart Disease 6:432–443. https://doi.org/10.1111/j.1747-0803.2011.00553.x

42. Kwon S, Feinstein JA, Dholakia RJ, LaDisa JF (2014) Quantification of Local Hemodynamic Alterations Caused by Virtual Implantation of Three Commercially Available Stents for the Treatment of Aortic Coarctation. Pediatr Cardiol 35:732–740. https://doi.org/10.1007/s00246-013-0845-7

43. Taelman L, Bols J, Degroote J, et al (2016) Differential impact of local stiffening and narrowing on hemodynamics in repaired aortic coarctation: an FSI study. Med Biol Eng Comput 54:497–510. https://doi.org/10.1007/s11517-015-1336-1

44. Saitta S, Pirola S, Piatti F, et al (2019) Evaluation of 4D flow MRI-based non-invasive pressure assessment in aortic coarctations. Journal of Biomechanics 94:13–21. https://doi.org/10.1016/j.jbiomech.2019.07.004

45. Camarda JA, Dholakia RJ, Wang H, et al (2022) A Pilot Study Characterizing Flow Patterns in the Thoracic Aorta of Patients With Connective Tissue Disease: Comparison to Age- and Gender-Matched Controls via Fluid Structure Interaction. Front Pediatr 10:772142. https://doi.org/10.3389/fped.2022.772142

46. Azarnoosh J, Ghorbannia A, Ibrahim E-SH, et al (2023) Temporal evolution of mechanical stimuli from vascular remodeling in response to the severity and duration of aortic coarctation in a preclinical model. Sci Rep 13:8352. https://doi.org/10.1038/s41598-023-34400-8

47. Ralovich K, Itu L, Vitanovski D, et al (2015) Noninvasive hemodynamic assessment, treatment outcome prediction and follow-up of aortic coarctation from MR imaging: Noninvasive assessment of coarctation from MRI. Med Phys 42:2143–2156. https://doi.org/10.1118/1.4914856

48. Shi Y, Valverde I, Lawford PV, et al (2019) Patient-specific non-invasive estimation of pressure gradient across aortic coarctation using magnetic resonance imaging. Journal of Cardiology 73:544–552. https://doi.org/10.1016/j.jjcc.2018.12.016

49. Keshavarz-Motamed Z, Garcia J, Pibarot P, et al (2011) Modeling the impact of concomitant aortic stenosis and coarctation of the aorta on left ventricular workload. Journal of Biomechanics 44:2817–2825. https://doi.org/10.1016/j.jbiomech.2011.08.001

50. Keshavarz-Motamed Z, Edelman ER, Motamed PK, et al (2015) The role of aortic compliance in determination of coarctation severity: Lumped parameter modeling, in vitro study and clinical evaluation. Journal of Biomechanics 48:4229–4237. https://doi.org/10.1016/j.jbiomech.2015.10.017

51. Witzenburg CM, Holmes JW (2018) Predicting the Time Course of Ventricular Dilation and Thickening Using a Rapid Compartmental Model. J of Cardiovasc Trans Res 11:109–122. https://doi.org/10.1007/s12265-018-9793-1

52. Wendell DC, Friehs I, Samyn MM, et al (2017) Treating a 20 mm Hg gradient alleviates myocardial hypertrophy in experimental aortic coarctation. Journal of Surgical Research 218:194–201. https://doi.org/10.1016/j.jss.2017.05.053

53. Isselbacher EM, Preventza O, Hamilton Black J, et al (2022) 2022 ACC/AHA Guideline for the Diagnosis and Management of Aortic Disease: A Report of the American Heart Association/American College of Cardiology Joint Committee on Clinical Practice Guidelines. Circulation 146:. https://doi.org/10.1161/CIR.0000000000001106

54. Santamore WP, Burkhoff D (1991) Hemodynamic consequences of ventricular interaction as assessed by model analysis. American Journal of Physiology-Heart and Circulatory Physiology 260:H146–H157. https://doi.org/10.1152/ajpheart.1991.260.1.H146

55. Burkhoff D, Tyberg JV (1993) Why does pulmonary venous pressure rise after onset of LV dysfunction: a theoretical analysis. American Journal of Physiology-Heart and Circulatory Physiology 265:H1819–H1828. https://doi.org/10.1152/ajpheart.1993.265.5.H1819

56. Sunagawa K, Maughan WL, Sagawa K (1983) Effect of regional ischemia on the left ventricular end-systolic pressure-volume relationship of isolated canine hearts. Circ Res 52:170–8. https://doi.org/10.1161/01.RES.52.2.170

57. Caggiano LR, Holmes JW, Witzenburg CM (2022) Individual variability in animal-specific hemodynamic compensation following myocardial infarction. Journal of Molecular and Cellular Cardiology 163:156–166. https://doi.org/10.1016/j.yjmcc.2021.10.008

58. Witzenburg CM, Holmes JW (2017) A Comparison of Phenomenologic Growth Laws for Myocardial Hypertrophy. J Elast 129:257–281. https://doi.org/10.1007/s10659-017-9631-8

59. Fomovsky GM, Clark SA, Parker KM, et al (2012) Anisotropic Reinforcement of Acute Anteroapical Infarcts Improves Pump Function. Circ Heart Fail 5:515–22. https://doi.org/10.1161/circheartfailure.111.965731

60. Mahaffey KW, Raya TE, Pennock GD, et al (1995) Left Ventricular Performance and Remodeling in Rabbits After Myocardial Infarction: Effects of a Thyroid Hormone Analogue. Circulation 91:794–801. https://doi.org/10.1161/01.CIR.91.3.794

61. Witzenburg CM, Holmes JW (2019) The Impact of Hemodynamic Reflex Compensation Following Myocardial Infarction on Subsequent Ventricular Remodeling. Journal of Biomechanical Engineering 141:091010. https://doi.org/10.1115/1.4043867

62. Kaye D, Shah SJ, Borlaug BA, et al (2014) Effects of an Interatrial Shunt on Rest and Exercise Hemodynamics: Results of a Computer Simulation in Heart Failure. Journal of Cardiac Failure 20:212–221. https://doi.org/10.1016/j.cardfail.2014.01.005

63. Vogt M, Kühn A, Baumgartner D, et al (2005) Impaired Elastic Properties of the Ascending Aorta in Newborns Before and Early After Successful Coarctation Repair: Proof of a Systemic Vascular Disease of the Prestenotic Arteries? Circulation 111:3269–3273. https://doi.org/10.1161/CIRCULATIONAHA.104.529792

64. Menon A, Wendell DC, Wang H, et al (2012) A coupled experimental and computational approach to quantify deleterious hemodynamics, vascular alterations, and mechanisms of long-term morbidity in response to aortic coarctation. Journal of Pharmacological and Toxicological Methods 65:18–28. https://doi.org/10.1016/j.vascn.2011.10.003

65. Smith R (2014) Uncertainty Quantification: Theory, Implementation, and Applications. Society for Industrial and Applied Mathematics, Philadelphia, Pennsylvania

66. Colebank MJ, Umar Qureshi M, Olufsen MS (2021) Sensitivity analysis and uncertainty quantification of 1-D models of pulmonary hemodynamics in mice under control and hypertensive conditions. Int J Numer Meth Biomed Engng 37:. https://doi.org/10.1002/cnm.3242

67. Luijendijk P, Bouma BJ, Vriend JWJ, et al (2013) Left ventricular fibrosis in adults after coarctation repair, does it play a role? International Journal of Cardiology 168:5029–5030. https://doi.org/10.1016/j.ijcard.2013.07.158

68. Dempsey AA, Parraga G, Altamirano-Diaz L, et al (2019) Increased blood pressure is associated with increased carotid artery intima–media thickness in children with repaired coarctation of the aorta. Journal of Hypertension 37:1689–1698. https://doi.org/10.1097/HJH.0000000000002077

69. Garcia D, Durand L-G (2006) Aortic Stenosis and Systemic Hypertension, Modeling of. In: Akay M (ed) Wiley Encyclopedia of Biomedical Engineering, 1st ed. Wiley

70. Stergiopulos N, Westerhof BE, Westerhof N (1999) Total arterial inertance as the fourth element of the windkessel model. American Journal of Physiology-Heart and Circulatory Physiology 276:H81–H88. https://doi.org/10.1152/ajpheart.1999.276.1.H81

71. Young DF, Tsai FY (1973) Flow characteristics in models of arterial stenoses — II. Unsteady flow. Journal of Biomechanics 6:547–559. https://doi.org/10.1016/0021-9290(73)90012-2

72. Stergiopulos N, Young DF, Rogge TR (1992) Computer simulation of arterial flow with applications to arterial and aortic stenoses. Journal of Biomechanics 25:1477–1488. https://doi.org/10.1016/0021-9290(92)90060-E

73. Steffens JC, Bourne MW, Sakuma H, et al (1994) Quantification of collateral blood flow in coarctation of the aorta by velocity encoded cine magnetic resonance imaging. Circulation 90:937–943. https://doi.org/10.1161/01.CIR.90.2.937

74. Fox EB, Latham GJ, Ross FJ, Joffe D (2019) Perioperative and Anesthetic Management of Coarctation of the Aorta. Semin Cardiothorac Vasc Anesth 23:212–224. https://doi.org/10.1177/1089253218821953

75. Nichols WW, O'Rourke MF, Vlachopoulos C (2011) McDonald's blood flow in arteries: theoretical, experimental and clinical principles, 6th ed. Hodder Arnold, London

76. Rolf-Pissarczyk M, Li K, Fleischmann D, Holzapfel GA (2021) A discrete approach for modeling degraded elastic fibers in aortic dissection. Computer Methods in Applied Mechanics and Engineering 373:113511. https://doi.org/10.1016/j.cma.2020.113511

77. Holzapfel GA, Gasser TC, Ogden RW (2004) A new Constitutive Framework for Arterial Wall Mechanics and a Comparative Study of Material Models. In: Cowin SC, Humphrey JD (eds) Cardiovascular Soft Tissue Mechanics. Kluwer Academic Publishers, Dordrecht, pp 1–48

78. Alford PW, Humphrey JD, Taber LA (2008) Growth and remodeling in a thick-walled artery model: effects of spatial variations in wall constituents. Biomech Model Mechanobiol 7:245–262. https://doi.org/10.1007/s10237-007-0101-2

79. Tsamis A, Stergiopulos N, Rachev A (2009) A Structure-Based Model of Arterial Remodeling in Response to Sustained Hypertension. Journal of Biomechanical Engineering 131:101004. https://doi.org/10.1115/1.3192142

80. Cyron CJ, Humphrey JD (2014) Vascular homeostasis and the concept of mechanobiological stability. International Journal of Engineering Science 85:203–223. https://doi.org/10.1016/j.ijengsci.2014.08.003

81. Latorre M, Bersi MR, Humphrey JD (2019) Computational modeling predicts immuno-mechanical mechanisms of maladaptive aortic remodeling in hypertension. International Journal of Engineering Science 141:35–46. https://doi.org/10.1016/j.ijengsci.2019.05.014

82. Mahutga RR, Barocas VH (2020) Investigation of Pathophysiological Aspects of Aortic Growth, Remodeling, and Failure Using a Discrete-Fiber Microstructural Model. Journal of Biomechanical Engineering 142:111007. https://doi.org/10.1115/1.4048031

83. Ghorbannia A, Maadooliat M, Woods RK, et al (2023) Aortic Remodeling Kinetics in Response to Coarctation-Induced Mechanical Perturbations. Biomedicines 11:1817. https://doi.org/10.3390/biomedicines11071817

84. Humphrey JD (2021) Constrained Mixture Models of Soft Tissue Growth and Remodeling – Twenty Years After. J Elast 145:49–75. https://doi.org/10.1007/s10659-020-09809-1

85. Perlini S, Palladini G, Ferrero I, et al (2005) Sympathectomy or Doxazosin, But Not Propranolol, Blunt Myocardial Interstitial Fibrosis in Pressure-Overload Hypertrophy. Hypertension 46:1213–1218. https://doi.org/10.1161/01.HYP.0000185689.65045.4c

86. Zile MR, Baicu CF, S. Ikonomidis J, et al (2015) Myocardial Stiffness in Patients With Heart Failure and a Preserved Ejection Fraction: Contributions of Collagen and Titin. Circulation 131:1247–1259. https://doi.org/10.1161/CIRCULATIONAHA.114.013215

87. Pieper T, Latus H, Schranz D, et al (2019) Aortic elasticity after aortic coarctation relief: comparison of surgical and interventional therapy by cardiovascular magnetic resonance imaging. BMC Cardiovasc Disord 19:286. https://doi.org/10.1186/s12872-019-01270-w

88. West GB, Brown JH, Enquist BJ (1997) A General Model for the Origin of Allometric Scaling Laws in Biology. Science 276:122–126. https://doi.org/10.1126/science.276.5309.122

89. Seymour RS, Blaylock AJ (2000) The Principle of Laplace and Scaling of Ventricular Wall Stress and Blood Pressure in Mammals and Birds. Physiological and Biochemical Zoology 73:389–405. https://doi.org/10.1086/317741

Chapter 4: A Computational Model of Ventricular Dimensions and Hemodynamics in Growing Infants

Abstract

Previous computer models have successfully predicted cardiac growth and remodeling in adults with pathologies. However, applying these models to infants is complicated by the fact that they also undergo normal, somatic cardiac growth and remodeling. Therefore, we designed a computational model to predict ventricular dimensions and hemodynamics in healthy, growing infants by modifying an adult canine left ventricular growth model. The heart chambers were modeled as time-varying elastances coupled to a circuit model of the circulation. Circulation parameters were allometrically scaled and adjusted for maturation to simulate birth through 3 yrs of age. Ventricular growth was driven by perturbations in myocyte strain. The model successfully matched clinical measurements of pressures, ventricular and atrial volumes, and ventricular thicknesses within two standard deviations of multiple infant studies. To test the model, we input 10th and 90th percentile infant weights. Predicted volumes and thicknesses decreased and increased within normal ranges and pressures were unchanged. When we simulated coarctation of the aorta, systemic blood pressure, left ventricular thickness, and left ventricular volume all increased, following trends in clinical data. Our model enables a greater understanding of somatic and pathological growth in infants with congenital heart defects. Its flexibility and

computational efficiency when compared to models employing more complex geometries allow for rapid analysis of pathological mechanisms affecting cardiac growth and hemodynamics.

1. Introduction

Congenital heart defects (CHDs), failures of the heart to develop properly in utero, are the most common birth defect, occurring in approximately 1 in 100 births [1]. A quarter of those infants will have a critical CHD, requiring surgery in their first year of life [2]. Fortunately, advances in care over the past 50 years have increased survival rates enormously; over 85% of children born with CHDs today can expect to live into adulthood [3]. As children live and grow with CHDs, their cardiovascular system also grows. In adults, cardiac hypertrophy is largely a function of pathology, occurring in response to hemodynamic overload from conditions such as valvular disease, hypertension, and myocardial infarction. In children, however, hypertrophy is a normal part of development. Complicating matters further, children with CHDs experience this somatic growth alongside pathologic growth, making it difficult to estimate how disease progression or intervention will change hemodynamics or heart size. Separating these growth mechanisms in vivo is extremely challenging, limiting our understanding of their interplay and our ability to predict changes in cardiac dimensions in children with CHDs. Computational models are useful tools for uncoupling processes that are inextricably linked in the body so they can be modified and studied in isolation. For example, Burkhoff and Tyberg investigated proposed sources of the rise in pulmonary venous pressure after ventricular dysfunction using a simple zero-dimensional model [4]. Other cardiovascular

models have evaluated hemodynamically induced stresses on aneurism development and rupture, oxygen transport, and atherosclerosis [5–8]. Computer models have become powerful aids in surgical planning for CHD patients [9–11]. Image-based computational fluid dynamics simulations have been produced for many different congenital defects including tetralogy of Fallot [12], Kawasaki disease [13], and coarctation of the aorta (CoA) [14]. The application of these models for "virtual surgery" in patients with single ventricle physiology has been the most active area of research, including in silico assessment of different surgical approaches and patient-specific modeling [15,16]. One of the most exciting new areas for computational modeling is the simulation of growth and remodeling. These models predict changes in the mass and structure of cardiovascular tissues over time, usually in response to acute alterations in hemodynamics. They utilize growth laws that relate stress and strain changes in the myocardium due to perturbances in hemodynamics with cardiomyocyte lengthening and thickening. In our recent review [17], we evaluated the ability of a number of published growth laws to reproduce the characteristic growth patterns resulting from strains typical of ventricular pressure and volume overload in adults. By altering hemodynamic inputs consistent with pathology, the models can predict the resultant pathologic growth and remodeling [18,19]. One such model, previously developed by our group [17,20], predicted the time-course of ventricular hypertrophy in adult canines under volume and pressure overload as well as myocardial infarction. In this study, we adapted this model for human infants and successfully predicted changes in ventricular thickness and volume for healthy infants from birth to 3 yrs of age. To demonstrate the model's capacity for pathologic growth in infants, we

simulated CoA, a defect which generally results in left ventricular (LV) pressure overload. The CoA simulation led to expected increases in LV thickness, end-diastolic volume, and systemic blood pressure.

2. Methods

A previously published computational model [17] capable of predicting LV growth in adult canines in response to hemodynamic overload was modified for human infants. For more flexibility in future simulations of pathology, additional compartments were created and right ventricular (RV) growth was implemented into the simulation. As explained in detail below, a strain-based growth law determined ventricular growth in both the circumferential and radial directions. Changes in ventricular geometry throughout growth were computed using analytic expressions relating strain and volume as well as stress and pressure in a thin-walled sphere. Allometric scaling was used to adjust input parameters from an adult canine model [17,20] and an adult human model [21] according to mean infant body mass. A maturation approach was used to adjust specific parameters in order to capture reported hemodynamic trends associated with birth. To test the predictive capacity of the model, infant weights at the 10th and 90th percentiles were inputted. Lastly, to evaluate the model's capacity to predict pathologic hypertrophy, CoA was simulated.

2.1. Expanding the Model to Simulate Infant Physiology

The original adult canine model [17,20] was composed of six compartments: LV, RV, systemic veins (SV), systemic arteries (SA), pulmonary veins (PV), and pulmonary arteries (PA). Briefly, the ventricles were simulated using time-varying elastances, systemic and

pulmonary arterial behavior were simulated by three-element Windkessels, distal vessels were represented by capacitors in parallel with resistors, and valves were represented by pressure-sensitive diodes. To better replicate infant physiology, particularly for cases of congenital heart defects, an additional six compartments were added, for a total of 12 compartments (Fig. 1).

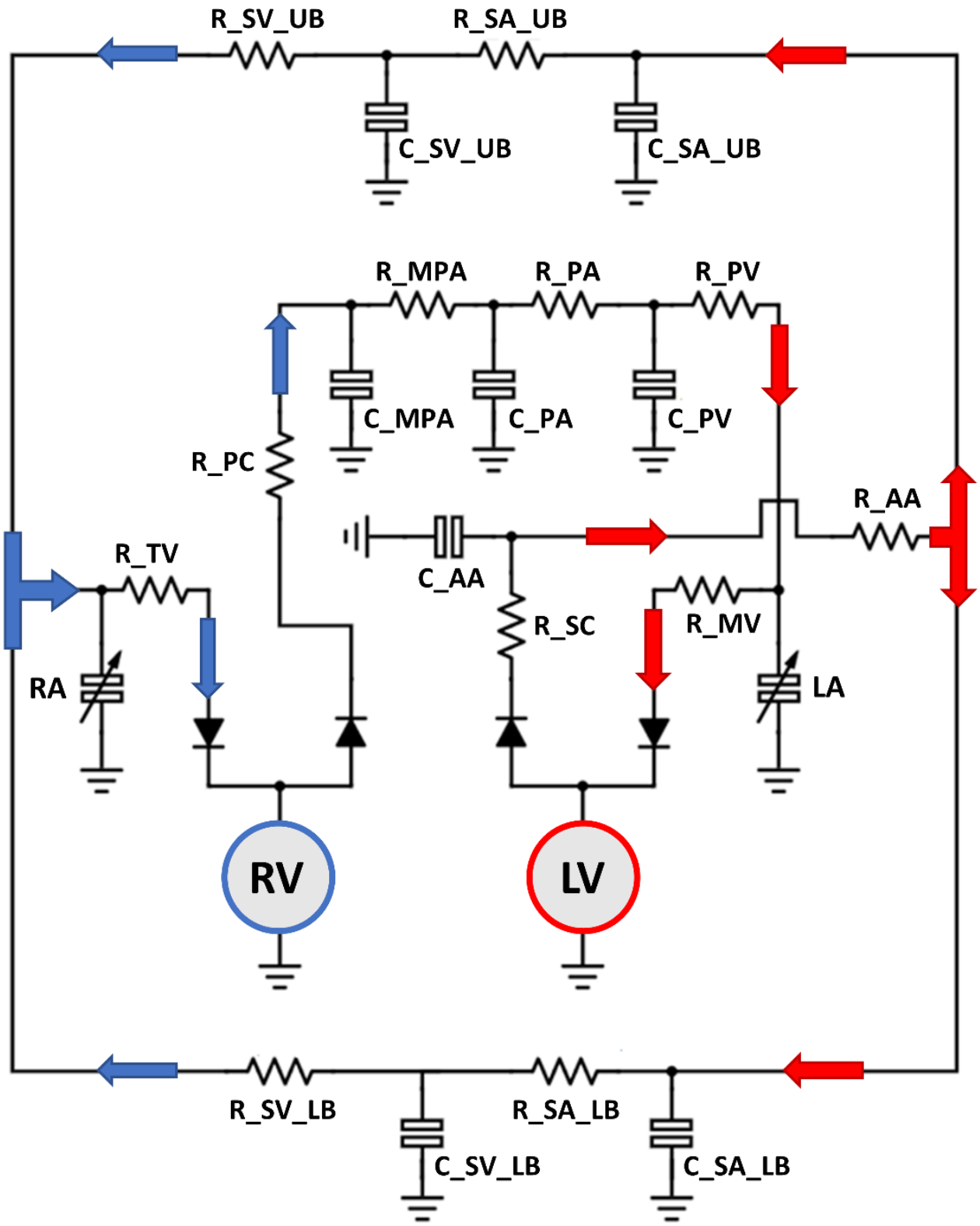
R_SV_UB
R_SA_UB
C_SV_UB
C_SA_UB
R_MPA
R_PA
R_PV
C_MPA
C_PA
C_PV
R_PC
R_AA
C_AA
R_TV
R_SC
R_MV
RA
LA
RV
LV
R_SV_LB
R_SA_LB
C_SV_LB
C_SA_LB

Figure 1: Schematic of the circuit model used to simulate the pressure-volume behavior of the cardiovascular system. The left and right atria (LA and RA) were simulated using time-varying elastances. The left and right ventricles (LV and RV) were simulated using time-varying elastances, and growth relied on strains computed assuming a thin-walled spherical geometry. The ascending aorta and main pulmonary artery behavior were simulated by three-element Windkessels consisting of a characteristic resistance (R_SC and R_PC), a capacitance (C_AA and C_MPA), and an arterial resistance (R_AA and R_MPA). Distal vessels were represented by capacitors in parallel with resistors for the pulmonary arteries (C_PA and R_PA), pulmonary veins (C_PV and R_PV), lower body systemic arteries (C_SA_LB and R_SA_LB), and upper body systemic arteries (C_SA_UB and R_SA_UB), lower body systemic veins (C_SV_LB and R_SV_LB), and upper body systemic veins (C_SV_UB and R_SV_UB). Pressure sensitive diodes (TV, PV, MV, and AV) represented the tricuspid, pulmonary, mitral, and aortic valves, respectively. Arrows indicate the direction of blood flow and blood oxygenation levels.

First, left and right atria were added using identical time-varying elastances, along with respective resistances for the mitral and tricuspid valves [21]. Parameter values for this eight-compartment model matching the hemodynamics of a healthy adult human are detailed in Table S1. To model the main pulmonary artery (MPA), the pulmonary arterial pool was split by adding an additional series resistor and parallel capacitor. The total pulmonary arterial compliance and resistance were

$$C_{total,PA} = C_{MPA} + C_{PA} \text{ and } R_{total,PA} = R_{MPA} + R_{PA}\,, \quad (5)$$

respectively. C_{MPA} and R_{MPA} indicate the capacitance and resistance of the main pulmonary artery, respectively. C_{PA} and R_{PA} indicate the capacitance and resistance of the remaining distal pulmonary arteries, respectively. The value of C_{MPA}/C_{PA} was set to 8 such that the mean pressure and pulse pressure in the main pulmonary artery was ≈1.5 mmHg and 2.5 mmHg higher than the distal vessels, respectively [22,23]. The ratio of main pulmonary artery resistance to that of the distal arteries,

$$R_{MPA}/R_{PA} = (C_{MPA}/C_{PA})^{(-3/4)}\,, \quad (6)$$

was determined using the dependence of vascular resistances and capacitances on vessel dimensions ($R \approx lr^{-4}$ and $C \approx lr^{3}$, where r and l are the radius and length of the vessel, respectively) [24,25]. The systemic arterial pool was split in a similar manner to model the ascending aorta (AA) and the distal systemic arteries. However, to simulate the upper and lower body separately the distal arteries were further divided. The new upper and lower

body systemic arterial resistors were placed in parallel and the capacitors were also in parallel. Thus, the total systemic arterial compliance and resistance were

$$C_{total,SA} = C_{AA} + C_{SA,UB} + C_{SA,LB} \text{ and} \quad (7)$$

$$R_{total,SA} = R_{AA} + \frac{R_{SA,UB}R_{SA,LB}}{R_{SA,UB}+R_{SA,LB}}\ , \quad (8)$$

respectively. C_{AA} and R_{AA} indicate the capacitance and resistance of the ascending aorta, $C_{SA,UB}$ and $R_{SA,UB}$ indicate the capacitance and resistance of the systemic arteries in the upper body, and $C_{SA,LB}$ and $R_{SA,LB}$ indicate the capacitance and resistance of the systemic arteries in the lower body. The value of $C_{AA}/(C_{SA,UB} + C_{SA,LB})$ was set to 16 such that the mean and pulse pressure in the ascending aorta were ≈4.4 mmHg and 2.7 mmHg higher than the distal vessels, respectively [26]. Again, using the dependence of vascular resistances and capacitances on vessel dimensions, the ratio of the ascending aortic resistance to that of the distal arteries was

$$R_{AA}\left(\frac{R_{SA,UB}+R_{SA,LB}}{R_{SA,UB}R_{SA,LB}}\right) = \left(\frac{C_{AA}}{C_{SA,UB}+C_{SA,LB}}\right)^{(-3/4)}. \quad (9)$$

The value of $C_{SA,LB}/C_{SA,UB}$ and $R_{SA,LB}/R_{SA,UB}$ were set to 1 based on the ratio of flow in the superior vena cava to the main pulmonary artery reported for infants by Salim et al [27].

Finally, the upper and lower systemic veins were divided in the same way as the upper and lower systemic arteries. The total systemic venous compliance and resistance were

$$C_{total,SV} = C_{SV,UB} + C_{SV,LB} \text{ and} \quad (6)$$

$$R_{total,SV} = \frac{R_{SV,UB}R_{SV,LB}}{R_{SV,UB}+R_{SV,LB}}, \quad (7)$$

respectively. $C_{SV,UB}$ and $R_{SV,UB}$ and $C_{SV,LB}$ and $R_{SV,LB}$ indicate the capacitances and resistances of the systemic veins in the upper and lower body, respectively. As in the arteries, the values of $C_{SV,LB}/C_{SV,UB}$ and $R_{SV,LB}/R_{SV,UB}$ were set to 1.

2.2. Scaling Model Parameters

To adapt the model to human infants, weight-based allometric scaling was employed for ventricular pressure-volume and timing parameters, capacitances, and the majority of resistances such that

$$Y_i = Y_0(M_i/M_0)^b, \quad (8)$$

where *Y* is the parameter under consideration, *M* is body weight, and *b* is a scaling factor [28]. The subscripts *i* and *0* indicate current and reference values, respectively. Reference parameters (Y_0 and M_0) were set to those of a healthy 70 kg adult human (Table S1). M_i was a vector of infant weights for ages 0 to 3 years, linearly interpolated from the Centers for Disease Control and Prevention's weight-for-age charts for 50th percentile male and female infants [29]. Based on theoretical and empirical measurements, resistances were scaled by b = -3/4 and capacitances were scaled linearly [30,28]. Other atrial and ventricular parameters were scaled using unit analysis. The scaling factor for the timing parameter indicating the percentage of the cardiac cycle spent in systole, b = -0.07, was computed

from reported percentages in rats [31] and dogs [20]. See Table S2 for a full list of scaling factors.

2.3. Customizing Model Parameters for Infant Development

Some parameters were not scaled throughout the entire age range of 0 to 3 years. While in utero, pulmonary vascular resistance (PVR) is high due to the fetus's lack of respiration. It plummets sharply after birth with ventilation, when the lungs open and alveolar PO2 increases dramatically [33]. Systemic vascular resistance (SVR) follows an opposite trend: the removal of the placenta and umbilical cord eliminates a low-resistance source of blood flow, thus SVR rises modestly post-birth [33]. To replicate these unique circumstances associated with birth, scaling was combined with an age-based function, sometimes called a "maturation approach" in pharmacology [34,35]. Therefore, at age in days, t,

$$PVR(t) = cQ(t) + PVR_i\big(1 - Q(t)\big), \text{ where} \tag{9}$$

$$Q(t) = \frac{1}{1 + \left(\frac{t}{c_1}\right)^{c_2}} . \tag{10}$$

PVR_i indicates the scaled value of pulmonary vascular resistance computed from Equation 8 based on the infant's weight at age t. Their associated capacitance,

$$PVC(t) = PVC_0 \left(\frac{PVR(t)}{PVR_0}\right)^{-4/3} , \tag{11}$$

was computed according to the dependencies of vascular resistances and compliances on vessel dimensions [24,25]. *SVR(t)* and its associated capacitance, *SVC(t)* were determined in the same manner. Maturation parameters c, c_1, and c_2 were fit using the built-in MATLAB function *fminsearch* to minimize the sum squared error between model outputs for mean pulmonary artery pressure (MPAP) and mean arterial pressure (MAP) and the mean values of reported measurements from ages 0 to 120 days [43-45]. Figure 2 compares resistances determined using the maturation function to those from allometric scaling alone, along with their resultant trajectories of MAP and MPAP. In the model, both MAP and MPAP were computed as the sum of one-third of the systolic pressure and two-thirds of the diastolic pressure, i.e., MAP = (SBP + 2*DBP)/3. For PVR the fitted values of c, c_1 and c_2 were 3.7 mmHg*s/mL, 1.3 days and 1.6, respectively, and for SVR they were 5.0 mmHg*s/mL, 29.9 days, and 4.1, respectively.

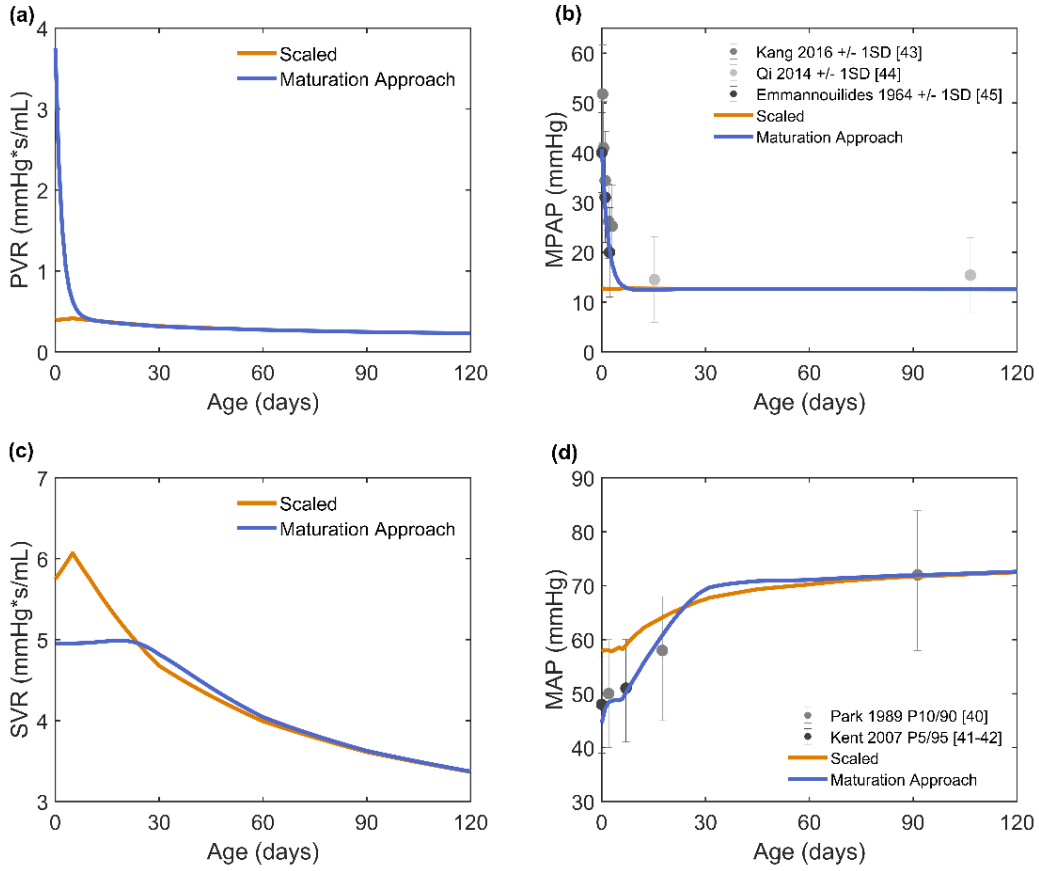

Figure 2: Scaled pulmonary and systemic vascular resistances and resistances produced via a maturation approach (A and C, respectively) as well as their resultant mean pulmonary and systemic pressures (B and D, respectively) for a median-weight infant in the four months of life, compared to measured data [40-45]. Error bars on data indicate 10th and 90th percentiles [40], 5th and 95th percentiles [41,42], or one standard deviation [43-45]. Measurements from Qi et al. were from the sea-level cohort only. PVR, pulmonary vascular resistance; MPAP, mean pulmonary arterial pressure; SVR, systemic vascular resistance; MAP, mean arterial pressure.

Heart rate was originally computed via weight-based allometric scaling (using b = -1/4 and adult reference heart rate = 70 beats/min). Though the weight-based scaled heart rate values were within the range reported for infants between 0-36 months, they peaked slightly early (at approximately 1 week of age), whereas heart rates reported by Fleming et al. [32] peaked at approximately 4 weeks (Figure S1A). Therefore, to capture the observed trend, the measured 50th percentile curve from Fleming et al. was inputted directly into the model.

With the exception of heart rate, PVR, and SVR, all model input parameters were determined by infant weight. The ability of the model to produce dimensions, namely LV and RV end-diastolic and end-systolic volumes and thicknesses as well as left atrial volume, within reported bounds at ages 0 to 3 years was evaluated for model validation. Infant body masses at the 10th and 90th percentiles were also considered for further model validation. In these cases, PVR and SVR were computed using Eqns 9 and 10, and the constants (c, c_1, and c_2) were kept at the values fitted based on the median weight. Heart rate was adjusted upward or downward according to weight (Figure S1B). Lastly, all other model parameters were scaled using the smaller or larger weight trajectories (Equation 8).

2.4. Simulating Somatic Growth

A previously published computational model that reproduced pathologic ventricular growth in response to pressure overload, volume overload, and myocardial infarction in canines was modified to reproduce both pathologic and somatic ventricular growth in infants [17,20]. A flowchart describing the model is shown in Figure 3. As discussed in the

previous sections, a combination of allometric scaling and a maturation approach were utilized to compute all model circulatory parameters for ages 0 to 3 years.

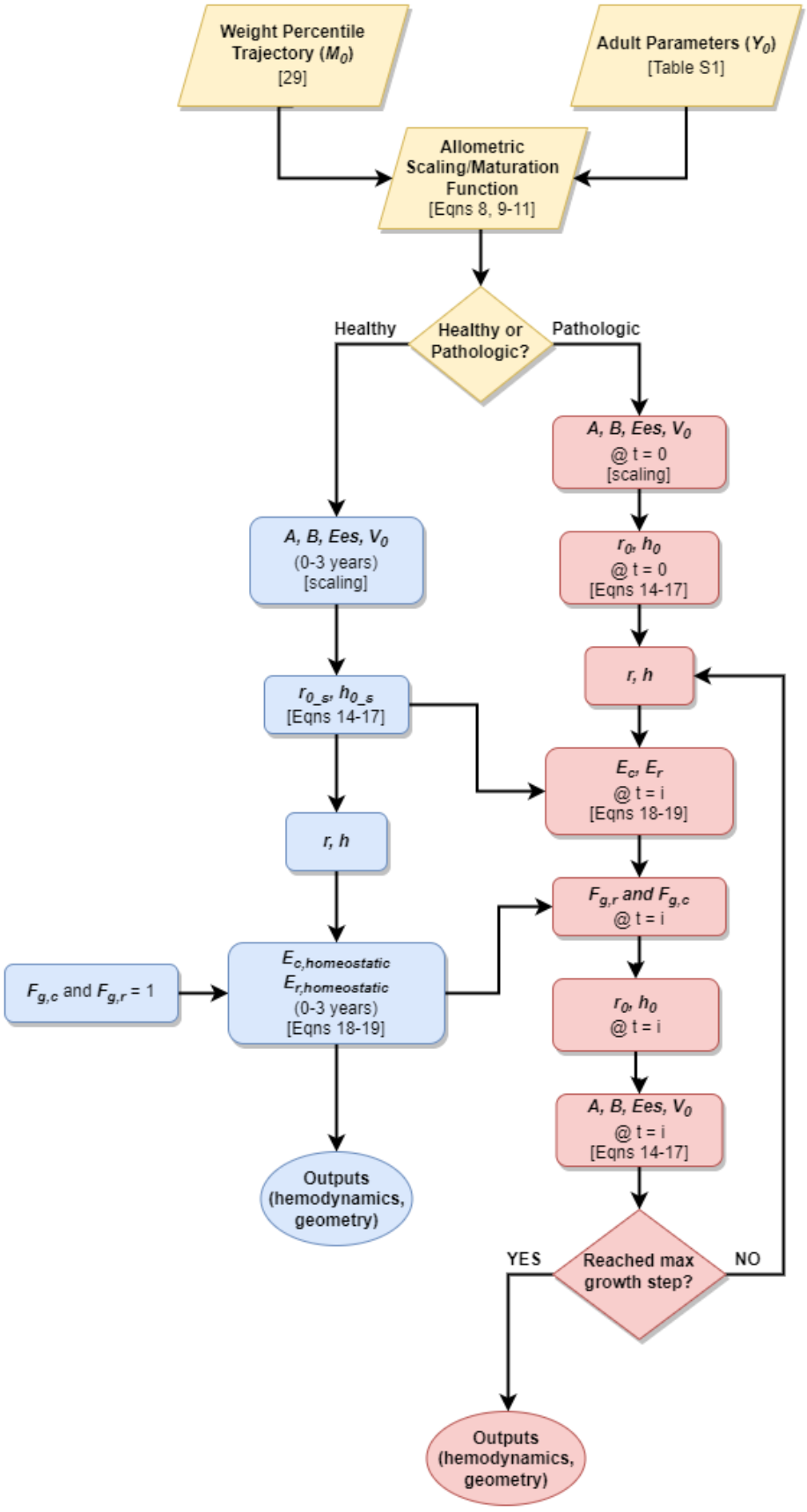
Weight Percentile Trajectory (M_0) [29]
Adult Parameters (Y_0) [Table S1]
Allometric Scaling/Maturation Function [Eqns 8, 9-11]
Healthy or Pathologic?
Healthy
Pathologic
A, B, Ees, V_0 @ t = 0 [scaling]
A, B, Ees, V_0 (0-3 years) [scaling]
r_0, h_0 @ t = 0 [Eqns 14-17]
r, h
r_{0_s}, h_{0_s} [Eqns 14-17]
E_c, E_r @ t = i [Eqns 18-19]
r, h
$F_{g,r}$ and $F_{g,c}$ @ t = i
$F_{g,c}$ and $F_{g,r}$ = 1
$E_{c,homeostatic}$ $E_{r,homeostatic}$ (0-3 years) [Eqns 18-19]
r_0, h_0 @ t = i
A, B, Ees, V_0 @ t = i [Eqns 14-17]
Outputs (hemodynamics, geometry)
YES
Reached max growth step?
NO
Outputs (hemodynamics, geometry)

Figure 3: Flowchart of model development. Input parameters were first determined using either allometric scaling or maturation functions, including all resistances and capacitances, stressed blood volume, and ventricular parameters A, B, Ees, and V0. In the healthy simulation, the full time course of A, B, Ees, and V0 was generated. In the pathologic simulation, only the first day (pre-growth) was generated. From there, the unloaded ventricular radius and thickness (r0_s and h0_s for the healthy simulation, r0 and h0 for the pathologic simulation) were determined and used to find the loaded radius and thickness (r and h) throughout the cardiac cycle. Strains were then calculated and used as homeostatic setpoints (in the healthy simulation) or to determine growth stretch tensor Fg (in the pathologic simulation). In the pathologic simulation, Fg was used to determine the new unloaded radius and thickness, which in turn gave new values for A, B, Ees, and V0. The cycle repeated until the maximum growth step was reached at the three year time point.

Ventricular end-diastolic and end-systolic pressure-volume relationships were defined by

$$P_{ED} = B\mathrm{e}^{\mathrm{A}(V_{ED}-V_0)} - B \quad (12)$$

$$P_{ES} = Ees(V_{ES} - V_0) \quad (13)$$

respectively, where Ees was the end-systolic elastance of the ventricle, V_0 was the unloaded volume of the ventricle, and A and B were coefficients describing the exponential shape of the end-diastolic pressure-volume relationship. For healthy infants at three different birth weights (10th, 50th, and 90th percentiles), allometric scaling was utilized to determine values of V_0, A, B, and Ees (see section 2.2 and Table S2) throughout the entire three year time-course. To account for changes in geometry with growth, analytic expressions based on the relationships between strain and volume and stress and pressure in a thin-walled sphere were developed [17,20] that relate material parameters (a, b, and e) to compartmental parameters (A, B, and Ees):

$$a = A\frac{4\pi}{3}\left(F_{g,c}r_{0_s}\right)^3 \quad (14)$$

$$b = \frac{B}{2}\frac{F_{g,c}r_{0_s}}{F_{g,r}h_{0_s}} \quad (15)$$

$$e = \frac{2\pi}{3}Ees\frac{\left(F_{g,c}r_{0_s}\right)^4}{F_{g,r}h_{0_s}} \quad (16)$$

r_{0_s} and h_{0_s} indicate the ventricle's homeostatic unloaded radius and thickness, respectively. The growth stretches, $F_{g,c}$ and $F_{g,r}$ (discussed in Section 2.5 in more detail),

indicate pathologic changes in the unloaded circumferential and radial dimensions of the ventricle, respectively. They were set to 1 at all times for the healthy simulations. In the previous adult canine simulations [17,20], r_{0s} and h_{0s} were constant, as the unloaded homeostatic ventricular dimensions are unchanged with time in healthy adults. To simulate growth in healthy infants, these parameters must change with age. r_{0s} was computed for each weight trajectory for each age in days as

$$r_{0\_s} = \frac{1}{F_{g,c}}\left(\frac{3}{4\pi}V_0\right)^{1/3} \tag{17}$$

Then, a single value of a (1.56 for the 50th percentile weight trajectory) was determined from Equation 14 for all ages. This was well within the range of a values from our previous studies [17, 20]. b was set to 0.14, the average value from our previous studies [17,20], and Equation 15 was rearranged to compute h_{0s} for each age:

$$h_{0_s} = \frac{B}{2}\frac{F_{g,c}r_{0_s}}{F_{g,r}b} \tag{18}$$

Then, from Equation 16 a single value for e (240 mmHg for the 50th percentile weight trajectory) was computed. Though compartmental parameters change during growth, myocardial properties are particularly difficult to measure and there is no consensus on changes during normal somatic development, therefore the material parameters were kept constant throughout the three year period.

For each growth step (corresponding to one day), the circulation portion of the model was run until it reached steady-state, defined as compartmental volumes being within 0.0001 mL of each other at the beginning and end of the cardiac cycle. The loaded LV and RV radii and thicknesses, r and h, were calculated throughout the cardiac cycle from the ventricular volumes.

In the previous adult canine model [17,20], pathologic growth in the circumferential and radial directions was driven by changes in the maximum circumferential and radial strain from homeostasis, respectively. However, in a growing infant, the ventricles' homeostatic unloaded ventricular dimensions, and thus their homeostatic strains, change with age. Circumferential strain,

$$E_c = 0.5\left(\frac{r}{r_{0_s}F_{g,c}}\right)^2 - 0.5 \tag{19}$$

and radial strain,

$$E_r = 0.5\left(\frac{h}{h_{0_s}F_{g,r}}\right)^2 - 0.5 \tag{20}$$

were computed for each ventricle from the loaded radii and thicknesses. Then, other model outputs, including ventricular volumes and thicknesses as well as atrial volumes and arterial pressures were computed and compared to clinical measurements.

2.5. Simulating Pathologic Growth: Coarctation of the Aorta

To explore the capacity of the model to produce simultaneous somatic and pathologic ventricular growth, CoA was simulated. This congenital heart defect presents as a narrowing of the descending aorta distal to the left subclavian artery, resulting in increased systolic blood pressure and LV hypertrophy [36,37]. In general, systemic vascular resistance drops as infants age and their vessels become larger. To simulate unrepaired CoA, the resistance of the lower body arteries was gradually increased from its peak somatic value at 23 days to a maximum of 25% over baseline (Figure 4A). The compliance of the lower body arteries was determined from the resistance via their dependence on vessel dimensions [24,25]. The gradual increase in resistance over the first year of life was simulated to replicate the time-course in the presentation of coarctation observed by Eerola et al [36] and Vogt et al [37], wherein systemic blood pressures in CoA patients are similar to control soon after birth before becoming significantly larger as the child grows. In previous simulations of pressure overload [38,17], it was necessary to increase stressed blood volume to capture increases in ventricular filling pressure. Therefore, stressed blood volume was increased proportionally with lower body artery resistance (Figure 4B).

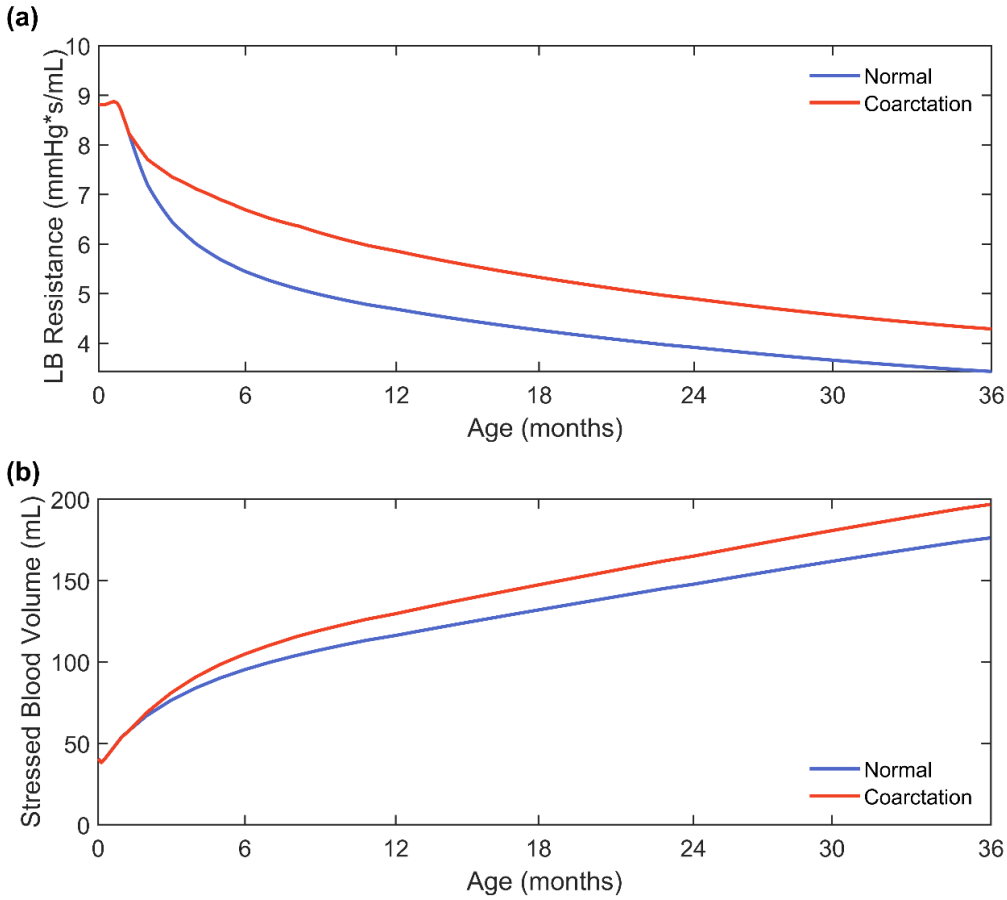

Figure 4: Resistance for the lower body arterial compartment (A) and stressed blood volume (B) for the healthy and coarctation simulations for a median-weight infant in the first three years of life. Resistance was gradually increased from its peak somatic value at 23 days to a maximum of 25% over baseline and stressed blood volume was increased 14% over baseline.

The pathologic growth mechanism follows the same path as somatic growth, with a few exceptions (see Figure 3). Simulating pathologic growth relied on iteration. Rather than generating the entire three year time-course of ventricular parameters V_0, A, B, and Ees from allometric scaling, only the initial day 0 set was determined via scaling. No pathologic growth was assumed in utero, therefore the initial values of r_0 and h_0 were equivalent to their somatic, healthy counterparts, r_{0_s} and h_{0_s}.

Next, the circulation portion of the model was run with the CoA parameters, and r and h were calculated throughout the cardiac cycle from the ventricular volumes. As lower body arterial resistance and stressed blood volume began to differ from their somatic values, so did the loaded radii and thicknesses, r and h, and therefore so did the resulting strain values from Eqns. 19-20.

Hill-type functions, described in detail in [17], determined the rate of pathologic circumferential and radial ventricular growth ($\Delta F_{g,c}$ and $\Delta F_{g,r}$, respectively) based on these deviations in circumferential and radial strains from their somatic values. The pathologic growth rate was governed by three parameters: the first parameter limited the maximum growth rate per day, the second dictated the slope of the sigmoid or the change in rate with strain difference, and the third defined a quiescent zone. These six parameters (three for the circumferential direction and three for the radial direction) were unchanged from the previous model of myocardial growth in adult canines [17,20]. Inputting the difference between the homeostatic strain and the pathologic strain into the Hill-type functions produced new values of $F_{g,c}$ and $F_{g,r}$, the pathologic growth amounts in the circumferential

and radial directions of the ventricle, respectively. At each time step, $F_{g,c}$ and $F_{g,r}$ were then multiplied by the previous step's values of r_0 and h_0, respectively, to give the current r_0 and h_0 (see Figure 5 for a comparison of somatic and pathologic unloaded radii and thicknesses). New values of the ventricular compartment parameters were then computed by rearranging Eqns. 14, 15, 16, and 17 and solving for A, B, Ees and V_0, respectively, for the current time step. Pathology was assumed to only alter ventricular mass, therefore material parameters a, b, and e were held constant throughout the simulation at their somatic values. The circulation portion of the model was run until it reached steady-state, and the loaded LV and RV radii and thicknesses, r and h, were calculated throughout the cardiac cycle from the ventricular volumes. Growth proceeded iteratively until the maximum growth step of 1095 days was reached, at which point all hemodynamic and geometric outputs were plotted. The ability of the model to produce dimensions, namely LV end-diastolic volume and thickness, was evaluated for model validation.

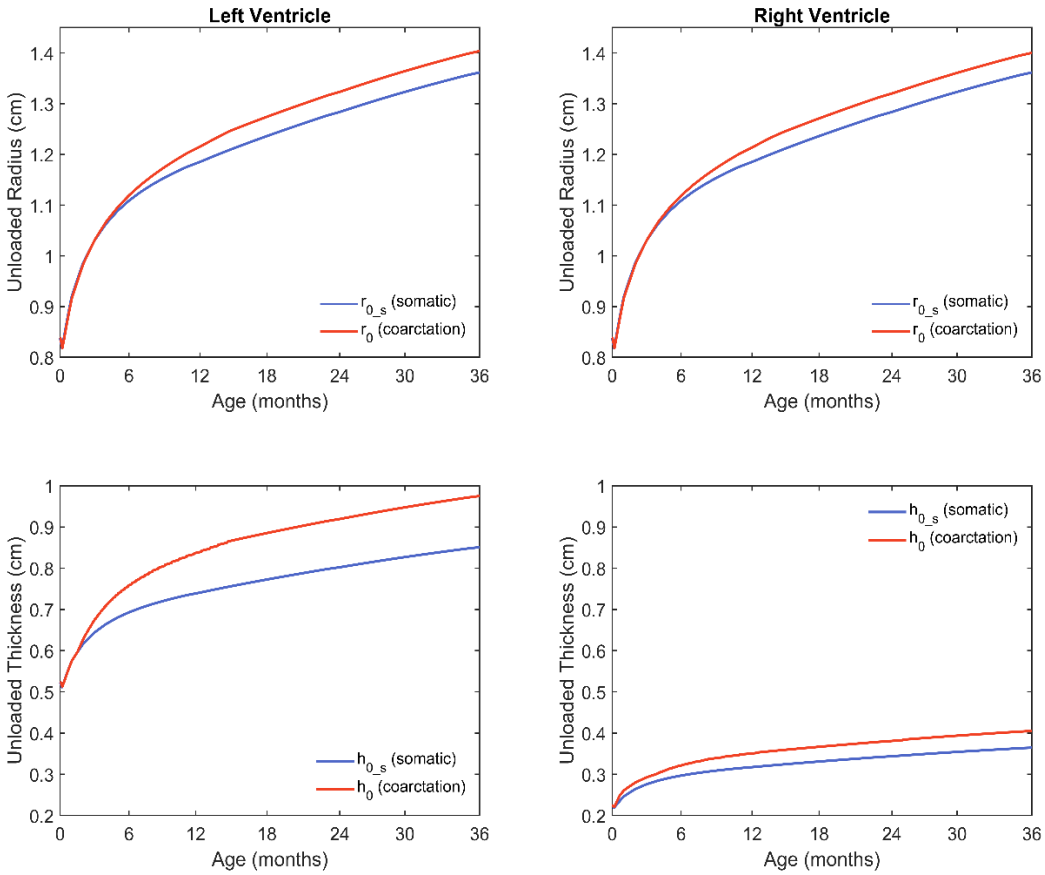

Figure 5: Top: Comparison of unloaded radii for somatic and CoA cases (r0_s and r0, respectively). Bottom: Comparison of unloaded thicknesses for somatic and CoA cases (h0_s and h0, respectively). Left-hand panels indicate the left ventricle, right-hand indicates the right ventricle. Unloaded radii and thicknesses were used to find loaded radii and thicknesses r and h, which were then used to compute strain at each time step.

3. RESULTS

The objective of this study was to modify a previously published computational model of left ventricular growth in adult canines for human infants. Homeostatic strain setpoints were fitted to capture somatic growth over time in median-weight infants. To test the maturation approach for parameter scaling, homeostatic strain setpoints were also fitted for infants in the 10th and 90th percentile of birth weight. Then, the ability of the model to predict pathologic growth in combination with somatic growth was tested by simulating coarctation of the aorta. Model volume and thickness outputs were validated against reported measurements for somatic and coarctation simulations.

3.1. Simulating Somatic Growth for the Median Infant

Three years of growth were simulated for an infant with a median weight trajectory. This trajectory included a typical drop and regain of weight shortly after birth [39], resulting in a similar trend in model outputs. As shown in Figure 6A, simulated MAP closely matched reported measurements. Model MAP fell between the 10th and 90th percentiles [40], 5th and 95th percentiles [41,42], and within one standard deviation [43-45] of reported means throughout the entire three-year period. In these studies, MAP was measured using a blood pressure cuff, therefore comparable model pressures were from the upper body arteries compartment. Likewise, Figure 6B shows the simulated MPAP was well within one standard deviation of the reported values throughout the entire three-year period. MPAP was measured in the main pulmonary artery by Doppler echocardiography [43,44] and cardiac catheterization [45], thus model pressures shown were from the main pulmonary artery

compartment. Pulmonary and systemic systolic and diastolic pressures also matched reported trajectories (Figure S2).

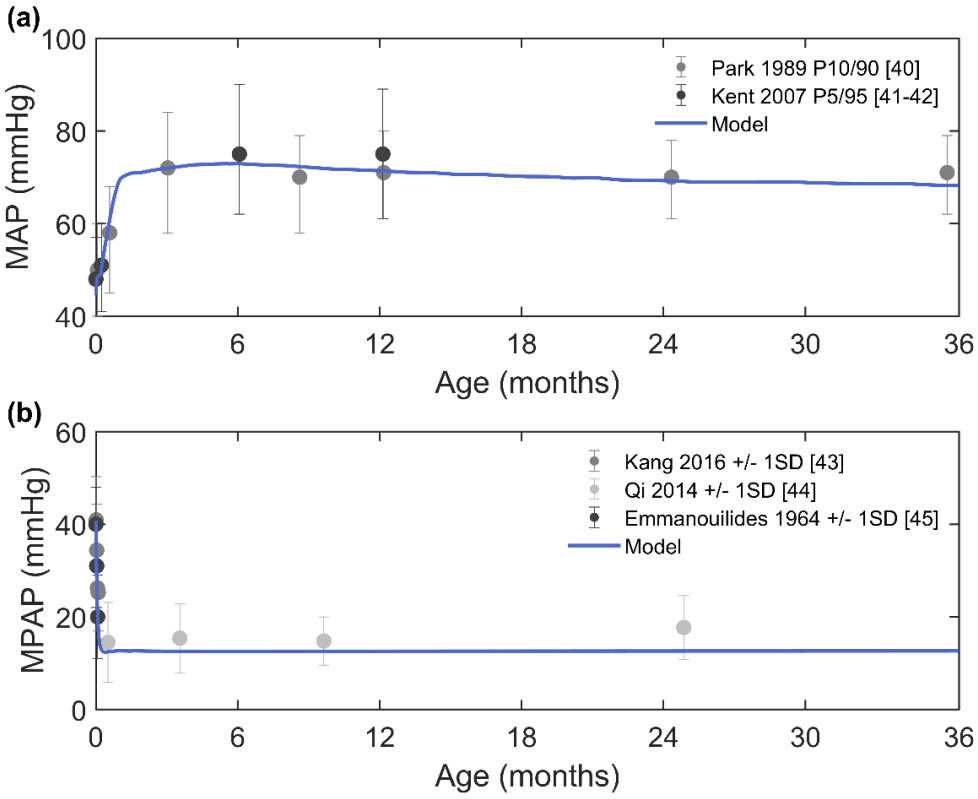

Figure 6: Simulated systemic (A) and pulmonary (B) mean arterial pressures throughout the first three years of life for a median weight infant compared to reported measurements [40-45]. In the studies referenced, MAP was measured using a blood pressure cuff, therefore comparable model pressures were from the upper body arteries compartment. MPAP was measured in the main pulmonary artery by Doppler echocardiography [43,44] and cardiac catheterization [45], thus model pressures shown were from the main pulmonary artery compartment. Measurements from Qi et al. were from the sea-level cohort only. Error bars on data indicate 10th and 90th percentiles [40], 5th and 95th percentiles [41,42], or one standard deviation [43-45]. MAP, mean arterial pressure; MPAP, mean pulmonary arterial pressure.

Simulated chamber volumes agreed well with reported echocardiographic measurements. Maximum left atrial volume followed reported trends [46,47] and was well within the 10th and 90th percentiles reported by Linden et al. [48] [Figure S6]. Model LV end-diastolic and end-systolic volumes (Figure 7A and B) were within two standard deviations of reported measurements. Simulated RV end-diastolic volumes were also within two standard deviations [50] and 10th and 90th percentiles [51] of reported measurements (Figure 7C) and simulated RV end-systolic volumes fell between measurements reported by Thilenius and Arcilla [52], Buechel et al. [53], and Lange et al. [54] (Figure 7D).

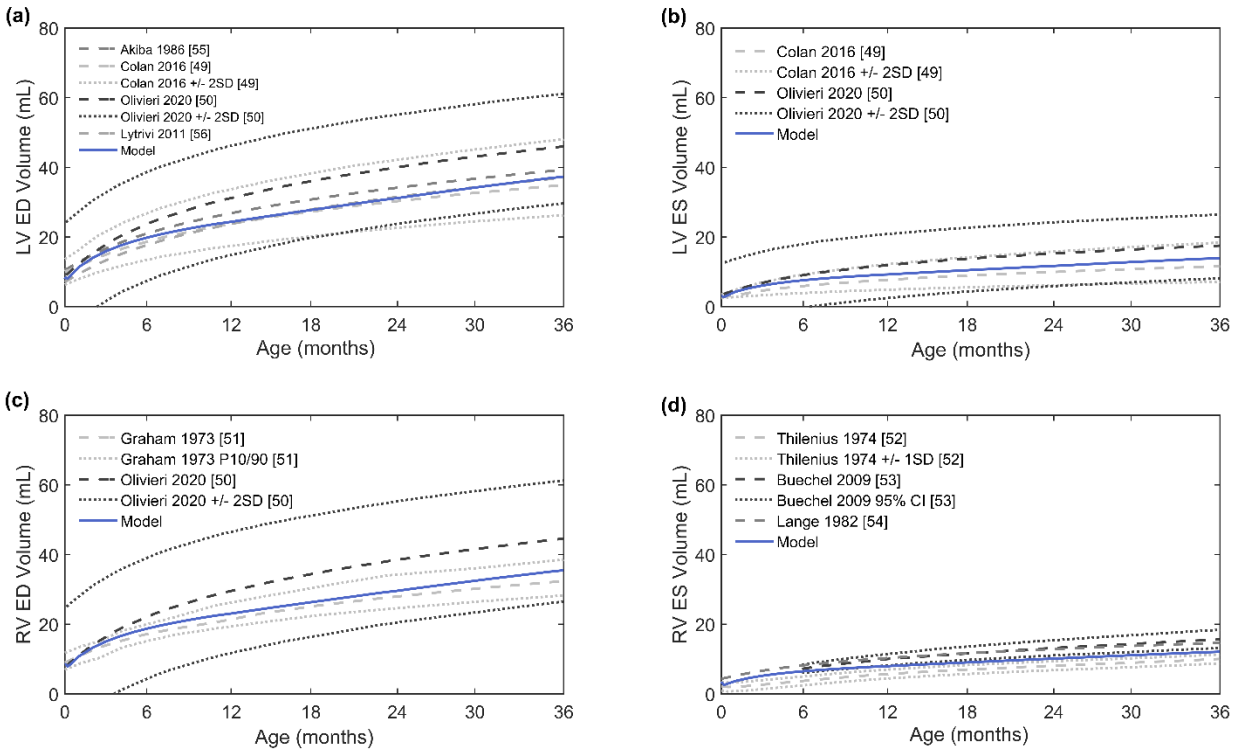

Figure 7: Simulated left and right ventricular volumes at end diastole (A and C, respectively) and end systole (B and D, respectively) for the first three years of life for a median-weight infant compared to reported measurements [49,50-55,71]. Dashed lines indicate mean values for reported data. Dotted lines indicate ± two standard deviations [49,50], ± one standard deviation [52], 10th and 90th percentiles [51], or 95% confidence interval [53]. LV, left ventricle; RV, right ventricle; ED, end diastole; ES, end systole.

Simulated ventricular thicknesses also matched reported echocardiographic measurements. LV wall thickness at end diastole and end systole followed trends reported by Akiba et al. [55] and was within the 10^{th} and 90^{th} percentiles reported by Kampmann [56] (Figure 8A and B). RV wall thickness at end diastole was within one standard deviation of measurements reported by Qi et al. [45] (Figure 8C). No measurements of RV wall thickness at end systole were available for healthy infants below 3 years of age.

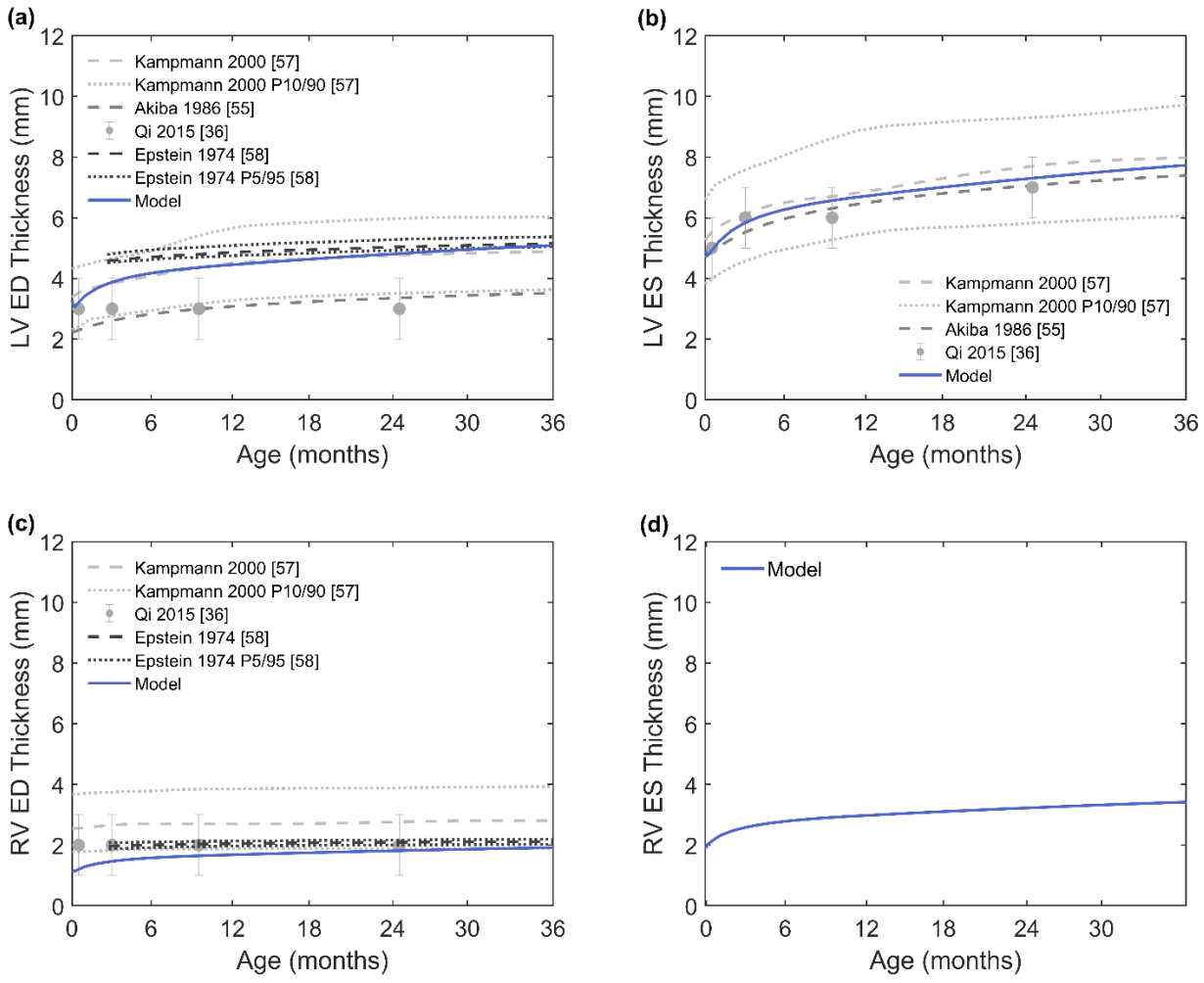
(a)
LV ED Thickness (mm)
Age (months)
Kampmann 2000 [57]
Kampmann 2000 P10/90 [57]
Akiba 1986 [55]
Qi 2015 [36]
Epstein 1974 [58]
Epstein 1974 P5/95 [58]
Model
(b)
LV ES Thickness (mm)
Age (months)
Kampmann 2000 [57]
Kampmann 2000 P10/90 [57]
Akiba 1986 [55]
Qi 2015 [36]
Model
(c)
RV ED Thickness (mm)
Age (months)
Kampmann 2000 [57]
Kampmann 2000 P10/90 [57]
Qi 2015 [36]
Epstein 1974 [58]
Epstein 1974 P5/95 [58]
Model
(d)
RV ES Thickness (mm)
Age (months)
Model

Figure 8: Simulated left and right ventricular thicknesses at end diastole (A and C, respectively) and end systole (B and D, respectively) for the first three years of life for a median-weight infant. Simulated left ventricular thicknesses are compared to posterior wall measurements and simulated right ventricular end diastolic thickness is compared to anterior wall measurements [45,55,56,74]. No data were available for right ventricular thicknesses at end systole during the first three years of life. Measurements from Qi et al. were from the sea-level cohort only. Dashed lines indicate mean values for reported data. Dotted lines indicate 10th and 90th percentiles [56] or 5th and 95th percentiles [74]. Error bars on data indicate ± one standard deviation [45]. LV, left ventricle; RV, right ventricle; ED, end diastole; ES, end systole.

3.2. Simulating Somatic Growth for Larger and Smaller Infants

To validate the model for infants at weights other than the 50th percentile, the 10th and 90th percentile weight curves were also used to simulate somatic growth. Maturation constants for pulmonary and systemic vascular resistance were not refitted. Heart rates computed from the 10th and 90th percentile weight curves input into the model are shown in [Figure S1B]. There was negligible difference in simulated MAP and MPAP (Figure S3) and in systemic and pulmonary systolic and diastolic pressures (not shown). Simulated end-diastolic LV volume and thickness increased with weight but were within the bounds of reported values (Figure 9). Other chamber volumes and thicknesses were also within the bounds of reported values (Figures S4 and S5).

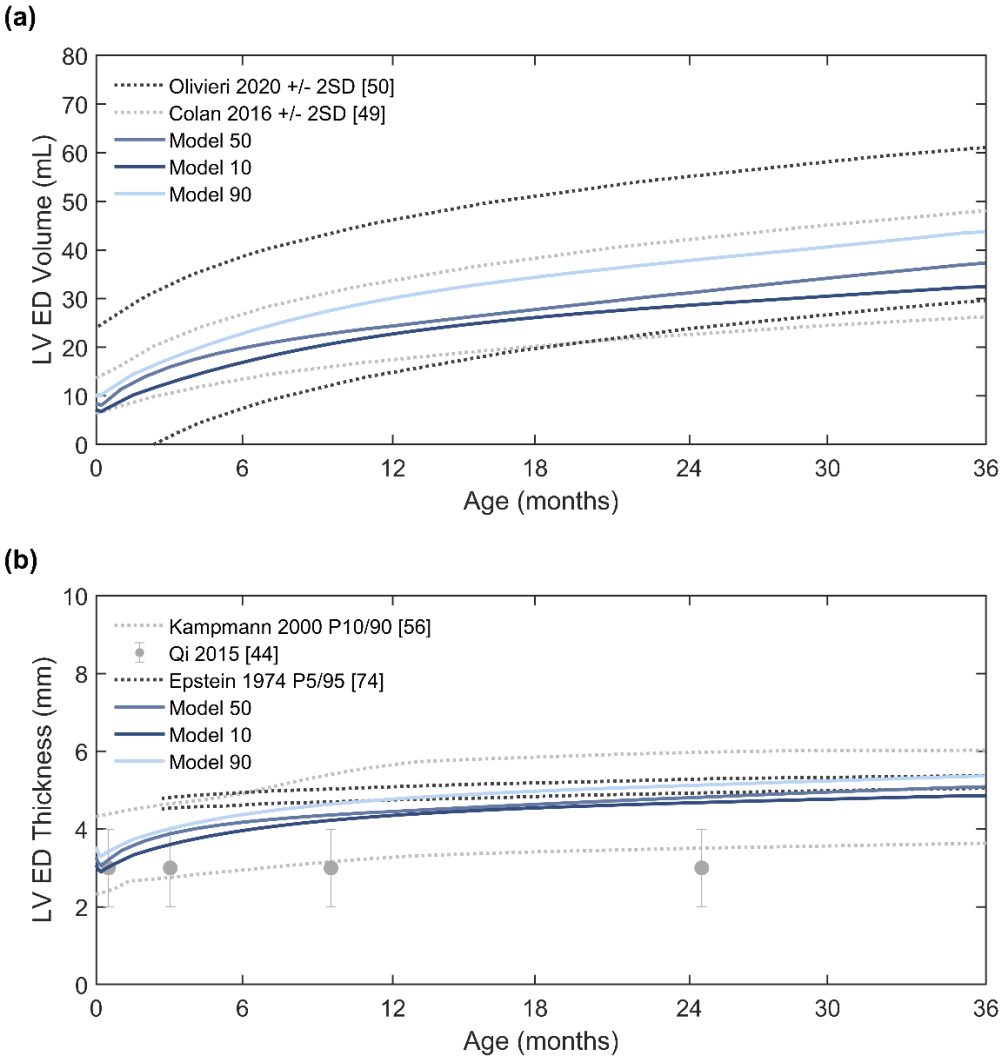

Figure 9: Comparison of 50th, 10th, and 90th weight percentile simulations for left ventricular (A) volume and (B) thickness at end diastole compared to bounds of reported measurements [45,49,50,56,74]. Measurements from Qi et al. were from the sea-level cohort only. Dotted lines indicate 10th and 90th percentiles [56], 5th and 95th percentiles [74], or ± two standard deviations [49,50]. Error bars on data indicate ± a standard deviation [45] LV, left ventricle; ED, end diastole.

3.3. Simulating Coarctation of the Aorta

In a simulation of CoA, the model predicted a substantial increase in end-diastolic LV thickness, comparable with the significant increase in both the end-diastolic LV posterior wall thickness and the interventricular septal thickness observed by Eerola et al. [36] (Figure 10A). It also predicted an increase in LV end-diastolic volume comparable with their reported significant increase in LV end-diastolic diameter (Figure 10B). An increase in systemic systolic and diastolic pressures in the upper body arteries (Figures 10C and D) was also produced, consistent with observed increases measured using a blood pressure cuff [36,37].

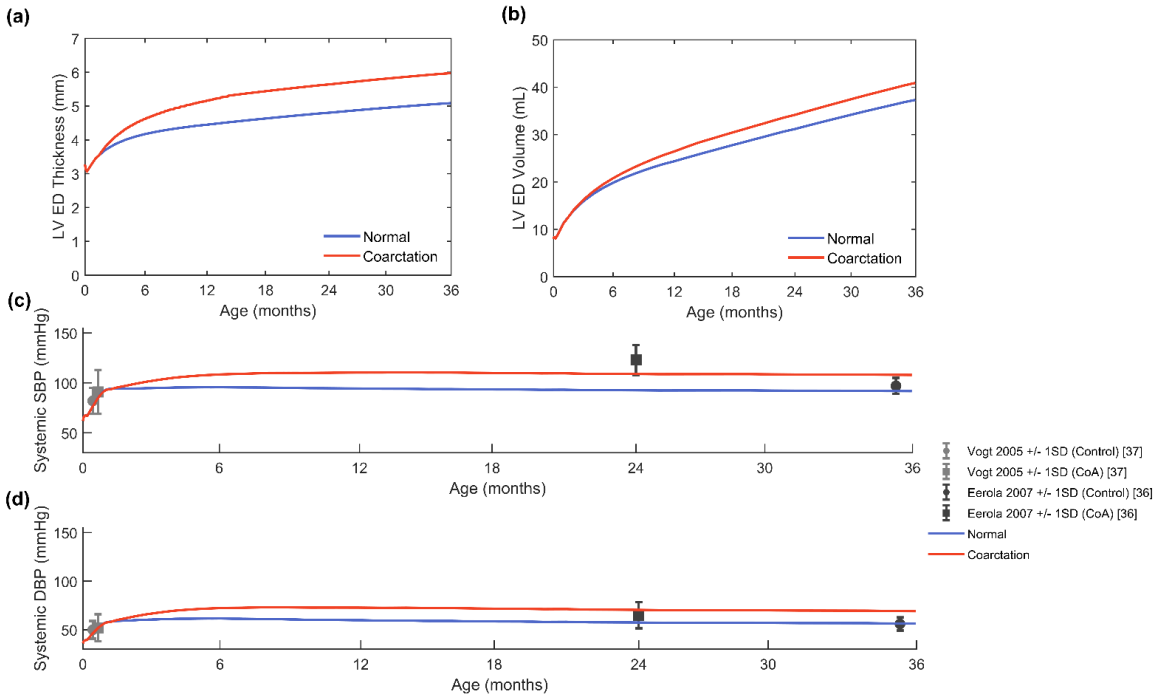

Figure 10: Comparison of normal and coarctation simulations for (A) left ventricular thickness at end diastole, (B) left ventricular volume at end diastole, (C) systolic and (D) diastolic systemic pressures compared to reported control and coarctation measurements [36,37]. Error bars on data indicate ± one standard deviation. LV, left ventricle; ED, end diastole; SBP, systolic blood pressure; DBP, diastolic blood pressure.

4. DISCUSSION

Our goal was to create and implement a predictive cardiac growth model for normal healthy infants that can be further modified to simulate pathology. To accomplish this, somatic growth was uncoupled from pathologic growth. We simulated somatic growth by adapting the input parameters of a model of adult canine LV growth for human infants using a combination of allometric and maturation approaches. The ventricular dimensions and hemodynamics produced by the model matched reported measurements for healthy infants aged 0-3 years. Simultaneously, the model produced time-varying homeostatic strain setpoints later used to determine pathologic growth in the case of CoA. Our model's speed and flexibility allow it to be used as a tool to quickly analyze pathological mechanisms affecting cardiac growth and hemodynamics in growing infants, and its modular nature makes it a potential base for more sophisticated approaches aimed at clinical integration and translation.

4.1. Adjusting Model Parameters for Infants

A major challenge in simulating the hemodynamics of infants and children arises from needing to change all parameters simultaneously to capture somatic growth, as dimensionalized parameters must change with body size. Furthermore, many model parameters (e.g., stressed blood volume, venous compliances and resistances) are not measurable clinically and require optimization from other measurable quantities (e.g., end-diastolic volume). Obtaining sufficient clinical data to optimize all parameters for infants

from 0 to 3 years of age over a range of weights is not possible. Therefore, in this study we used allometric scaling and a maturation approach to determine parameter sets for infants at different weights and ages. Allometric scaling relates a biological variable to body mass [28]. It has been widely used to translate computational models between species [30] and even to simulate somatic development [24,25]. For example, Pennati and Fumero (2000) created a computer model of fetal development from 20 to 40 weeks of gestation by assuming a set weight at each gestational age and fitting allometric scaling exponents for each vascular structure and organ [25]. A maturation function, used in anesthesiology for predicting drug clearance in pediatric patients, takes both weight and age into consideration when calculating output to account for differences between neonates and adults that cannot be explained solely by size [34,35]. In this study, the maturation approach enabled separation of postnatal deviations in resistance associated with birth from those occurring due to increasing size. Using this approach, the model produced reasonable values for chamber dimensions as well as arterial pressures for infants of different weights across a wide range of ages (Figure 9, [Figures S3-5]). While early values of MAP and MPAP in normal infants with mean body weight trajectories were initially necessary to fit maturation constants, these constants were then used successfully for infants with different weight trajectories and CoA. Thus, with these constants, weight and heart rate alone are the necessary inputs to the model.

4.2. Predicting Ventricular Dimensions

We utilized alterations in homeostatic strains across time to simulate somatic heart growth (r_{0_s} and h_{0_s} in Figure 5). The computed strain setpoints changed rapidly in the first 10 days,

however, this variation was largely driven by age—when the 10th and 90th percentile weight trajectories were input along with the base fitted maturation constants, there was little change to the homeostatic setpoint trajectories. Therefore, this strategy is well-suited to a wide range of birth weights, indicating promise for future simulations of pediatric patients with complex CHDs, who tend to weigh less than their healthy peers. For example, using this approach, homeostatic setpoints could be established for an infant with normal anatomy but abnormally low weight trajectory. Then, a simulation including the anatomic features of the congenital defect could be run with the established setpoints. Resulting deviations in myocardial strain would predict pathologic changes in unloaded heart radius and thickness. In this way, we could uncouple deficiencies in overall growth (weight) and somatic ventricular development from pathologic ventricular hypertrophy.

Our model predictions of ventricular dimensional changes were within empirical ranges for healthy infants and those with CoA from 0 to 3 years of age. Notably, when capturing the pathologic growth associated with CoA, it was unnecessary to alter the growth parameters that relate the rates of pathologic circumferential and radial growth with deviations in circumferential and radial strain. Fitted homeostatic maximum circumferential strain was within the range of previously fitted values for adult canines (0.44 to 0.80) throughout the entire three-year period despite the change in species and age [17, 20]. Fitted homeostatic maximum radial strain was within the range of previously fitted values (-0.11 to -0.01) throughout the entire three-year period for the LV and after day 3 for the RV. Thus,

differences in strain produced reasonable growth rates regardless of their application to developing children or adult canines.

In all simulations the active and passive intrinsic material properties of the myocardium were constant at all times. Changes in these parameters can be prescribed easily if warranted. In a previous simulation of myocardial infarction, when the passive stiffness of the ventricle was increased at a rate matching increased collagen content, the difference between predicted and observed ventricular volumes narrowed [17]. Fibrosis is commonly observed clinically in patients with aortic stenosis [57-59] as well as in animal experiments of aortic banding [60-62]. However, the clinical studies on aortic coarctation referenced [36, 37] did not comment on LV myocardial fibrosis. When we simulated a 20% increase in b, the parameter dictating the passive stiffness of the LV in Equation 15, there were minimal changes in arterial pressure or LV end-diastolic thickness, however there was substantially less LV dilation (Figure S7).

Our rationale for using CoA to model pathologic growth was twofold: first, CoA is a relatively simple defect in comparison to more complex CHDs, such as hypoplastic left heart syndrome or tetralogy of Fallot. Simulating it does not require extensive changes to our model, only an increase in lower body arterial resistance. Second, uncorrected CoA results in LV pressure overload, which we have successfully modeled previously in adult canines [17]. Pressure overload results in predictable and measurable changes in LV geometry, namely increased LV thickness and larger end-diastolic diameters (and, relatedly, end-diastolic volume) than healthy controls [36]. Though the cause of this

diameter increase is unclear for coarctation, in other types of hypertension presenting with reduced arterial compliance, vasodilation and congestion have been implicated (rather than ventricular growth and remodeling) for increased end-diastolic LV volume [65, 66]. Thus, consistent with previous models, stressed blood volume was increased proportionally with increased arterial resistance to capture this change in hemodynamic compensation.

4.3. Limitations

We assumed a simplified spherical geometry when representing the ventricles in our model. While finite element (FE) models can generate undoubtedly more accurate representations of the anatomy derived from high-resolution imaging, children rarely receive multiple cardiac MRIs or CTs, making it impractical to fit and validate spatially-varying growth predictions and supporting a simpler analytic approach. Additionally, simulating growth is numerically intensive and current FE models are already computationally expensive. Though advances in computing strategies are being developed to reduce computation time [63,64], current models often require hours to run a single cardiac cycle and thus weeks to simulate a month of growth, even when utilizing computing clusters [67]. In contrast, our MATLAB model predicts three years of growth in 40.5 minutes on a desktop computer with 16 GB RAM, a 64-bit operating system, and a 3.0 GHz Intel Core i7-9700 CPU. In our previous usages of the thin-walled spherical geometry we successfully predicted relative changes in radius and wall thickness following pressure overload, volume overload, and myocardial infarction [17,20]. Others have also successfully simulated changes in ventricular dimensions due to both overload [68] and

dyssynchrony [69, 70] with similar geometries, implying a similar effect of alterations in ventricular pressure and volume changes on myocardial stress as in more complex geometries. It is possible more intricate geometries will be needed in the future to replicate more complex CHDs. In particular, the RV has a more irregular shape than the LV and has generally received less attention by the modeling community [71]. Thus, the spherical assumption may impact the predictions of RV growth under an RV-specific pathology such as hypoplastic heart syndrome. In similar complex cases, however, lower order models have proven to be critical tools in determining boundary conditions, initial conditions, and parameter optimization for higher order models, suggesting continued utility of our approach [24].

As mentioned in section 4.2, the growth parameters relating rates of pathologic growth to deviations in strain were unchanged with time or from previous simulations. Thus, we assumed that a myocyte's abilities to sense and respond to stretch do not depend on developmental stage or species. Situations where the inherent responsiveness of the myocytes to stretch is abnormal will likely require modified parameters. For example, they would likely need to be altered for patients taking pharmacologic agents known to modulate intracellular signaling (e.g., beta-blockers), or in the case of genetic abnormalities such as mutations in beta-cardiac myosin, which can cause hypercontractility [72]. A systems biology approach explicitly modeling cell signaling could potentially capture the detailed interactions driving stretch-responsiveness in the setting of medical treatment or genetic disorders.

In both healthy and pathologic simulations, circulatory parameters were prescribed based on weight via allometric scaling, weight and age via a maturation function (pulmonary and vascular resistance), or based on reported data (heart rate). Allometric scaling might not be appropriate for all of the input parameters. We suspect other parameters in our model that are difficult or impossible to measure might behave similarly to heart rate, varying from their scaled values somewhat in magnitude but generally following a similar trend. Pennati and Fumero [25] approached this issue by comparing model outputs to measured data and adjusting their scaling factors. Ultimately, a more mechanistic approach, such as that employed by Beard et al. [73] is likely necessary to capture long-term interactions between pathologic ventricular hypertrophy and circulatory hemodynamic compensation. This may be particularly relevant to simulate treatments involving medications, as they often affect these mechanisms (e.g., prostaglandin).

5. CONCLUSION

Treatment and management of pediatric cardiovascular pathology often involves estimating how hemodynamics and ventricular dimensions will change as a child grows. While computational modeling has become a powerful tool for clinical decision-making in adults, growth remains a barrier in adapting these approaches to children. In particular, models of the cardiovascular system typically require several parameters that are not measurable clinically and change with body size—even our simple model required over 30 parameters. Using a combined allometric scaling and maturation approach, we were able to estimate these parameters and their evolution for a range of weights. The final computational growth model presented here was able to capture the time-course of

circulatory hemodynamics and ventricular hypertrophy in both healthy infants and those with aortic coarctation, a common congenital defect, from birth through three years of life with simulation times of less than one hour. In addition, the model was able to replicate the pathologic hypertrophic pattern associated with aortic coarctation, demonstrating that our previous approach for pathologic LV hypertrophy [17,20] was successful in this new context without reparameterization. In the future, our model could serve as a foundation for predictive approaches to customize surgical timing by enabling clinicians to project the future extent and rate of ventricular dilation and thickening for a range of congenital defects.

ACKNOWLEDGMENT

This research was funded by the American Heart Association, Grant #20CDA35210754 and the National Science Foundation Graduate Research Fellowship Program.The authors declare that the research was conducted in the absence of any commercial or financial relationships that could be construed as a potential conflict of interest.

REFERENCES

1. van der Linde, D., Konings, E. E. M., Slager, M. A., Witsenburg, M., Helbing, W. A., Takkenberg, J. J. M., and Roos-Hesselink, J. W., 2011, "Birth Prevalence of Congenital Heart Disease Worldwide," Journal of the American College of Cardiology, **58**(21), pp. 2241–2247. DOI: 10.1016/j.jacc.2011.08.025

2. Steurer, M. A., Baer, R. J., Keller, R. L., Oltman, S., Chambers, C. D., Norton, M. E., Peyvandi, S., Rand, L., Rajagopal, S., Ryckman, K. K., Moon-Grady, A. J., and Jelliffe-Pawlowski, L. L., 2017, "Gestational Age and Outcomes in Critical Congenital Heart Disease," Pediatrics, **140**(4), p. e20170999. DOI: 10.1542/peds.2017-0999

3. Gurvitz, M., Dunn, J. E., Bhatt, A., Book, W. M., Glidewell, J., Hogue, C., Lin, A. E., Lui, G., McGarry, C., Raskind-Hood, C., Van Zutphen, A., Zaidi, A., Jenkins, K., and Riehle-Colarusso, T., 2020, "Characteristics of Adults With Congenital Heart Defects in the United States," Journal of the American College of Cardiology, **76**(2), pp. 175–182. DOI: 10.1016/j.jacc.2020.05.025

4. Burkhoff, D., and Tyberg, J. V., 1993, "Why Does Pulmonary Venous Pressure Rise after Onset of LV Dysfunction: A Theoretical Analysis," American Journal of Physiology-Heart and Circulatory Physiology, **265**(5), pp. H1819–H1828. DOI: 10.1152/ajpheart.1993.265.5.H1819

5. Giannoglou, G., Giannakoulas, G., Soulis, J., Chatzizisis, Y., Perdikides, T., Melas, N., Parcharidis, G., and Louridas, G., 2006, "Predicting the Risk of Rupture of Abdominal Aortic Aneurysms by Utilizing Various Geometrical Parameters: Revisiting the Diameter Criterion," Angiology, **57**(4), pp. 487–494. DOI: 10.1177/0003319706290741

6. Fillinger, M., 2007, "Who Should We Operate On and How Do We Decide: Predicting Rupture and Survival in Patients with Aortic Aneurysm," Seminars in Vascular Surgery, **20**(2), pp. 121–127. DOI: 10.1053/j.semvascsurg.2007.04.001

7. Perktold, K., Leuprecht, A., Prosi, M., Berk, T., Czerny, M., Trubel, W., and Schima, H., 2002, "Fluid Dynamics, Wall Mechanics, and Oxygen Transfer in Peripheral Bypass Anastomoses," Annals of Biomedical Engineering, **30**(4), pp. 447–460. DOI: 10.1114/1.1477445

8. Augst, A. D., Ariff, B., McG. Thom, S. A. G., Xu, X. Y., and Hughes, A. D., 2007, "Analysis of Complex Flow and the Relationship between Blood Pressure, Wall Shear Stress, and Intima-Media Thickness in the Human Carotid Artery," American Journal of Physiology-Heart and Circulatory Physiology, **293**(2), pp. H1031–H1037. DOI: 10.1152/ajpheart.00989.2006

9. Gallo, D., Montanaro, C., and Morbiducci, U., 2019, "Computational Modelling in Congenital Heart Disease: Challenges and Opportunities," International Journal of Cardiology, **276**, pp. 116–117. DOI: 10.1016/j.ijcard.2018.11.109

10. Trusty, P. M., Slesnick, T. C., Wei, Z. A., Rossignac, J., Kanter, K. R., Fogel, M. A., and Yoganathan, A. P., 2018, “Fontan Surgical Planning: Previous Accomplishments, Current Challenges, and Future Directions,” J. of Cardiovasc. Trans. Res., **11**(2), pp. 133–144. DOI: 10.1007/s12265-018-9786-0

11. Wei, Z. A., and Fogel, M. A., 2021, “Engineering Perspective on Cardiovascular Simulations of Fontan Hemodynamics: Where Do We Stand with a Look Towards Clinical Application,” Cardiovasc Eng Tech, **12**(6), pp. 618–630. DOI: 10.1007/s13239-021-00541-y

12. Loke, Y.-H., Capuano, F., Balaras, E., and Olivieri, L. J., 2022, “Computational Modeling of Right Ventricular Motion and Intracardiac Flow in Repaired Tetralogy of Fallot,” Cardiovasc Eng Tech, **13**(1), pp. 41–54. DOI: 10.1007/s13239-021-00558-3

13. Sengupta, D., Kahn, A. M., Burns, J. C., Sankaran, S., Shadden, S. C., and Marsden, A. L., 2012, “Image-Based Modeling of Hemodynamics in Coronary Artery Aneurysms Caused by Kawasaki Disease,” Biomech Model Mechanobiol, **11**(6), pp. 915–932. DOI: 10.1007/s10237-011-0361-8

14. Andersson, M., Lantz, J., Ebbers, T., and Karlsson, M., 2015, “Quantitative Assessment of Turbulence and Flow Eccentricity in an Aortic Coarctation: Impact of Virtual Interventions,” Cardiovasc Eng Tech, **6**(3), pp. 281–293. DOI: 10.1007/s13239-015-0218-x

15. Martin, M. H., Feinstein, J. A., Chan, F. P., Marsden, A. L., Yang, W., and Reddy, V. M., 2015, “Technical Feasibility and Intermediate Outcomes of Using a Handcrafted, Area-Preserving, Bifurcated Y-Graft Modification of the Fontan Procedure,” The Journal of Thoracic and Cardiovascular Surgery, **149**(1), pp. 239-245.e1. DOI: 10.1016/j.jtcvs.2014.08.058

16. Kanter, K. R., Haggerty, C. M., Restrepo, M., de Zelicourt, D. A., Rossignac, J., Parks, W. J., and Yoganathan, A. P., 2012, “Preliminary Clinical Experience with a Bifurcated Y-Graft Fontan Procedure—A Feasibility Study,” The Journal of Thoracic and Cardiovascular Surgery, **144**(2), pp. 383–389. DOI: 10.1016/j.jtcvs.2012.05.015

17. Witzenburg, C. M., and Holmes, J. W., 2018, “Predicting the Time Course of Ventricular Dilation and Thickening Using a Rapid Compartmental Model,” J. of Cardiovasc. Trans. Res., **11**(2), pp. 109–122. DOI: 10.1007/s12265-018-9793-1

18. Arumugam, J., Mojumder, J., Kassab, G., and Lee, L. C., 2019, “Model of Anisotropic Reverse Cardiac Growth in Mechanical Dyssynchrony,” Sci Rep, **9**(1), p. 12670. DOI: 10.1038/s41598-019-48670-8

19. Kerckhoffs, R. C. P., Omens, J. H., and McCulloch, A. D., 2012, “A Single Strain-Based Growth Law Predicts Concentric and Eccentric Cardiac Growth during Pressure and Volume Overload,” Mechanics Research Communications, **42**, pp. 40–50. DOI: 10.1016/j.mechrescom.2011.11.004

20. Witzenburg, C. M., and Holmes, J. W., 2019, “The Impact of Hemodynamic Reflex Compensation Following Myocardial Infarction on Subsequent Ventricular Remodeling,” Journal of Biomechanical Engineering, **141**(9), p. 091010. DOI: 10.1115/1.4043867

21. Kaye, D., Shah, S. J., Borlaug, B. A., Gustafsson, F., Komtebedde, J., Kubo, S., Magnin, C., Maurer, M. S., Feldman, T., and Burkhoff, D., 2014, “Effects of an Interatrial Shunt on Rest and Exercise Hemodynamics: Results of a Computer Simulation in Heart Failure,” Journal of Cardiac Failure, **20**(3), pp. 212–221. DOI: 10.1016/j.cardfail.2014.01.005

22. Alisiddiq, Z., and Butler, R., 2018, “Pulmonary Artery Catheterization,” Medicine, **46**(8), pp. 496–498. DOI: 10.1016/j.mpmed.2018.05.002

23. Takala, J., 2003, “Pulmonary Capillary Pressure,” Intensive Care Med, **29**(6), pp. 890–893. DOI: 10.1007/s00134-003-1749-4

24. Baretta, A., Corsini, C., Yang, W., Vignon-Clementel, I. E., Marsden, A. L., Feinstein, J. A., Hsia, T.-Y., Dubini, G., Migliavacca, F., Pennati, G., and The Modeling of Congenital Hearts Alliance (MOCHA) Investigators, 2011, “Virtual Surgeries in Patients with Congenital Heart Disease: A Multi-Scale Modelling Test Case,” Phil. Trans. R. Soc. A., **369**(1954), pp. 4316–4330. DOI: 10.1098/rsta.2011.0130

25. Pennati, G., and Fumero, R., 2000, “Scaling Approach to Study the Changes Through the Gestation of Human Fetal Cardiac and Circulatory Behaviors,” Annals of Biomedical Engineering, **28**(4), pp. 442–452. DOI: 10.1114/1.282

26. Figueroa, C. A., and Humphrey, J. D., 2014, “Pressure Wave Propagation in Full-Body Arterial Models: A Gateway to Exploring Aging and Hypertension,” Procedia IUTAM, **10**, pp. 382–395. DOI: 10.1016/j.piutam.2014.01.033

27. Salim, M. A., DiSessa, T. G., Arheart, K. L., and Alpert, B. S., 1995, “Contribution of Superior Vena Caval Flow to Total Cardiac Output in Children: A Doppler Echocardiographic Study,” Circulation, **92**(7), pp. 1860–1865. DOI: 10.1161/01.CIR.92.7.1860

28. West, G. B., Brown, J. H., and Enquist, B. J., 1997, “A General Model for the Origin of Allometric Scaling Laws in Biology,” Science, **276**(5309), pp. 122–126. DOI: 10.1126/science.276.5309.122

29. Centers for Disease Control and Prevention, National Center for Health Statistics. CDC growth charts: United States, 2000. https://www.cdc.gov/growthcharts/clinical_charts.htm

30. Seymour, R. S., and Blaylock, A. J., 2000, “The Principle of Laplace and Scaling of Ventricular Wall Stress and Blood Pressure in Mammals and Birds,” Physiological and Biochemical Zoology, **73**(4), pp. 389–405. DOI: 10.1086/317741

31. Caggiano, L. R., Holmes, J. W., and Witzenburg, C. M., 2022, “Individual Variability in Animal-Specific Hemodynamic Compensation Following Myocardial Infarction,” Journal of Molecular and Cellular Cardiology, **163**, pp. 156–166. DOI: 10.1016/j.yjmcc.2021.10.008

32. Fleming, S., Thompson, M., Stevens, R., Heneghan, C., Plüddemann, A., Maconochie, I., Tarassenko, L., and Mant, D., 2011, “Normal Ranges of Heart Rate and Respiratory Rate in Children from Birth to 18 Years of Age: A Systematic Review of Observational Studies,” The Lancet, **377**(9770), pp. 1011–1018. DOI: 10.1016/S0140-6736(10)62226-X

33. Lakshminrusimha, S., 2012, “The Pulmonary Circulation in Neonatal Respiratory Failure,” Clinics in Perinatology, **39**(3), pp. 655–683. DOI: 10.1016/j.clp.2012.06.006

34. Anderson, B. J., and Holford, N. H. G., 2009, “Mechanistic Basis of Using Body Size and Maturation to Predict Clearance in Humans,” Drug Metabolism and Pharmacokinetics, **24**(1), pp. 25–36. DOI: 10.2133/dmpk.24.25

35. Bi, Y., Liu, J., Li, F., Yu, J., Bhattaram, A., Bewernitz, M., Li, R., Ahn, J., Earp, J., Ma, L., Zhuang, L., Yang, Y., Zhang, X., Zhu, H., and Wang, Y., 2021, “Model-Informed Drug Development in Pediatric Dose Selection,” The Journal of Clinical Pharmacology, **61**(S1). DOI: 10.1002/jcph.1848

36. Eerola, A., Jokinen, E., Boldt, T., Mattila, I. P., and Pihkala, J. I., 2007, “Left Ventricular Hypertrophy Persists after Successful Treatment for Coarctation of the Aorta,” Scandinavian Cardiovascular Journal, **41**(6), pp. 370–377. DOI: 10.1080/14017430701397839

37. Vogt, M., Kühn, A., Baumgartner, D., Baumgartner, C., Busch, R., Kostolny, M., and Hess, J., 2005, “Impaired Elastic Properties of the Ascending Aorta in Newborns Before and Early After Successful Coarctation Repair: Proof of a Systemic Vascular Disease of the Prestenotic Arteries?,” Circulation, **111**(24), pp. 3269–3273. DOI: 10.1161/CIRCULATIONAHA.104.529792

38. Segers, P., Stergiopulos, N., Schreuder, J. J., Westerhof, B. E., and Westerhof, N., 2000, “Left Ventricular Wall Stress Normalization in Chronic Pressure-Overloaded Heart: A Mathematical Model Study,” American Journal of Physiology-Heart and Circulatory Physiology, **279**(3), pp. H1120–H1127. DOI: 10.1152/ajpheart.2000.279.3.H1120

39. World Health Organization. WHO child growth standards. Geneva: World Health Organization, 2006. https://www.who.int/tools/child-growth-standards/standards

40. Park, M. K., 1989, “Normative Oscillometric Blood Pressure Values in the First 5 Years in an Office Setting,” Arch Pediatr Adolesc Med, **143**(7), p. 860. DOI: 10.1001/archpedi.1989.02150190110034

41. Kent, A. L., Kecskes, Z., Shadbolt, B., and Falk, M. C., 2007, “Normative Blood Pressure Data in the Early Neonatal Period,” Pediatr Nephrol, **22**(9), pp. 1335–1341. DOI: 10.1007/s00467-007-0480-8

42. Kent, A. L., Kecskes, Z., Shadbolt, B., and Falk, M. C., 2007, “Blood Pressure in the First Year of Life in Healthy Infants Born at Term,” Pediatr Nephrol, **22**(10), pp. 1743–1749. DOI: 10.1007/s00467-007-0561-8

43. Kang, C., Zhao, E., Zhou, Y., Zhao, H., Liu, Y., Gao, N., Huang, X., and Liu, B., 2016, “Dynamic Changes of Pulmonary Arterial Pressure and Ductus Arteriosus in Human Newborns From Birth to 72 Hours of Age,” Medicine, **95**(3), p. e2599. DOI: 10.1097/MD.0000000000002599

44. Qi, H.-Y., Ma, R.-Y., Jiang, L.-X., Li, S.-P., Mai, S., Chen, H., Ge, M., Wang, M.-Y., Liu, H.-N., Cai, Y.-H., Xu, S.-Y., and Li, J., 2015, “Anatomical and Hemodynamic Evaluations of the Heart and Pulmonary Arterial Pressure in Healthy Children Residing at High Altitude in China,” IJC Heart & Vasculature, **7**, pp. 158–164. DOI: 10.1016/j.ijcha.2014.10.015

45. Emmanouilides, G. C., Moss, A. J., Duffie, E. R., and Adams, F. H., 1964, “Pulmonary Arterial Pressure Changes in Human Newborn Infants from Birth to 3 Days of Age,” The Journal of Pediatrics, **65**(3), pp. 327–333. DOI: 10.1016/S0022-3476(64)80395-4

46. Bhatla, P., Nielsen, J. C., Ko, H. H., Doucette, J., Lytrivi, I. D., and Srivastava, S., 2012, “Normal Values of Left Atrial Volume in Pediatric Age Group Using a Validated Allometric Model,” Circ: Cardiovascular Imaging, **5**(6), pp. 791–796. DOI: 10.1161/CIRCIMAGING.112.974428

47. Tanaka, N., Takigiku, K., Takahashi, K., Kuraoka, A., Matsui, K., Iwashima, S., Nii, M., Toyono, M., Takeuchi, M., Kishiro, M., Yasukochi, S., and Shimizu, T., 2015, “Assessment of the Developmental Change in the Left Atrial Volume Using Real Time Three-Dimensional Echocardiography,” Echocardiography, **32**(7), pp. 1131–1139. DOI: 10.1111/echo.12829

48. Linden, K., Goldschmidt, F., Laser, K. T., Winkler, C., Körperich, H., Dalla-Pozza, R., Breuer, J., and Herberg, U., 2019, “Left Atrial Volumes and Phasic Function in Healthy Children:

Reference Values Using Real-Time Three-Dimensional Echocardiography," Journal of the American Society of Echocardiography, **32**(8), pp. 1036-1045.e9. DOI: 10.1016/j.echo.2019.03.018

49. Colan, S. D., 2016, "Normal Echocardiographic Values for Cardiovascular Structures," *Echocardiography in Pediatric and Congenital Heart Disease*, W.W. Lai, L.L. Mertens, M.S. Cohen, and T. Geva, eds., John Wiley & Sons, Ltd, Oxford, UK, pp. 883–901.

50. Olivieri, L. J., Jiang, J., Hamann, K., Loke, Y.-H., Campbell-Washburn, A., Xue, H., McCarter, R., and Cross, R., 2020, "Normal Right and Left Ventricular Volumes Prospectively Obtained from Cardiovascular Magnetic Resonance in Awake, Healthy, 0- 12 Year Old Children," J Cardiovasc Magn Reson, **22**(1), p. 11. DOI: 10.1186/s12968-020-0602-z

51. Graham, T. P., Jarmakani, J. M., Atwood, G. F., and Canent, R. V., 1973, "Right Ventricular Volume Determinations in Children: Normal Values and Observations with Volume or Pressure Overload," Circulation, **47**(1), pp. 144–153. DOI: 10.1161/01.CIR.47.1.144

52. Thilenius, O. G., and Arcilla, R. A., 1974, "Angiographic Right and Left Ventricular Volume Determination in Normal Infants and Children," Pediatr Res, **8**(2), pp. 67–74. DOI: 10.1203/00006450-197402000-00001

53. Buechel, E. V., Kaiser, T., Jackson, C., Schmitz, A., and Kellenberger, C. J., 2009, "Normal Right- and Left Ventricular Volumes and Myocardial Mass in Children Measured by Steady State Free Precession Cardiovascular Magnetic Resonance," J Cardiovasc Magn Reson, **11**(1), p. 19. DOI: 10.1186/1532-429X-11-19

54. Lange, P. E., Onnasch, D. G. W., Schaupp, G. H., Zill, C., and Heintzen, P. H., 1982, "Size and Function of the Human Left and Right Ventricles during Growth: Normative Angiographic Data," Pediatr Cardiol, **3**(3), pp. 205–211. DOI: 10.1007/BF02240454

55. Akiba, T., Yoshikawa, M., Otaki, S., Kobayashi, Y., Nakasato, M., Suzuki, H., and Sato, T., 1986, "Echocardiographic Measurements of Left Ventricle in Normal Infants and Children.," Tohoku J. Exp. Med., **149**(1), pp. 31–37. DOI: 10.1620/tjem.149.31

56. Kampmann, C., 2000, "Normal Values of M Mode Echocardiographic Measurements of More than 2000 Healthy Infants and Children in Central Europe," Heart, **83**(6), pp. 667–672. DOI: 10.1136/heart.83.6.667

57. Villari, B., Vassalli, G., Monrad, E. S., Chiariello, M., Turina, M., and Hess, O. M., 1995, "Normalization of Diastolic Dysfunction in Aortic Stenosis Late After Valve Replacement," Circulation, 91(9), pp. 2353–2358. DOI: 10.1161/01.CIR.91.9.2353

58. Yarbrough, W. M., Mukherjee, R., Ikonomidis, J. S., Zile, M. R., and Spinale, F. G., 2012, "Myocardial Remodeling with Aortic Stenosis and after Aortic Valve Replacement: Mechanisms and Future Prognostic Implications," The Journal of Thoracic and Cardiovascular Surgery, 143(3), pp. 656–664. DOI: 10.1016/j.jtcvs.2011.04.044

59. Treibel, T. A., Kozor, R., Schofield, R., Benedetti, G., Fontana, M., Bhuva, A. N., Sheikh, A., López, B., González, A., Manisty, C., Lloyd, G., Kellman, P., Díez, J., and Moon, J. C., 2018, "Reverse Myocardial Remodeling Following Valve Replacement in Patients With Aortic Stenosis," Journal of the American College of Cardiology, 71(8), pp. 860–871. DOI: 10.1016/j.jacc.2017.12.035

60. Cutilletta, A., 1975, "Regression of Myocardial Hypertrophy I. Experimental Model, Changes in Heart Weight, Nucleic Acids and Collagen," Journal of Molecular and Cellular Cardiology, 7(10), pp. 767–781. DOI: 10.1016/0022-2828(75)90042-5

61. Gao, X.-M., Kiriazis, H., Moore, X.-L., Feng, X.-H., Sheppard, K., Dart, A., and Du, X.-J., 2005, "Regression of Pressure Overload-Induced Left Ventricular Hypertrophy in Mice," American Journal of Physiology-Heart and Circulatory Physiology, 288(6), pp. H2702–H2707. DOI: 10.1152/ajpheart.00836.2004

62. Zhao, Z., Chen, L., Xiao, Y.-B., Hao, J., Tang, C.-Z., and Zheng, D.-Z., 2013, "A Rabbit Model to Study Regression of Ventricular Hypertrophy," Heart, Lung and Circulation, 22(5), pp. 373–382. DOI: 10.1016/j.hlc.2012.11.021

63. Sadrabadi, M. S., Eskandari, M., Feigenbaum, H. P., and Arzani, A., 2021, "Local and Global Growth and Remodeling in Calcific Aortic Valve Disease and Aging," Journal of Biomechanics, 128, p. 110773. DOI: 10.1016/j.jbiomech.2021.110773

64. Dong, H., Liu, M., Qin, T., Liang, L., Ziganshin, B., Ellauzi, H., Zafar, M., Jang, S., Elefteriades, J., Sun, W., and Gleason, R. L., 2022, "A Novel Computational Growth Framework for Biological Tissues: Application to Growth of Aortic Root Aneurysm Repaired by the V-Shape Surgery," Journal of the Mechanical Behavior of Biomedical Materials, 127, p. 105081.

65. Chemla, D., Antony, I., Lecarpentier, Y., and Nitenberg, A., 2003, "Contribution of Systemic Vascular Resistance and Total Arterial Compliance to Effective Arterial Elastance in Humans," American Journal of Physiology-Heart and Circulatory Physiology, **285**(2), pp. H614–H620. DOI: 10.1152/ajpheart.00823.2002

66. Safar, M. E., and London, G. M., 1987, "Arterial and Venous Compliance in Sustained Essential Hypertension.," Hypertension, **10**(2), pp. 133–139. DOI: 10.1161/01.HYP.10.2.133

67. Holmes, J. W., and Lumens, J., 2018, “Clinical Applications of Patient-Specific Models: The Case for a Simple Approach,” J. of Cardiovasc. Trans. Res., **11**(2), pp. 71–79. DOI: 10.1007/s12265-018-9787-z

68. Lumens, J., Delhaas, T., Kirn, B., and Arts, T., 2009, “Three-Wall Segment (TriSeg) Model Describing Mechanics and Hemodynamics of Ventricular Interaction,” Ann Biomed Eng, **37**(11), pp. 2234–2255. DOI: 10.1007/s10439-009-9774-2

69. Walmsley, J., Arts, T., Derval, N., Bordachar, P., Cochet, H., Ploux, S., Prinzen, F. W., Delhaas, T., and Lumens, J., 2015, “Fast Simulation of Mechanical Heterogeneity in the Electrically Asynchronous Heart Using the MultiPatch Module,” PLoS Comput Biol, **11**(7), p. e1004284. DOI: 10.1371/journal.pcbi.1004284

70. Oomen, P. J. A., Phung, T.-K. N., Weinberg, S. H., Bilchick, K. C., and Holmes, J. W., 2022, “A Rapid Electromechanical Model to Predict Reverse Remodeling Following Cardiac Resynchronization Therapy,” Biomech Model Mechanobiol, **21**(1), pp. 231–247. DOI: 10.1007/s10237-021-01532-7

71. Bozkurt, S., 2019, “Mathematical Modeling of Cardiac Function to Evaluate Clinical Cases in Adults and Children,” PLoS ONE, **14**(10), p. e0224663. DOI: 10.1371/journal.pone.0224663

72. Vander Roest, A. S., Liu, C., Morck, M. M., Kooiker, K. B., Jung, G., Song, D., Dawood, A., Jhingran, A., Pardon, G., Ranjbarvaziri, S., Fajardo, G., Zhao, M., Campbell, K. S., Pruitt, B. L., Spudich, J. A., Ruppel, K. M., and Bernstein, D., 2021, “Hypertrophic Cardiomyopathy β-Cardiac Myosin Mutation (P710R) Leads to Hypercontractility by Disrupting Super Relaxed State,” Proc. Natl. Acad. Sci. U.S.A., **118**(24), p. e2025030118. DOI: 10.1073/pnas.2025030118

73. Beard, D. A., Wu, F., Cabrera, M. E., and Dash, R. K., 2008, “Modeling of Cellular Metabolism and Microcirculatory Transport,” Microcirculation, **15**(8), pp. 777–793. DOI: 10.1080/10739680802019709

74. Epstein, M. L., Goldberg, S. J., Allen, H. D., Konecke, L., and Wood, J., 1975, “Great Vessel, Cardiac Chamber, and Wall Growth Patterns in Normal Children.,” Circulation, **51**(6), pp. 1124–1129. DOI: 10.1161/01.CIR.51.6.1124

75. Lytrivi, I. D., Bhatla, P., Ko, H. H., Yau, J., Geiger, M. K., Walsh, R., Parness, I. A., Srivastava, S., and Nielsen, J. C., 2011, “Normal Values for Left Ventricular Volume in Infants and Young Children by the Echocardiographic Subxiphoid Five-Sixth Area by Length (Bullet) Method,” Journal of the American Society of Echocardiography, **24**(2), pp. 214–218. DOI: 10.1016/j.echo.2010.12.002

Chapter 5: A Computational Model of Left Ventricular Growth in Borderline Left Heart Patients: Predicting Staged Ventricular Recruitment Outcomes

Abstract

Management of borderline left heart (BLH) presents a major clinical challenge, as early decisions between single-ventricle palliation and biventricular repair carry substantial long-term consequences. Staged left ventricular recruitment (SLVR) has emerged as a strategy to delay this commitment by promoting left ventricular (LV) growth during infancy. Although SLVR success is traditionally assessed using indexed LV end-diastolic volume (LVEDVi) and end-diastolic pressure (LVEDP), these metrics may not adequately capture true myocardial remodeling, as increases in cavity size do not necessarily reflect proportional changes in LV wall thickness or mass. Existing clinical studies have reported inconsistent patterns of hypertrophy during SLVR, and comprehensive analysis is limited by small sample sizes and heterogeneity in BLH presentation.

To address these gaps, we developed a computational framework that couples a lumped parameter model of the circulation with a strain-based cardiac growth law to simulate somatic and pathology-driven LV remodeling. After calibrating the model using published hemodynamic and morphometric data for a generalized BLH patient undergoing SLVR at 6 months of age, we generated a synthetic cohort of 5,306 virtual patients with randomly

selected phenotypical characteristics associated with BLH. Growth simulations from 6 to 24 months allowed classification of SLVR success, failure, or non-physiologic outcomes.

Successful SLVR was characterized by commensurate LV dilatation and wall thickening, whereas failures exhibited minimal adaptive hypertrophy beyond somatic growth. Machine learning identified initial LVEDV Z-score, endocardial fibroelastosis, and aortic valve regurgitation as the strongest predictors of SLVR outcome.

This work introduces the first computational framework for predicting SLVR-mediated ventricular growth and highlights key anatomic and physiologic determinants of successful LV recruitment.

Abbreviations

AR: aortic valve regurgitation

AS: aortic valve stenosis

ASD: atrial septal defect

BLH: borderline left heart

LV: left ventricle

LVEDP: left ventricular end-diastolic pressure

LVEDVi: left ventricular end-diastolic volume, indexed

mBTT: modified Blalock-Thomas-Taussig (shunt)

MR: mitral valve regurgitation

MS: mitral valve stenosis

PVR: pulmonary vascular resistance

RVPA: right ventricle to pulmonary artery (shunt)

SLVR: staged left ventricular recruitment

SVR: systemic vascular resistance

TR: tricuspid regurgitation

1. Introduction

Left ventricular (LV) hypoplasia describes an underdevelopment of left heart structures associated with LV outflow tract obstruction in utero [1]. For patients with severe hypoplasia, such as those with aortic and mitral atresia, single ventricle palliation is the preferred method of treatment [2]. For patients with mild hypoplasia, biventricular repair can be performed soon after birth [2, 3]. Appropriate treatment for patients who do not fit neatly into either category—termed “borderline left heart” (BLH)—is more difficult to determine. For these patients, an incorrect choice of early biventricular repair can have disastrous consequences, including recurring obstructive lesions, pulmonary hypertension, and death [4–6]. However, defaulting to the single ventricle pathway, which consists of three staged palliative surgeries, presents its own quandaries: Fontan physiology (the final stage) is associated with liver disease, renal dysfunction, pulmonary hypertension, and lymphatic complications [7]. Despite the necessity of making the correct treatment decision with limited predictive capacity, the severity of these conditions means time is of the essence— ideally, clinicians will choose which path to pursue before the patient is born [3].

Recently, staged left ventricular recruitment (SLVR) has emerged as a way to delay that critical decision, giving clinicians much-needed breathing room to observe some degree of left heart growth potential before committing to a bi- or univentricular anatomy. Typically, SLVR patients start on the single ventricle pathway in the neonatal period, undergoing a variation of the Norwood procedure with an aortopulmonary amalgamation, where both ventricles contribute to cardiac output. In the second stage operation, the atrial septal defect (ASD) is restricted, which forces pulmonary venous return into the left ventricle, promoting growth. During this stage, the superior vena cava is anastomosed to the pulmonary artery as in the univentricular route, but other repairs can also enhance left ventricular rehabilitation, such as valve repair/replacement or endocardial fibroelastosis resection. The patient is then monitored until typical Fontan age, when the final decision is made. If SLVR is successful, the patient may proceed to biventricular repair. If unsuccessful, clinicians can fall back to a Fontan conversion or continue the recruitment process [8, 9].

Success in SLVR is quantified using end-diastolic LV volume indexed to body surface area (LVEDVi) and pressure (LVEDP): an LVEDVi greater than 40 ml/m^2 with an LVEDP less than 13 mmHg is associated with a successful biventricular repair [9]. However, using volume as the sole indicator of LV growth may be inadequate, as it does not capture LV thickness or overall wall mass. An LV that has dilatated without simultaneously thickening is not well-suited to providing systemic blood flow in a biventricular circulation—indeed, this pattern may be indicative of impending decompensation [10]. Though clinicians acknowledge that

LVEDVi is not fully representative of true growth [7, 11–13], LV thickness and mass data are currently not routinely reported in studies of SLVR. Of those that have reported LV mass, the results are mixed. In a study of SLVR in BLH patients with large ventricular septal defects, despite a significant post-recruitment increase in LVEDVi, there was no significant difference in LV mass [14]. A similar finding was reported by Kwak et al., also in BLH patients with large ventricular septal defects [15]. Conversely, Marathe et al. (2021) found a different trend in patients receiving accessory pulmonary flow during SLVR, with significant increases in both LVEDVi and indexed LV mass over time [16], as did Barnet et al. [17]. None of the studies of SLVR reported LV wall thickness before or after recruitment. However, one study of primary biventricular repair in the neonatal period (i.e., non-staged) did. Shimada et al. found that while LVEDVi had adequately increased at a mean follow-up time of 6 years post-repair, overall indexed LV mass remained unchanged, and relative wall thickness decreased [18]. While these conflicting reports suggest that caution should be exercised when interpreting SLVR results, the rarity of single ventricle conditions and their broad presentation make this interpretation very challenging.

In contrast, computational models are ideally suited for such challenges and have been used extensively to model both ventricular growth and single ventricle pathologies for the past 30 years. For further details of computational growth and single ventricle models, readers are referred to reviews by Yoshida and Holmes [19] and Garber et al. [20], respectively. However, no existing models have simulated ventricular growth in the context of single ventricle pathologies, in children or adults. To that end, we have developed a

predictive model of ventricular growth that considers maladaptive remodeling due to pathology in tandem with normal, somatic growth. The model couples a reduced-order compartmental model of the circulation with a strain-based growth law [21]. We altered the circulatory component to represent a generalized BLH patient undergoing SLVR at 6 months of age by fitting the most sensitive model parameters to available literature data. Then, to better capture the wide range of phenotypes seen in BLH, we created a synthetic population of 5,306 patients by randomly selecting from a uniform distribution of 10 metrics associated with BLH, such as mitral and aortic valve annulus size, LVEDV Z-score, and severity of valve regurgitation. After simulating growth in all 5,306 patients from 6 to 24 months, we evaluated the patients' LV size and function and separated them into three groups: SLVR success, SLVR failure, and "non-physiologic" (patients whose cardiac output or systemic pressures were incompatible with life). We then compared groups using statistical analysis and machine learning, determining which characteristics were associated with SLVR success or failure.

According to model results, thickening generally matched dilatation in successful SLVR. In contrast, patients in the failure group did not experience much growth beyond somatic, i.e., they did not experience additional adaptive growth from SLVR. A predictive model trained on model results determined that initial LVEDV Z-score, the presence of endocardial fibroelastosis, and aortic valve regurgitation were the most important factors governing SLVR success and failure.

The following sections describe the basis and function of the growth model, our synthetic patient population generation process, comparisons between success and failure groups, and how model results fit within the current body of clinical knowledge.

2. Methods

2.1. Model Overview

The model comprises two main components: circulation and growth. The circulation is simulated for one heartbeat using a zero-dimensional lumped parameter model. The outputs of the circulation model inform the growth model, which uses a strain-based growth law to iteratively grow the left and right ventricles (RV) at each time step (equivalent to one day). The new geometry then informs the circulation model, and the cycle continues through time (in seconds for the circulation and in days for growth) until the designated stopping point (age, in days) is reached.

2.1.1. Circulatory Model

We modified our previously published lumped parameter model of the circulation [22–24] to represent the anatomy of a patient undergoing SLVR (Figure 1). Specifically, we a) combined LV and RV outflows to simulate a Damus-Kaye-Stansel amalgamation, b) simulated a bidirectional Glenn by connecting the upper body venous compartment to the main pulmonary artery compartment, c) placed a nonlinear impedance between the atria to serve as the interatrial communication, and d) connected either the aortic compartment or the RV to the main pulmonary artery compartment to represent a modified 2.5 mm Blalock-Thomas-Taussig (mBTT) or a 4 mm RV-to-pulmonary artery (RVPA) shunt,

respectively. The circulatory model components can be classified into four categories: vessels, shunts, heart chambers, and valves.

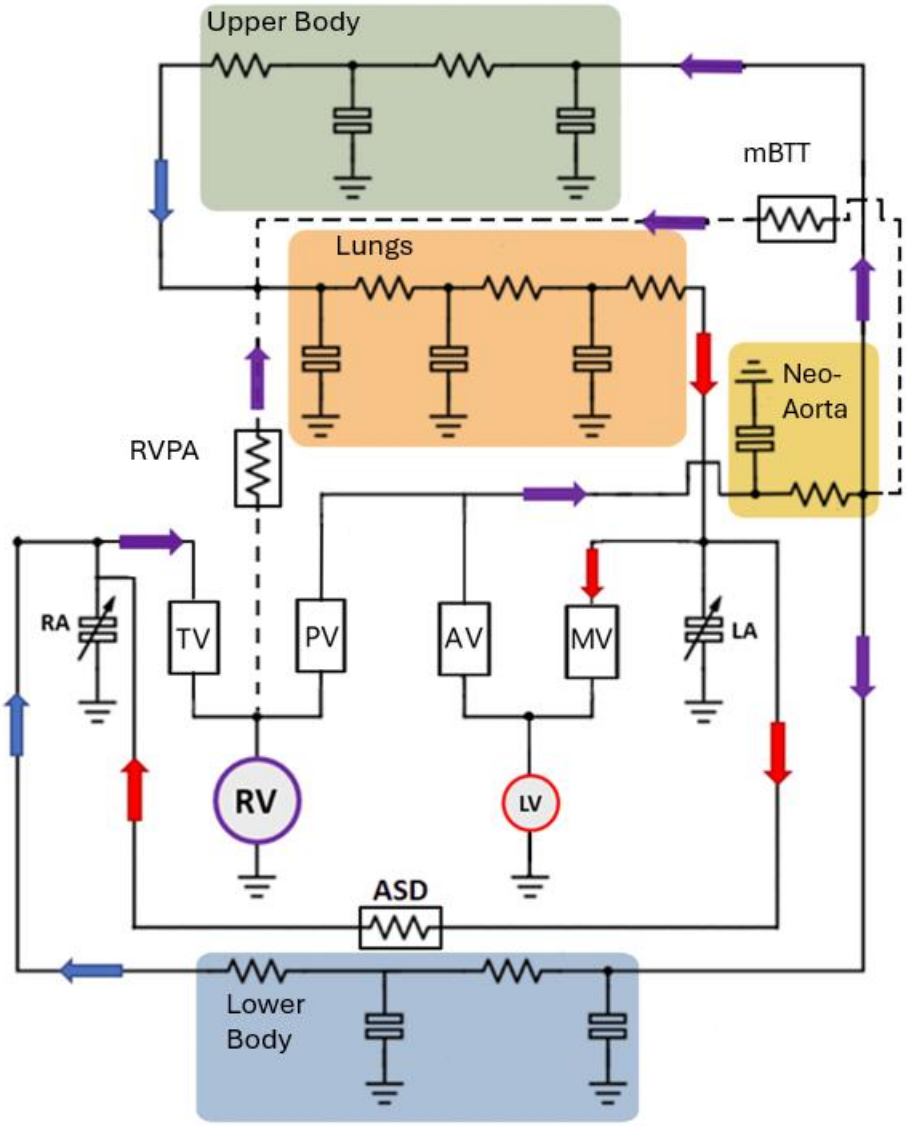

Figure 4: Schematic of the lumped parameter model simulating SLVR physiology. ASD: atrial septal defect; AV: aortic valve; LA: left atrium; LV: left ventricle; mBTT: modified Blalock-Thomas-Taussig shunt; MV: mitral valve; PV: pulmonary valve; RA: right atrium; RV: right ventricle; RVPA: right ventricle to pulmonary artery shunt; TV: tricuspid valve

Vessels

The vessels are modeled by a capacitor in parallel with a resistor. Using electrical circuit concepts, the pressure drop *ΔP* across the resistor *R* is linear, analogous to the voltage drop in Ohm's law:

$$\Delta P = Q * R \tag{1}$$

where flow *Q* is analogous to current. At each capacitor, instantaneous pressure P at time *t* during the cardiac cycle is also linear:

$$P(t) = \frac{V(t)}{C} \tag{2}$$

where $V(t)$ is the compartment volume at time *t*. The change in compartment volume throughout the cardiac cycle is simply the combined flows out of the compartment subtracted from the combined inflows:

$$\frac{dV(t)}{dt} = \sum Q_{in} - \sum Q_{out} \tag{3}$$

Shunts

The pressure drop across the ASD (R_ASD in Figure 1) is nonlinear and estimated using the ideal orifice relation (derived from Bernoulli's principle):

$$\Delta P_{ASD} = \frac{8\rho {Q_{ASD}}^2}{\pi^2 D^4} \quad (4)$$

where D is the diameter of the ASD in centimeters, Q_{ASD} is the flow between the atria, and ρ is blood viscosity (1.06 g/ml).

The pressure drop across the RVPA or mBTT shunt is given by:

$$\Delta P_{shunt} = \frac{k_1 Q_{shunt}}{D^4} + \frac{k_2 {Q_{shunt}}^2}{D^4} \quad (5)$$

where D = 2.5 mm for the mBTT shunt and 4 mm for the RVPA shunt, from the fitting process described in Section 2.2. k_1 (0.00576 mmHg*cm^4*s/ml) and k_2 (0.001872 mmHg*cm^4*s^2/ml^2) are proportionality constants, previously evaluated [25].

Heart Chambers

The four heart chambers are modeled as time-varying elastances. Instantaneous pressure P at time *t* during the cardiac cycle is:

$$P(t) = E(t)[V(t) - V_0] \quad (6)$$

where $V(t)$ is instantaneous chamber volume and V_0 is the unloaded volume, i.e., the volume axis intercept of the end-systolic pressure-volume relationship. $E(t)$ governs instantaneous, load-independent chamber elastance and reaches a maximum value of E_{ES} at end systole, where pressure is calculated as:

$$P_{ES}(t) = E_{ES} * [V_{ES}(t) - V_0] \quad (7)$$

where P_{ES} is pressure at end systole and V_{ES} is volume at end systole. The end-diastolic pressure-volume relationship is defined by an exponential function:

$$P_{ED}(t) = B * \exp[A * (V_{ED}(t) - V_0)] - B \quad (8)$$

P_{ED} and V_{ED} are end-diastolic pressure and volume, respectively, and A and B are coefficients describing the exponential shape of the end-diastolic pressure-volume relationship. Thus, combining Eqns. 6-8, instantaneous chamber pressure can be determined via:

$$P(t) = e(t) * [P_{ES}(t) - P_{ED}(t)] + P_{ED}(t) \quad (9)$$

where $e(t)$ is $E(t)$ normalized with respect to time during the cardiac cycle and amplitude, thus acting as an activation function that describes only the timing of systole and diastole.

In the model, $E(t)$ is defined as a double-Hill function:

$$E(t) = k\left(\frac{g_1}{1 + g_1}\right)\left(\frac{1}{1 + g_2}\right) + E_{min} \quad (10)$$

where

$$g_1 = \left(\frac{t}{\tau_1}\right)^{m_1}, \; g_2 = \left(\frac{t}{\tau_2}\right)^{m_2} \tag{11}$$

and

$$k = \frac{E_{max} - E_{min}}{max\left[\left(\frac{g_1}{1+g_1}\right)\left(\frac{1}{1+g_2}\right)\right]} \tag{12}$$

Values for τ_1, τ_2, m_1, m_2, E_{max}, and E_{min} are taken from [26]. The $E(t)$ vector is then divided by its maximum value to generate the normalized activation function $e(t)$ in Eqn. 9.

Valves

The valves are simulated using the model developed by Mynard et al. [26], where the net instantaneous pressure difference across each valve is governed by:

$$\Delta P = BQ|Q| + L\frac{dQ}{dt} \tag{13}$$

where B is the Bernoulli resistance:

$$B = \frac{\rho}{2{A_{eff}}^2} \tag{14}$$

And blood inertance, L, is:

$$L = \frac{\rho l_{eff}}{A_{eff}(t)} \tag{15}$$

A_{eff} is the effective cross-sectional area at time t, l_{eff} is the effective length of the valve, and Q is flow through the valve.

A_{eff} is determined by valve state ζ ($0 \leq \zeta \leq 1$, where 0 is fully closed and 1 is fully open):

$$A_{eff}(t) = \zeta(t)\left[A_{eff,max} - A_{eff,min}\right] + A_{eff,min} \tag{16}$$

where $A_{eff,max}$ is the maximum effective area:

$$A_{eff,max} = M_{rg}A_{ann} \tag{17}$$

and $A_{eff,min}$ is the minimum effective area:

$$A_{eff,min} = M_{st}A_{ann} \tag{18}$$

M_{rg} and M_{st} are constants between 0 and 1 governing regurgitation and stenosis, respectively, where a healthy ideal valve is characterized by $M_{rg} = 0$ and $M_{st} = 1$. $M_{rg} > 0$ indicates regurgitation, with larger values indicating increased severity; if $M_{rg} = 1$, the valve cannot close at all. $M_{st} < 1$ indicates stenosis, with smaller values indicating increased severity; if $M_{st} = 0$, the valve is atretic. A_{ann} is the valve annulus size.

Opening and closing rates are driven by the pressure gradient across the valve—as the gradient increases, the valve opens or closes faster, slowing as the valve nears a fully closed or open state. The rate of opening, which begins when ΔP exceeds the opening pressure threshold ΔP_{open}, is given by:

$$\frac{d\zeta}{dt} = (1-\zeta)K_{vo}\left(\Delta P - \Delta P_{open}\right) \tag{19}$$

where K_{vo} is a rate coefficient for valve opening. When ΔP is less than closing pressure threshold ΔP_{close}, the rate of closure is given by:

$$\frac{d\zeta}{dt} = \zeta K_{vc}(\Delta P - \Delta P_{close}) \tag{20}$$

where K_{vc} is a rate coefficient for valve closing.

A flowchart of the circulation model operation is shown in Figure 2. The circulation model is initialized by assuming the initial volumes for the 12 compartments are equal. Next, initial vessel and chamber pressures are solved using Eqns. 2 and 6, respectively, at the beginning of the cardiac cycle. Then a 4th order fixed-step Runge-Kutta method determines compartmental volumes, pressures, valve states, and valve flows throughout the cardiac cycle for 5000 time steps using Eqns. 3, 13, 19, and 20. Next, there is a check to determine if steady state has been reached, defined as volumes at the end of the cardiac cycle being within 0.1% of the volumes at the start. If steady state has not been achieved, initial

volumes are set to the current ending volumes, and the process begins again. If steady state has been reached, the outputs of the circulation model are used for the growth model.

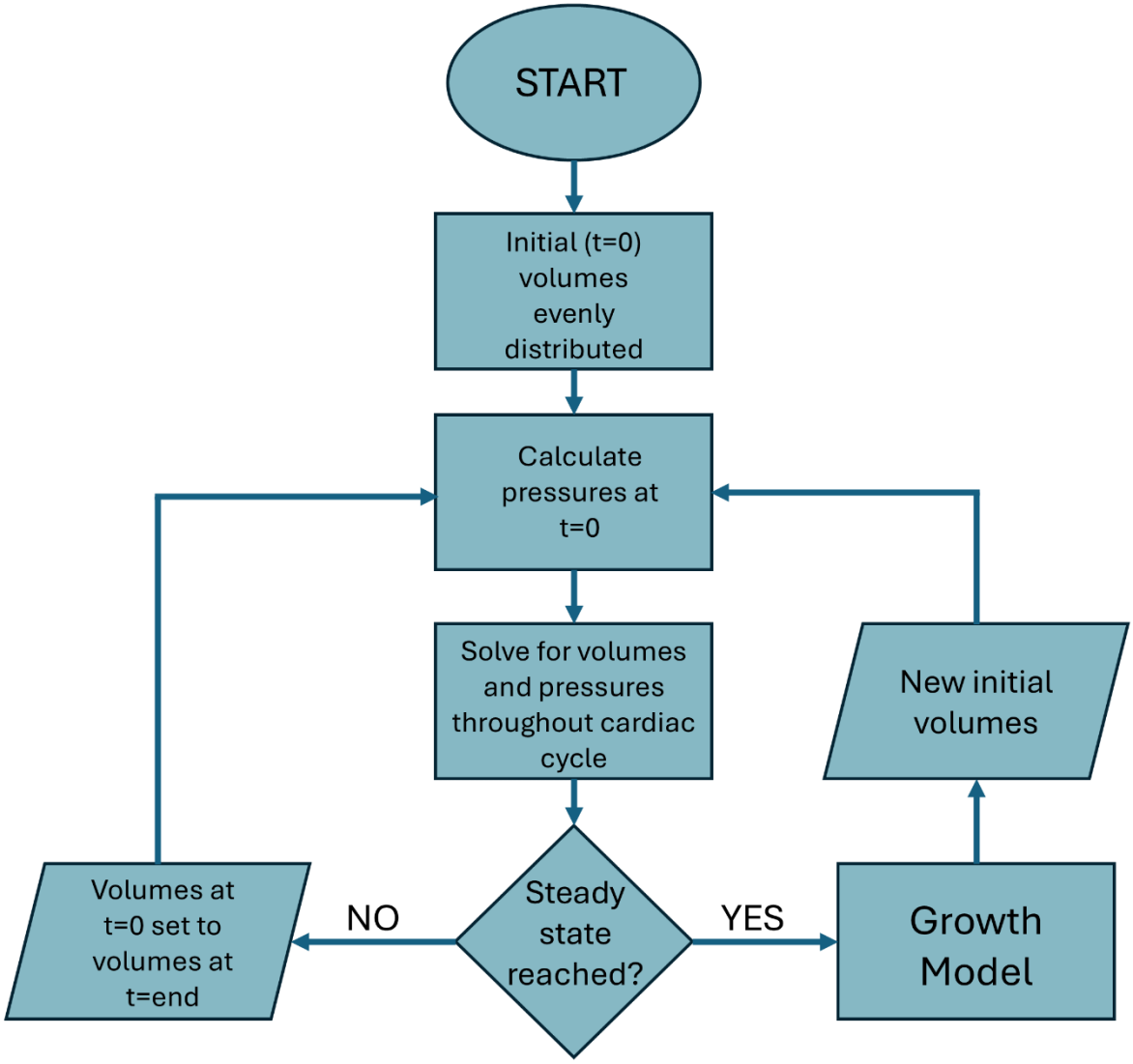

Figure 5: Flowchart of circulation model operation

2.1.2. Growth Model

Two types of ventricular growth are considered in the model: normal somatic growth and pathologic growth. As pathologic growth is determined by comparing ventricular strains to homeostatic strains, somatic growth for an equivalent-sized healthy infant must be simulated prior to a pathologic growth simulation to generate a trajectory of homeostatic strain setpoints. These setpoints are then used in the pathologic simulation to determine how much pathologic growth (or atrophy) to superimpose onto somatic growth.

Somatic Growth

The circulatory model operates in a timescale of seconds, across a single heartbeat. Growth, however, is on a timescale of days, months, and years. To account for this, model parameters must change over the growth simulation period. First, an input parameter set is generated using weight-based allometric scaling [27]:

$$Y_i = Y_0 * \left(\frac{W_i}{W_0}\right)^b \tag{21}$$

where Y is the parameter under consideration, W is weight, and b is a scaling factor. The subscripts *i* and *0* indicate the current (infant) subject and the reference (adult) subject, respectively. Infant weights are taken from the World Health Organization's weight-for-age charts from 6-24 months [28]. Male and female values are averaged together and then linearly interpolated to create weights for each day, using the 25th percentile to capture the typically smaller size of patients with severe CHDs [29, 30]. Scaling factor b is -0.75 for

resistances and 1 for capacitances [27, 31]. Systemic and pulmonary resistances (*SVR, PVR, Rvs, Rvp)* and capacitances (*Cas, Cap, Cvs, Cvp*) are distributed as described in [22].

For the ventricular parameters (A, B, E_{ES}, and V_0 in Eqns. 7-8), unit analysis is used to determine appropriate scaling factors, assuming pressures do not scale and volumes scale linearly with weight [31]: B (mmHg) is unscaled, A (ml^{-1}) has a scaling factor of -1, E_{ES} (mmHg/ml) has a scaling factor of -1, and V_0 (ml) has a scaling factor of 1.

For the valves, trajectories of annulus sizes (A_{ann} in Eqns. 17-18) are generated using Z-score formulations from Cantinotti et al. [32]:

$$Measurement = BSA^{B} * \exp(SEE * Z + Intercept) \quad (22)$$

Body surface area is calculated using the Haycock formula [33] and 25th percentile weights and heights. Z-scores for all valves are assumed to be 0. Valve parameter reference values are from Mynard et al. [26], and scaling factors for K_{vc}, K_{vo}, and aortic l_{eff} are from Zhang et al. [34], adjusted for an adult reference weight of 70 kg. Scaling factors for mitral, tricuspid, and pulmonary l_{eff} were manually adjusted to produce appropriate valve opening and closing patterns [35–37]. Somatic input parameters with adult reference values, scaling factors, and initial (6 month) values can be found in Table 1.

Table 1: Parameters used in the circulation model to simulate somatic growth from 6-24 months, assuming a starting infant weight of 7.05 kg

Parameter	Units	Reference Value for Scaling (70 kg adult)	Scaling Factor	Initial (6 month) value
Systemic vascular resistance (SVR)	mmHg*s/ml	0.5715	-0.75	3.1967
Pulmonary vascular resistance (PVR)	mmHg*s/ml	0.0314	-0.75	0.1757
Systemic arterial capacitance (Cas)	ml/mmHg	2.1751	1	0.2191
Pulmonary arterial capacitance (Cap)	ml/mmHg	2.7362	1	0.2756
Pulmonary venous resistance (Rvp)	mmHg*s/ml	0.00586	-0.75	0.0328
Systemic venous resistance (Rvs)	mmHg*s/ml	0.00586	-0.75	0.0328
Pulmonary venous capacitance (Cvp)	ml/mmHg	10.5	1	1.058
Systemic venous capacitance (Cvs)	ml/mmHg	59.5	1	5.993
MPA:PA Ratio	-	8	0	8
Aorta:SA Ratio	-	16	0	16
LB:UB Arteries Ratio	-	1	0	1
LB:UB Veins Ratio	-	1	0	1
Exponential stiffness coefficient (A)	1/ml	0.0235 (LV) 0.0235 (RV) 0.0525 (LA)	-1	0.2333 (LV) 0.2333 (RV) 0.5213 (LA)

		0.0525 (RA)		0.5213 (RA)
Linear stiffness coefficient (B)	mmHg	0.175 (LV) 0.175 (RV) 0.44 (LA) 0.44 (RA)	0	0.175 (LV) 0.175 (RV) 0.44 (LA) 0.44 (RA)
Unloaded volume (V_0)	ml	17.5 (LV) 29.732 (RV) 9.333 (LA) 9.333 (RA)	1	1.7625 (LV) 2.9944 (RV) 0.94 (LA) 0.94 (RA)
End-systolic elastance (E_{ES})	mmHg/ml	5.1852 (LV) 2.0741 (RV) 0.86 (LA) 0.66 (RA)	-1	19.8582 (LV) 7.9433 (RV) 8.539 (LA) 6.553 (RA)
Aortic capacitance (Cao)	ml/mmHg	2.0474	1	0.2062
Stressed blood volume (SBV)	ml	875	1	88.1250
Valve opening coefficient (K_{vo})	dyne*cm^2/s	0.0124 (AV) 0.0310 (MV) 0.0621 (TV) 0.0207 (PV)	-0.5	0.0391 (AV) 0.0978 (MV) 0.1957 (TV) 0.0652 (PV)
Valve closing coefficient (K_{vc})	dyne*cm^2/s	0.0124 (AV) 0.0414 (MV) 0.0414 (TV) 0.0207 (PV)	-0.5	0.0391 (AV) 0.1305 (MV) 0.1305 (TV) 0.0652 (PV)
Valve effective length (l_{eff})	cm	0.9695 (AV) 1.8667 (MV) 1.9055 (TV) 1.4293 (PV)	0.45 (AV) 1 (MV) 0.7 (TV) 0.7 (PV)	0.3451 (AV) 0.1880 (MV) 0.3821 (TV) 0.2866 (PV)

AV: aortic valve; LA: left atrium; LB: lower body; LV: left ventricle; MPA: main pulmonary artery; MV: mitral valve; PA: pulmonary arteries (distal); PV: pulmonary valve; RA: right atrium; RV: right ventricle; SA: systemic arteries; TV: tricuspid valve; UB: upper body

To account for changes in geometry with growth, analytic expressions based on the relationships between strain and volume and stress and pressure in a thin-walled sphere were developed that relate material parameters a, b, and e to ventricular parameters A, B, and E_{ES} [23, 38]:

$$a = \frac{4\pi}{3} A^i \left({r_{0s}}^i * {F_{g,f}}^i \right)^3 \tag{23}$$

$$b = \frac{B^i}{2} * \frac{{r_{0s}}^i * {F_{g,f}}^i}{{h_{0s}}^i * {F_{g,r}}^i} \tag{24}$$

$$e = \frac{2\pi}{3} {E_{ES}}^i \frac{\left({r_{0s}}^i * {F_{g,f}}^i \right)^4}{{h_{0s}}^i * {F_{g,r}}^i} \tag{25}$$

Where $r_{0,s}{}^i$ and $h_{0,s}{}^i$ indicate the ventricle's homeostatic unloaded radius and thickness at each day i, respectively, and $F_{g,f}$ and $F_{g,r}$ are components of the pathologic growth deformation tensor $\boldsymbol{F_g}$, described in detail in the following section. All components of $\boldsymbol{F_g}$ are set to 1 for the duration of a somatic growth simulation.

Using the scaled vectors of V_0 and B, $r_{0,s}{}^i$ and $h_{0,s}{}^i$ are generated for the full 6-24 month growth period:

$${r_{0,s}}^i = \left(\frac{3}{4\pi} {V_0}^i \right)^{\frac{1}{3}} \tag{26}$$

$$h_{0,s}{}^{i} = \frac{B^{i}}{2} * \frac{* r_{0,s}{}^{i}}{* b} \tag{27}$$

Material property b is set to 0.0379 for the LV and 0.0975 for the RV to produce indexed LV and RV masses in line with reported measurements in healthy 6 month children [39, 40]. a and e are then calculated using Eqns. 23 and 25. Note that material parameters are held constant throughout growth.

Initial values of $h_{0,s}$ and $r_{0,s}$ are then passed into the circulatory model, where they are loaded using the ventricular volumes throughout the cardiac cycle:

$$r = \left(\frac{3}{4\pi} * V(t)\right)^{\frac{1}{3}} \tag{28}$$

$$h = (h_{0,s}{}^{3} + 3h_{0,s}{}^{2} * r_{0,s} + 3h_{0,s} * r_{0,s}{}^{2} + r^{3})^{\frac{1}{3}} - r \tag{29}$$

Next, circumferential strain within the ventricular wall in the direction of the myofibers is calculated, again assuming $F_{g,f}$ and $F_{g,r}$ = 1. The maximum value is saved as the homeostatic strain setpoint for day *i*, to be used in the pathologic growth simulation:

$$E_{f,set}{}^{i} = max\left(\left[0.5 * \frac{r}{r_{0,s}{}^{i}} * \frac{1}{F_{g,f}{}^{i}}\right]^{2} - 0.5\right) \tag{30}$$

Similarly, the strain setpoint along the radius of the myofibers (across the ventricular wall), $E_{r,set}$, is given by:

$$E_{r,set}{}^{i} = max\left(\left[0.5 * \frac{h}{h_{0,s}{}^{i}} * \frac{1}{F_{g,r}{}^{i}}\right]^{2} - 0.5\right) \quad (31)$$

Pathologic Ventricular Growth

Ventricular growth is simulated by a modified version of the strain-based growth law proposed by Kerckhoffs et al. for predicting pathologic concentric and eccentric cardiac hypertrophy [21]. The Kerkhoffs model decomposes the total deformation gradient $\boldsymbol{F}$ into growth deformation tensor $\boldsymbol{Fg}$, which describes dimensional changes due to addition or subtraction of material in a stress-free (unloaded) state, and elastic deformation tensor $\boldsymbol{Fe}$, which restores continuity by introducing residual stress.

Once a pathologic physiology is imposed in the circulatory model, resulting ventricular strains will differ from somatic values. To determine $\boldsymbol{Fg}$, maximum strains are determined using Eqns. 30-31. The difference between maximum pathologic E_{ff} and the homeostatic fiber strain setpoint $E_{f,set}$ produces the stimulus for growth along the myofiber axis (lengthening), s_l:

$$s_l{}^{i} = \max\left(E_{ff}{}^{i}\right) - E_{f,set}{}^{i} \quad (22)$$

Note that maximum E_{ff} typically occurs at end diastole.

In the radial direction, maximum pathologic E_{rr} is used with the homeostatic radial strain setpoint $E_{r,set}$ to produce the stimulus for fiber radial growth (thickening), s_t:

$$s_t{}^i = \max\left(E_{rr}{}^i\right) - E_{r,set}{}^i \tag{24}$$

where maximum E_{rr} typically occurs at end systole. Strain within the plane of the ventricular wall and perpendicular to the fibers (E_{cc}) is assumed equal to E_{ff}, and cross-fiber radial shear (E_{cr}) is assumed to be zero.

These stimuli are used to compute the components of $\boldsymbol{Fg}^{i+1}$:

$$F_{g,f}{}^{i+1} = F_{g,cc}{}^{i+1} \begin{cases} F_{g,f}{}^i * \sqrt{\dfrac{f_{ff,max}}{1+\exp\left(-f_f * \left(s_l{}^i - s_{l,50}\right)\right)} + 1} & s_l{}^i \geq 0 \\ F_{g,f}{}^i * \sqrt{\dfrac{-f_{ff,max}}{1+\exp\left(f_f * \left(s_l{}^i + s_{l,50}\right)\right)} + 1} & s_l{}^i < 0 \end{cases} \tag{25}$$

$$F_{g,r}{}^{i+1} = \begin{cases} F_{g,r}{}^i * \left[\dfrac{f_{rr,max}}{1+\exp\left(-r_{f,positive} * \left(s_t{}^i - s_{t,50,positive}\right)\right)} + 1\right] & s_t{}^i \geq 0 \\ F_{g,r}{}^i * \left[\dfrac{-f_{rr,max}}{1+\exp\left(r_{f,negative} * \left(s_t{}^i + s_{t,50,negative}\right)\right)} + 1\right] & s_t{}^i < 0 \end{cases} \tag{26}$$

Parameters $f_{ff,max}$, $f_{rr,max}$, f_f, $r_{f,positive}$, $r_{f,negative}$, $s_{l,50}$, $s_{t,50,positive}$, and $s_{t,50,negative}$ are fitted to longitudinal mass and volume data of SLVR patients (see Section 2.2 for details). Then, $\boldsymbol{Fg}^{i+1}$ is used to update the unloaded pathologic configuration:

$$r_0{}^{i+1} = r_{0,s}{}^{i} * F_{g,f}{}^{i+1} \tag{27}$$

$$h_0{}^{i+1} = h_{0,s}{}^{i} * F_{g,r}{}^{i+1} \tag{28}$$

Connecting Growth to Circulation

This new grown state is then loaded at day *i* by the circulatory model, and cavity volume and wall thickness are computed throughout the cardiac cycle once the circulatory model reaches steady state.

Hoop stress in a thin-walled spherical pressure vessel is given by:

$$\sigma_{hoop} = \frac{r}{2h} * P \tag{29}$$

where P is pressure, r is radius, and h is thickness. Using Eqns. 7-8, the hoop stresses at end systole and end diastole at each day *i* become:

$$\sigma_{hoop,ES}{}^{i} = \frac{r_{ES}{}^{i}}{2h_{ES}{}^{i}} * E_{ES}{}^{i} * \left(V_{ES}{}^{i} - V_0{}^{i}\right) \tag{30}$$

$$\sigma_{hoop,ED}{}^{i} = \frac{r_{ED}{}^{i}}{2h_{ED}{}^{i}} * B^{i} * \left(\exp\left[A^{i} * \left(V_{ED}{}^{i} - V_0{}^{i}\right)\right] - 1\right) \tag{31}$$

As the ventricle grows, a constant relationship is maintained between hoop stress and stretch at end diastole and end systole, which requires the material properties of the

ventricle and its passive and active behavior to remain constant. To achieve this, the parameters governing the pressure-volume behavior of the ventricle (A, B, E_{ES}, and V_0) must change at each day i. First, Eqns. 30-31 are rewritten in terms of stretch:

$$\sigma_{hoop,ES}{}^{i} = \frac{r_{ES}{}^{i}}{r_{0,s}{}^{i}} * \frac{h_{0,s}{}^{i}}{h_{ES}{}^{i}} * \frac{F_{g,r}{}^{i}}{F_{g,f}{}^{i}} * e * \left[\left(\frac{r_{ES}{}^{i}}{r_{0,s}{}^{i}} * \frac{1}{F_{g,f}{}^{i}}\right)^{3} - 1\right] \tag{32}$$

$$\sigma_{hoop,ED}{}^{i} = \frac{r_{ED}{}^{i}}{r_{0,s}{}^{i}} * \frac{h_{0,s}{}^{i}}{h_{ED}{}^{i}} * \frac{F_{g,r}{}^{i}}{F_{g,f}{}^{i}} * b * \left(exp\left[a * \left(\frac{r_{ED}{}^{i}}{r_{0,s}{}^{i}} * \frac{1}{F_{g,f}{}^{i}}\right)^{3} - a\right] - 1\right) \tag{33}$$

where a, b, and e are material properties governing the nonlinear relationships between circumferential and radial stretches and hoop stress at end diastole and end systole. Assuming a, b, and e are unchanged with growth, A, B, E_{ES}, and V_0 for day i+1 can be determined using the new grown values of r_0 and h_0:

$$A^{i+1} = a * \frac{3}{4\pi} * \left(\frac{1}{r_0{}^{i+1}}\right)^{3} \tag{34}$$

$$B^{i+1} = 2 * b * \frac{h_0{}^{i+1}}{r_0{}^{i+1}} \tag{35}$$

$$E_{ES}{}^{i} = \frac{3}{2\pi} * e * \frac{h_0{}^{i+1}}{(r_0{}^{i+1})^{4}} \tag{36}$$

$$V_0{}^{i} = \frac{4\pi}{3} * \left(r_0{}^{i+1}\right)^{3} \tag{37}$$

Circulatory Adaptation

Throughout growth, stressed blood volume (SBV) is adjusted to maintain mean arterial pressure (MAP) within 0.2% of the previous day's value. While MAP is outside of the 0.2% threshold, the model adjusts SBV until 20 attempts are made or SBV exceeds the current day's weight*75, i.e., all the blood in the body is contributing to vessel and chamber wall stress [41].

2.2. Parameterization and Baseline BLH Patient

We determined a generalized "baseline" BLH patient undergoing SLVR, which was later customized to create the synthetic patient population.

2.2.1. Fitting 6-month BLH Circulation

First, to replicate the unique hemodynamics of BLH patients with a reduced parameter set, a local sensitivity analysis was performed by varying parameters uniformly around their reference value (-50%, -25%, +50%, +100%) and noting how the model's 6-month hemodynamic outputs (atrial and ventricular pressures, Qp:Qs, ventricular volumes, systemic and pulmonary blood pressures) changed. The 13 parameters with the overall largest effects on the greatest number of outputs were selected for adjustment: SVR, PVR, A_{LV}, A_{RV}, B_{LV}, B_{RV}, $V_{0,LV}$, $V_{0,RV}$, $E_{ES,LV}$, $E_{ES,RV}$, A_{LA}, aortic capacitance (Cao), and SBV. Using the *fminsearchbnd* MATLAB function [42], the 13 parameters were optimized simultaneously by iteratively adjusting their reference values ($Y0$ in Eqn. 21), using their somatic values as initial conditions. The fitting process concluded when the weighted sum-squared error between d number of model outputs Y and literature values $\hat{Y}$ was minimized:

$$\min\left[\sum_{i=1}^{d}\left(\frac{Y_i - \hat{Y}_i}{\sigma}\right)^2\right] \tag{42}$$

Model outputs included in the fitting process were: LV end-diastolic and end-systolic volumes [8], LV ejection fraction [8], the pressure gradient across the ASD [8], left atrial pressure [43], LVEDP [43], RV end-diastolic and end-systolic volumes [44], RV end-diastolic and end-systolic pressures [44], systolic and diastolic systemic blood pressure [44], and mean pulmonary arterial pressure [44]. In addition, systemic vascular resistance (SVR), pulmonary vascular resistance (PVR), and shunt diameters were refit for the two shunt options (mBTT and RVPA). A list of fitted parameters can be found in Table 2 and fitted model outputs (without the optional RVPA or mBTT shunt) compared to literature data are shown in Table 3.

Table 2: Parameters fitted to BLH patient data

Parameter	Units	Initial (6 month) value, Somatic	Initial (6 month) value, BLH
Systemic vascular resistance (SVR)	mmHg*s/ml	3.1967	2.593 (no shunt) 3.439 (RVPA) 4.929 (mBTT)
Pulmonary vascular resistance (PVR)	mmHg*s/ml	0.1757	0.4316 (no shunt) 0.2377 (RVPA) 0.2503 (mBTT)
A_{LV}	1/ml	0.2333	0.4687
A_{RV}	1/ml	0.2333	0.1321
B_{LV}	mmHg	0.175	0.2188
B_{RV}	mmHg	0.175	0.2851
$V_{0,LV}$	ml	1.7625	0.4000
$V_{0,RV}$	ml	2.9944	3.743
$E_{ES,LV}$	mmHg/ml	19.8582	22.618
$E_{ES,RV}$	mmHg/ml	7.9433	5.8621
A_{LA}	1/ml	0.5213	0.9590
Aortic capacitance (Cao)	ml/mmHg	2.0474	0.1447
Stressed blood volume (SBV)	ml	875	129.9
Diameter, RVPA shunt	cm	0.4	N/A
Diameter, mBTT shunt	cm	0.25	N/A

LV: left ventricle; mBTT: modified Blalock-Thomas-Taussig; LA: left atrium; RA: right atrium; RV: right ventricle; RVPA: right ventricle to pulmonary artery;

A standard value of 4 mm was chosen for the initial ASD diameter [8]. To represent the gradual closure of the ASD due to fibrin deposition and growth of surrounding tissues [3, 9], the diameter is linearly reduced to produce a 5 mmHg pressure gradient 30 days after initiation of recruitment [8], resulting in a diameter 44% of its original size at Day 30. Closure is then slowed, resulting in a final 24-month ASD diameter 38% of its original size.

Because simulation begins at 6 months of age and BLH develops in utero, we assumed patients would already have some amount of pathologic growth, i.e., the initial values of $\boldsymbol{Fg}$ would not equal 1. Therefore, after generating fitted BLH vectors of ventricular parameters A, B, E_{ES}, and $V0$, the initial values of $F_{g,f}$ and $F_{g,r}$ as well as material properties a and e are solved by rearranging and solving Eqns. 34-37. Material property b is set to 0.0480 for the LV and 0.0975 for the RV to produce masses in line with literature data of children with hypoplastic left heart syndrome and measurable LVs [44].

2.2.2. Simulating BLH Growth

Heart rate throughout growth is determined by taking the 50th percentile heart rates by Fleming et al. [45] and allometrically scaling them using 50th percentile weights as reference values and a scaling factor of -0.25 [31].

The pathologic LV growth parameters detailed in Eqns. 25-26 also required fitting for both the BLH LV and RV. Due to the timeframes of available literature data, the growth simulation was temporarily extended from 24 months to 28 months during fitting. Growth parameters were manually adjusted until indexed LV mass, RV mass, LVEDV, and RVEDV at 28 months fell within the interquartile range reported by Marathe et al. [16]. Results of the

fitting process can be found in Table 3, and final growth parameter values are listed in Table 4.

Table 3: Comparison of fitted model outputs to literature data of BLH patients

Fitting Circulatory Parameters (6 Months)			
Output	**Literature Value**	**Model Value**	**% Error**
LV ED volume (ml)	8.63 ± 1.12	8.67	0.46%
LV ES volume (ml)	4.23 ± 4.23	4.73	11.8%
LV ejection fraction (%)	51 ± 5	46	9.8%
ASD pressure gradient (mmHg)	5 ± 1	4	20.0%
Left atrial pressure (mmHg)	11 ± 3	10	9.1%
LV ED pressure (mmHg)	11 ± 3	9	18.2%
LV mass, indexed (g/m^2)	9.88 ± 6.4	10.34	4.7%
RV ED volume (ml)	23.75 ± 6.25	25.29	6.5%
RV ES volume (ml)	12.99 ± 4.10	15.03	15.7%
RV ED pressure (mmHg)	8.44 ± 3.01	8.97	6.3%
RV ES pressure (mmHg)	87.92 ± 16.19	97.71	11.1%
RV mass, indexed (g/m^2)	40.07 ± 9.95	36.3	9.4%
Systolic blood pressure (mmHg)	86.84 ± 13.15	87.66	0.94%
Diastolic blood pressure (mmHg)	45.93 ± 12.20	47.70	3.9%
Mean pulmonary arterial pressure (mmHg)	13 ± 2.5	11	15.4%
Fitting Growth Parameters (28 Months)			
Output	**Literature Value**	**Model Value**	**% Error**
LV ED volume, indexed (ml/m^2)	31.5 (IQR: 23.9-40.2)	28.7	8.9%
LV ES volume, indexed (ml/m^2)	11.94 (IQR: 8.17-16.01)	12.02	0.67%
LV mass, indexed (g/m^2)	26.1 (IQR: 19.7-34.9)	26.1	0%
RV ED volume, indexed (ml/m^2)	106.67 (IQR: 82.70-119.83)	81.04	24.0%
RV ES volume, indexed (ml/m^2)	43.75 (32.34-54.89)	60.72	38.8%
RV mass, indexed (g/m^2)	38.8 (29.52-41.89)	40.81	5.2%

ASD: atrial septal defect; ED: end diastole; ES: end systole; LV: left ventricle; RV: right ventricle.

Table 4: Growth parameters and values

Parameter	Left Ventricle	Right Ventricle
$F_{ff,max}$	0.003	0.071
$F_{rr,max}$	0.055	0.032
f_f	31	31
$r_{f,positive}$	36.42	36.42
$r_{f,negative}$	575.7	575.7
$s_{l,50}$	1.354	0.549
$s_{t,50,positive}$	0.267	0.428
$s_{t,50,negative}$	0.034	0.034

2.3. Generating Synthetic Patient Population

To capture the wide variety of phenotypes in BLH patients, 10 metrics associated with BLH, along with their diagnostic ranges if applicable, were used to create a synthetic patient population [8, 18, 46, 47] (Table 5). Included metrics are mitral and aortic valve annulus Z-scores, presence of mitral, aortic, and tricuspid valve regurgitation (MR, AR, and TR, respectively), presence of mitral and aortic stenosis (MS and AS, respectively), optional mBTT or RVPA shunt, ASD size, and initial LVEDV Z-score. For each simulated patient, values for each of the metrics are randomly selected from a uniform distribution inclusive of endpoints. Continuous variables (valve annulus Z-scores, initial ASD size, LVEDV Z-scores) are linearly spaced by 0.1. Annulus Z-scores are input into Eqn. 22 directly to determine the full 6-24 month trajectory of annulus sizes. Valve regurgitation and valve stenosis are simulated using M_{rg} and M_{st} from Eqns. 17-18, respectively (Table 6); values were determined by manually adjusting M_{rg} and M_{st} in the baseline model until appropriate regurgitant fraction (regurgitation) or pressure difference across the valve (stenosis) were produced, based on current diagnostic criteria [48, 49]. Shunt type is controlled by a simple flag (0 = no shunt, 1 = mBTT, 2 = RVPA) dictating the appropriate lumped parameter model geometry (Figure 1). ASD diameter is input into Eqn. 4 and subjected to the same two-part gradual reduction as in the baseline BLH model. With the exception of the LVEDV Z-score, all metrics are implemented directly in the model. As LVEDV is a model output rather than an input, *fminsearchbnd* is used to optimize the LV ventricular parameters (A, B, E_{ES}, V_0) to produce the desired LVEDV prior to growth (at age 6 months), using the baseline

BLH values as initial conditions. If the target LVEDV cannot be produced within 2%, the combination of input metrics is rejected and a new patient is generated.

Next, a high-throughput computing system [50] simultaneously simulated ventricular growth for the 5,306 synthetic patients from 6-24 months of age, utilizing the pathologic ventricular growth parameters fitted for baseline BLH. The randomized input metrics, unloaded and loaded ventricular geometry, and hemodynamic outputs for each synthetic patient were saved at the beginning and endpoint of growth for further analysis.

Then, to investigate the effects of endocardial fibroelastosis (EFE), an additional 3,000 patients were generated using the same randomly distributed 6-month input metrics and varying severity of EFE (1,000 patients each for mild, moderate, and severe grades). As the diagnosis of EFE is qualitative rather than quantitative, EFE is simulated by either doubling (mild), tripling (moderate), or quadrupling (severe) passive LV stiffness parameter B and associated material property b after the initial values are determined for the patient's randomly assigned LVEDV Z-score.

Table 5: Randomized BLH metrics

Metric	Range
Mitral valve annulus Z-score	-2.0 to -5.0
Aortic valve annulus Z-score	-2.0 to -5.0
Mitral regurgitation	Absent, Mild, Moderate, Severe
Aortic regurgitation	Absent, Mild, Moderate, Severe
Tricuspid regurgitation	Absent, Mild, Moderate, Severe
Mitral stenosis	Absent, Mild, Moderate, Severe
Aortic stenosis	Absent, Mild, Moderate, Severe
Initial ASD size	2.0 to 6.0 mm
Shunt type	None, mBTT, RVPA
LVEDV Z-score	-0.5 to -5.0

ASD: atrial septal defect; LVEDV: left ventricular end-diastolic volume

Table 6: Values of Mrg and Mst used to produce grades of regurgitation and stenosis

	Absent	**Mild**	**Moderate**	**Severe**
MV_Mrg	0	0.005	0.026	0.07
AV_Mrg	0	0.01	0.05	0.15
TV_Mrg	0	0.006	0.03	0.09
MV_Mst	1	0.5	0.1	0.025
AV_Mst	1	0.5	0.2	0.15

AV: aortic valve; MV: mitral valve; TV: tricuspid valve

2.4. Assessing Staged Left Ventricular Recruitment Success in the Model

After simulating ventricular growth, patients were separated into three groups (Success, Failure, and Non-Physiologic) using their 24-month hemodynamics. Group designation was based on SLVR success criteria and consultation with our clinical collaborators:

- SLVR Success [9]
    - LVEDVi > 40 ml/m^2, and
    - LVEDP < 13 mmHg
- SLVR Failure [9]
    - LVEDVi <= 40 ml/m^2, or
    - LVEDP >= 13 mmHg
- Non-physiologic
    - SBP < 60 mmHg, or
    - CO < 1.5 L/m2, or
    - LVEDV Z-score > 5, or
    - LVEDP < 2 mmHg, or
    - LVEDP > 20 mmHg

Mann-Whitney U tests were performed on continuous variables (valve annulus Z-scores, initial ASD size, LVEDV Z-scores) and Chi-squared tests with post-hoc Bonferroni correction were performed on categorical variables (valve regurgitation, stenosis, and shunt type). To examine patterns within each group (e.g., whether some categories occurred more frequently than others within the same group), pairwise two-proportion z-

tests were performed between categories, also corrected for multiple comparisons using Bonferroni adjustment.

Finally, we used a Random Forest algorithm (MATLAB function *fitcensemble* with bootstrap aggregation) to create a predictive machine learning model, using the 10 random phenotype variables as features and SLVR success or failure as labels. Each tree was built using random subsets of predictors to reduce overfitting and improve model generalizability. Categorical variables were encoded as ordinal or one-hot numeric features prior to training. All continuous features were standardized to zero mean and unit variance. The machine learning model performance was assessed using 5-fold cross-validation, and classification error was quantified as the average misclassification rate across folds. Out-of-bag error estimates were also obtained as an internal validation metric. Feature importance was evaluated using out-of-bag permuted predictor importance, which measures the decrease in classification accuracy when each feature is randomly permuted.

3. Results

3.1. Group Designation: Success, Failure, and Non-Physiologic

After the growth simulation concluded, synthetic BLH patients (n = 5,306) were separated into groups as discussed in Section 2.4 (Figure 3): non-physiological (n = 3,664), SLVR success (n = 903), and SLVR failure (n = 739).

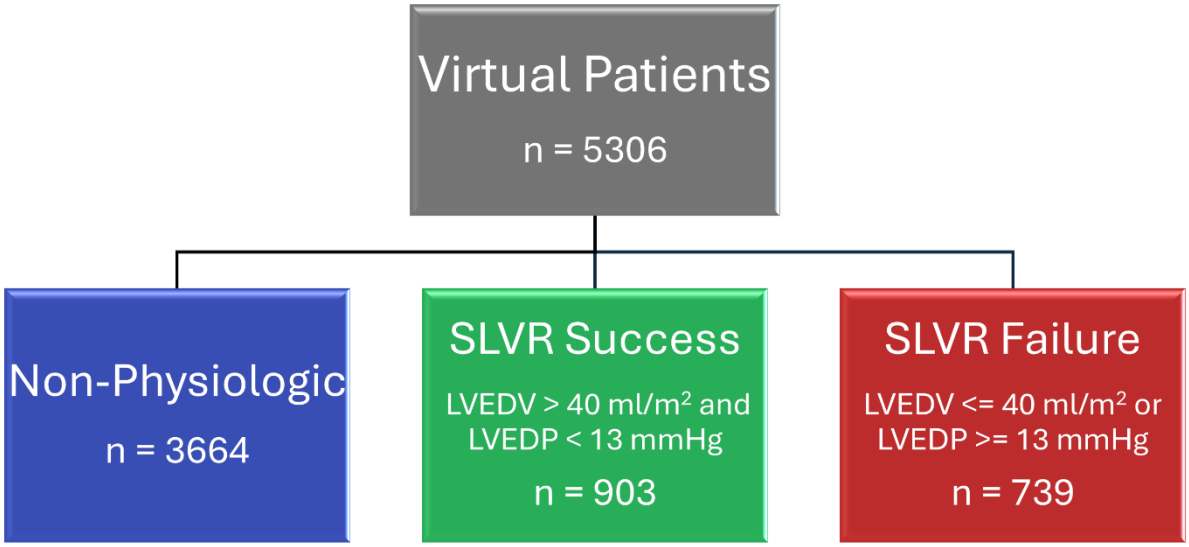

Figure 3: Group designation for synthetic patient population

In general, hemodynamics and ventricular dimensions were statistically significantly different between the success and failure groups, though differences were not always clinically significant (Table 7). For example, despite a *p*-value < 0.001, median indexed RV mass had only a 0.03 g/m^2 difference between groups and a relatively modest effect size of r = 0.25. In contrast, mean pulmonary arterial pressure had a 9.64 mmHg difference between groups and a larger effect size of r = -0.60.

Table 7: Comparison of 24-month model outputs for SLVR success and failure groups

24 Month Output	Success Group	Failure Group	*p*-value	r
SBP (mmHg)	78.16 (IQR: 69.48-87.35)	69.72 (IQR: 65.03-76.35)	< 0.001	0.36
DBP (mmHg)	37.48 (IQR: 29.92-43.65)	38.02 (IQR: 33.54-41.27)	0.961	0
MPAP (mmHg)	11.18 (IQR: 9.54-14.74)	20.82 (IQR: 17.51-26.04)	< 0.001	-0.60
LAP (mmHg)	9.97 (IQR: 7.20-14.15)	19.91 (IQR: 16.36-25.76)	< 0.001	-0.58
LVESP (mmHg)	102.33 (IQR: 84.33-134.95)	78.03 (IQR: 67.78-91.64)	< 0.001	0.44
LVEDP (mmHg)	5.60 (IQR: 3.51-7.43)	9.85 (IQR: 6.48-15.98)	< 0.001	-0.49
RVESP (mmHg)	79.18 (IQR: 68.36-89.57)	70.16 (IQR: 64.44-78.12)	< 0.001	0.29
LVEDVi (ml/m^2)	64.88 (IQR: 51.52-87.63)	29.55 (IQR: 22.59-39.08)	< 0.001	0.68
LVEDV Z-Score	1.37 (IQR: 0.42 to 2.60)	-1.86 (IQR: -2.96 to -0.71)	< 0.001	0.86
LV mass, indexed (g/m^2)	37.50 (IQR: 28.47-59.47)	19.23 (IQR: 14.62-25.75)	< 0.001	0.60
RV mass, indexed (g/m^2)	40.23 (IQR: 40.20-40.36)	40.20 (IQR: 40.19-40.25)	< 0.001	0.25
LVEDd (cm)	1.99 (IQR: 1.85-2.20)	1.53 (IQR: 1.40-1.68)	< 0.001	0.68

SBP: Systolic blood pressure; DBP: diastolic blood pressure; MPAP: mean pulmonary arterial pressure; LAP: left atrial pressure; LVESP: left ventricular end-systolic pressure; LVEDP: left ventricular end-diastolic pressure; RVESP: right ventricular end-systolic pressure; LVEDVi: indexed left ventricular end-diastolic volume; LV: left ventricle; RV: right ventricle; LVEDd: left ventricular end-diastolic dimension

3.2. Continuous Variables: Valve Annulus Size, ASD Size, and LVEDV

Group splits for continuous variables are shown in Figure 4. The mitral valve annulus Z-score had a median value of -3.5 (IQR: -4.3 to -2.8) for the non-physiological group, which was significantly lower than the success group (Median: -3.3, IQR: -4.2 to -2.7). Whereas the mitral valve annulus Z-score for the failure group (Median: -3.7, IQR: -4.3 to -2.8) was significantly lower than the success group. The aortic valve annulus Z-score had a median value of -3.5 (IQR: -4.2 to -2.8) for the non-physiological group, -3.4 (IQR: -4.2 to -2.7) for the success group, and -3.4 (IQR: -4.2 to -2.7) for the failure group, none of which differed significantly. The initial ASD size had a median value of 0.39 cm (IQR: 0.29-0.49) for the non-physiological group, which was significantly lower than both the success group (Median: 0.41 cm, IQR: 0.31-0.52) and the failure group (Median: 0.44 cm, IQR: 0.33-0.52). Further, initial ASD size was significantly higher in the failure group than the success group. The initial LVEDV Z-score had median values of -2.9 (IQR: -4.1 to -1.5) for the non-physiological group, which was significantly lower than the success group (Median: -2.0, IQR: -2.5 to -1.5) and higher than the failure group (Median: -3.2, IQR: -3.8 to -2.9), which also differed significantly. Thus, at 6 months a larger MV annulus, moderate ASD size, and larger LVEDV were all associated with success.

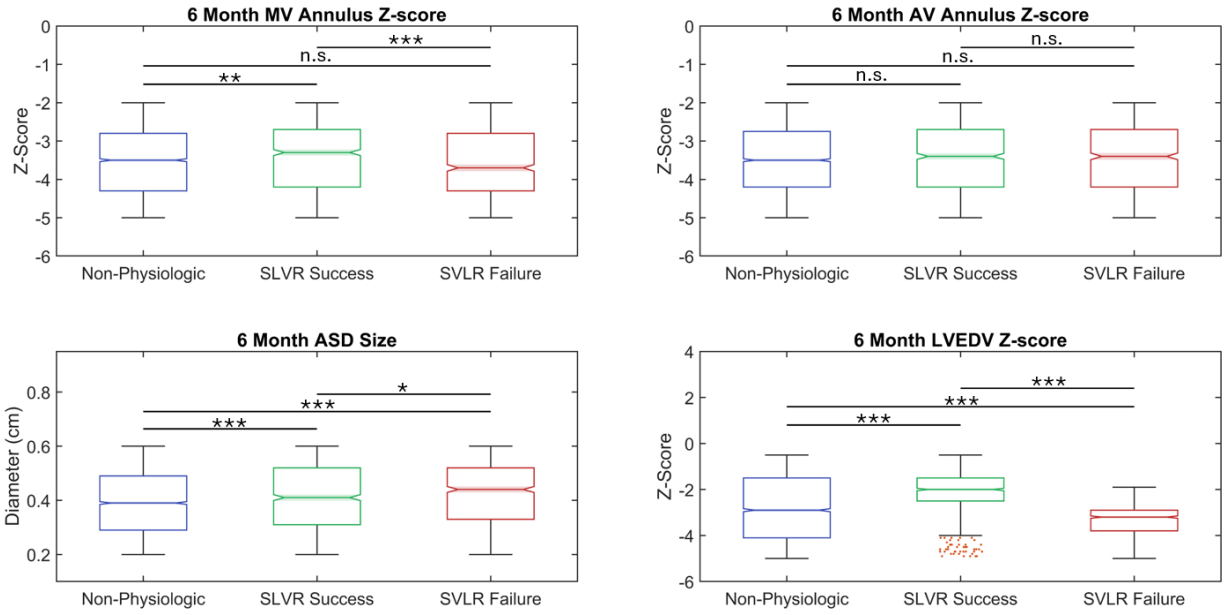

Figure 4: Box plots of continuous variables, compared between groups. MV: mitral valve; AV: aortic valve; ASD: atrial septal defect; LVEDV: left ventricular end-diastolic volume. *p < 0.05; **p < 0.01; ***p < 0.001; n.s. p > 0.05

3.3. Categorical Variables: Valve Regurgitation, Stenosis, and Shunt Type

Group splits for categorical variables are shown in Figures 5-6. The non-physiologic group was consistently significantly larger than the success or failure groups, therefore we focused on comparing only success and failure when considering valve regurgitation, valve stenosis, and shunt type. For MR, the success group had significantly fewer Absent ($p < 0.001$) cases and significantly more Mild ($p = 0.47$), Moderate ($p = 0.007$) and Severe ($p < 0.001$) cases than the failure group. For AR, the success group had significantly fewer Absent ($p = 0.019$) and Mild ($p < 0.001$) cases and significantly more Severe ($p < 0.001$) cases than the failure group. For TR, there were no significant differences between the success and failure groups. For MS, the success group had significantly more Absent ($p < 0.001$) and Mild ($p < 0.001$) cases and significantly fewer Moderate ($p < 0.001$) and Severe ($p < 0.001$) cases than the failure group. For AS, the success group had significantly more Mild ($p = 0.004$) cases and significantly fewer Severe ($p = 0.004$) cases than the failure group. For shunt type, the success group had significantly more RVPA shunts ($p = 0.041$) and mBTT shunts ($p < 0.001$) than the failure group. There were no significant differences between the groups when a shunt was not present. Overall, increasing severity of valve stenosis was associated with decreased rates of success, while some degree of MR and AR appeared to increase rates of success. Table S1 shows comparisons between groups, and Table S2 shows intragroup comparisons.

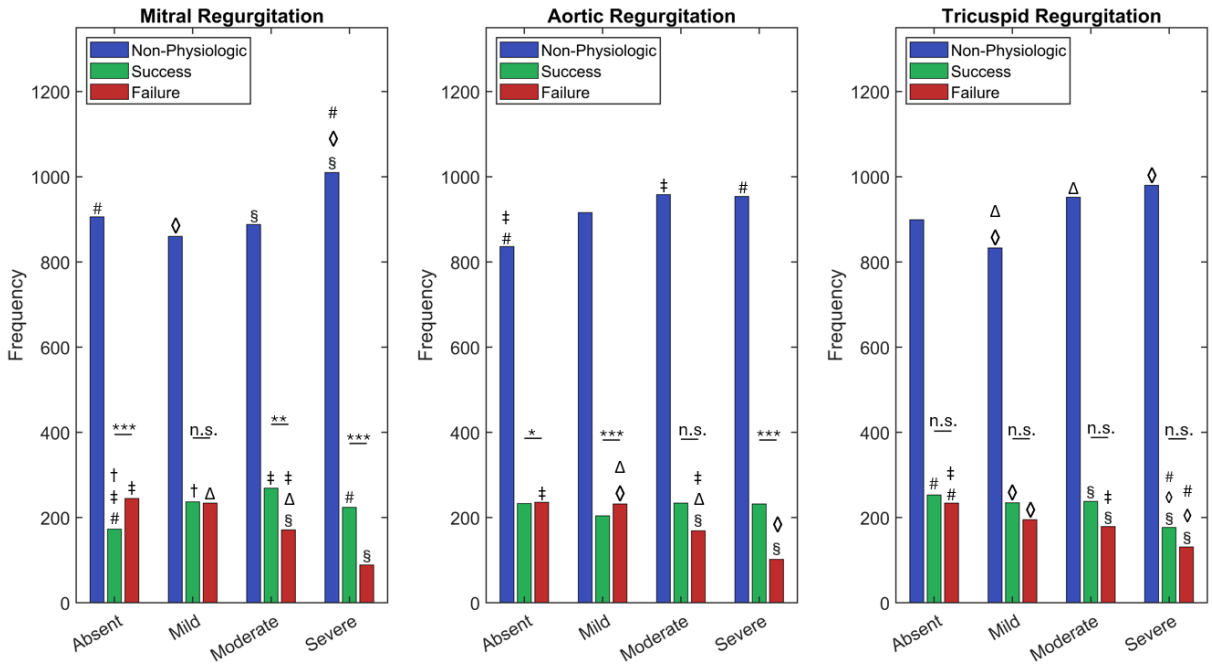

Figure 5: Mitral, aortic, and tricuspid regurgitation severity frequencies for each group. †: significant ($p < 0.05$) difference between absent and mild; ‡: significant ($p < 0.05$) difference between absent and moderate; #: significant ($p < 0.05$) difference between absent and severe; Δ: significant ($p < 0.05$) difference between mild and moderate; ◊: significant ($p < 0.05$) difference between mild and severe; §: significant ($p < 0.05$) difference between moderate and severe; *$p < 0.05$; **$p < 0.01$; ***$p < 0.001$; n.s. $p > 0.05$

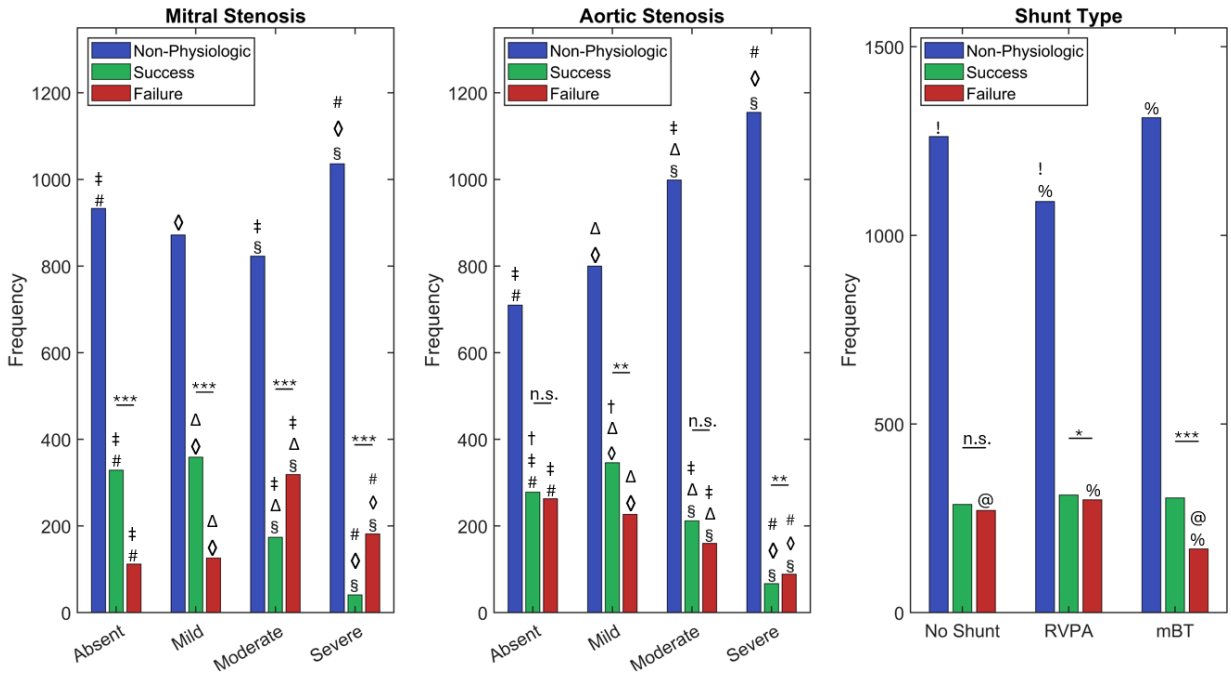

Figure 6: Mitral and aortic stenosis severity frequencies and shunt type for each group. †: significant ($p < 0.05$) difference between absent and mild; ‡: significant ($p < 0.05$) difference between absent and moderate; #: significant ($p < 0.05$) difference between absent and severe; Δ: significant ($p < 0.05$) difference between mild and moderate; ◊: significant ($p < 0.05$) difference between mild and severe; §: significant ($p < 0.05$) difference between moderate and severe; *$p < 0.05$; **$p < 0.01$; ***$p < 0.001$; n.s. $p > 0.05$

3.4. Pathologic Ventricular Growth from 6 to 24 Months of Age

As mentioned previously, SLVR success is designated by a final LVEDVi > 40 ml/m^2 and an LVEDP < 13 mmHg, without considering either LV mass or thickness. To determine if these criteria are adequate to describe true LV hypertrophy, we tracked changes in mass, thickness, and chamber radius in the simulated patient population. Figure 7 shows the change in LV mass, unloaded ventricular thickness (h_0), and unloaded ventricular radius (r_0) between the initial 6-month value and the final 24-month value for success and failure groups. The success group had a median increase in LV mass of 26.97 g/m^2 (IQR: 18.23-49.14), a median increase in LV h_0 of 0.81 cm (IQR: 0.63-1.15), and a median increase in LV r_0 of 0.30 cm (IQR: 0.24-0.37). These increases were all significantly larger than those observed in the failure group ($p < 0.001$), which were often similar to those expected somatically (indicated by dashed lines in Figure 7). The failure group had a median increase in LV mass of 7.56 g/m^2 (IQR: 4.04-13.80), a median increase in h_0 of 0.40 cm (IQR: 0.29-0.54), and a median increase in r_0 of 0.13 cm (IQR: 0.08-0.19).

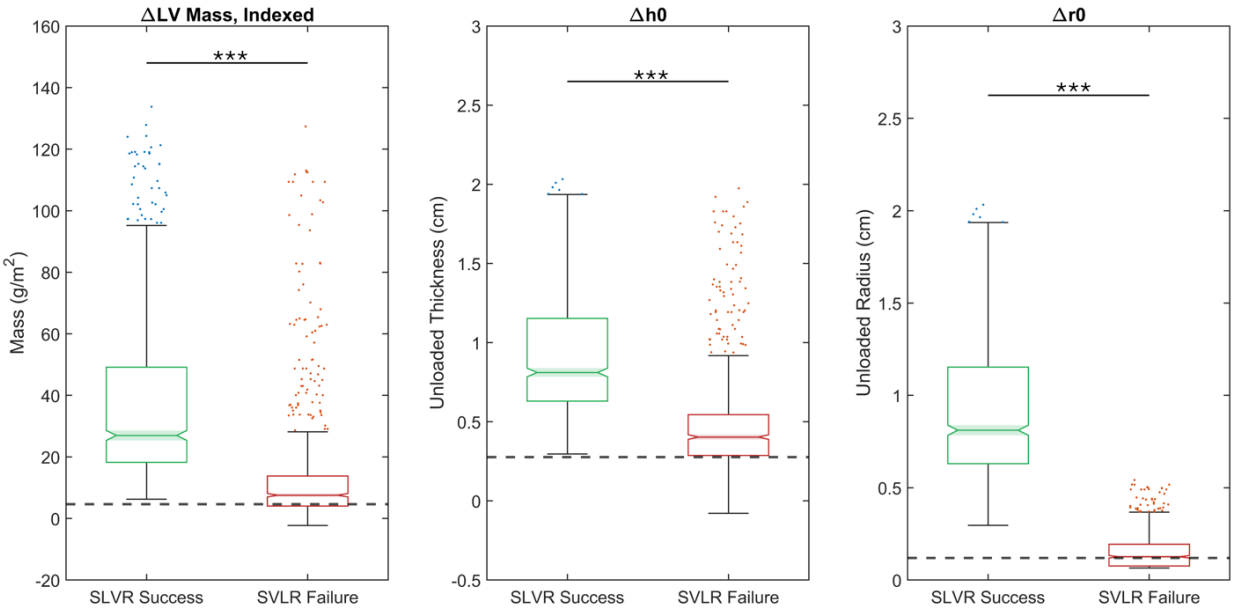

Figure 7: Boxplots of growth throughout the SLVR period, compared between success and failure groups. Left: change in LV mass, indexed to BSA. Center: change in unloaded thickness (h0). Right: change in unloaded radius (r0). Dashed lines indicate equivalent values from the somatic infant model. ***p < 0.001

3.5. Predictive Machine Learning Model

Next, we consider the predictive capabilities of the Random Forest classifier, which determines the probability of SLVR success or failure based on the 6-month input metrics. The classifier achieved a cross-validated classification loss of 0.0859, corresponding to an overall accuracy of approximately 91.4% in distinguishing between success and failure patient groups from the ten random 6-month input metrics alone. The receiver operating characteristic (ROC) curve (Figure 8a) has an area under the curve of 0.976. Feature importance analysis (Figure 8b) revealed that initial LVEDV Z-score was by far the strongest predictor of outcome (importance score = 9.70), followed by MS (2.25), initial ASD size (2.09), and MR (2.01). Additional contributors: AR (1.91), AS (1.86), MV annulus size (1.78), TR (1.62), AV annulus size (1.40), and shunt type (1.02).

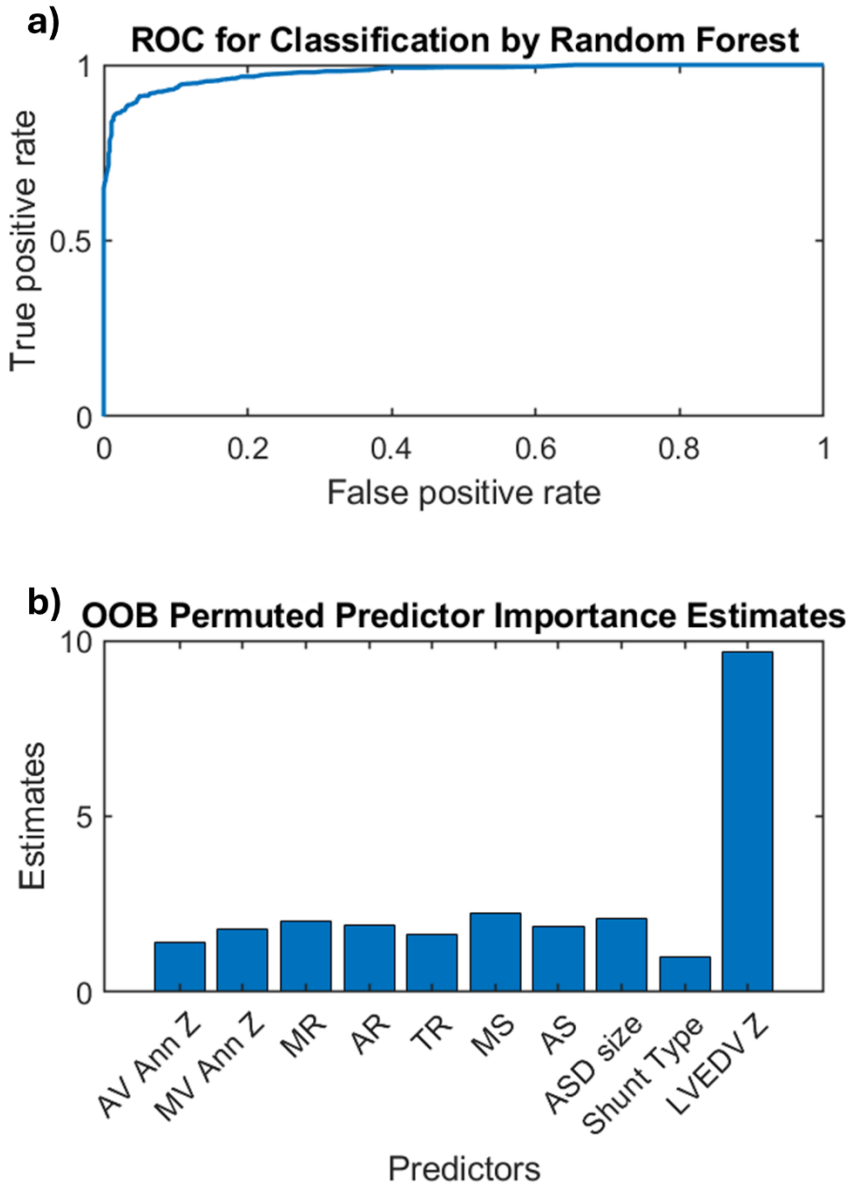

Figure 8: Performance of Random Forest classifier. A) Receiver operating characteristic (ROC) curve; B) Out-of-bag (OOB) permuted predictor importance estimates. AV: aortic valve; Ann: annulus; MV: mitral valve; MR: mitral regurgitation; AR: aortic regurgitation; TR: tricuspid regurgitation; MS: mitral stenosis; AS: aortic stenosis; ASD: atrial septal defect; LVEDV: left ventricular end-diastolic volume

3.6. EFE Results

Figure 9 shows the group composition for the patient population without simulated EFE versus the populations with increasing EFE severity, where EFE was simulated by increasing passive LV stiffness. In general, increasing EFE severity led to increases in non-physiological patients (69.1% of total population for no EFE, 68.6% for mild EFE, 75.6% for moderate EFE, and 81.2% for severe EFE). Mild EFE led to an increase in failures (18.3% of total population versus 13.9% for no EFE), but moderate and severe EFE led to decreases in failure group percentage (13.2% and 11.3%, respectively). Increasing EFE severity also led to decreases in success rates (17% for none, 13.1% for mild, 11.2% for moderate, 7.43% for severe).

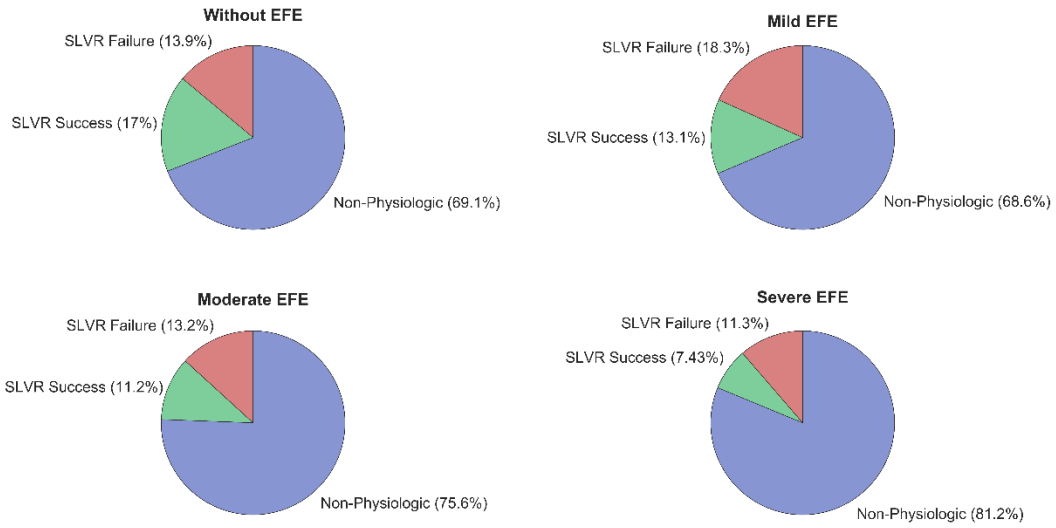

Figure 9: Group classifications based on endocardial fibroelastosis (EFE) severity

Simulation of EFE led to an increase in LVEDP for both success and failure groups (Figure 10). Within the success group, patients without EFE had a median LVEDP of 5.60 mmHg (IQR: 3.51-7.43). For mild EFE, the median LVEDP was significantly larger ($p < 0.001$) with a value of 6.98 mmHg (IQR: 5.24-9.34). Moderate EFE LVEDP was 8.49 mmHg (IQR: 6.06-10.69), significantly larger than mild ($p = 0.0032$). For severe EFE, median LVEDP was 8.83 (IQR: 6.46-11.34), with no significant difference from moderate EFE ($p = 0.525$). Within the failure group, patients without EFE had a median LVEDP of 9.85 mmHg (IQR: 6.48-15.98). For mild EFE, the median LVEDP was significantly larger ($p < 0.001$) with a value of 14.01 mmHg (IQR: 10.7-17.1). Moderate EFE LVEDP was 15.87 mmHg (IQR: 13.31-18.04), significantly larger than mild ($p < 0.001$). For severe EFE, median LVEDP was 16.00 mmHg (IQR: 13.07-17.94), with no significant difference from moderate EFE ($p = 0.749$).

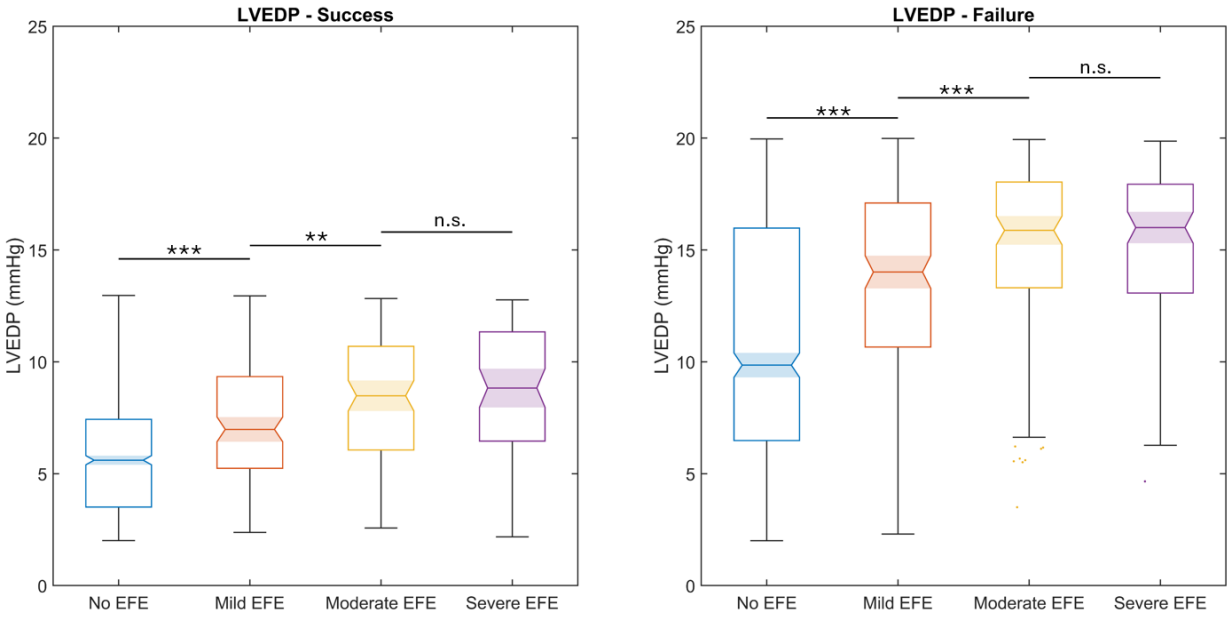

Figure 10: Boxplots of left ventricular end-diastolic pressure (LVEDP), compared between endocardial fibroelastosis (EFE) severities. Left: patients meeting the criteria for SLVR success. Right: patients who did not meet the criteria for SLVR success. **p < 0.01; ***p < 0.001; n.s. p > 0.05

EFE affected LV growth in similar ways in the success and failure groups (Figure 11). Any degree of EFE reduced the overall increase in LV mass from 6 months to 24 months and impacted both thickness and radius. In the success group, the change in LV mass was significantly decreased ($p < 0.001$) from a median value of 26.97 g/m^2 (IQR: 18.23-49.14) with no EFE to 19.63 g/m^2 (IQR: 14.39-41.22) with mild EFE. Change in h_0 significantly decreased ($p < 0.001$) from 0.81 cm (IQR: 0.63-1.15) with no EFE to 0.65 (IQR: 0.53-1.05) with mild EFE. Change in r_0 significantly decreased ($p < 0.001$) from 0.30 cm (IQR: 0.24-0.37) to 0.26 cm (IQR: 0.22-0.33). In the failure group, change in LV mass significantly decreased ($p = 0.0022$) from a median value of 7.56 g/m^2 (IQR: 4.04-13.80) with no EFE to 4.86 g/m^2 (IQR: 2.95-11.57) with mild EFE. Change in h_0 significantly decreased ($p = 0.0022$) from 0.40 cm (IQR: 0.29-0.54) with no EFE to 0.32 cm (IQR: 0.25-0.54) with mild EFE. Change in r_0 significantly decreased ($p = 0.0165$) from 0.13 cm (IQR: 0.08-0.19) with no EFE to 0.11 (IQR: 0.07 to 0.17). Increasing the severity of EFE had no significant impact ($p > 0.05$) on growth for either success or failure groups.

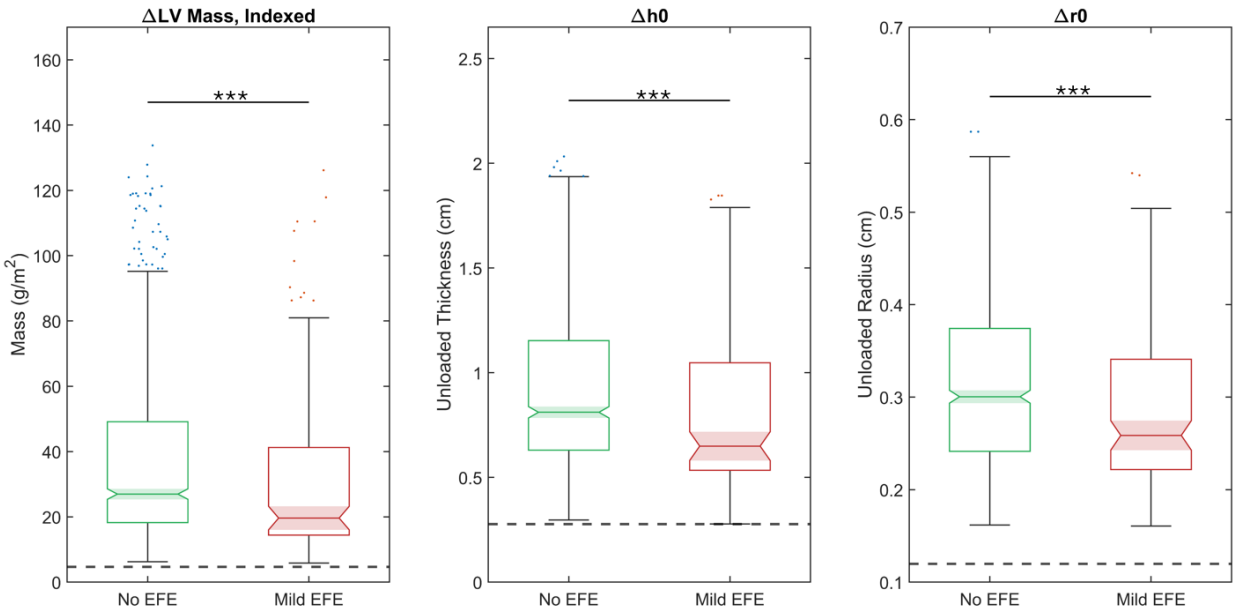

Figure 11: Boxplots of growth throughout the SLVR period for the success group, compared between patients with no simulated endocardial fibroelastosis (EFE) and mild EFE. Left: change in LV mass, indexed to BSA. Center: change in unloaded thickness (h_0). Right: change in unloaded radius (r_0). Dashed lines indicate equivalent values from the somatic infant model. ***p < 0.001

4. Discussion

We modified our modeling framework of the heart and circulation to simulate the LV growth of patients with BLH undergoing SLVR. Our primary goal was to determine factors that influence SLVR success and patterns of LV hypertrophy. We hypothesized that some SLVR patients are not experiencing true adaptive hypertrophy, where changes in wall thickness and overall LV mass are on par with chamber dilatation. To evaluate this hypothesis, we simulated a broad range of potential BLH phenotypes by adjusting 10 metrics across their diagnostic ranges, including valve annulus size, the presence of valve regurgitation and stenosis, optional mBTT or RVPA shunt, ASD size, and initial LVEDV Z-score. Model outputs at the conclusion of growth (i.e., 24 months of age) were largely within range of available reported measurements.

4.1. Left Ventricular Hypertrophy

As expected—and specified by current diagnostic criteria—"successful" synthetic BLH patients had a larger LVEDVi than those that "failed" SLVR. Median LVEDVi was 65 ml/m^2 for the success group and only 30 ml/m^2 for the failure group. Further, the change in LVEDV differed significantly between groups, with the success group experiencing a median change in indexed LVEDVi of 38.34 ml/m^2 (IQR: 26.97-60.17) and the failure group experiencing a median change of 10.64 ml/m^2 (IQR: 4.47-20.07). Using an equivalent 25th percentile weight trajectory, our model of normal somatic infant growth [22] produces a change in LVEDVi of 10.5 ml/m^2 over the same 18-month timeframe. Thus, on average the failure group failed to exhibit adaptive LV dilatation, only dilatating at a normal rate. No

synthetic success patients exhibited a change in LVEDVi less than the somatic level. We observed similar results for changes in indexed LV mass: on average, the success group exhibited a median increase of 26.97 g/m^2 (IQR: 18.23-49.13) and the failure group an increase of only 7.56 g/m^2 (IQR: 4.04-13.79), again on par with normal somatic levels (4.6 g/m^2). There was also a strong correlation between changes in LVEDVi and changes in indexed LV mass for both the success and failure groups ($r^2 = 0.75$ and $r^2 = 0.87$, respectively). In addition, for our simulated successful SLVR cases, changes in thickness were generally comparable to dilatation (Figure 12). This suggests that our original hypothesis that LV dilatation could occur without commensurate thickening is likely false and that using LVEDVi as a surrogate for growth at the conclusion of SLVR is adequate.

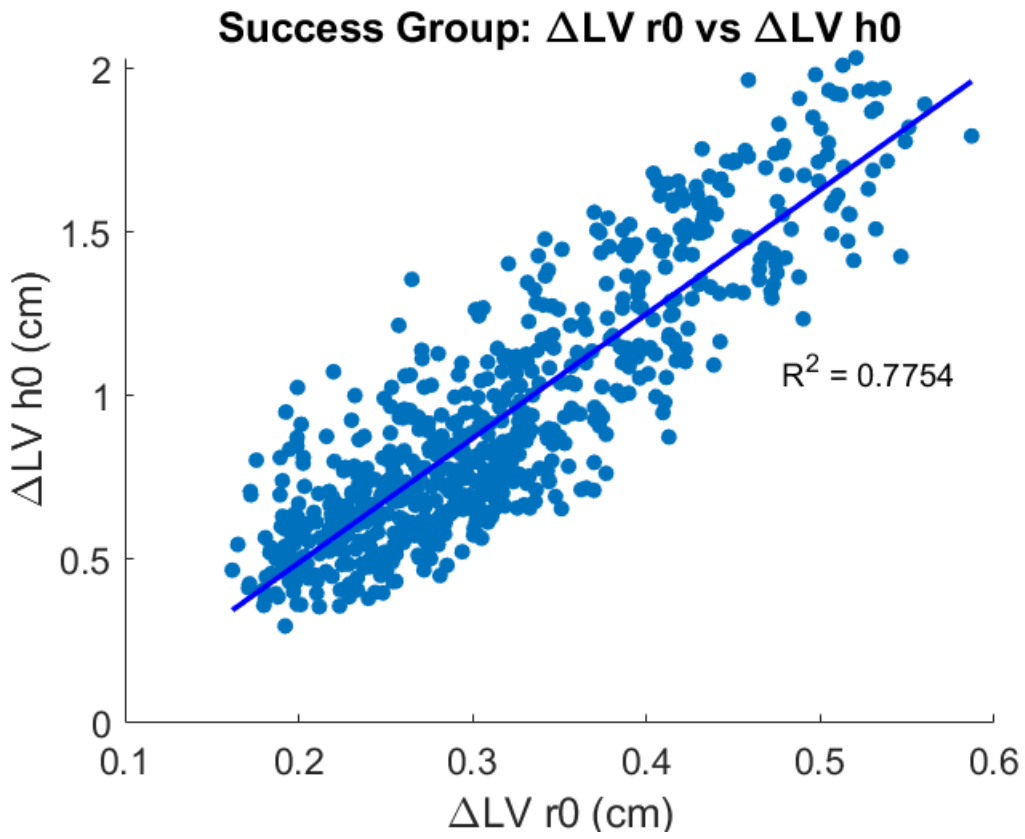

Figure 12: Comparison of change in unloaded radius (r_0) and thickness (h_0) throughout the SLVR period for the success group

4.2. Comparison to Clinical Trials of SLVR

4.2.1. Model Outputs

In general, model results at 24 months were within range of reported measurements for patients with borderline HLHS undergoing SLVR. The mean LVEDVi for the success group was 72.6 ml/m^2 without EFE and 68.4 ml/m^2 with mild EFE, which aligns well with the pre-biventricular repair LVEDVi reported by Emani et al. (67 +/- 5.5 ml/m^2) [8]. The median value (64.9 ml/m^2 without EFE and 58.0 ml/m^2 with mild EFE) is also in good agreement with measurements reported by Kalish et al. prior to biventricular repair (58.1 ml/m^2, range 26.6 – 92.5) [51], though it is slightly higher than measurements reported by Marathe et al. after the inclusion of additional pulmonary flow (51.96 ml/m^2, IQR: 41.13–64.73). Median left atrial pressure was 10 mmHg for non-EFE and EFE patients in the success group, which was low but within range of reported measurements from Herrin et al. (Median: 12.5, IQR: 8-14 mmHg) [42] and Banka et al. (Median: 13.75 mmHg, Range: 5-15) [45] prior to biventricular repair. Median LVEDP in the success group (6 mmHg without EFE, 7 mmHg with EFE) was lower than expected compared to reported measurements from Herrin et al. (Median: 12 mmHg, IQR: 10-16) [42] and Banka et al. (Median: 14.25 mmHg, Range: 8-22) [45].

Notably, we chose to model a subset of BLH patients with an intact ventricular septum, four valves, and normal vessel physiology, such as those with non-atretic varieties of HLHS or Shone's syndrome. In practice, staged left ventricular recruitment is also utilized for patients with unbalanced atrioventricular canal defects, ventricular septal defects (with or without interrupted aortic arch), complex transposition of the great arteries, double outlet

right ventricle, and straddling atrioventricular valves [11]. The timing of SLVR also varies: though recruitment procedures are most commonly performed at the second surgical stage with biventricular repair occurring before the third stage [11], biventricular repair has been performed after all three surgical stages at a wide range of ages [8, 52, 53]. It is therefore important to consider these specific patient characteristics when comparing model outputs to data from clinical trials of SLVR.

4.2.2. Predicting SLVR Success

There are currently no discriminant functions available to evaluate the prognosis of SLVR. Results from our Random Forest classifier (Figure 8b) indicate that a synthetic patient's initial 6-month LVEDV Z-score is the most important predictor of SLVR success at 24 months by far, more than 4x higher than the next most important metric (mitral valve stenosis). Discriminant functions for BLH patients undergoing direct biventricular conversion in the neonatal period indicates that initial LVEDV is a significant factor for successful repair [47], while another does not consider it as a variable [54]. Commonly used discriminant functions for biventricular repair of critical aortic stenosis—a less complex diagnosis than BLH—have mixed results for LVEDV. The Congenital Heart Surgeons' Society (CHSS) score did not consider LVEDV for multivariate analysis in the original 2001 study [55] or the 2007 follow-up [4]. In contrast Rhodes et al. [56] found that patients who did not survive after biventricular repair had significantly smaller LVEDV than those who did, though LVEDV was not an influential variable, ranking 8 of 11 in correlation size. Colan et al. found no significant difference in LVEDV between survivors and non-survivors in their Discriminant Score model [57]. However, as scores were determined

retrospectively, it is possible LVEDV was inherently used in the decision process for single ventricle palliation versus biventricular conversion, i.e., patients with smaller LVEDVs were selected for single ventricle palliation and therefore not considered in biventricular conversion survival analysis.

Similarly, other metrics of LV size, implicit or otherwise, are used to inform these models. Mitral valve annulus size is an influential factor in 4 of the 6 discriminant functions listed above [4, 47, 54, 56], as is aortic valve annulus size [47, 54, 55, 57], though our predictive model ranked them 7th and 9th out of 10 in predictive power, respectively. In contrast, mitral and aortic stenosis were ranked 2nd and 6th in our predictive model, neither of which are included in any of the published 6 discriminant functions for neonatal biventricular conversion. This could be a consequence of our synthetic patient generation approach, which treated annulus size and degree of stenosis independently, when in reality they are likely coupled and covary. If we had imposed covariance, it is possible annulus size would have ranked more highly, consistent with previous studies.

4.2.3. Simulation of EFE

EFE, common in both BLH and critical congenital aortic stenosis, leads to a pernicious fibrotic layer in the endocardium of the LV that impedes ventricular filling and growth [58]. When we included the additional 3,000 synthetic patients with EFE (simulated by increasing LV passive stiffness, see Sections 2.3 and 3.6) into our predictive model, the presence of EFE became the second most powerful factor for determining SLVR success (Figure 13). This was consistent with previous studies, as EFE grade is included in the Discriminant Score and both CHSS scores as a detrimental factor for patients with critical

congenital aortic stenosis [4, 55, 57]. It has also been implicated in failure of biventricular repair for BLH patients [59, 60]. Despite resection, EFE often recurs, requiring further invasive procedures to remove it [58, 61, 62]. Though Boston Children's Hospital—the primary developer of SLVR—prefers aggressive resection of EFE [11], in other centers patients with EFE are excluded from SLVR [63], or EFE is left unresected [52]. Thus, while the presence of EFE is clearly detrimental to SLVR and biventricular conversion, the efficacy of resection is still unclear.

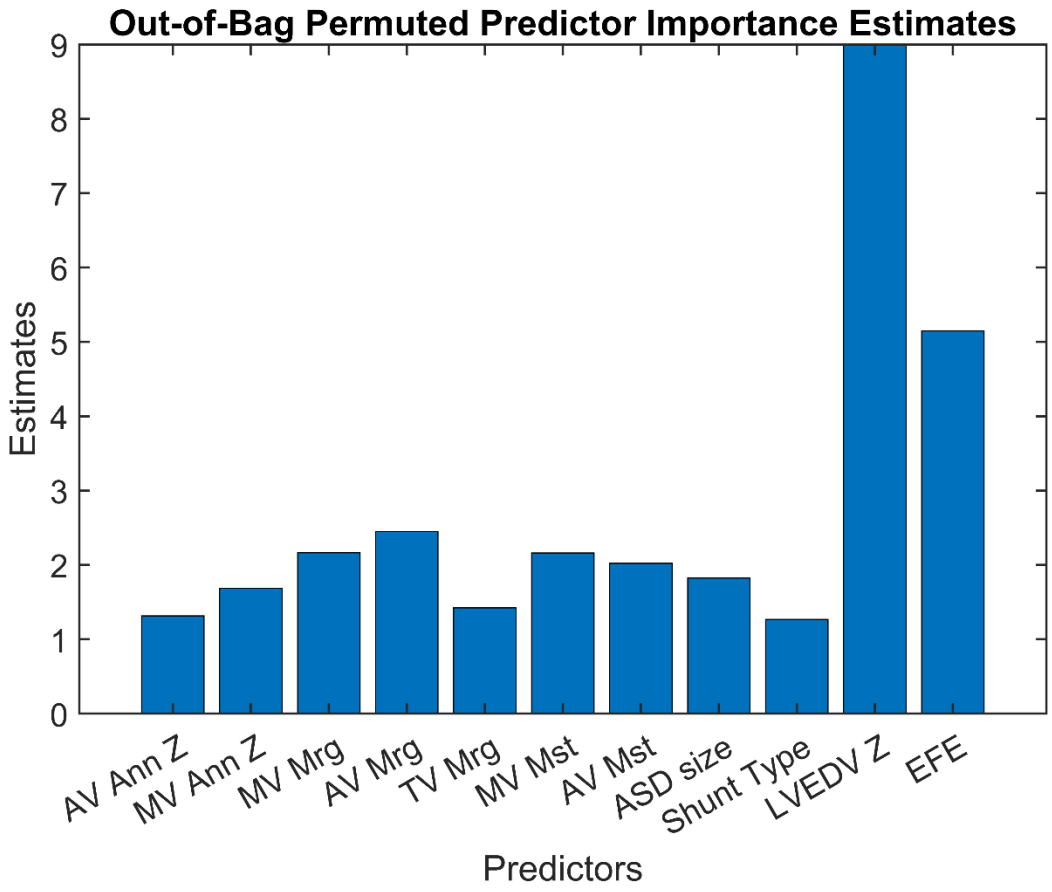

Figure 13: Feature importance derived from the Random Forest classifier, with presence of EFE included as an additional feature. Bars represent out-of-bag permuted predictor importance scores, reflecting the relative contribution of each feature to model accuracy.

Managing LVEDP appears to be important to the success of biventricular repair: a pre-operative LVEDP >= 13 mmHg is associated with death, heart transplantation, and takedown to single ventricle after biventricular repair [43, 53, 59]. In the model, mild EFE led to a shift in simulated patients from success to failure (Figure 9), largely due to increases in LVEDP. For both the SLVR success and failure groups, LVEDP was increased beyond that of their peers without EFE (Figure 10). Further, increasing severity of EFE led to increasing rates of non-physiologic cases, primarily caused by an elevation of LVEDP to a degree considered incompatible with life.

4.3. Limitations

Our models and approach have a few important limitations to consider. First, the ventricular growth model assumes a simplified spherical geometry. Though this assumption did not hinder us previously in predicting radial and circumferential ventricular growth in healthy infants [22] or adult canines with aortic coarctation, mitral valve regurgitation or myocardial infarction [23], disparate growth of the short and long axes of the left ventricle (i.e. ventricular shape) may be important in LV systolic and diastolic function as well as the dilatation and growth of the mitral and aortic valves of BLH patients. Venardos et al. reported that in utero, the borderline LV has two main patterns of morphology: a globular, non-apex-forming LV, associated with severe mitral stenosis and systolic dysfunction, and a narrow, apex-forming LV, where the mitral and aortic valves are hypoplastic but not severely stenotic. The apex-forming phenotype exhibited faster growth in utero, and patients with the phenotype were more likely to be selected for biventricular

repair at birth [64]. However, it is impossible to determine if shape is driven by function, or vice-versa, and a study investigating LV shape during SLVR found no particular shape parameter to be associated with outcome after biventricular repair [17].

Second, our ventricular growth model neglected feedback between regurgitation, annulus size, and LV dilatation. Physiologically, MR and LV dilatation are thought to be coupled in a feedback loop: regurgitation increases volume overloading on the LV, leading to ventricular dilatation, which in turn further exacerbates MR [65]. In Fontan patients, atrioventricular regurgitation has been associated with heart failure, morbidity, and premature mortality [66, 67], with one study estimating a two-fold increase in Fontan failure incidence among patients with moderate or severe regurgitation [68]. In our study, synthetic patients in the success group were *more likely* to have moderate or severe MR and *less likely* for MR to be absent than those in the failure group, a difference that could not be explained by an increase in non-physiological cases (Figure 5). From the model's point of view, it could be that the volume overloading of the LV due to MR is "helpful" for achieving the LVEDV 40 ml/m^2 threshold for SLVR success. MR increases the volume of blood in the left atrium during ventricular systole via retrograde flow from the previous LV contraction, which then refills the LV during ventricular diastole. Thus, while forward cardiac output is not increased, volume at end-diastole is. Further, since the LV growth model utilizes end-diastolic stretch as a stimulus, increased LVEDV promotes predicted dilatation. This is consistent with the phenotype observed in adults and Fontan patients with MR, however because it is not accompanied by commensurate increases in LV mass, this dilatation is a

maladaptive response. In our synthetic SLVR group there were strong correlations between dilatation and increased LV mass (Figure 7). For SLVR patients, MR is also undesirable and has been associated with poor outcomes after biventricular conversion [11, 17]. It is possible our model is not capturing the full consequences of MR because of the lack of valve-ventricle feedback, or perhaps a longer simulation span (beyond 24 months) would reveal more deleterious effects. Furthermore, adjunct procedures such as valve repairs are commonly performed during the recruitment process [8], making it less likely that severe regurgitation (or stenosis) would occur in the final patient population and emphasizing the need for more quantitative evaluation of the acute and chronic efficacy of these procedures.

To reduce our parameter set prior to fitting, we performed a local sensitivity analysis and fit the 13 parameters with the overall largest effects on the greatest number of outputs. Though performing a local analysis is much faster than a global analysis, a global analysis is likely more appropriate for nonlinear systems with many interactions [69]. The parameters in the baseline 6-month-old BLH model were fitted to summary data from multiple datasets which contained patients with a range of ages and comorbidities. In particular, the atrial and ventricular pressures, RV pressure and volumes, and systemic and pulmonary arterial pressures were sourced from the Single Ventricle Reconstruction Trial [44] due to a lack of data on SLVR patients at 6 months of age. Though we limited our use to only patients with measurable LVs, all patients in the trial were undergoing single ventricle palliation, which could result in a bias of the base parameters that were not refit when

generating the synthetic SLVR population toward a more severe phenotype, i.e., those who are less suitable for SLVR.

As our goal was to investigate the full range of BLH phenotypes, we made two assumptions while generating the random phenotypes of the simulated patient population: 1) each metric was selected from a uniform distribution, e.g., a patient had the same probability of receiving an LVEDV Z-score of -5 as -2 or -0.5, and 2) metrics were treated as independent of one another. While this resulted in a wide range of phenotypes, it also led to the generation of "impossible" patients, such as those with severe mitral regurgitation and an LVEDV Z-score of -5. Though we believe most of these cases were ultimately sorted into the "non-physiologic" category, it is possible some were erroneously included in the SLVR success or failure groups and their accompanying statistical analysis.

Lastly, our predictive model and growth model upon which it was built have not yet been validated with real (i.e., non-simulated) patient data. We intend to collect retrospective BLH patient data for a follow-up study, which will be used to test the model's ability to predict SLVR success and failure in individual patients. We also will adapt the ventricular growth model to test its ability to predict changes in ventricular size and mass throughout the recruitment period for specific patients.

5. Conclusion

We created a novel computational framework linking a reduced-order circulation model with a strain-based cardiac growth law to simulate somatic and pathology-driven LV remodeling in BLH patients undergoing SLVR. Model parameters were fitted to SLVR literature data, then a subset of parameters associated with the diagnosis of BLH were randomized within diagnostic ranges to represent the full spectrum of BLH phenotypes. We then simulated LV growth from age 6 months to 24 months in our synthetic cohort before designating patients as having a successful SLVR (LVEDVi > 40 ml/m^2 and LVEDP < 13 mmHg), an unsuccessful SLVR (LVEDVi <= 40 ml/m^2 and LVEDP >= 13 mmHg), or hemodynamics incompatible with life. Machine learning identified initial LVEDV Z-score, endocardial fibroelastosis, and aortic valve regurgitation as the strongest predictors of SLVR outcome. Though we hypothesized that successful SLVR patients could be experiencing maladaptive dilatation, our model demonstrated otherwise: successful patients exhibited commensurate dilatation and thickening, while failed SLVR patients showed minimal adaptive hypertrophy beyond expected somatic growth. Our results suggest that LVEDVi is an adequate surrogate for LV hypertrophy in SLVR, though further validation with more robust individual patient data is needed.

References

1. Hickey EJ, Caldarone CA, McCrindle BW (2012) Left Ventricular Hypoplasia. Journal of the American College of Cardiology 59:S43–S54. https://doi.org/10.1016/j.jacc.2011.04.046

2. Alphonso N, Angelini A, Barron DJ, et al (2020) Guidelines for the management of neonates and infants with hypoplastic left heart syndrome: The European Association for Cardio-Thoracic Surgery (EACTS) and the Association for European Paediatric and Congenital Cardiology (AEPC) Hypoplastic Left Heart Syndrome Guidelines Task Force. European Journal of Cardio-Thoracic Surgery 58:416–499. https://doi.org/10.1093/ejcts/ezaa188

3. Albrahimi E, Korun O (2024) Contemporary management of borderline left ventricle. European Journal of Cardio-Thoracic Surgery 66:ezae247. https://doi.org/10.1093/ejcts/ezae247

4. Hickey EJ, Caldarone CA, Blackstone EH, et al (2007) Critical left ventricular outflow tract obstruction: The disproportionate impact of biventricular repair in borderline cases. The Journal of Thoracic and Cardiovascular Surgery 134:1429-1437.e7. https://doi.org/10.1016/j.jtcvs.2007.07.052

5. Cavigelli-Brunner A, Bauersfeld U, Prêtre R, et al (2012) Outcome of Biventricular Repair in Infants With Multiple Left Heart Obstructive Lesions. Pediatr Cardiol 33:506–512. https://doi.org/10.1007/s00246-011-0142-2

6. Freund JE, den Dekker M, Blank C, et al (2015) Midterm Follow-Up After Biventricular Repair of the Hypoplastic Left Heart Complex. Ann Thorac Surg 99:2150–6. http://dx.doi.org/10.1016/j.athoracsur.2015.02.030

7. Roche Rodriguez M, DiNardo JA (2022) Biventricular repair as an alternative to single-ventricle palliation in a child with hypoplastic left heart structures: What the anesthesiologist should know. Journal of Cardiothoracic and Vascular Anesthesia 36:3927–3938. https://doi.org/10.1053/j.jvca.2022.06.009

8. Emani SM, McElhinney DB, Tworetzky W, et al (2012) Staged Left Ventricular Recruitment After Single-Ventricle Palliation in Patients With Borderline Left Heart Hypoplasia. Journal of the American College of Cardiology 60:1966–1974. https://doi.org/10.1016/j.jacc.2012.07.041

9. Emani SM (2016) Staged Left Ventricular Recruitment and Biventricular Conversion for Patients With Borderline Left Heart. Operative Techniques in Thoracic and Cardiovascular Surgery 21:112–123. https://doi.org/10.1053/j.optechstcvs.2017.02.003

10. Kantor PF, Shi L, Colan SD, et al (2024) Progressive Left Ventricular Remodeling for Predicting Mortality in Children With Dilated Cardiomyopathy: The Pediatric Cardiomyopathy Registry. JAHA 13:e022557. https://doi.org/10.1161/JAHA.121.022557

11. Dafflisio G, Emani SM (2025) Don't Give up on the Left Ventricle! Surgical Strategies for Recruitment of the Borderline Left Heart. Seminars in Thoracic and Cardiovascular Surgery: Pediatric Cardiac Surgery Annual 28:13–20. https://doi.org/10.1053/j.pcsu.2025.02.009

12. Emani SM (2019) Biventricular Repair in Patients With Borderline Left Heart—The "Growing" Experience. World J Pediatr Congenit Heart Surg 10:18–19. https://doi.org/10.1177/2150135118819418

13. Kumar SR, Detterich J (2022) Considerations for Biventricular Conversion of Fontan Circulation. Seminars in Thoracic and Cardiovascular Surgery: Pediatric Cardiac Surgery Annual 25:11–18. https://doi.org/10.1053/j.pcsu.2022.04.003

14. Oladunjoye OO, Piekarski B, Banka P, et al (2018) Staged ventricular recruitment in patients with borderline ventricles and large ventricular septal defects. The Journal of Thoracic and Cardiovascular Surgery 156:254–264. https://doi.org/10.1016/j.jtcvs.2018.03.111

15. Kwak JG, Del Nido PJ, Piekarski B, et al (2022) Restriction of Atrial Septal Defect Leads to Growth of Hypoplastic Ventricle in Patients with Borderline Right or Left Heart. Seminars in Thoracic and Cardiovascular Surgery 34:215–223. https://doi.org/10.1053/j.semtcvs.2021.03.039

16. Marathe SP, Piekarski B, Beroukhim RS, et al (2021) Super Glenn for staged biventricular repair: impact on left ventricular growth? European Journal of Cardio-Thoracic Surgery 60:534–541. https://doi.org/10.1093/ejcts/ezab126

17. Barnet IR, Schulz NE, Ghelani SJ, et al (2025) Wide variation in shape of hypoplastic left ventricles undergoing recruitment and biventricular repair: A statistical shape modeling study. Journal of Cardiovascular Magnetic Resonance 27:101131. https://doi.org/10.1016/j.jocmr.2024.101131

18. Shimada M, Hoashi T, Nakata T, et al (2019) Surgical Outcomes of Biventricular Repair for Hypoplastic Left Ventricle With Congenital Mitral Valve Stenosis. World J Pediatr Congenit Heart Surg 10:11–17. https://doi.org/10.1177/2150135118808748

19. Yoshida K, Holmes JW (2021) Computational models of cardiac hypertrophy. Progress in Biophysics and Molecular Biology 159:75–85. https://doi.org/10.1016/j.pbiomolbio.2020.07.001

20. Garber L, Khodaei S, Keshavarz-Motamed Z (2022) The Critical Role of Lumped Parameter Models in Patient-Specific Cardiovascular Simulations. Archives of Computational Methods in Engineering 29:2977–3000

21. Kerckhoffs RCP, Omens JH, McCulloch AD (2012) A single strain-based growth law predicts concentric and eccentric cardiac growth during pressure and volume overload. Mechanics Research Communications 42:40–50. https://doi.org/10.1016/j.mechrescom.2011.11.004

22. Hiebing AA, Pieper RG, Witzenburg CM (2023) A Computational Model of Ventricular Dimensions and Hemodynamics in Growing Infants. Journal of Biomechanical Engineering 145:101007. https://doi.org/10.1115/1.4062779

23. Witzenburg CM, Holmes JW (2018) Predicting the Time Course of Ventricular Dilation and Thickening Using a Rapid Compartmental Model. J of Cardiovasc Trans Res 11:109–122. https://doi.org/10.1007/s12265-018-9793-1

24. Caggiano LR, Holmes JW, Witzenburg CM (2022) Individual variability in animal-specific hemodynamic compensation following myocardial infarction. Journal of Molecular and Cellular Cardiology 163:156–166. https://doi.org/10.1016/j.yjmcc.2021.10.008

25. Migliavacca F, Pennati G, Dubini G, et al (2001) Modeling of the Norwood circulation: effects of shunt size, vascular resistances, and heart rate. American Journal of Physiology-Heart and Circulatory Physiology 280:H2076–H2086. https://doi.org/10.1152/ajpheart.2001.280.5.H2076

26. Mynard JP, Davidson MR, Penny DJ, Smolich JJ (2012) A simple, versatile valve model for use in lumped parameter and one-dimensional cardiovascular models. Numer Methods Biomed Eng 28:626–641. https://doi.org/10.1002/cnm.1466

27. West GB, Brown JH, Enquist BJ (1997) A General Model for the Origin of Allometric Scaling Laws in Biology. Science 276:122–126. https://doi.org/10.1126/science.276.5309.122

28. Weltgesundheitsorganisation (2006) Length/height-for-age, weight-for-age, weight-for-length, weight-for-height and body mass index-for-age; methods and development. WHO Press, Geneva

29. Vogt KN, Manlhiot C, Van Arsdell G, et al (2007) Somatic Growth in Children With Single Ventricle Physiology. Journal of the American College of Cardiology 50:1876–1883. https://doi.org/10.1016/j.jacc.2007.07.050

30. Hessel TW, Greisen G, Idorn L, Reimers JI (2013) Somatic growth in 94 single ventricle children – comparing systemic right and left ventricle patients. Acta Paediatrica 102:35–39. https://doi.org/10.1111/apa.12032

31. Seymour RS, Blaylock AJ (2000) The Principle of Laplace and Scaling of Ventricular Wall Stress and Blood Pressure in Mammals and Birds. Physiological and Biochemical Zoology 73:389–405. https://doi.org/10.1086/317741

32. Cantinotti M, Giordano R, Scalese M, et al (2017) Nomograms for two-dimensional echocardiography derived valvular and arterial dimensions in Caucasian children. Journal of Cardiology 69:208–215. https://doi.org/10.1016/j.jjcc.2016.03.010

33. Haycock GB, Schwartz GJ, Wisotsky DH (1978) Geometric method for measuring body surface area: A height-weight formula validated in infants, children, and adults. The Journal of Pediatrics 93:62–66. https://doi.org/10.1016/S0022-3476(78)80601-5

34. Zhang X, Haneishi H, Liu H (2019) Multiscale modeling of the cardiovascular system for infants, children, and adolescents: Age-related alterations in cardiovascular parameters and hemodynamics. Computers in Biology and Medicine 108:200–212. https://doi.org/10.1016/j.compbiomed.2019.03.021

35. Zaky A, Nasser WK, Feigenbaum H (1968) A Study of Mitral Valve Action Recorded by Reflected Ultrasound and Its Application in the Diagnosis of Mitral Stenosis. Circulation 37:789–799. https://doi.org/10.1161/01.CIR.37.5.789

36. Lew W, Karliner JS (1979) Assessment of pulmonary valve echogram in normal subjects and in patients with pulmonary arterial hypertension. Heart 42:147–161. https://doi.org/10.1136/hrt.42.2.147

37. Tei C, Pilgrim JP, Shah PM, et al (1982) The tricuspid valve annulus: study of size and motion in normal subjects and in patients with tricuspid regurgitation. Circulation 66:665–671. https://doi.org/10.1161/01.CIR.66.3.665

38. Witzenburg CM, Holmes JW (2019) The Impact of Hemodynamic Reflex Compensation Following Myocardial Infarction on Subsequent Ventricular Remodeling. Journal of Biomechanical Engineering 141:091010. https://doi.org/10.1115/1.4043867

39. Olivieri LJ, Jiang J, Hamann K, et al (2020) Normal right and left ventricular volumes prospectively obtained from cardiovascular magnetic resonance in awake, healthy, 0-12 year old children. Journal of Cardiovascular Magnetic Resonance 22:11. https://doi.org/10.1186/s12968-020-0602-z

40. Buechel EV, Kaiser T, Jackson C, et al (2009) Normal right- and left ventricular volumes and myocardial mass in children measured by steady state free precession cardiovascular magnetic resonance. Journal of Cardiovascular Magnetic Resonance 11:19. https://doi.org/10.1186/1532-429X-11-19

41. Howie SR (2011) Blood sample volumes in child health research: review of safe limits. Bull World Health Organ 89:46–53. https://doi.org/10.2471/BLT.10.080010

42. D'Errico J (2025) fminsearchbnd, fminsearchcon

43. Herrin MA, Zurakowski D, Baird CW, et al (2017) Hemodynamic parameters predict adverse outcomes following biventricular conversion with single-ventricle palliation takedown. The Journal of Thoracic and Cardiovascular Surgery 154:572–582. https://doi.org/10.1016/j.jtcvs.2017.02.070

44. Ohye RG, Gaynor JW, Ghanayem NS, et al (2008) Design and rationale of a randomized trial comparing the Blalock–Taussig and right ventricle–pulmonary artery shunts in the Norwood procedure. The Journal of Thoracic and Cardiovascular Surgery 136:968–975. https://doi.org/10.1016/j.jtcvs.2008.01.013

45. Fleming S, Thompson M, Stevens R, et al (2011) Normal ranges of heart rate and respiratory rate in children from birth to 18 years of age: a systematic review of observational studies. The Lancet 377:1011–1018. https://doi.org/10.1016/S0140-6736(10)62226-X

46. Kang S-L, Chaturvedi RR, Wan A, et al (2022) Biventricular Repair in Borderline Left Hearts. JACC: Advances 1:100066. https://doi.org/10.1016/j.jacadv.2022.100066

47. Mart CR, Eckhauser AW (2014) Development of an Echocardiographic Scoring System to Predict Biventricular Repair in Neonatal Hypoplastic Left Heart Complex. Pediatr Cardiol 35:1456–1466. https://doi.org/10.1007/s00246-014-1009-0

48. Zoghbi WA, Adams D, Bonow RO, et al (2017) Recommendations for Noninvasive Evaluation of Native Valvular Regurgitation. Journal of the American Society of Echocardiography 30:303–371. https://doi.org/10.1016/j.echo.2017.01.007

49. Baumgartner H, Hung J, Bermejo J, et al (2009) Echocardiographic Assessment of Valve Stenosis: EAE/ASE Recommendations for Clinical Practice. Journal of the American Society of Echocardiography 22:1–23. https://doi.org/10.1016/j.echo.2008.11.029

50. Center for High Throughput Computing (2006) Center for High Throughput Computing

51. Kalish BT, Banka P, Lafranchi T, et al (2013) Biventricular Conversion After Single Ventricle Palliation in Patients With Small Left Heart Structures: Short-Term Outcomes. The Annals of Thoracic Surgery 96:1406–1412. https://doi.org/10.1016/j.athoracsur.2013.05.060

52. Yerebakan C, Murray J, Valeske K, et al (2015) Long-term results of biventricular repair after initial Giessen hybrid approach for hypoplastic left heart variants. The Journal of Thoracic and Cardiovascular Surgery 149:1112-1122.e2. https://doi.org/10.1016/j.jtcvs.2014.09.028

53. Banka P, Schaetzle B, Komarlu R, et al (2014) Cardiovascular magnetic resonance parameters associated with early transplant-free survival in children with small left hearts following conversion from a univentricular to biventricular circulation. Journal of Cardiovascular Magnetic Resonance 16:73. https://doi.org/10.1186/s12968-014-0073-1

54. Plymale JM, Frommelt PC, Nugent M, et al (2017) The Infant with Aortic Arch Hypoplasia and Small Left Heart Structures: Echocardiographic Indices of Mitral and Aortic Hypoplasia Predicting Successful Biventricular Repair. Pediatr Cardiol 38:1296–1304. https://doi.org/10.1007/s00246-017-1661-2

55. Lofland GK, McCrindle BW, Williams WG, et al (2001) Critical aortic stenosis in the neonate: A multi-institutional study of management, outcomes, and risk factors. The Journal of Thoracic and Cardiovascular Surgery 121:10–27. https://doi.org/10.1067/mtc.2001.111207

56. Rhodes LA, Colan SD, Perry SB, et al (1991) Predictors of survival in neonates with critical aortic stenosis. Circulation 84:2325–2335. https://doi.org/10.1161/01.CIR.84.6.2325

57. Colan SD, McElhinney DB, Crawford EC, et al (2006) Validation and Re-Evaluation of a Discriminant Model Predicting Anatomic Suitability for Biventricular Repair in Neonates With Aortic Stenosis. Journal of the American College of Cardiology 47:1858–1865. https://doi.org/10.1016/j.jacc.2006.02.020

58. Diaz-Gil D, Silva-Gomez N, Morton SU, et al (2025) Predictive modeling of endocardial fibroelastosis recurrence in patients with congenital heart disease. The Journal of Thoracic and Cardiovascular Surgery 169:366–374. https://doi.org/10.1016/j.jtcvs.2024.08.036

59. Beattie MJ, Sleeper LA, Lu M, et al (2023) Factors associated with morbidity, mortality, and hemodynamic failure after biventricular conversion in borderline hypoplastic left hearts. The Journal of Thoracic and Cardiovascular Surgery 166:933-942.e3. https://doi.org/10.1016/j.jtcvs.2023.01.018

60. Akintürk H, Yörüker U, Müller M, Schranz D (2022) Hypoplastic Left Ventricle: Left Ventricular Recruitment With Hybrid Approach. World J Pediatr Congenit Heart Surg 13:637–644. https://doi.org/10.1177/21501351221116274

61. Barry OM, Friedman KG, Bergersen L, et al (2018) Clinical and Hemodynamic Results After Conversion from Single to Biventricular Circulation After Fetal Aortic Stenosis Intervention. The American Journal of Cardiology 122:511–516. https://doi.org/10.1016/j.amjcard.2018.04.035

62. Weixler V, Marx GR, Hammer PE, et al (2020) Flow disturbances and the development of endocardial fibroelastosis. The Journal of Thoracic and Cardiovascular Surgery 159:637–646. https://doi.org/10.1016/j.jtcvs.2019.08.101

63. Andersen ND, Overbey DM, Prabhu NK, et al (2024) Staged repair of borderline hypoplastic heart disease with early biventricular conversion. JTCVS Techniques 24:150–163. https://doi.org/10.1016/j.xjtc.2024.02.006

64. Venardos A, Colquitt J, Morris SA (2022) Fetal growth of left-sided structures and postnatal surgical outcome in borderline left heart varies by cardiac phenotype. Ultrasound in Obstet & Gyne 59:642–650. https://doi.org/10.1002/uog.23689

65. Enriquez-Sarano M, Loulmet DF, Burkhoff D (2008) The Conundrum of Functional Mitral Regurgitation in Chronic Heart Failure**Editorials published in the Journal of the American College of Cardiology reflect the views of the authors and do not necessarily represent the views of JACC or the American College of Cardiology. Journal of the American College of Cardiology 51:487–489. https://doi.org/10.1016/j.jacc.2007.09.046

66. Moon J, Shen L, Likosky DS, et al (2020) Relationship of Ventricular Morphology and Atrioventricular Valve Function to Long-Term Outcomes Following Fontan Procedures. Journal of the American College of Cardiology 76:419–431. https://doi.org/10.1016/j.jacc.2020.05.059

67. Tseng SY, Siddiqui S, Di Maria MV, et al (2020) Atrioventricular Valve Regurgitation in Single Ventricle Heart Disease: A Common Problem Associated With Progressive Deterioration and Mortality. JAHA 9:e015737. https://doi.org/10.1161/JAHA.119.015737

68. King G, Ayer J, Celermajer D, et al (2019) Atrioventricular Valve Failure in Fontan Palliation. Journal of the American College of Cardiology 73:810–822. https://doi.org/10.1016/j.jacc.2018.12.025

69. Colebank MJ, Umar Qureshi M, Olufsen MS (2021) Sensitivity analysis and uncertainty quantification of 1-D models of pulmonary hemodynamics in mice under control and hypertensive conditions. Numer Methods Biomed Eng 37:e3242. https://doi.org/10.1002/cnm.3242

Chapter 6: Conclusions and Future Directions

Overview and Summary of Findings

As recently as the 1970s, severe CHDs such as hypoplastic left heart syndrome were invariably fatal [1]. While advances in surgical techniques have drastically increased survival rates, there is more to patient care than merely preventing death. As children with CHDs grow, their cardiovascular systems grow with them, bringing new abnormal loading patterns and altering old ones with each surgery. These changes—and the comorbidities they can lead to—are not easy to predict. Indeed, as shown by our literature review of single ventricle lumped parameter models (Chapter 2), modelers have largely avoided exploring longitudinal temporal changes associated with growth and development, treating virtual surgery as solely two points in time: before and after. Thus, the overarching goal of my dissertation work was to develop computational frameworks that bridge physiological development and pathological remodeling in the left ventricle over an extended timescale. Our findings in the CoA model (Chapter 3) underline the importance of this kind of temporal modeling—rabbits with corrected CoA displayed some degree of reverse LV remodeling during the 4 months following correction yet had persistent ascending aortic remodeling. Understanding the time-course of ventricular and aortic remodeling could provide valuable insight into optimal timing of CoA repair. However, because imaging and pressure measurements were taken only at the study's termination for all three groups (CoA, corrected, and control), temporal changes could only be inferred [2]. Fortunately, data for healthy children at a wide range of ages are plentiful, allowing us to develop and validate a computational model of normal somatic ventricular growth in human infants

from birth through 3 years of age, which offered a baseline for distinguishing healthy versus pathological adaptation due to CoA (Chapter 4). These simulations became the foundation for our model of BLH patients undergoing SLVR (Chapter 5), determining that the volume-based criteria for successful SLVR is an effective surrogate for LV hypertrophy, with unsuccessful SLVR patients failing to achieve additional adaptive growth beyond normal somatic amounts.

Scientific and Clinical Implications

Collectively, these models form a continuum from normal development to disease, demonstrating that cardiac growth is itself a continuum, with its response to mechanical load spanning from adaptive to maladaptive. They advance the field of computational cardiovascular growth modeling in two ways: 1) for the first time, a coupled circulation-growth model has been applied to developing children experiencing both normal somatic and pathologic ventricular growth, and 2) using a simplified ventricular geometry to efficiently simulate years of growth with less than an hour of runtime on a typical desktop computer. Beyond the obvious gain in computational efficiency, reduced-order frameworks such as ours have advantages over higher-order models in transparency, interpretability, and extensibility. We explicitly link each model element (resistors, capacitors, valves, shunts, chambers) to a physiological quantity or mechanism that can—in theory if not always in practice—be measured. This negates the “black box effect” of higher-order models and allows us and other researchers to determine if model parameters make sense biologically. Parameters and outputs have causal, mechanistic relationships rather than correlational. For example, an increase in afterload, such as the increase in the descending

aortic resistance in the rabbit CoA model, directly maps to an increase in ventricular strain, which itself directly maps to a quantifiable increase in concentric hypertrophy. In this way, we can use the models to test hypotheses and explain the potential underlying cause of an outcome in a way empirical data on their own cannot, while still maintaining physiological relevance in both inputs and outputs. This is best illustrated in the results of the SLVR model, where we decoupled the "apparent success" of increased LVEDV with true physiological success of proportional LV thickening. Finally, because their assumptions and governing equations are accessible, reduced-order models can be easily modified and extended by future investigators to simulate other CHDs or determine patient-specific growth by fitting model parameters to patient measurements, either directly (e.g., heart rate, systemic vascular resistance) or indirectly (e.g., compliances, valve parameters). Indeed, all three models described in this dissertation were extensions of a simpler coupled circulation-growth model of canines [3], which was itself an extension of an adult human circulation-only model [4].

The transparency, interpretability, and extensibility of reduced-order models are especially important when modeling children. Due to their vulnerable status, need for parental consent, and relatively small population compared to adults, pediatric data are more limited and heterogeneous than that of their adult counterparts [5]. This makes parameterization—for any order model—difficult, increasing the amount of non-identifiable parameters and uncertainty in model outputs. In mitigating this challenge, the simplicity of reduced-order models is a strength. While more complex models can "hide" uncertainty in a high-dimensional parameter space, the assumptions required by reduced-

order models make it explicit. In this way, uncertainty can be tracked and, using a priori reasoning to constrain physiologically interpretable parameters, be reduced [6, 7]. For modelers seeking clinical translation, this is of critical importance.

The Philosophy and Purpose of Modeling

> "All models are wrong, but some are useful."
>
> —George Box, founder of University of Wisconsin-Madison's Department of Statistics [8]

Cardiovascular models are inherently (whether deliberately or inadvertently) collaborations between engineers and clinicians. At best, engineers and clinicians are enthusiastic partners united in a shared goal, weaving each other's experience and knowledge into the model throughout its development, from conception to implementation to interpretation of results. At worst, they can be borderline adversarial: engineers disparage what they believe is a resistance to innovation and a lack of quantitative reasoning, while clinicians view models with suspicion or even derision, considering them purely hypothetical tools lacking any grounding in the harsh reality they must contend with in the clinic every day.

The tension between these groups is pervasive and enduring—in 30 years of CHD simulations, precious few have fulfilled their promise of impacting clinical decision-making [9–11]. Even patient-specific models are almost always created retrospectively, the decisions leading to the virtual surgeries they simulate having long since been made in the real world [10]. Though we (myself included) make bold claims in research papers and grant applications of our models' translational capacities, how much of this capacity has

truly been realized? If this is in part due to a lack of trust between clinicians and engineers, an inability to reconcile the “wrongness” of models with their usefulness, how do we bridge that disconnect?

Perhaps a good place to start (or restart) is for engineers and clinicians to develop a mutual understanding of what models are and what they are not. Imagine that we could create a true “digital twin,” a model that fully and flawlessly captures every biological process in an individual human’s body, down to the sub-cellular level. While such a model would be an engineering marvel, it would have no practical value—the model would be as difficult to understand as the human it replicates, a phenomenon known as Bonini’s paradox [12]. Instead of thinking of models as mirrors, they should be thought of as lenses. A mirror reflects all incoming light rays at the same angle they hit, presenting a replication of reality. In contrast, a lens is deliberately designed to refract light at different angles, showing us an isolated aspect of reality that is warped yet useful. A useful model will never perfectly replicate biology; rather, it isolates what is essential while ignoring what is not.

Because model design choices are made by humans, the process unavoidably injects human biases into the model, but it can also provide insight in and of itself, as we are forced to reflect on which mechanisms really matter. In addition, model design is never a singular event—when the model inevitably produces results that deviate from data, modelers must interrogate their assumptions and refine their methods, learning more about the system they are attempting to simulate. When the time comes—as it always

does—to return to the drawing board, engineers should not be the only ones standing in front of it. To increase transparency and build confidence in simulation results, clinicians must be involved at every step of the modeling process.

Now that we know what models *are*, we can address what models are *for*. Simply (perhaps tritely) put, models are for answering questions. These questions should have the following qualities: 1) clinical origins, 2) specificity, 3) an appropriate scale of abstraction, and 4) an ability to provide insight even when disconfirmed.

- **Clinical origins:** Models should be driven by clinical uncertainty, answering questions about something clinicians observe but cannot easily measure or explain. While modelers tend to think in terms of mechanisms and parameters, clinicians are more focused on outcomes and observations. The best modeling questions come from finding common ground between these mindsets.
- **Specificity:** Questions must be narrow enough to be answerable while being broad enough to reveal mechanisms. They should be based on quantitative rather than qualitative logic (e.g., the model makes a falsifiable prediction or explores a defined variable space), rooted in the mechanics of how or why something happens, and clinically interpretable. “Can we simulate remodeling in CoA?” fails the specificity requirement. “What magnitude of aortic stiffening reproduces the observed pressure gradient seen in post-repair CoA patients?” passes muster.

- **Appropriate scale of abstraction:** When using a previously developed model to answer new questions, modelers should keep its structure in mind. For reduced-order models, this means focusing on system-level relationships rather than tissue- or cell-level, such as exploring how altering local parameters changes global function (e.g., how do varying shunt diameters impact systemic oxygen delivery?).
- **Designed for disconfirmation:** A good model does more than demonstrate our physiological intuitions—it clarifies if those intuitions are valid. Questions should be posed such that even if the model cannot reproduce an observation under plausible conditions, the result is still scientifically valuable.

All models are indeed wrong, and some are indeed useful. For clinicians and biomedical engineers to realize our shared goal of helping patients, we must learn to use these tools—flaws and all—not as substitutes for understanding, but as frameworks for dialogue. Models are collaborative efforts, structured spaces merging physiology, data, and human intuition. They may never be perfect, but if they help us ask and answer better questions and improve patient care, they have done their job.

Future Directions

There are many avenues branching from these models that I wish I had more time to explore. In particular, the SLVR growth model developed in this work represents an initial step in predicting LV adaptation in BLH patients. In its present form, it serves primarily as a proof of concept, demonstrating that a reduced-order model can reproduce the

characteristic features of SLVR physiology. The next logical step is to collaborate further with our clinician partners to refine this prototype into a patient-specific modeling pipeline.

Parameter estimation is an obvious and immediate area for improvement. Current input parameters were either held over from the somatic model (i.e., allometrically scaled from adult humans or canines) or fitted to means from multiple studies of BLH patients. Future efforts should focus on implementing automated or semi-automated parameter identification, using unscented Kalman filters [13] or Bayesian inference techniques [14] to fit model parameters directly to hemodynamic and imaging data. Such approaches would reduce model uncertainty while enhancing reproducibility and scalability. By mapping model parameters to measurable physiologic quantities, it could be possible to simulate individualized disease trajectories and test how different interventions influence growth outcomes. For such a heterogeneous patient population, a robust parameter-fitting pipeline would move the model beyond hypothesis generation toward a clinically contextualized decision support tool.

Similarly, we used the outcomes of our simulated patient population to train a Random Forest classifier to identify features associated with SLVR success or failure. While this analysis revealed promising trends, the next essential step is validation using real patient data to assess whether those trends hold true in practice. Using retrospective BLH patient data collected close to the Glenn procedure—at the beginning of LV recruitment—we could determine if the model makes the correct prediction for patients who proceeded to biventricular repair as well as those who were deemed a better fit for the Fontan procedure.

Close collaborations with clinical teams will be vital to ensure that the model's predictions align with the metrics clinicians actually use to guide care.

Beyond personalization, several opportunities exist to increase the physiologic fidelity of the model. One compelling direction is the coupling of our lumped parameter circulatory model with a three-dimensional representation of cardiac geometry derived from patient imaging, creating a multiscale model similar to those described in Chapter 2. We could consider using a volumetric growth framework such as that employed by Arumugam et al. [15], improving on their method by incorporating circulatory adaptation. This would allow us to capture regional variations in wall stress and strain that are inaccessible to our current reduced-order model. However, integrating growth at this scale presents substantial computational challenges [16], and validation would require imaging at multiple timepoints.

Even within the reduced-order framework, refinements in our geometric assumptions could yield insight. The current model assumes independent spherical ventricles for mathematical simplicity. While this approximation appears to capture relative changes in chamber volumes and wall thicknesses well, absolute values are not quite as accurate, nor are estimations of wall stress [17]. Modeling the ventricles as prolate spheroids [18] with left-right interaction [19] would more closely reflect cardiac anatomy and function. These extensions would also allow the exploration of how asymmetric load sharing influences growth, a particularly relevant question in SLVR physiology where the left and right ventricles compete for systemic output.

A Closing Reflection

In theory, we can break any biological process down into mathematical equations, including cardiac growth and remodeling. At the start of my graduate school career, that was the aspect of modeling I found most attractive—a way to feel in control, to obliterate the entropy inherent to life. At the conclusion of my PhD, however, I no longer feel the same. The heart is not merely a set of equations; it is, like every living organism, a dynamic entity, unique to each individual, affecting and affected by its surroundings across time. Each model in this dissertation, with its abstractions and imperfections, sought to illustrate the heart as a system striving to balance growth and function. Each taught the same lesson: when one attempts to maximize simplicity, one illuminates complexity. Both actions bring us closer to understanding not only our physical bodies, but ourselves as humans, perpetually changing, from our first breath to our last.

References

1. Ohye RG, Schranz D, D'Udekem Y (2016) Current Therapy for Hypoplastic Left Heart Syndrome and Related Single Ventricle Lesions. Circulation 134:1265–1279. https://doi.org/10.1161/CIRCULATIONAHA.116.022816

2. Wendell DC, Friehs I, Samyn MM, et al (2017) Treating a 20 mm Hg gradient alleviates myocardial hypertrophy in experimental aortic coarctation. J Surg Res 218:194–201. https://doi.org/10.1016/j.jss.2017.05.053

3. Witzenburg CM, Holmes JW (2018) Predicting the Time Course of Ventricular Dilation and Thickening Using a Rapid Compartmental Model. J Cardiovasc Transl Res 11:109–122. https://doi.org/10.1007/s12265-018-9793-1

4. Santamore WP, Burkhoff D (1991) Hemodynamic consequences of ventricular interaction as assessed by model analysis. Am J Physiol-Heart Circ Physiol 260:H146–H157. https://doi.org/10.1152/ajpheart.1991.260.1.H146

5. Dunne J, Rodriguez WJ, Murphy MD, et al (2011) Extrapolation of Adult Data and Other Data in Pediatric Drug-Development Programs. Pediatrics 128:e1242–e1249. https://doi.org/10.1542/peds.2010-3487

6. Eck VG, Donders WP, Sturdy J, et al (2016) A guide to uncertainty quantification and sensitivity analysis for cardiovascular applications. Int J Numer Methods Biomed Eng 32:e02755. https://doi.org/10.1002/cnm.2755

7. Sankaran S, Marsden AL (2011) A Stochastic Collocation Method for Uncertainty Quantification and Propagation in Cardiovascular Simulations. J Biomech Eng 133:031001. https://doi.org/10.1115/1.4003259

8. Box GEP (1976) Science and Statistics. J Am Stat Assoc 71:791–799. https://doi.org/10.1080/01621459.1976.10480949

9. Biglino G, Capelli C, Bruse J, et al (2017) Computational modelling for congenital heart disease: how far are we from clinical translation? Heart 103:98–103. https://doi.org/10.1136/heartjnl-2016-310423

10. De Zélicourt DA, Kurtcuoglu V (2016) Patient-Specific Surgical Planning, Where Do We Stand? The Example of the Fontan Procedure. Ann Biomed Eng 44:174–186. https://doi.org/10.1007/s10439-015-1381-9

11. Ganta S, Bock MJ, Haley J, et al (2025) Single ventricle care: challenges, successes and the future in a single center program. Transl Pediatr 14:2271–2303. https://doi.org/10.21037/tp-2024-602

12. Turner BM, Miletić S, Forstmann BU (2018) Outlook on deep neural networks in computational cognitive neuroscience. NeuroImage 180:117–118. https://doi.org/10.1016/j.neuroimage.2017.12.078

13. Pant S, Fabrèges B, Gerbeau J, Vignon-Clementel IE (2014) A methodological paradigm for patient-specific multi-scale CFD simulations: from clinical measurements to parameter estimates for individual analysis. Int J Numer Methods Biomed Eng 30:1614–1648. https://doi.org/10.1002/cnm.2692

14. Schiavazzi DE, Baretta A, Pennati G, et al (2017) Patient-specific parameter estimation in single-ventricle lumped circulation models under uncertainty. Int J Numer Methods Biomed Eng 33:e02799. https://doi.org/10.1002/cnm.2799

15. Arumugam J, Mojumder J, Kassab G, Lee LC (2019) Model of Anisotropic Reverse Cardiac Growth in Mechanical Dyssynchrony. Sci Rep 9:12670. https://doi.org/10.1038/s41598-019-48670-8

16. Holmes JW, Lumens J (2018) Clinical Applications of Patient-Specific Models: The Case for a Simple Approach. J Cardiovasc Transl Res 11:71–79. https://doi.org/10.1007/s12265-018-9787-z

17. Arts T, Bovendeerd PH, Prinzen FW, Reneman RS (1991) Relation between left ventricular cavity pressure and volume and systolic fiber stress and strain in the wall. Biophys J 59:93–102. https://doi.org/10.1016/S0006-3495(91)82201-9

18. Dewan S, Krishnamurthy A, Kole D, et al (2017) Model of Human Fetal Growth in Hypoplastic Left Heart Syndrome: Reduced Ventricular Growth Due to Decreased Ventricular Filling and Altered Shape. Front Pediatr 5:. https://doi.org/10.3389/fped.2017.00025

19. Sun Y, Beshara M, Lucariello RJ, Chiaramida SA (1997) A comprehensive model for right-left heart interaction under the influence of pericardium and baroreflex. Am J Physiol-Heart Circ Physiol 272:H1499–H1515. https://doi.org/10.1152/ajpheart.1997.272.3.H1499

APPENDIX TO CHAPTER 3

Section 1: Figures – Compartment Configurations

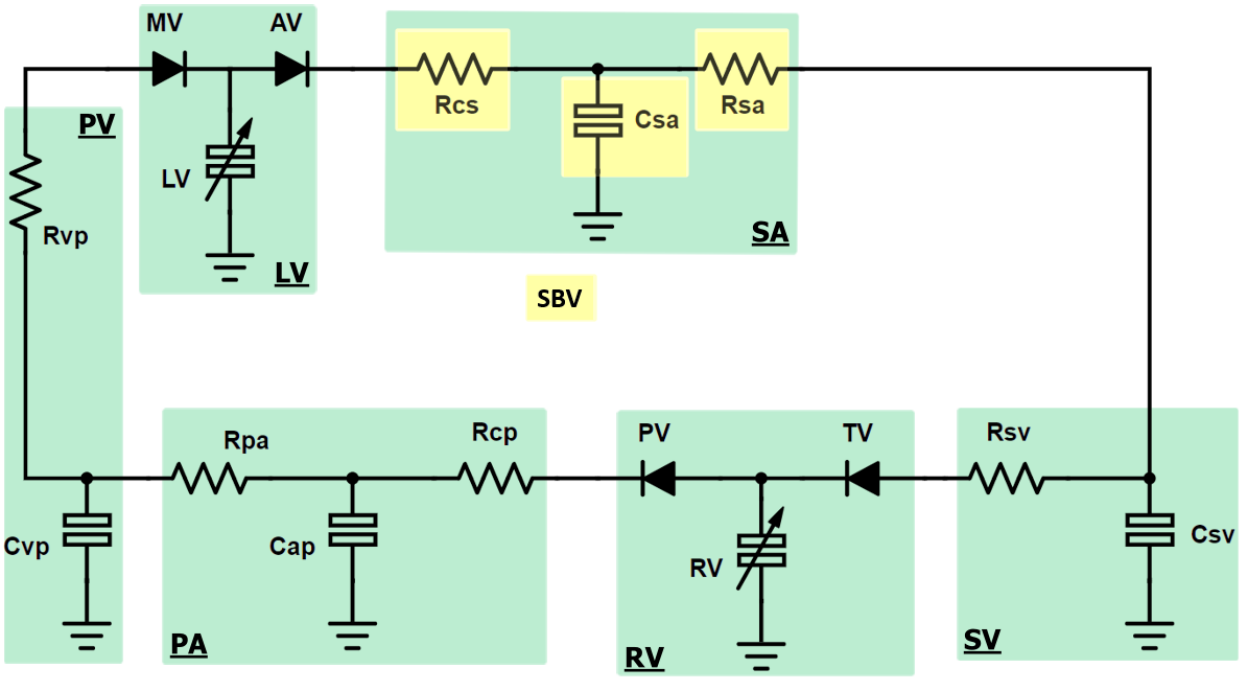

Supplemental Fig. 1 Schematic of the base six-compartment circuit model used to simulate the pressure-volume relationship of the cardiovascular system, with the six compartments designated by teal boxes (PV, pulmonary veins; LV, left ventricle; SA, systemic arteries; SV, systemic veins; RV, right ventricle; PA, pulmonary arteries). Initial parameter values were allometrically scaled for rabbits from the original canine model *[51]*. Systemic arterial behavior was simulated by a three-element Windkessel consisting of a characteristic resistance (Rcs), a capacitance (Csa), and an arterial resistance (Rsa). Then, the parameters associated with the systemic arteries as well as stressed blood volume (highlighted in yellow) were fitted to stroke volume, ejection fraction, systolic and diastolic ascending aortic pressures, and peak ascending aortic flow in the control group *[52]*. Abbreviations: Rpv, pulmonary venous resistance; Cpv, pulmonary venous capacitance; MV, mitral valve; AV, aortic valve; Rcs, characteristic systemic resistance; Csa, systemic arterial capacitance; Rsa, systemic arterial resistance; SBV, stressed blood volume; Rsv, systemic venous resistance; Csv, systemic venous capacitance; TV, tricuspid valve; PV, pulmonary valve; Rcp, characteristic pulmonary resistance; Cpa, pulmonary arterial capacitance; Rpa, pulmonary arterial resistance.

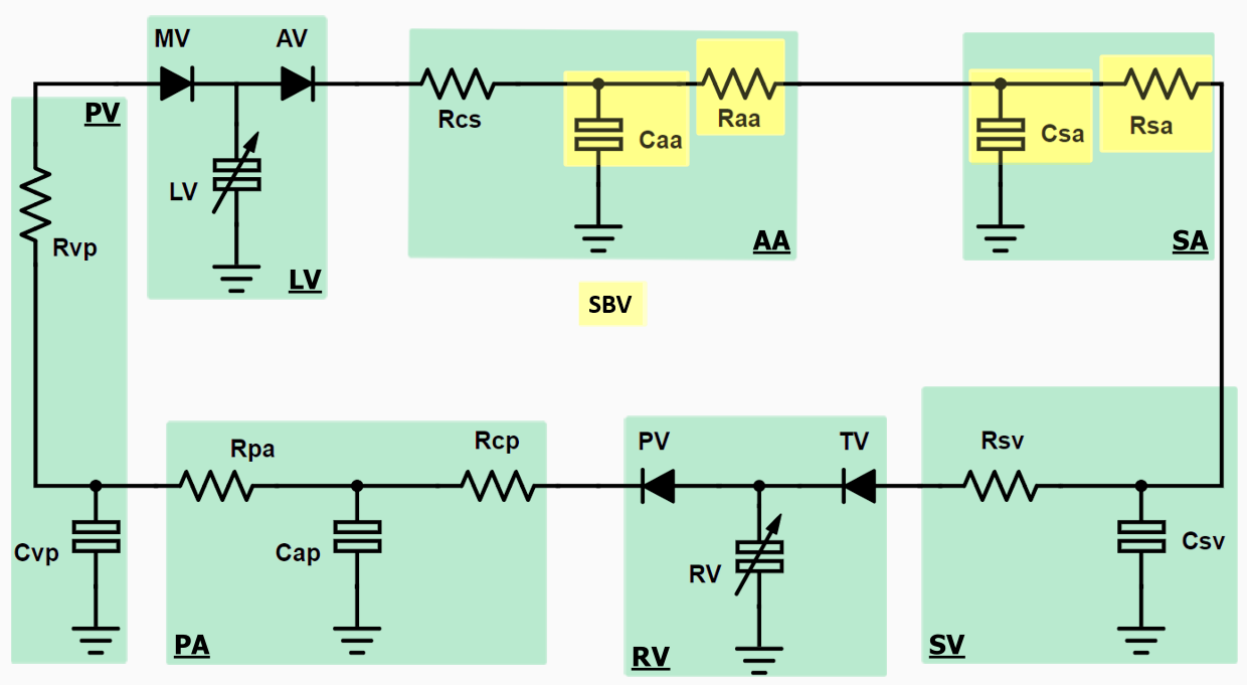

Supplemental Fig. 2 Schematic of the seven-compartment circuit model used to simulate the pressure-volume relationship of the cardiovascular system, with the seven compartments designated by teal boxes (PV, pulmonary veins; LV, left ventricle; AA, ascending aorta; SA, systemic arteries; SV, systemic veins; RV, right ventricle; PA, pulmonary arteries). The systemic arterial resistance (Rsa) in the six-compartment model was split into an ascending aortic resistance (Raa) and a distal systemic arterial resistance (Rsa). Similarly, the systemic arterial capacitance (Csa) in the six-compartment model was split into an ascending aortic compliance (Caa) and a distal systemic arterial compliance (Csa). Then, these four parameters along with stressed blood volume (highlighted in yellow) were fitted to reported stroke volume, ejection fraction, systolic and diastolic ascending aortic pressures, peak ascending aortic flow, and mean and peak aortic blood pressure gradients reported by Wendell et al. 2017.

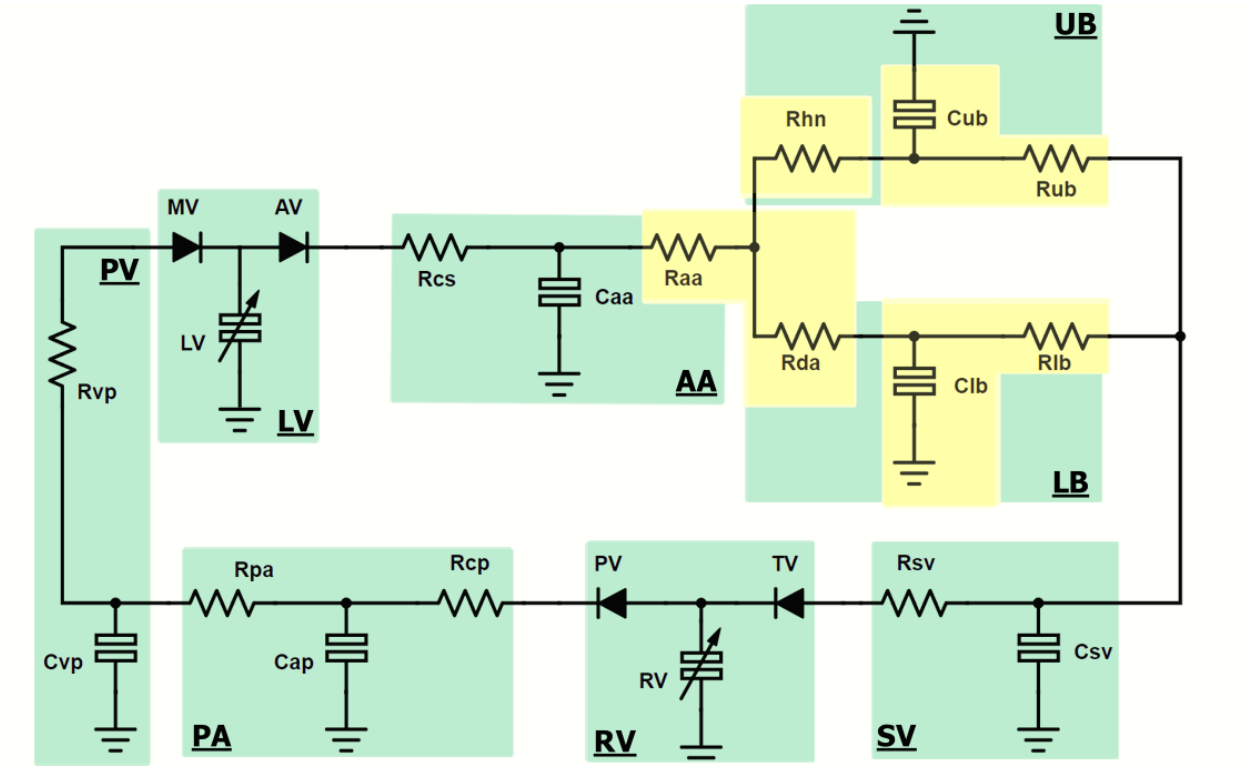

Supplemental Fig. 3 Schematic of the eight-compartment circuit model used to simulate the pressure-volume relationship of the cardiovascular system, with the eight compartments designated by teal boxes (PV, pulmonary veins; LV, left ventricle; AA, ascending aorta; UB, upper body arteries; LB, lower body arteries; SV, systemic veins; RV, right ventricle; PA, pulmonary arteries). The systemic arterial resistance (Rsa) in the seven-compartment model was split into head and neck arterial resistance (Rhn), distal upper body systemic arterial resistance (Rub), descending aortic resistance (Rda), and distal lower body systemic arterial resistance (Rla). Similarly, the systemic arterial capacitance (Csa) in the seven-compartment model was split into an upper body systemic arterial compliance (Cub) and a lower body arterial compliance (Clb). The resistance of the ascending aorta (Raa) and descending aorta (Rda) were set to the same value based on diameters reported by Menon et al. 2012a. Also, the ratio between the resistances and capacitances simulating the upper and lower body systemic arteries was determined by a proportionality constant (x). s. With these constraints only 3 parameters (Raa, Rhn, and x) were fitted to reported stroke volume, ejection fraction, systolic and diastolic ascending aortic pressures, peak ascending aortic flow, and mean and peak aortic blood pressure gradients reported by Wendell et al. 2017 as well as the flow split (unpublished data from Menon et al. 2012a).

Section 2: Tables – Inclusion of upper body parameters into fitting scheme

Supplemental Table 1: Parameter adjustments for each group when Rhn and Cub were included

Parameter	Control	CoA	Corrected
Rda	0.594	7.63 [+]	0.594[+]
h_0	0.580	0.841[+]	0.748[+]
Raa	0.594	0.418[+]	0.509[+]
Rhn	3.48	2.45[+]	2.98[+]
Caa	0.100	0.061•	0.038•
Rub	36.7	45.7•	31.1•
Rlb	16.0	21.5•	15.6•
Cub	0.0862	0.0525•	0.0858•

[+] prescribed based on reported differences in measured dimensions

•fitted based on reported differences in measured hemodynamics

Supplemental Table 2: Model results compared to reported experimental measurements when Rhn and Cub were included

Index	Control	Model	Z-score	CoA	Model	Z-score	Corrected	Model	Z-score
BPG, mean (mmHg)	3.27 ± 4.32	3.76	0.11	20.1 ± 4.75	20.6	0.12	2.61 ± 3.46	4.11	0.43
BPG, peak (mmHg)	10.8 ± 7.34	9.90	-0.12	31.0 ± 8.64	32.0	0.11	17.0 ± 4.32	14.1	-0.67
SV (mL)	1.87 ± 0.53	1.95	0.15	1.99 ± 0.56	1.89	-0.18	1.93 ± 0.26	2.18	0.95
EF %	60.6 ± 4.82	60.8	0.04	66.4 ± 6.24	61.6	-0.77	65.0 ± 7.88	68.5	0.45
Upper/lower flow split	0.30 ± 0.04	0.30	0	0.37 ± 0.04	0.37	0.06	0.33 ± 0.04	0.33	-0.01
Maximum AA flow (mL/min)	1435 ± 110	1424	-0.10	1445 ± 143	1469	0.17	1704 ± 68.3	1664	-0.22
AA SBP (mmHg)	67 ± 7.67	67.2	0.02	99 ± 18.0	92.4	-0.37	69 ± 8.73	71.0	0.23
AA DBP (mmHg)	56 ± 9.79	57.0	0.10	74 ± 25.9	75.2	0.05	54 ± 10.05	55.1	0.11

Section 3: Circulation Model of Control Group

3.1 Schematic of the circulatory compartment model:

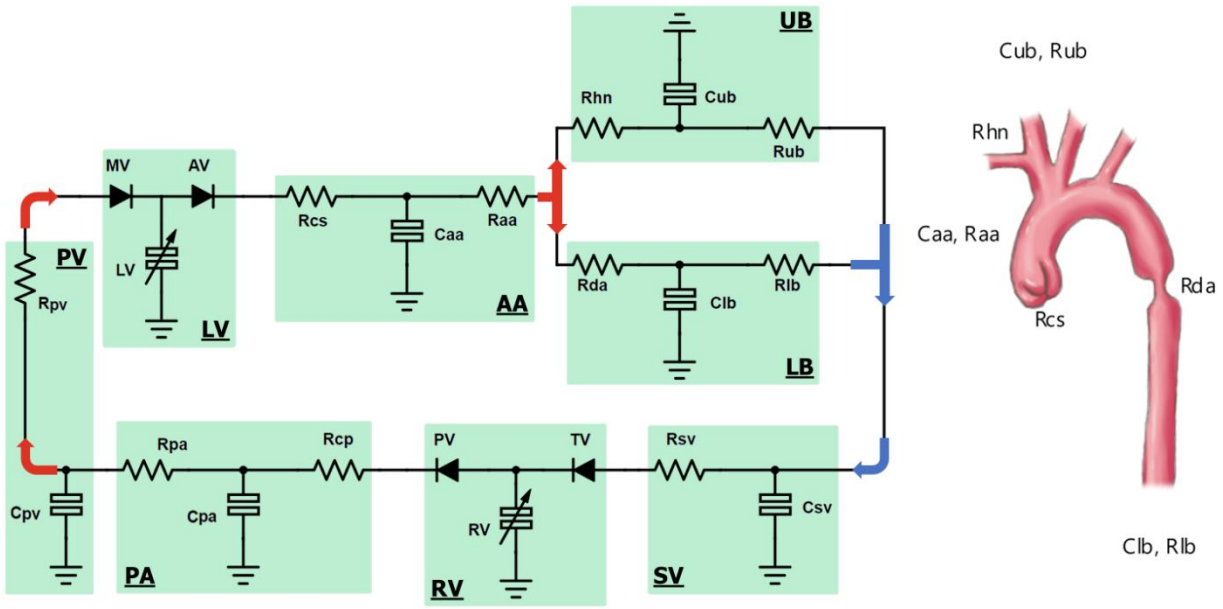

Model Compartments

1: Pulmonary veins (PV)

2: Left ventricle (LV)

3: Ascending aorta (AA)

4: Upper body arteries (UB)

5: Lower body arteries (LB)

6: Systemic veins (SV)

7: Right ventricle (RV)

8: Pulmonary arteries (PA)

3.2 Allometric scaling:

Compartments associated with the systemic arteries (AA, UB, LB) had their input parameters fitted using a serialized approach (see Methods, Section 2.1). All others were allometrically scaled [88]:

$$Y = Y_0 \left(\frac{M}{M_0}\right)^b \quad \text{(S10)}$$

where Y is the new (rabbit) parameter value, Y_0 is the reference (canine) parameter value, M is the new (rabbit) mass, M_0 is the reference (canine) mass, and b is a scaling exponent. Canine masses and parameter values from [51]. Scaling factors from [88, 89] and unit analysis. Following is a list of all compartments, their input parameters, and their respective governing equations for pressure and flow.

3.3 Foundational equations:

(1) Pulmonary veins (PV)

Inputs

Name	Meaning	Value	Source
Rpv	Pulmonary venous resistance	0.063 mmHg*s/mL	$0.015\ \frac{mmHg \cdot s}{mL} * \left(\frac{3.47\ kg}{23.4\ kg}\right)^{\frac{-3}{4}}$
Cpv	Pulmonary venous capacitance	0.445 mL/mmHg	$3.0\ \frac{mmHg \cdot s}{mL} * \left(\frac{3.47\ kg}{23.4\ kg}\right)^{1}$

Outputs

Pressure:

$$P_{pv}(t) = \frac{V_{pv}(t)}{Cpv} \quad \text{(S2)}$$

Flow:

$$\frac{dV_{pv}(t)}{dt} = \frac{P_{pa}(t) - P_{pv}(t)}{Rpa} - \frac{P_{pv}(t) - P_{lv}(t)}{Rpv} * (P_{pv}(t) > P_{lv}(t)) \quad \text{(S3)}$$

(2) Left ventricle (LV)

Inputs

Name	Meaning	Value	Source
Ees	End-systolic elastance	65.2 mmHg/mL	$\frac{P_{ES}}{V_{ES} - V0} = \frac{P_{ES}}{(V_{ED} - SV) - V0}$
V0	Unloaded volume	0.188 mL	$\frac{V_{ED}}{2.54^3}$
B	Coefficient for EDPVR	0.35 mmHg	[54]
A	Coefficient for EDPVR	1.05 mL^{-1}	$\frac{1}{V_{ED} - V_0}\left(\ln\left(\frac{P_{ED}}{B} + 1\right)\right.$

P_{ES} assumed equivalent to systolic blood pressure (67 mmHg) [52]
P_{ED} = 7 mmHg [60]
V_{ED} = SV/EF = 1.87 mL/0.61 = 3.1 mL [52]
2.54 allometrically scaled [51, 54]

Outputs

Pressure at end systole:

$$P_{ES\_lv} = Ees_{lv} * (V_{ES} - V_0) \quad \text{(S4)}$$

Pressure at end diastole:

$$P_{ED\_lv} = B_{lv} * \exp[A * (V_{ED} - V_0)] - B_{lv} \quad \text{(S5)}$$

Pressure at current time step:

$$P_{lv}(t) = e(t) * \left(P_{ES\_lv} - P_{ED\_lv}\right) + P_{ED\_lv} \quad \text{(S6)}$$

where e(t) is a normalized time-varying elastance relationship [57]

Flow:

$$\frac{dV_{lv}(t)}{dt} = \frac{P_{pv}(t) - P_{lv}(t)}{Rpv} * (P_{pv}(t) > P_{lv}(t)) - \frac{P_{lv}(t) - P_{aa}(t)}{Rcs} * (P_{lv}(t) > P_{aa}(t)) \quad \text{(S7)}$$

(3) Ascending aorta (AA)

Inputs

Name	Meaning	Value	Source
Rcs	Characteristic systemic resistance	0.709 mmHg*s/mL	Fitted using 6 compartment model
Raa	Ascending aortic resistance	0.594 mmHg*s/mL	Fitted using 8 compartment model
Caa	Ascending aortic capacitance	0.1 mL/mmHg	Fitted using 7 compartment model

Outputs

Pressure:

$$P_{aa}(t) = \frac{V_{aa}(t)}{Caa} \quad \text{(S8)}$$

Flow:

$$\frac{dV_{aa}(t)}{dt} = \frac{P_{lv}(t) - P_{aa}(t)}{Rcs} * (P_{lv}(t) > P_{aa}(t)) - \frac{P_{aa}(t) - P_{ub}(t)}{Raa + Rhn} - \frac{P_{aa}(t) - P_{lb}(t)}{Raa + Rda} \quad \text{(S9)}$$

(4) Upper body arteries (UB)

Inputs

Name	Meaning	Value	Source

Rhn	Head and neck arterial resistance	3.48 mmHg*s/mL	Fitted using 8 compartment model
Rub	Distal upper body arterial resistance	36.7 mmHg*s/mL	Fitted using 8 compartment model
Cub	Upper body arterial capacitance	0.0862 mL/mmHg	Fitted using 8 compartment model

Outputs

Pressure:

$$P_{ub}(t) = \frac{V_{ub}(t)}{Cub} \quad \text{(S10)}$$

Flow:

$$\frac{dV_{ub}(t)}{dt} = \frac{P_{aa}(t) - P_{ub}(t)}{Raa + Rhn} - \frac{P_{ub}(t) - P_{sv}(t)}{Rub} \quad \text{(S11)}$$

(5) Lower body arteries (LB)

Inputs

Name	**Meaning**	**Value**	**Source**
Rda	Descending aortic resistance	0.594 mmHg*s/mL	Fitted using 8 compartment model
Rlb	Distal lower body arterial resistance	16.0 mmHg*s/mL	Fitted using 8 compartment model
Clb	Lower body arterial capacitance	0.197 mL/mmHg	Fitted using 8 compartment model

Outputs

Pressure:

$$P_{lb}(t) = \frac{V_{lb}(t)}{Clb} \quad \text{(S12)}$$

Flow:

$$\frac{dV_{lb}(t)}{dt} = \frac{P_{aa}(t) - P_{lb}(t)}{Raa + Rda} - \frac{P_{lb}(t) - P_{sv}(t)}{Rlb} \quad \text{(S13)}$$

(6) Systemic veins (PV)

Inputs

Name	Meaning	Value	Source
Rsv	Systemic venous resistance	0.063 mmHg*s/mL	$0.015\ \frac{mmHg \cdot s}{mL} * \left(\frac{3.47\ kg}{23.4\ kg}\right)^{\frac{-3}{4}}$
Csv	Systemic venous capacitance	2.52 mL/mmHg	$17.0\ \frac{mmHg \cdot s}{mL} * \left(\frac{3.47\ kg}{23.4\ kg}\right)^{1}$

Outputs

Pressure:

$$P_{sv}(t) = \frac{V_{sv}(t)}{Csv} \tag{S14}$$

Flow:

$$\frac{dV_{sv}(t)}{dt} = \frac{P_{ub}(t) - P_{sv}(t)}{Rub} + \frac{P_{lb}(t) - P_{sv}(t)}{Rlb} - \frac{P_{sv}(t) - P_{rv}(t)}{Rsv} * (P_{sv}(t) > P_{rv}(t)) \tag{S15}$$

(7) Right ventricle (RV)

Inputs

Name	Meaning	Value	Source
Ees	End-systolic elastance	27.9 mmHg/mL	$Ees_{LV} * \left(\frac{3}{7}\right)$
V0	Unloaded volume	0.188 mL	Same as LV
B	Coefficient for EDPVR	0.15 mmHg	$B_{LV} * \left(\frac{3}{7}\right)$
A	Coefficient for EDPVR	1.05 mL^{-1}	Same as LV

(3/7) factor from [55]

Outputs

Pressure at end systole:

$$P_{ES\_rv} = Ees_{rv} * (V_{ES} - V_0) \tag{S16}$$

Pressure at end diastole:

$$P_{ED\_rv} = B_{rv} * \exp[A * (V_{ED} - V_0)] - B_{rv} \tag{S17}$$

Pressure at current time step:

$$P_{rv}(t) = e(t) * \left(P_{ES\_rv} - P_{ED\_rv}\right) + P_{ED\_rv} \tag{S18}$$

where e(t) is a normalized time-varying elastance relationship [57]

Flow:

$$\frac{dV_{rv}(t)}{dt} = \frac{P_{sv}(t) - P_{rv}(t)}{Rsv} * \left(P_{sv}(t) > P_{rv}(t)\right) - \frac{P_{rv}(t) - P_{pa}(t)}{Rcp} * \left(P_{rv}(t) > P_{pa}(t)\right) \quad \text{(S19)}$$

(8) Pulmonary arteries (PA)

Inputs

Name	Meaning	Value	Source
Rcp	Characteristic pulmonary resistance	0.251 mmHg*s/mL	$0.06\ \frac{mmHg \cdot s}{mL} * \left(\frac{3.47\ kg}{23.4\ kg}\right)^{\frac{-3}{4}}$
Rpa	Pulmonary arterial resistance	1.26 mmHg*s/mL	$0.3\ \frac{mmHg \cdot s}{mL} * \left(\frac{3.47\ kg}{23.4\ kg}\right)^{\frac{-3}{4}}$
Cpa	Pulmonary arterial capacitance	0.297 mL/mmHg	$2.0\ \frac{mmHg \cdot s}{mL} * \left(\frac{3.47\ kg}{23.4\ kg}\right)^{1}$

Outputs

Pressure:

$$P_{pa}(t) = \frac{V_{pa}(t)}{Cpa} \quad \text{(S20)}$$

Flow:

$$\frac{dV_{pa}(t)}{dt} = \frac{P_{rv}(t) - P_{pa}(t)}{Rcp} * (P_{rv}(t) > P_{pa}(t)) - \frac{P_{pa}(t) - P_{pv}(t)}{Rpa} \quad \text{(S21)}$$

3.4 Initial volumes:

$$V_{aa} = 0.5 * \frac{SBV}{6} \quad \text{(S22)}$$

$$V_{ub}, V_{lb} = 0.25 * \frac{SBV}{6} \quad \text{(S23)}$$

$$V_{pv}, V_{lv}, V_{sv}, V_{rv}, V_{pa} = \frac{SBV}{6} \quad \text{(S24)}$$

where SBV is circulatory stressed blood volume. Once initial volumes are determined, initial pressures for each compartment can be calculated. Then, volumes and pressures are iteratively solved for throughout the cardiac cycle using a 4th order Runge-Kutta method

with a fixed timestep of 0.0001 s until steady state has occurred, defined as volumes at the beginning and end of the cardiac cycle being within 0.05 mL of each other.

APPENDIX TO CHAPTER 4

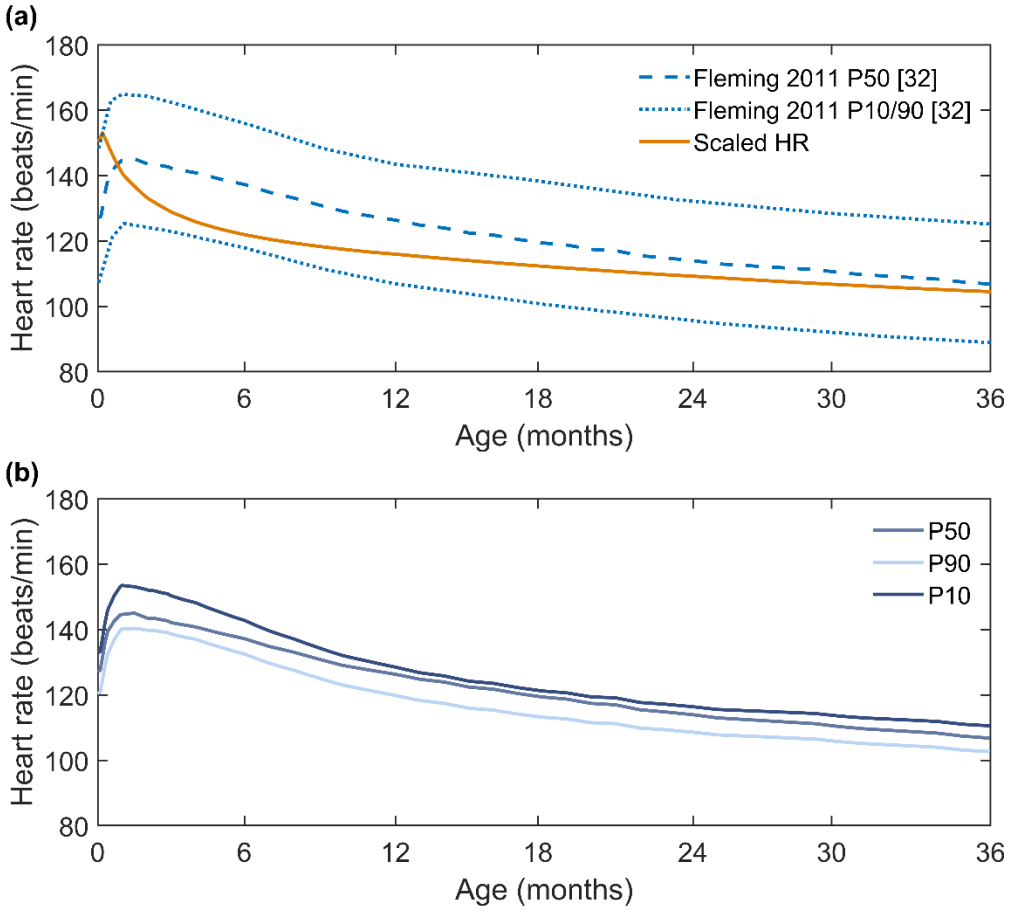

Figure S1: (A) Heart rate computed from scaling using an exponent of b = -1/4, an adult reference weight of 70 kg, and an adult reference heart rate of 70 beats/min, compared to the reported median heart rate for children aged 0-3 years [32]. Dashes lines indicate mean values for reported data. Dotted lines indicate the 10^{th} and 90^{th} percentiles for reported data. The reported median heart rate from Fleming et al. was inputted directly into the model.

(B) Heart rates for 50th, 10th, and 90th percentile infant weight. 10th and 90th percentile heart rates were scaled from Fleming et al. using an exponent of b = -1/4 and the 50th percentile infant weights as reference.

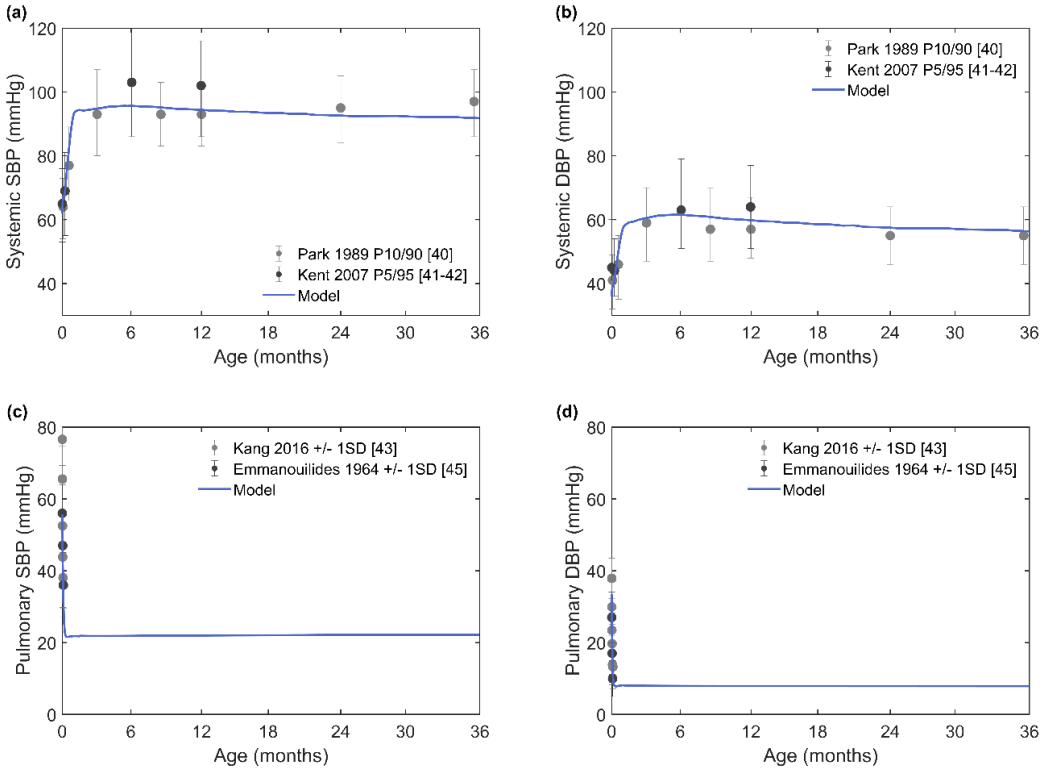

Figure S2: (A) Systemic systolic, **(B)** systemic diastolic, **(C)** pulmonary systolic, **(D)** pulmonary diastolic blood pressures for the first three years of life for a median-weight infant, compared to reported measurements [40-44]. In the studies referenced, MAP was measured using a blood pressure cuff, therefore comparable model pressures were from the upper body arteries compartment. MPAP was measured in the main pulmonary artery by Doppler echocardiography [44] and cardiac catheterization [43], thus model pressures shown were from the main pulmonary artery compartment. Error bars on data indicate 10^{th} and 90^{th} percentiles [40], 5^{th} and 95^{th} percentiles [41,42], or one standard deviation [43-44]. SBP, systolic blood pressure; DBP, diastolic blood pressure.

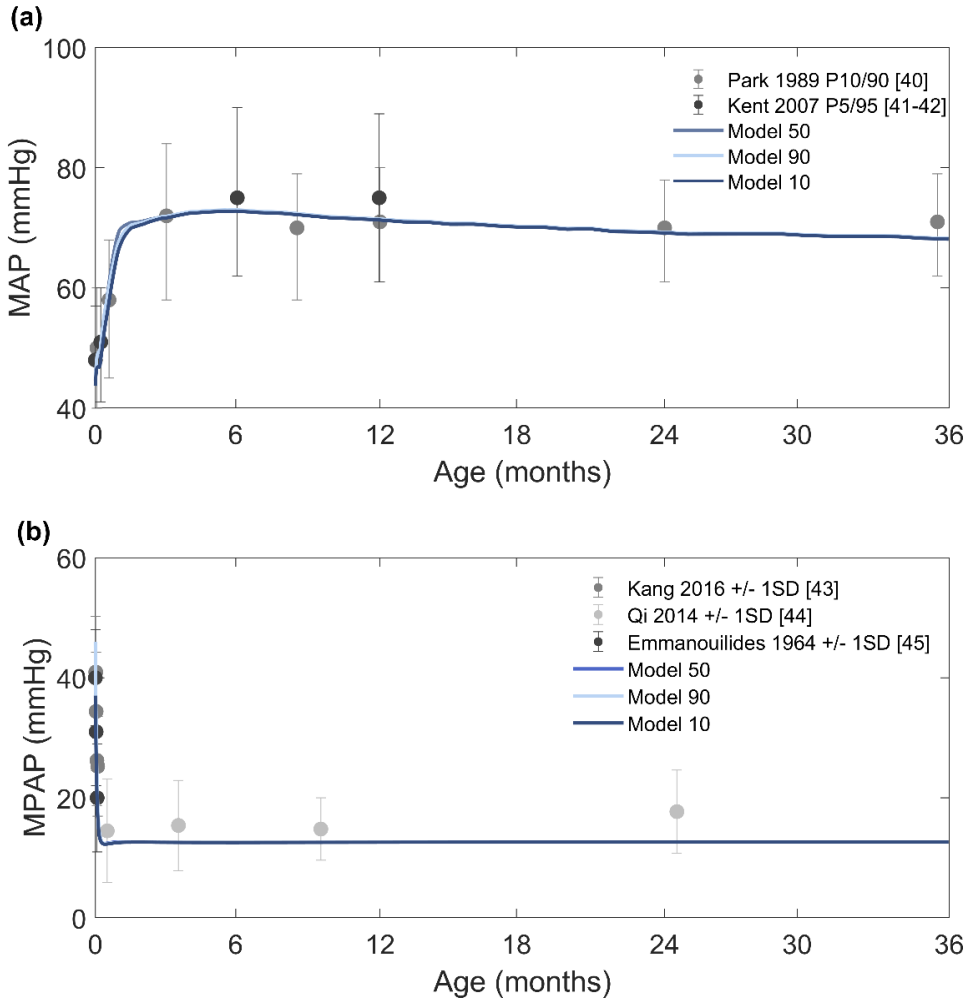

Figure S3: Simulated **(A)** systemic and **(B)** pulmonary mean arterial pressures throughout the first three years of life for an infant at 10th, 50th, and 90th percentile weight trajectories compared to reported measurements [40-45]. In the studies referenced, MAP was measured using a blood pressure cuff, therefore comparable model pressures were from the upper body arteries compartment. MPAP was measured in the main pulmonary artery by Doppler echocardiography [43,44] and cardiac catheterization [45], thus model pressures shown were from the main pulmonary artery compartment. Measurements from Qi et al. were from the sea-level cohort only. Error bars on data indicate 10^{th} and 90^{th} percentiles [40], 5^{th} and 95^{th} percentiles [41,42], or one standard deviation [43-45]. MAP, mean arterial pressure; MPAP, mean pulmonary arterial pressure.

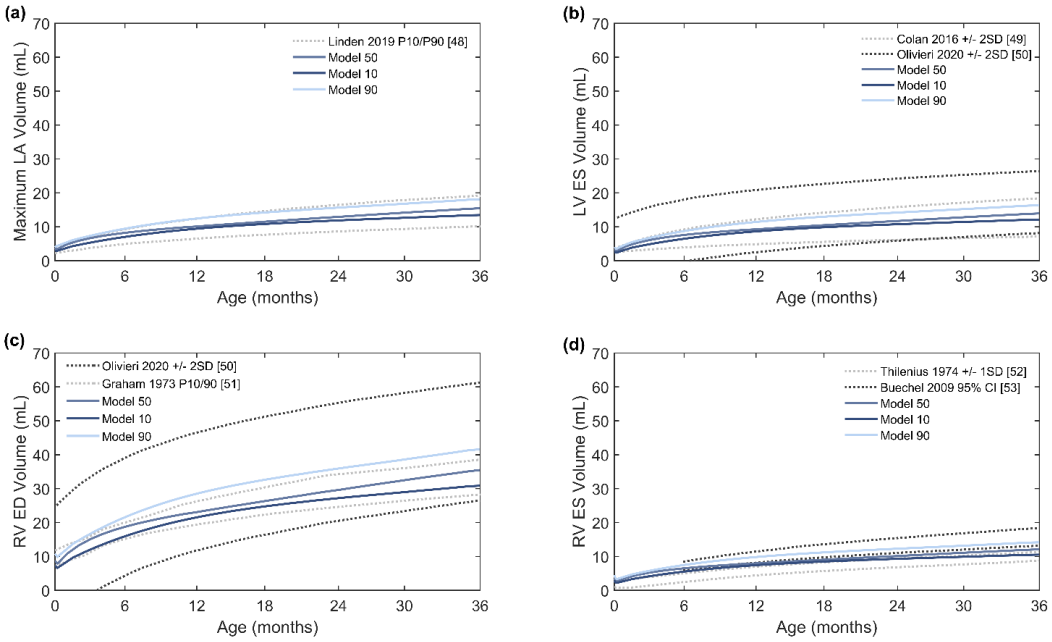

Figure S4: (A) Maximum left atrial volume, **(B)** left ventricular end-systolic volume, **(C)** right ventricular end-diastolic volume, and **(D)** right ventricular end-systolic volume for infants having a 10th, 50th, and 90th percentile weight trajectory for the first three years of life, compared to reported measurements [48-53]. Dotted lines indicate ± two standard deviations [49,50], ± one standard deviation [52], 10th and 90th percentiles [48, 51], or 95% confidence interval [53]. LA, left atrium; LV, left ventricle; RV, right ventricle; ED, end diastole; ES, end systole.

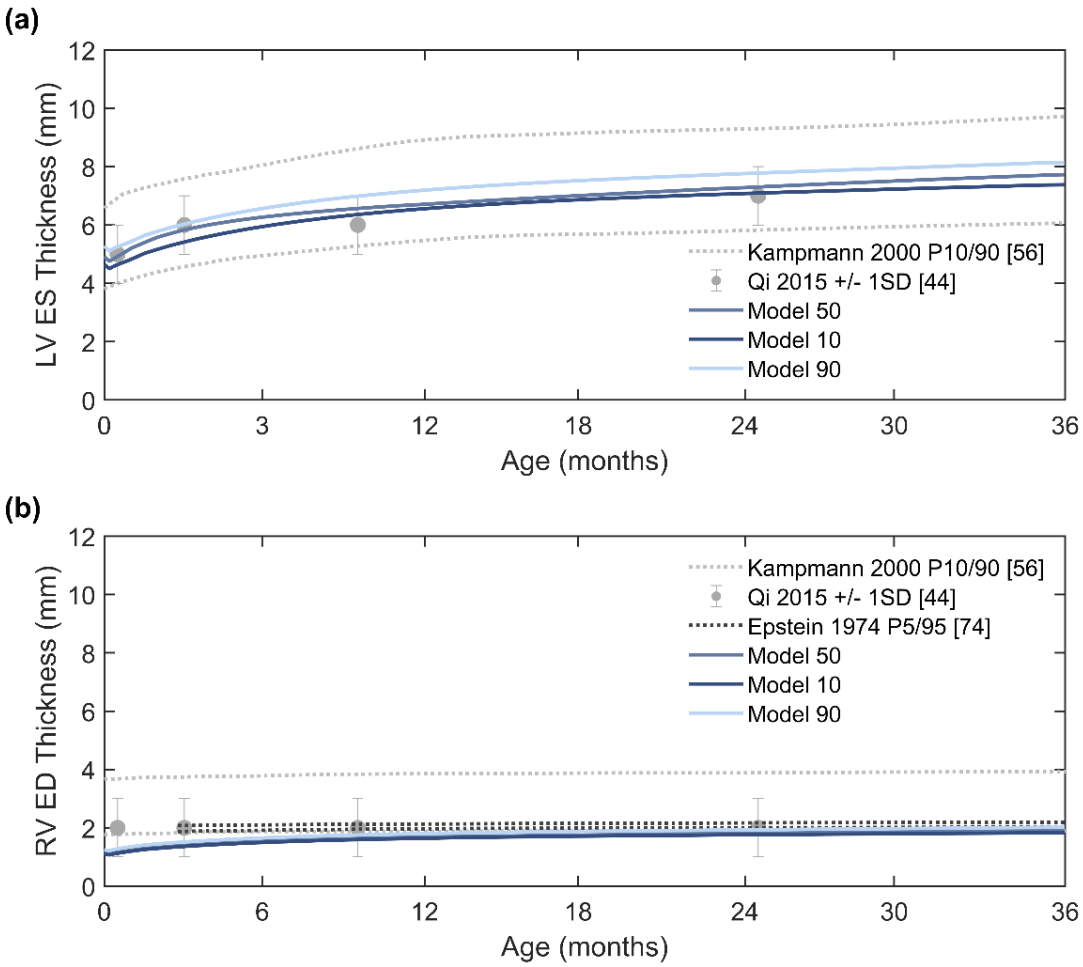

Figure S5: (A) Left ventricular end-systolic thickness and **(B)** right ventricular end-diastolic thickness for infants having a 10th, 50th, and 90th percentile weight trajectory for the first three years of life, compared to reported measurements [45,56,74]. Measurements from Qi et al. were from the sea-level cohort only. Dotted lines indicate 10^{th} and 90^{th} percentiles [56] or 5^{th} and 95^{th} percentiles [74]. Error bars on data indicate ± one standard deviation [45]. LV, left ventricle; RV, right ventricle; ES, end systole; ED, end diastole.

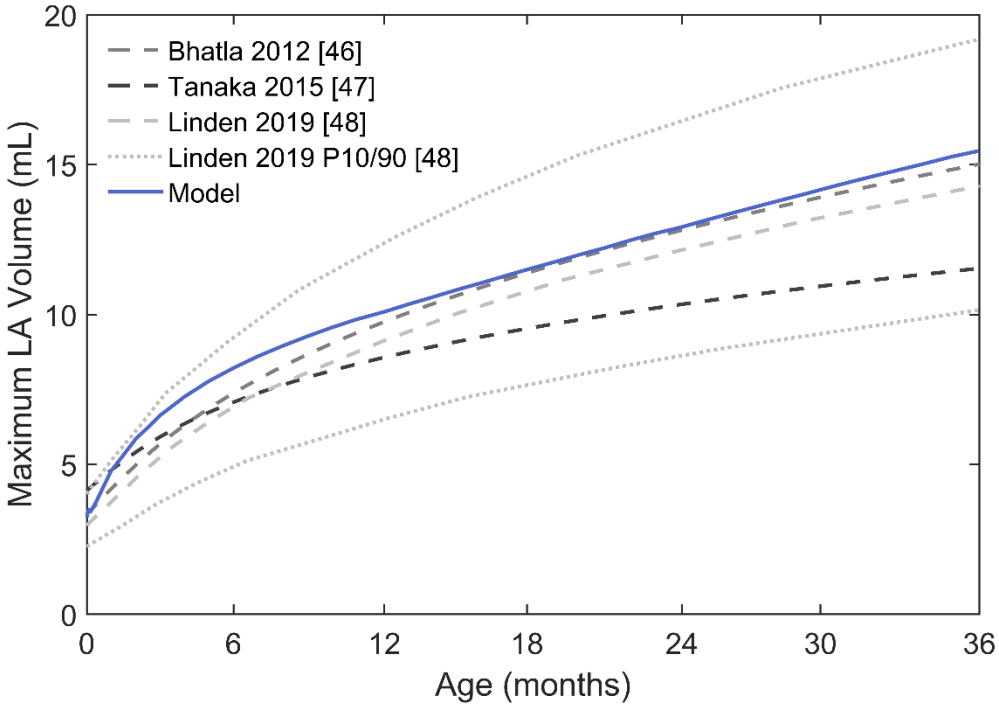

Figure S6: Simulated maximum left atrial volume for the first three years of life for a median-weight infant compared to reported measurements [46-48]. Dashed lines indicate mean values for reported data. Dotted lines indicate the 10th and 90th percentiles for reported data.

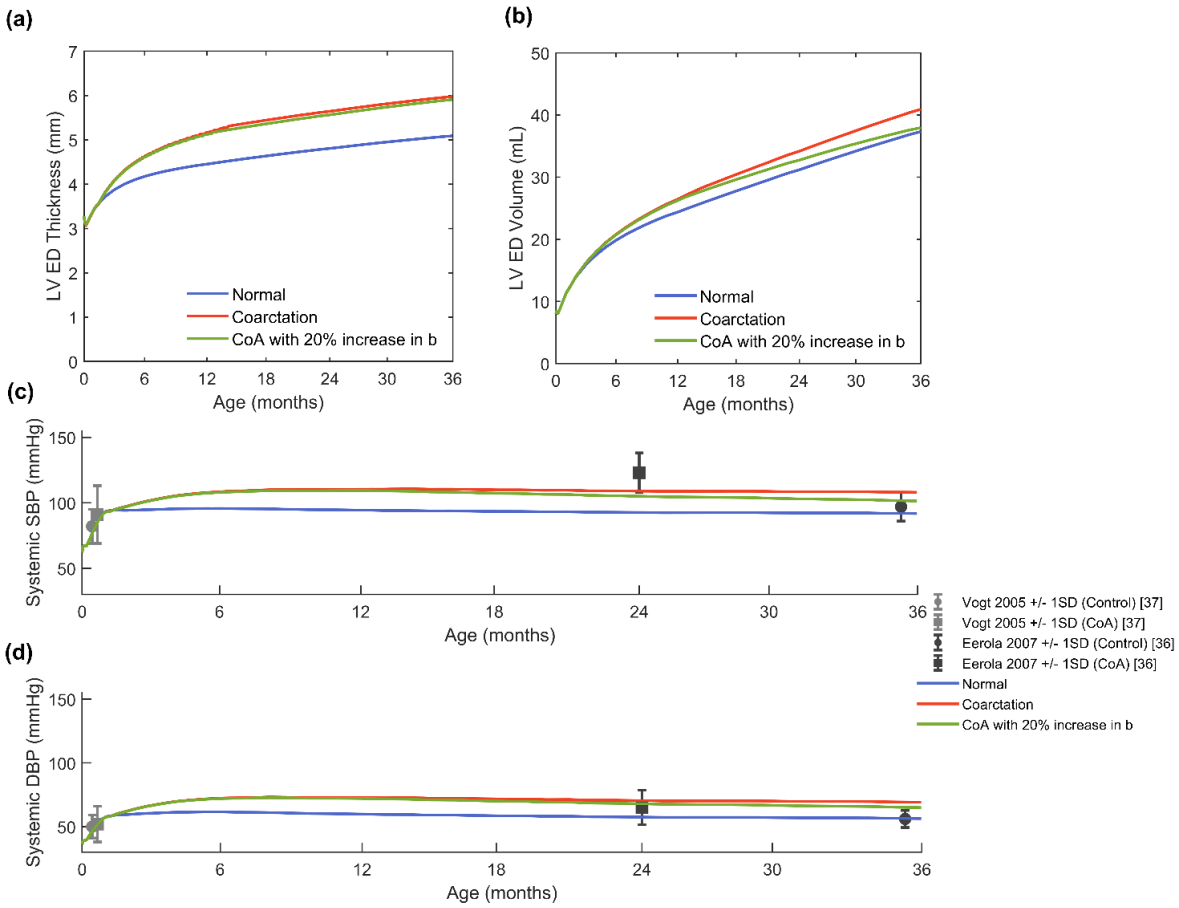

Figure S7: Comparison of normal (blue), standard coarctation (red), and coarctation with left ventricular fibrosis (green) simulations for **(A)** left ventricular thickness at end diastole, **(B)** left ventricular volume at end diastole, **(C)** systolic systemic pressure and **(D)** diastolic systemic pressure compared to reported control and coarctation measurements [36,37]. Fibrosis was simulated by gradually increasing stiffness material parameter b to a maximum of 20% over baseline. Error bars indicate ± one standard deviation. LV, left ventricle; RV, right ventricle; ED, end diastole; SBP, systolic blood pressure; DBP, diastolic blood pressure.

Table S1: Baseline Parameter Values for Eight-Compartment Model of Healthy 70 kg Adult Human			
Heart Parameters			
Parameter	*LA and RA*	*LV*	*RV*
End-systolic Elastance (Ees), mmHg/mL	0.69 (Hay 2005)	5.71 (Witzenburg 2018)	2.45 (Witzenburg 2018)
Unloaded Volume (V0), mL	17.5 (Hay 2005)	52.5 (Witzenburg 2018)	52.5 (Witzenburg 2018)
Scaling factor for EDPVR (B), mmHg	0.60 (Hay 2005)	0.18 (Witzenburg 2018)	0.08 (Witzenburg 2018)
Exponent for EDPVR (A), mL^{-1}	0.048 (Hay 2005)	0.030 (Witzenburg 2018)	0.030 (Witzenburg 2018)
Time to end systole (Tes), ms	130 (Kaye 2014, Morley 2007)	200 (Kaye 2014, Morley 2007)	200 (Kaye 2014, Morley 2007)
	MV		*TV*
Valve Resistance (RTV/RMV), mmHg*s/mL	0.0025 (Kaye 2014, Morley 2007)		0.0025 (Kaye 2014, Morley 2007)
Circulation Parameters			
Heart Rate (HR), beats/min	70 (Morley 2007)		
Stressed Blood Volume (SBV), mL	880 (Kaye 2014)		
Atrioventricular Delay (AVdelay), ms	160 (Kaye 2014, Morley 2007)		
	Pulmonic		*Systemic*
Characteristic Resistance (RCP/RCS), mmHg*s/mL	0.002 (Witzenburg 2018)		0.012 (Witzenburg 2018)
Vascular Resistance	0.04 (Kaye 2014)		0.58 (Witzenburg 2018)

(PVR/SVR), mmHg*s/mL		
Venous Resistance (RVP/RVS), mmHg*s/mL	0.006 (Santamore 1991)	0.006 (Santamore 1991)
Vascular Capacitance (CAP/CAS), mL/mmHg	4.1	2.5
Venous Capacitance (CVP/CVS), mL/mmHg	10.5 (Santamore 1991)	59.5 (Santamore 1991)

Table S1: Reference parameters for the eight-compartment model. LA, left atria; RA, right atria; LV, left ventricle; RV, right ventricle; MV, mitral valve; TV, tricuspid valve; EDPVR, end-diastolic pressure-volume relationship. Most parameters were taken from literature or scaled from healthy adult dogs weighing ~20kg. However, arterial resistances were fitted such that all systemic and pulmonary blood pressures were within normal ranges. Systemic arterial pressures: 70, 93/58 mmHg, pulmonary arterial pressures: 13, 22/8 mmHg (mean, systolic/diastolic).

Table S2: Scaling Factor for Model Parameters		
Parameter	*Units*	*Scaling Factor*
End-systolic Elastance (Ees)	mmHg/mL	-1
Unloaded Volume (V0)	mL	1
Scaling factor for EDPVR (B)	mmHg	0
Exponent for EDPVR (A)	1/mL	-1
Fraction of Cardiac Cycle in Systole (Tmax_percent)		-0.07
Resistance (R)	mmHg*s/mL	- 3/4
Capacitance (C)	mL/mmHg	1
Stressed Blood Volume (SBV)	mL	1
Product of Atrioventricular Delay and Heart Rate (Tmax)		0

Table S2: Allometric scaling factors. Fraction of the cardiac cycle in systole and the product of atrioventricular delay and heart rate are unitless.

APPENDIX TO CHAPTER 5

Table S1: Categorical variable comparisons between groups

Metric	Category	Non-Physiologic n	Success n	Failure n	Non-Physiologic vs Success *p*-value	Non-Physiologic vs Failure *p*-value	Success vs Failure *p*-value
Mitral valve regurgitation	Absent	906	173	245	0.001	< 0.001	< 0.001
	Mild	860	237	234	0.241	< 0.001	0.47
	Moderate	888	269	171	0.002	1	0.007
	Severe	1010	224	89	0.283	< 0.001	< 0.001
Aortic valve regurgitation	Absent	836	233	236	0.173	< 0.001	0.0186
	Mild	916	204	232	0.396	< 0.001	< 0.001
	Moderate	958	234	169	1	0.188	0.461
	Severe	954	232	102	1	< 0.001	< 0.001
Tricuspid valve regurgitation	Absent	899	253	234	0.093	< 0.001	0.323
	Mild	833	235	195	0.109	0.097	1
	Moderate	952	238	179	1	0.953	0.968
	Severe	980	177	131	< 0.001	< 0.001	0.999
Mitral valve stenosis	Absent	933	329	112	< 0.001	< 0.001	< 0.001
	Mild	872	359	126	< 0.001	< 0.001	< 0.001
	Moderate	823	174	319	0.113	< 0.001	< 0.001
	Severe	1036	41	182	< 0.001	0.130	< 0.001
Aortic valve stenosis	Absent	710	278	263	< 0.001	< 0.001	0.118
	Mild	800	346	227	< 0.001	< 0.001	0.004
	Moderate	999	212	160	0.063	0.005	1
	Severe	1155	67	89	< 0.001	< 0.001	0.004
Shunt type	None	1262	287	271	0.391	0.738	0.112
	RVPA	1090	312	299	0.015	< 0.001	0.041
	mBTT	1312	304	169	0.684	< 0.001	< 0.001

Table S2: Categorical variables, intragroup comparisons

Metric	Category	Non-Physiologic *p*-value	Success *p*-value	Failure *p*-value
Mitral valve regurgitation	Absent vs Mild	1	0.002	1
	Absent vs Moderate	1	< 0.001	< 0.001
	Absent vs Severe	0.034	0.023	< 0.001
	Mild vs Moderate	1	0.562	0.001
	Mild vs Severe	< 0.001	1	< 0.001
	Moderate vs Severe	0.007	0.105	< 0.001
Aortic valve regurgitation	Absent vs Mild	0.171	0.666	1
	Absent vs Moderate	0.006	1	< 0.001
	Absent vs Severe	0.008	1	< 0.001
	Mild vs Moderate	1	0.597	0.001
	Mild vs Severe	1	0.742	< 0.001
	Moderate vs Severe	1	1	< 0.001
Tricuspid valve regurgitation	Absent vs Mild	0.417	1	0.152
	Absent vs Moderate	0.925	1	0.009
	Absent vs Severe	0.181	< 0.001	< 0.001
	Mild vs Moderate	0.007	1	1
	Mild vs Severe	< 0.001	0.007	< 0.001
	Moderate vs Severe	1	0.004	0.013
Mitral valve stenosis	Absent vs Mild	0.589	0.876	1
	Absent vs Moderate	0.016	< 0.001	< 0.001
	Absent vs Severe	0.040	< 0.001	< 0.001

	Mild vs Moderate	1	< 0.001	< 0.001
	Mild vs Severe	< 0.001	< 0.001	0.002
	Moderate vs Severe	< 0.001	< 0.001	< 0.001
Aortic valve stenosis	Absent vs Mild	0.056	0.005	0.280
	Absent vs Moderate	< 0.001	0.003	< 0.001
	Absent vs Severe	< 0.001	< 0.001	< 0.001
	Mild vs Moderate	< 0.001	< 0.001	< 0.001
	Mild vs Severe	< 0.001	< 0.001	< 0.001
	Moderate vs Severe	< 0.001	< 0.001	< 0.001
Shunt type	None vs RVPA	< 0.001	0.634	0.404
	None vs mBTT	0.663	1	< 0.001
	RVPA vs mBTT	< 0.001	1	< 0.001